Karlsruhe Institute of Technology

Analysis tools and methods for tritium data taking with the KATRIN experiment

Zur Erlangung des akademischen Grades eines
Doktors der Naturwissenschaften
von der KIT-Fakultät für Physik
des Karlsruher Instituts für Technologie
genehmigte
Dissertation
von

M. Sc. Florian Heizmann

aus Stuttgart-Bad Cannstatt

Referent:	Prof. Dr. G. Drexlin
	Institut für Experimentelle Teilchenphysik, KIT
Korreferent:	Prof. Dr. U. Husemann
	Institut für Experimentelle Teilchenphysik, KIT
Korreferent:	Dr. K. Valerius
	Institut für Kernphysik, KIT

Tag der mündlichen Prüfung: 14.12.2018

Declaration of authorship Herewith I affirm that I wrote the current thesis on my own and without the usage of any other sources or tools than the cited ones and that this thesis has not been handed neither in this nor in equal form at any other official commission.

Erklärung der Selbstständigkeit Hiermit versichere ich, die vorliegende Arbeit selbstständig angefertigt zu haben und keine Hilfsmittel jenseits der kenntlich gemachten verwendet zu haben. Weiterhin habe ich weder diese noch eine äquivalente Version dieser Arbeit bei einer anderen Prüfungskommission vorgelegt.

Karlsruhe, 27.11.2018

. . . . . .

Florian Heizmann

ABSTRACT

The KArlsruhe TRItium Neutrino (KATRIN) experiment is targeted to determine the neutrino mass with an unprecedented sensitivity of 200 meV (90 % C.L.). To this end, KATRIN employs an intense gaseous tritium source combined with a precision retardation spectrometer of MAC-E-filter type. Since the completion of the KATRIN beamline in the fall of 2016, several pivotal milestones towards the start of neutrino-mass measurements have been achieved. In the thesis at hand, a tritium source gas model for the latest one among these milestones, the First Tritium campaign in May and June 2018, is developed and validated by several measures. This gas model is used for the analysis of the first KATRIN tritium spectra, including various approaches to account for gas model related systematic effects. Strategies for performing a blind neutrino mass analysis of the upcoming KATRIN neutrino mass data are developed, subject to a critical comparison, and tested on krypton commissioning data. Besides its main goal of neutrino mass search, KATRIN offers the potential to probe physics beyond the neutrino mass. For three example cases, the statistical sensitivity is evaluated and compared to existing limits.

Das KArlsruhe TRItium Neutrino (KATRIN) Experiment ist konstruiert, um die Neutrinomasse mit einer bisher unerreichten Sensitivität von 200 meV (90 % C.L.) zu bestimmen. Dafür kombiniert KATRIN eine starke gasförmige Tritiumquelle mit einem hochauflösendem MAC-E-Filter-Spektrometer. Seit der Fertigstellung des experimentellen Aufbaus im Herbst 2016 hat das KATRIN-Experiment mehrere zentrale Meilensteine erreicht. In der vorliegenden Arbeit wird ein Gasmodell für den letzten dieser Meilensteine – die erste Tritium-Zirkulation in der Tritium-Quelle im Mai und Juni 2018 – vorgestellt, und mit unterschiedlichen Messmethoden verglichen. Mit Hilfe des Gasmodells werden die ersten Tritiumspektren analysiert, wobei verschiedene Methoden zur Berücksichtigung von Systematiken am Beispiel des Gasmodells untersucht werden. Vorbereitend auf die kommenden Neutrinomassendaten werden in dieser Arbeit Methoden für eine blinde Neutrinomassenanalyse von β-Zerfall-basierten Tritiumspektren vorgestellt, miteinander verglichen, und an Hand von Kryptondaten getestet. Die Arbeit schließt mit einem Ausblick auf das Potential von KATRIN, Physik jenseits der Neutrinomasse zu untersuchen. Für drei Beispiele wird exemplarisch die statistische Sensitivität von KATRIN bestimmt und mit bestehenden experimentellen Erkenntnissen verglichen.

INTRODUCTION

Neutrinos fill a special role in particle physics, astrophysics and cosmology since they link the physics of the microcosm with the largest scales of the universe. This premise of the neutrinos to contribute to our understanding of a broad range of open questions in modern astroparticle physics is based on their particle nature and characteristics. The absolute neutrino mass scale probes the mass generation of the Standard Model of particle physics. KATRIN represents the most recent effort to determine the absolute mass scale of neutrinos in a model-independent way, after the predecessor experiments in Mainz [Kra+05] and Troitsk [Ase+11] could determine an upper limit of 2 eV (95 % C.L.) [Tan+18].

Motivation Located at the Karlsruhe Institute of Technology, the KATRIN experiment is targeted to determine the effective electron neutrino mass with an unprecedented sensitivity of 200 meV (90 % C.L.), based on three net years worth of data (corresponding to approximately five calendar years of data-taking). To reach this ambitious goal, KATRIN combines an ultra-luminous tritium source with high-resolution β-spectroscopy. In the course of the past two years, KATRIN successfully completed several milestones, ranging from first transmission of electrons through the entire beam line in 2016 to first recording of tritium β-decay spectra in 2018. The strategies and technical framework for the high-level analysis of tritium spectra form the basis for analysing the upcoming neutrino mass data. In order to prevent human observer's bias, a widely used method is the one of a blind analysis. However, since blinding was not applied in any of the previous β-decay neutrino mass experiments, appropriate analysis techniques and their implementation need to be developed from the ground up.

Objectives The objectives of this thesis are all closely linked to the tritium source of the KATRIN experiment. They span the complete analysis chain of the KATRIN experiment, from sensor-informed gas dynamics simulation to the high-level tritium spectrum analysis. In particular, these research goals include the following:

- The development and preparation of the source model for use in neutrino mass analysis. This requires extensions towards reading of sensor data and combining magnetic field and gas dynamics calculations.
- Blind analysis methods suitable for KATRIN's neutrino mass analysis should be identified, designed, implemented in the analysis framework, and subject to thorough testing and a critical comparative evaluation.
- The potential of KATRIN to constrain various new physics scenarios beyond the neutrino mass shall be explored through sensitivity studies.

Outline

1. In chapter 1, a brief overview of the current status of the field of neutrino physics is given.
2. The measuring principle and key components of the KATRIN experiment are presented in the second chapter 2.
3. As it is the central KATRIN component with regard to the thesis at hand, the tritium source is presented in more detail in chapter 3.
4. The various parts forming the source model of the KATRIN experiment are described in chapter 4, covering temperature, gas flow, and magnetic fields.
5. This source model is then used to analyse spectra from the First Tritium commissioning campaign (chapter 5) of the KATRIN experiment, a major milestone towards neutrino mass data taking.
6. In order to be prepared for an unbiased neutrino mass analysis, methods for a blind analysis of β-decay spectra are introduced and tested on simulations as well as on krypton commissioning data in chapter 6.
7. An outlook towards the interesting potential to employ precision measurements of the tritium β-decay spectrum for the exploration of new physics opportunities beyond the neutrino mass search is given in chapter 7.
8. The findings of this work are summarised in the concluding chapter 8.

CONTENTS

CHAPTER 1

NEUTRINO PHYSICS

*"**Neutrino:** Another a-tom in the lepton family. There are three different kinds. [...] They win the minimalist contest: zero charge, zero radius, and very possibly zero mass."*

– Leon M. Lederman in [LT93], 1993 –

From the very beginning of neutrino physics, the unique attributes of neutrinos described by L. Lederman in the quote above put neutrinos into the mystery box of particle physics. Another piece in this mystery puzzle was added when the non-zero mass of neutrinos was discovered by neutrino oscillation experiments [Ahm+01, Fuk+98]. The unique combination of interacting only weakly while being the most abundant massive particles in nature empowers neutrinos to help unravelling some of the outstanding open questions in particle physics and cosmology. Neutrinos provide the link from the smallest structures in the universe up to the largest, possibly holding a key to understanding the origin of matter and the structure formation in the early universe. Those answers are closely linked to the particle characteristics of the neutrino like charge, spin, chirality, and mass. Especially the latter is of special interest for cosmologists and particle physicists, as it probes the mass generation mechanism of the Standard Model (SM) of particle physics as well as the development of the universe on cosmological scales. The KATRIN experiment is dedicated to determining the effective electron anti-neutrino mass with unprecedented sensitivity of 200 meV (90 % C.L.) in a laboratory experiment. This chapter aims to give an overview of the current status of neutrino physics as the context in which the KATRIN experiment (see ch. 2) is carried out.

1.1. The story of the neutrino – or "what we know"

Though neutrinos were postulated about 100 years ago, it took decades and a vast number of dedicated experiments to acquire the knowledge about neutrinos that we have today. This section will briefly recapitulate the theoretical and experimental efforts taken to learn about what has become to be known as "ghost particle".

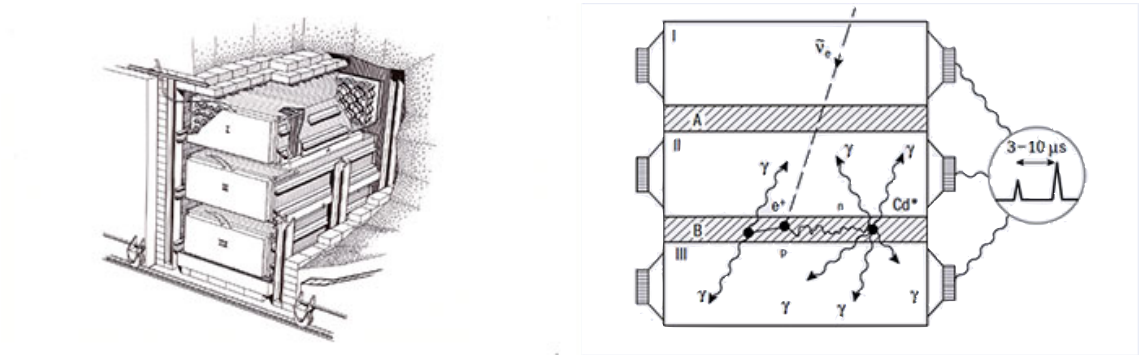

Figure 1.1.: **Project Poltergeist.** Left side shows the experimental set-up, right side the sandwich principle. Figure adapted from [Sut16].

1.1.1. Postulation and discovery of the neutrino

It was in the beginning of the 20$^{\text{th}}$ century, a time often referred to as a "golden age of physics" when Chadwick published his findings about the continuous shape of the spectrum of electrons emitted in β-decay [Cha14], which should mark the start of what is today known as neutrino physics.

The continuous β-spectrum – or why we need the neutrino The continuous β-decay spectrum measured by Chadwick in 1914 [Cha14] could not be explained at that time as β-decay was thought of as a two-body decay. In a "desperate attempt" to circumvent the apparent non-conservation of energy and momentum, Pauli postulated a third particle to be produced in β-decay [PKW64]. After Fermi came up with a point-like interaction model as theory of the β-decay [Fer34], experimentalists struggled for decades to detect the postulated ghostly particle.

Project Poltergeist and successive discoveries Due to the predicted low cross section of the order of $10^{-44}\,\text{cm}^2$ [BP34], the experimental detection took until 1956, when Cowan and Reines successfully carried out their "Project Poltergeist" [Cow+56] near the Savannah River nuclear power plant. Cowan and Reines used the large electron (anti-) neutrino flux of the nuclear reactor to detect the inverse β^+-decay products, positron e^+ and neutron n:

$$\bar{\nu}_\text{e} + \text{p} \rightarrow \text{e}^+ + \text{n}. \tag{1.1}$$

A unique identifier was found by using a sandwich layout of target and detector material. The "meat" of the sandwich consisted of a water tank with dissolved cadmium salt as target while the "bread" was made of liquid scintillator tanks with attached photomultiplier tubes (PMT). This layout enables safe discrimination of a neutrino signal. Neutrino signals are identified as two delayed gamma-ray pulses. The first gamma pulse is due to prompt annihilation of the positron with an electron in the target tank, while the second gamma pulse is emitted due to the neutron being captured by cadmium after a some µs long, moderated random walk.

Soon after, the second neutrino species was detected at the Brookhaven National Laboratory [Dan+62] by investigating the charged pion decay

$$\pi^+ \rightarrow \mu^+ + \nu_\mu \qquad \text{and} \qquad \pi^- \rightarrow \mu^- + \bar{\nu}_\mu. \tag{1.2}$$

The pions were produced by shooting 15 GeV protons from the Alternating Gradient Synchrotron onto a beryllium target. Danby et al. managed to obtain a pure neutrino beam by focussing the pion beam onto a massive iron block. The neutrinos in turn were detected via a spark chamber that could differentiate between the straight track of a muon and the electromagnetic shower of an electron. Thereby it was shown that there must be another neutrino species, called muon neutrino.

Last but not least, the tau neutrino completed the neutrino family. Perl et al. announced an anomalous lepton production in e^+e^- collisions at SLAC-LBL [Per+75], but it took another 25 years until the discovery was confirmed [Kod+01]. At Fermilab's Tevatron, accelerated 800 GeV protons were shot onto a tungsten target, resulting in tau neutrinos via the decay of charmed mesons

$$D_S^+ \to \tau^+ + \nu_\tau \qquad \text{and} \qquad D_S^- \to \tau^- + \bar{\nu}_\tau. \tag{1.3}$$

A series of lead, concrete and iron shields filtered out most of the background, enabling the detection of the residual tau-neutrinos via alternating steel and nuclear emulsion plates. The signature of a tau neutrino is then the decay of the produced tau-lepton, visible by a kink in the recorded trajectory. After applying all cuts, the DONUT collaboration harvested a total of four tau neutrino events [Kod+01].

Hints for the existence of a third generation of neutrinos already came from the observed decay width of the Z^0 boson. An early analysis of the decay width and cross section found the best fit at $N_\nu = 3.27 \pm 0.30$ [Dec+89] with subsequent improvements through the combination of more data sets from several detectors.

1.1.2. Neutrinos in the Standard Model of particle physics

The aforementioned three different flavours of neutrinos can be matched in the Standard Model (SM) of particle physics to three different charged leptons of the same flavour, forming the three weak isospin doublets. Neutrinos in the SM are uncharged, stable fermions interacting only via the weak force. This combination is unique in the SM, and it enables neutrinos to be their own anti-particle. The beauty of the SM is its concise description of the elementary particles and their origin of mass by virtue of the Higgs-mechanism. Verification of the Higgs prediction was announced in 2012, when the ATLAS and the CMS collaborations published the discovery of a Higgs-like particle [ATL12, CMS12]. This major breakthrough together with the previously found neutrino-related characteristics of the weak interaction contribute to the beauty of the overall picture of the successful Standard Model. Among those previously found characteristics are the violation of parity of the weak interaction [Wu+57] and the helicity of neutrinos [GGS58].

Helicity of neutrinos In 1957, Wu et al. discovered the parity violation of the weak interaction by using a magnetised ^{60}Co β-source [Wu+57]. Verified by subsequent experiments as in [GLW57], Wu and coworkers could show that the β-electrons favour emission anti-parallel to the nuclear spin, resulting in maximum parity violation of the weak interaction. This finding was also confirmed when Goldhaber et al.

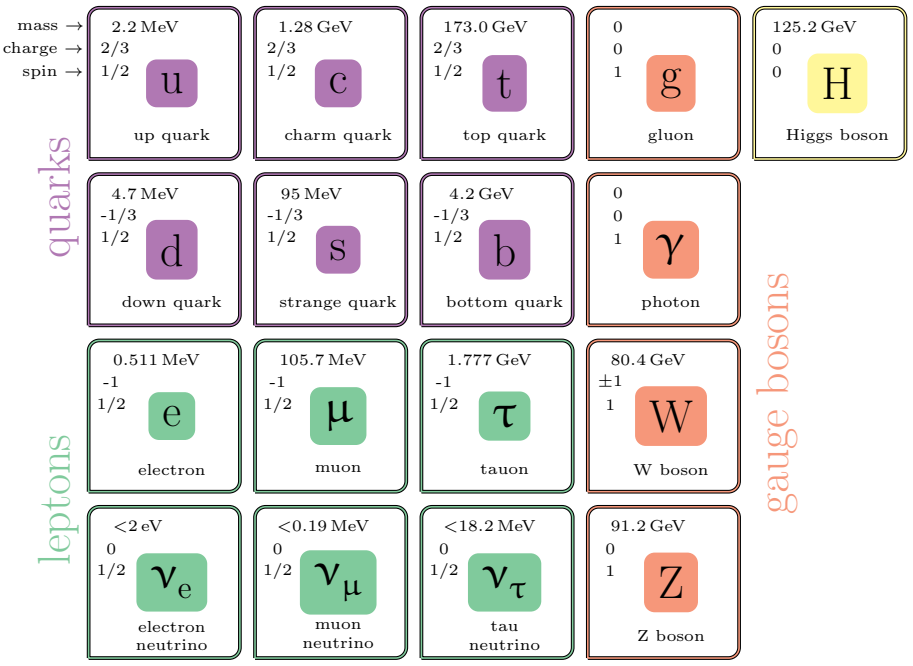

Figure 1.2.: **The Standard Model of particle physics.** It contains three generations of leptons and quarks (elementary particles of matter), four gauge bosons and the Higgs Boson. Particle properties taken from PDG [Tan+18].

measured the helicity of the neutrino in the year after [GGS58]. The helicity is defined as the projection of the spin $\boldsymbol{s}$ onto its momentum $\boldsymbol{p}$

$$h = \frac{\boldsymbol{s} \cdot \boldsymbol{p}}{s \cdot p}, \tag{1.4}$$

with positive helicity defined as right handed. An important characteristic of the helicity operator is its non-preservation of Lorentz-invariance for massive particles: we can always find a reference system in which the momentum is flipped for massive particles, while for massless particles the helicity is fixed.

Goldhaber et al. [GGS58] investigated the electron capture of $^{152\mathrm{m}}$Eu and the following deexcitation of the daughter nucleus ^{152}Sm* into ^{152}Sm. Due to the set-up they used, the helicity of the photons h_γ equals the helicity of the neutrinos h_ν, resulting in

$$h_\nu = -1.0 \pm 0.3. \tag{1.5}$$

Besides confirming Wu's result, this measurement directly implies the existence of only massless left-handed neutrinos and massless right-handed anti-neutrinos.

Combining these findings with the aforementioned detections, we have a total of three different, massless, uncharged, left-handed neutrinos in the SM (complemented by their respective right-handed anti-particles).

1.1.3. Neutrino flavour mixing – or why neutrinos need mass

Even though the SM can explain most characteristics of the neutrinos in a unified way, it cannot explain what was worth the 2015 Nobel Prize in Physics: neutrino

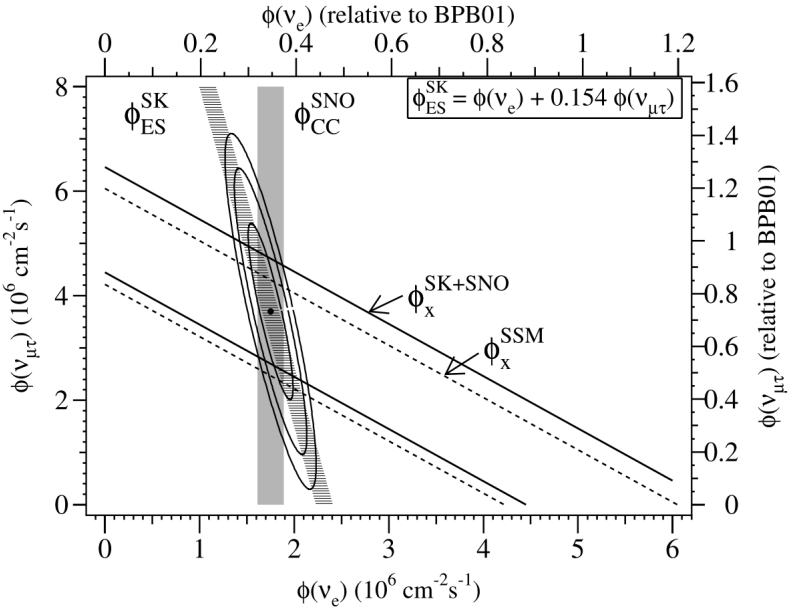

Figure 1.3.: **Solar neutrino flux.** Flux of ^{8}B solar neutrinos of μ or τ type versus electron neutrino flux. Dotted diagonal band shows the prediction by Bahcall et al. [BPB01], solid band shows the flux derived from SuperK and SNO measurements. Figure reprinted with permission from ref. [Ahm+01]. Copyright 2018 by the American Physical Society.

oscillations. T. Kajita (SuperK collaboration) and A. B. McDonald (SNO collaboration) received the prize "for the discovery of neutrino oscillations, which shows that neutrinos have mass" [The15].

The solar neutrino problem The results of the SNO collaboration also solved a long-standing mismatch between the Standard Solar Model (SSM) prediction and the measured flux of solar neutrinos. Ever since the first results of Davis' Homestake experiment [DHH68], the measured solar neutrino flux was just 1/3 of the SSM prediction by Bahcall [Bah64a, Bah64b]. Davis used a radio-chemical method to measure the neutrino flux from the sun via the transformation process

$$^{37}\mathrm{Cl} + \nu_\mathrm{e} \underset{\text{capture}}{\overset{\text{inv. decay}}{\rightleftharpoons}} {}^{37}\mathrm{Ar} + \mathrm{e}^-, \tag{1.6}$$

where he had to extract fewer than 100 ^{37}Ar atoms out of the 600 t of liquid perchlorethylene inside the Homestake gold mine. A proportional counter could then be used to detect the electron capture of ^{37}Ar as it resulted in a 2.8 keV Auger electron during the deexcitation of the produced $^{37}\mathrm{Cl}^*$. Though Davis lost information about the energy and the direction of the neutrinos by that method, he was able to calculate the neutrino flux that corresponds to the number of argon decays he observed. The solar neutrino flux deficit he determined was also confirmed by e.g. the GALLEX experiment [Ham+99], as well as by the first real-time experiment Kamiokande [Fuk+96].

In 2001, the SNO experiment finally resolved the solar neutrino problem and showed the SSM to be correct [Ahm+01]. The unique feature of the SNO experiment was that it could not only measure the elastic neutrino-electron scattering and the

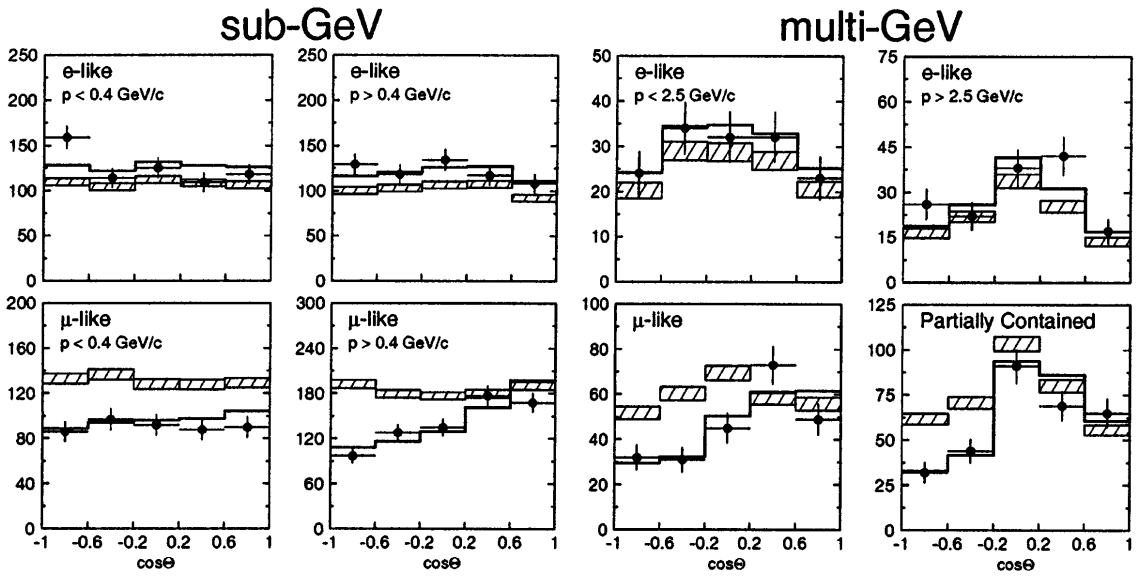

Figure 1.4.: **Atmospheric neutrinos zenith angle distributions.** Upward-going particles with $\cos\theta < 0$, downward-going $\cos\theta > 0$. Hatched region shows the MC expectation for no oscillations, bold line is the best-fit expectation for $\nu_\mu \leftrightarrow \nu_\tau$ oscillations. Figure reprinted with permission from ref. [Fuk+98]. Copyright 2018 by the American Physical Society.

charged current (CC) process, but it could also measure the neutral current (NC) process, which is sensitive to all three flavours. In order to discriminate between the two, SNO made use of heavy water D_2O as target for the solar neutrinos

$$\nu_e + D \to p + p + e^- \qquad \text{(CC)} \tag{1.7}$$

$$\nu_\alpha + D \to p + n + \nu_\alpha \qquad (\alpha = e, \mu, \tau) \qquad \text{(NC)}. \tag{1.8}$$

Even more, the SNO experiment found the electron neutrinos to only contribute 1/3 of the overall flux, the latter being in excellent agreement with the SSM prediction, compare fig. 1.3.

Atmospheric neutrino deficit The same behaviour was found for a different neutrino flavour by the SuperK experiment. The large volume of SuperK enabled the study of atmospheric neutrinos [Fuk+98]. Those neutrinos are produced as spallation products of cosmic rays interacting with the Earth's atmosphere. The atmospheric neutrinos travel through the Earth and may interact with matter to produce muons. Those muons in turn cause a sharp Cherenkov ring in the SuperK detector, in contrast to the diffuse EM-shower of electrons. As the muons are produced forward-peaked with regard to the neutrino momentum, spatial information is preserved. This enables investigations of the zenith-angle distribution of the neutrinos, which is expected to be flat as the cosmic rays hit the Earth isotropically. However, SuperK observed a significant deficit for up-going muon neutrinos [Fuk+98], compare fig. 1.4.

Neutrino mixing The solution to both problems, the solar neutrino deficit as well as the atmospheric neutrino deficit, is found by a process called neutrino oscillations. This process enables neutrinos to be produced as e.g. electron neutrinos

and be detected as muon neutrinos. The theoretical description was developed in the 50's and 60's by Pontecorvo [Pon57, Pon58, Pon68], and Maki, Nakagawa, and Sakata [MNS62]. The weak interaction creates the neutrinos in one of their weak flavour eigenstate $|\nu_\alpha\rangle$ ($\alpha = \mathrm{e}, \mu, \tau$). When neutrinos travel through spacetime, they are in a mass eigenstate $|\nu_i\rangle$ ($i = 1, 2, 3$) with well-defined masses. The connection between the weak flavour eigenstate and the mass eigenstate is what enables the neutrino oscillation mechanism. It can be thought of as a rotation matrix, the so-called PMNS matrix U, named after the founders of the formalism. The 3×3 matrix transforms weak flavour eigenstates into mass eigenstates via [Pon57, Pon58, MNS62]

$$|\nu_\alpha\rangle = \sum_i U_{\alpha i} |\nu_i\rangle \qquad \text{and} \qquad |\nu_i\rangle = \sum_\alpha U^*_{\alpha i} |\nu_\alpha\rangle \,, \tag{1.9}$$

defining U as

$$\begin{aligned} U &= \begin{bmatrix} U_{\mathrm{e}1} & U_{\mathrm{e}2} & U_{\mathrm{e}3} \\ U_{\mu 1} & U_{\mu 2} & U_{\mu 3} \\ U_{\tau 1} & U_{\tau 2} & U_{\tau 3} \end{bmatrix} \\ &= \begin{bmatrix} c_{12}c_{13} & s_{12}c_{13} & s_{13}\mathrm{e}^{-\mathrm{i}\delta} \\ -s_{12}c_{23} - c_{12}s_{23}s_{13}\mathrm{e}^{\mathrm{i}\delta} & c_{12}c_{23} - s_{12}s_{23}s_{13}\mathrm{e}^{\mathrm{i}\delta} & s_{23}c_{13} \\ s_{12}s_{23} - c_{12}c_{23}s_{13}\mathrm{e}^{\mathrm{i}\delta} & -c_{12}s_{23} - s_{12}c_{23}s_{13}\mathrm{e}^{\mathrm{i}\delta} & c_{23}c_{13} \end{bmatrix} \cdot \begin{bmatrix} 1 & 0 & 0 \\ 0 & \mathrm{e}^{\mathrm{i}\alpha_{21}/2} & 0 \\ 0 & 0 & \mathrm{e}^{\mathrm{i}\alpha_{31}/2} \end{bmatrix}, \end{aligned} \tag{1.10}$$

with $s_{ij} = \sin\theta_{ij}$ and $c_{ij} = \cos\theta_{ij}$. This leaves us with the following fundamental parameters describing neutrino mixing:

1. three mixing angles θ_{12}, θ_{13}, θ_{23},
2. depending on the Dirac or Majorana nature of the neutrinos, a Dirac CP violation phase $\delta = [0, 2\pi]$, and two Majorana CP violation phases α_{21}, α_{31},
3. three neutrino masses m_1, m_2, m_3.

Depending whether neutrinos are Dirac or Majorana neutrinos, we have seven (similar to the CKM matrix for quarks) or nine additional parameters to describe particle interactions with three massive neutrinos.

For the case of n neutrino flavours and accompanying massive neutrinos, the mixing matrix (1.10) has to be extended to an $n \times n$ matrix, having $n \cdot (n-1)/2$ mixing angles and masses, plus $(n-1)(n-2)/2$ Dirac CP-phases or $(n-1)$ Majorana CP-phases [Tan+18].

Neutrino oscillations As shown by e.g. Giunti [Giu04], the covariant fully-relativistic treatment of neutrino oscillations results in the same transition probability as the classical derivation via the Schrödinger equation. For reasons of simplicity, we will stick to the latter and further derive the calculations for one dimension x only.

In vacuum, the mass eigenstates $|\nu_i\rangle$ are physical eigenstates of the free Hamiltonian $\mathcal{H}$ with energy eigenvalues E_i, $\mathcal{H}\,|\nu_i\rangle = E_i\,|\nu_i\rangle$. The propagation along x can be

treated as plane wave solutions $|\nu_i(x,t)\rangle$ to the Schrödinger equation

$$\mathcal{H}\,|\nu_i(x,t)\rangle = \mathrm{i}\hbar\frac{\partial}{\partial t}\,|\nu_i(x,t)\rangle\,, \tag{1.11}$$

with

$$|\nu_i(x,t)\rangle = \mathrm{e}^{-\frac{\mathrm{i}}{\hbar}(E_i t - p_i x)}\,|\nu_i\rangle\,. \tag{1.12}$$

The time dependency of the mass eigenstates may now be used to find the time dependency of the flavour eigenstates as

$$\begin{aligned}|\nu_\alpha(x,t)\rangle &\overset{(1.9)}{=} \sum_i U_{\alpha i}\,|\nu_i(x,t)\rangle \overset{(1.12)}{=} \sum_i U_{\alpha i}\mathrm{e}^{-\frac{\mathrm{i}}{\hbar}(E_i t - p_i x)}\,|\nu_i\rangle \\ &\overset{(1.9)}{=} \sum_{i,\beta} U_{\alpha i}\mathrm{e}^{-\frac{\mathrm{i}}{\hbar}(E_i t - p_i x)}U^*_{\beta i}\left|\nu_\beta\right\rangle, \end{aligned} \tag{1.13}$$

where we have introduced a second flavour β. At times $t > 0$, this shows that a generated pure flavour α may evolve into a different flavour β, with an amplitude of

$$A_{\nu_\alpha\to\nu_\beta}(x,t) = \left\langle \nu_\beta \,\middle|\, \nu_\alpha(x,t)\right\rangle \overset{(1.13)}{=} \sum_i U_{\alpha i}U^*_{\beta i}\mathrm{e}^{-\frac{\mathrm{i}}{\hbar}(E_i t - p_i x)}\,, \tag{1.14}$$

and a time- and space-dependent transition probability of

$$P_{\nu_\alpha\to\nu_\beta}(x,t) \;=\; \left|A_{\nu_\alpha\to\nu_\beta}(x,t)\right|^2 \;\overset{(1.14)}{=} \sum_{i,j} U_{\alpha i}U^*_{\beta i}U^*_{\alpha j}U_{\beta j}\mathrm{e}^{-\frac{\mathrm{i}}{\hbar}(E_i t - p_i x)}\mathrm{e}^{\frac{\mathrm{i}}{\hbar}\left(E_j t - p_j x\right)}. \tag{1.15}$$

As all currently observed neutrinos have energies in the MeV range [Tan+18] with masses less than 2 eV (see sec. 1.3), we can treat neutrinos in the ultra-relativistic limit $m_i c^2 \ll p_i c \approx E$, resulting in

$$E_i = \sqrt{m_i^2c^4 + p_i^2c^2} \approx p_i c + \frac{m_i^2c^4}{2E}. \tag{1.16}$$

Together with the travelled distance of the neutrinos $x = L = v\cdot t \approx c\cdot t$, we can rewrite the exponent of eq. (1.12) as

$$E_i t - p_i x \overset{(1.16)}{=} \left(p_i c + \frac{m_i^2c^4}{2E}\right)\cdot t - p_i L = \frac{m_i^2c^3}{2}\frac{L}{E}. \tag{1.17}$$

Now the well-known mass squared differences appear in the transition probability as

$$P_{\nu_\alpha\to\nu_\beta}(x,t) \overset{(1.17)}{=} \sum_{i,j} U_{\alpha i}U^*_{\beta i}U^*_{\alpha j}U_{\beta j}\mathrm{e}^{-\frac{\mathrm{i}}{\hbar}\frac{\Delta m_{ij}^2 c^3}{2}\frac{L}{E}} = P_{\nu_\alpha\to\nu_\beta}(L,E), \tag{1.18}$$

using $\Delta m_{ij}^2 = m_i^2 - m_j^2$.

Two flavour oscillations For a system with two flavours α and β, eq. (1.18) reduces to

$$P_{\nu_\alpha\to\nu_\beta}(L,E) = \sin^2(2\theta)\sin^2\left(\frac{\Delta m^2c^3}{4\hbar}\frac{L}{E}\right), \tag{1.19}$$

with the mixing angle θ and the two-dimensional rotation matrix

$$U = \begin{bmatrix} \cos\theta & \sin\theta \\ -\sin\theta & \cos\theta \end{bmatrix}. \tag{1.20}$$

From eq. (1.19), we can intuitively see the oscillation mechanism characteristics. Generated with the same energy, heavier mass eigenstates travel at lower phase velocity than the lighter ones, resulting in changing interference of the corresponding flavour components. Thereby, we can detect a neutrino created in flavour state α as neutrino of flavour β with the probability given in eq. (1.15) and (1.19), respectively. The "survival probability" to detect the neutrino in the flavour it was generated is

$$P_{\nu_\alpha \to \nu_\alpha}(L, E) = 1 - P_{\nu_\alpha \to \nu_\beta}(L, E). \tag{1.21}$$

A key characteristic for each oscillation type is its amplitude defined by the mixing angle θ_{ij}, and its frequency defined by the mass difference Δm^2_{ij}. A full oscillation cycle in the two flavour case is defined as the so-called oscillation length

$$L_{\text{osc}} = \frac{4\pi\hbar E}{\Delta m^2 c^3}. \tag{1.22}$$

Note that the absolute mass scale is not accessible from the determination of the oscillation parameters. From eq. (1.19) we can see the parameters of interest of oscillation experiments: they use the energy E and the travelled distance L of the neutrinos to determine the mixing angle and the squared mass difference.

Experimental results Over the last decades, a vast number of experiments determined the oscillation parameters of mixing angle and mass squared difference using different neutrino sources, detection baselines and techniques. An overview of present results is given in tab. 1.1, obtained from the listings in [Tan+18].

A direct measurement of θ_{13} is possible with *reactor neutrino experiments*, using the large flux of $\bar{\nu}_e$ from nuclear power plants. As the energy of these neutrinos is limited to about 10 MeV [Tan+18], the only channel that can be observed is the $\bar{\nu}_e$-disappearance. In order to study reactor neutrinos, mostly liquid scintillators are used to identify the inverse β-decay events from $\bar{\nu}_e + p \to e^+ + n$. The detection principle is identical to the one used by Cowan and Reines for the detection of the neutrino [Cow+56], a prompt positron signal followed by a delayed neutron capture to reject background events. Commonly, gadolinium-doped liquid scintillator is used to effectively detect the neutrons. Most recent experiments in the field of reactor neutrino measurements are Double Chooz [Abe+12a, Abe+12b], Daya Bay [An+12, An+13], and RENO [Ahn+12]. In order to mitigate systematic effects, all of them used a multiple detector set-up with at least two detectors, a detector near (about 400 m) and far (about 1 km) from the power plant. The near detector provides the calibration for the $\bar{\nu}_e$-disappearance measured by the far detector, enabling the determination of $\theta_{13} \approx 8°$ [Tan+18] listed in tab. 1.1. A future reactor neutrino experiment is JUNO [Li14], a 20 kton detector at medium-distance (50 km) but with very good energy resolution to determine the neutrino mass ordering [Tan+18].

For historical reasons, measurements of θ_{12} are typically associated with *solar neutrino experiments*, while θ_{23} is attributed to *atmospheric neutrino experiments* (same

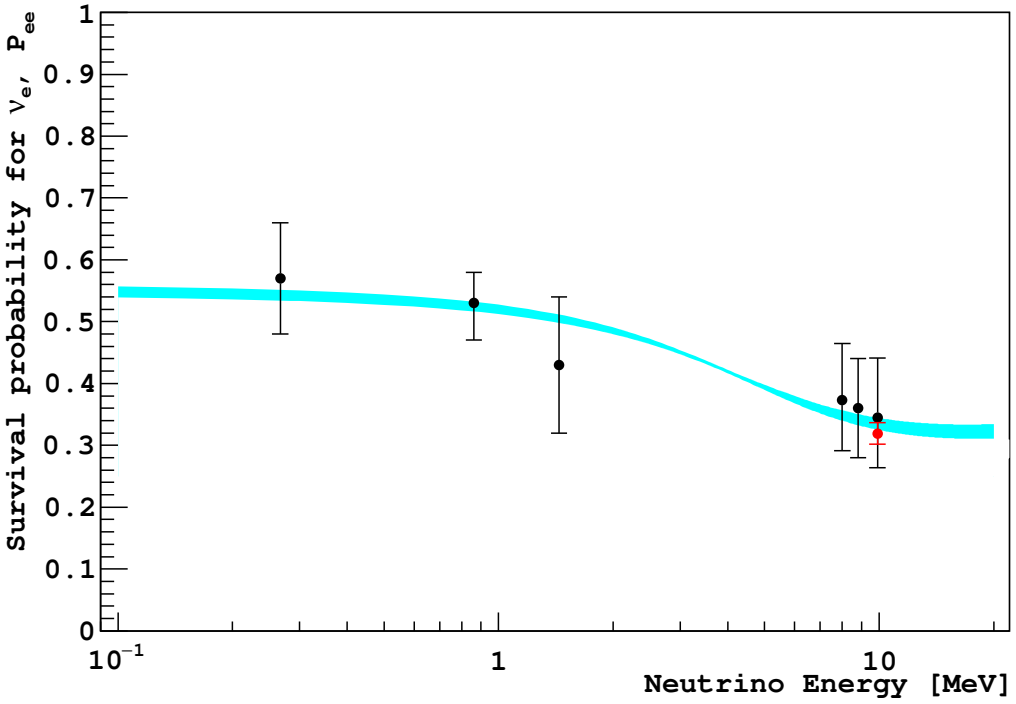

Figure 1.5.: **Energy dependent survival probability of solar neutrinos.** Error bars represent 1σ theo.+exp. uncertainties, error band states the prediction of MSW-LMA solution. Figure reprinted with permission from ref. [Tan+18]. Copyright 2018 by the American Physical Society.

for the corresponding mass squared differences). Solar neutrino experiments nowadays usually rely on detecting the Cherenkov light of the charged particles in a large water tank, resulting from the solar neutrino interaction. In contrast to the reactor neutrino mixing angle θ_{13}, the solar neutrino oscillation experiments SuperK and SNO, complemented by the reactor disappearance experiment KamLAND [Egu+03, Ara+05] showed a rather large (though not maximal) mixing of $\theta_{12} \approx 34^\circ$ [Abe+16] with a mass difference Δm^2_{21} of order $10^{-5}\,\mathrm{eV}^2$ [Gan+13]. With the measurement of the low-energy solar neutrinos, KamLAND [Gan+15, Abe+11] and Borexino [Ago+17a, Ago+17b] could show that the MSW-LMA[1] is the solution to the solar neutrino problem (sec. 1.1.3). The MSW effect results in an effectively higher mass for the electron neutrinos in matter, due to CC-interactions, and is energy dependent. Spectroscopic measurements by Borexino revealed [Ago+17a, Ago+17b] that the best agreement is found with the LMA solution of the MSW effect, see fig. 1.5.

Atmospheric neutrino experiments like SuperK mostly use the Cherenkov technique to detect neutrinos produced by the spallation processes of cosmic rays in the Earth's atmosphere. The characteristics of atmospheric neutrinos were mainly determined by SuperK, and nowadays are constrained by accelerator disappearance experiments [Tan+18]. Both, mixing angle and mass difference, are larger than for the solar neutrinos. The particle data group uses data from MINOS [Ada+14], IceCube [Aar+15], NOvA [Ada+17], and T2K [Abe+17] to estimate the mixing an-

[1] Mikheyev, Smirnov, and Wolfenstein predicted the influence of matter on neutrino oscillations [MS86, Wol78]. LMA is short for large mixing angle.

Table 1.1.: **Experimental results of the neutrino oscillation parameters.** Values obtained through three neutrino mixing scheme using results of several experiments [Tan+18]. The values for $\sin^2(\theta_{23})$ and Δm^2_{32} are the ones from assuming normal neutrino mass hierarchy.

parameter	value	source
$\sin^2(\theta_{12})$	0.307 ± 0.013	sun, reactor
Δm^2_{21}	$(7.53 \pm 0.18) \cdot 10^{-5}\,\mathrm{eV}^2$	sun, reactor
$\sin^2(\theta_{23})$	$0.417^{+0.025}_{-0.028}$	atmosphere, accelerator
$\left\lvert\Delta m^2_{32}\right\rvert$	$(2.51 \pm 0.05) \cdot 10^{-3}\,\mathrm{eV}^2$	atmosphere, accelerator
$\sin^2(\theta_{13})$	$(2.12 \pm 0.08) \cdot 10^{-2}$	reactor

gle $\theta_{23} \approx 40°$ for normal hierarchy. Adding data from RENO [Cho+16], and Daya Bay [An+17], the absolute value of the mass difference is estimated to $2.5 \times 10^{-3}\,\mathrm{eV}^2$ for normal hierarchy.

One of the key open questions of neutrino oscillations is the sign of Δm^2_{23}, equal to knowing the mass ordering of neutrinos, and whether neutrinos conserve or violate CP symmetry by their CP phases. Those are addressed by long-baseline accelerator (anti-)neutrino oscillation experiments like NOvA [Ayr+04] and DUNE [Ada+13].

1.2. Current research – or "what we do not know"

As introduced in the previous section, two of the remaining riddles of neutrinos are their mass ordering and whether neutrinos violate CP symmetry. Furthermore, the absolute mass scale cannot be addressed with oscillation experiments. This section lists the missing characteristics and outlines possible theories and the experimental effort to determine the missing pieces in the neutrino puzzle.

1.2.1. Can neutrinos explain the missing anti-matter?

The sign of atmospheric mass differences is linked to both, the modification of flavour transformation due to the MSW effect, as well as the possible CP-violation. Up to now, we have three possible configurations for the absolute mass values of neutrinos, as the sign of the atmospheric neutrino mass difference is not known (also compare fig. 1.6):

- **Normal hierarchy**: $m_1 < m_2 \ll m_3$
- **Inverted hierarchy**: $m_3 \ll m_1 < m_2$
- **Quasi-degenerate**: $m_1 \approx m_2 \approx m_3 \approx m_0$.

The JUNO experiment is currently being set up to explore the mass hierarchy and help in identifying the CP-violating phase by a scintillation-experiment with an

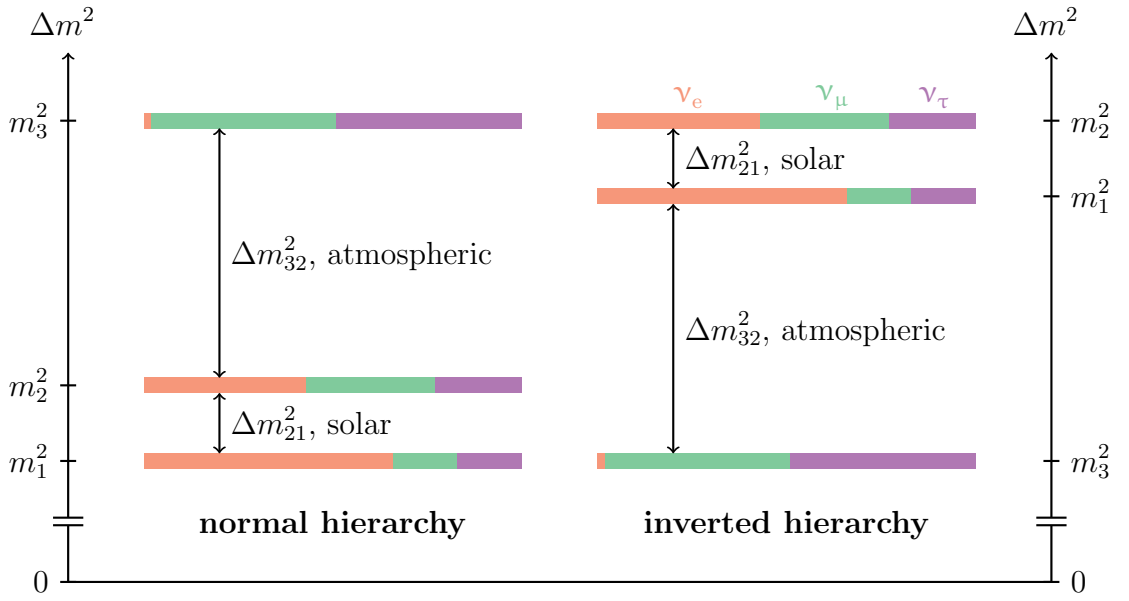

Figure 1.6.: **Neutrino mass hierarchy.** Left side shows the normal hierarchy, right side the inverted one; the quasi-degenerate case is not shown. The squared mass differences are not to scale. The flavours are symbolised by the different colours: orange for electron, green for muon, and purple for tau flavour. Figure drawn after [Tan+18].

energy resolution of 3 %/MeV. This unprecedented energy resolution will enable resolving the tiny difference between normal and inverted mass ordering in the sub-dominant atmospheric neutrino oscillation pattern [An+16]. With the mass ordering known, determining the CP-violating phase is possible with long-baseline accelerator (anti-)neutrino oscillation experiments like NOvA [Ayr+04] and DUNE [Ada+13]. For long-baseline accelerator experiments, there might be a degeneracy in the CP-phase δ and the mass ordering. However a separate measurement of the mass ordering like provided from JUNO [An+16] would resolve this degeneracy and enable determination of both, mass hierarchy and CP-phase.

The determination of the CP-phase might eventually help to resolve one of the greatest cosmological and particle physics mysteries: the dominance of matter over anti-matter in the universe. CP violation in the neutrino sector could potentially lead to the so-called leptogenesis [FY86, KRS85], resulting in a lepton asymmetry, which is in turn linked to the baryon asymmetry in the universe and thereby to the matter-to-antimatter relation.

One mechanism which nicely links the CP-violation and thereby the matter-anti-matter ratio to the generation of neutrino mass is the see-saw mechanism [FY86, Min77, GRS79, Yan80, MS80, SV80], which will be discussed in the next section.

1.2.2. Extensions to the Standard Model - or how neutrinos might get their mass

In the SM, the mass of a particle is generated via coupling to the Higgs field ϕ. The Higgs field has several ground states, connected via SU(2) gauge transformations.

Therefore we can choose a ground state according to the vacuum expectation value

$$\langle\phi\rangle = \frac{1}{\sqrt{2}}\begin{pmatrix}0\\v\end{pmatrix}, \tag{1.23}$$

being the only free parameter in the SM which bears the dimension of mass [PS95]. The coupling of the fermions to the Higgs field is of Yukawa type, resulting in the Lagrangian [PS95]

$$\mathcal{L}_{\text{Fermion}}(\phi, A, \psi) = \bar{\psi}\gamma^{\mu}D_{\mu}\psi + G_{\psi}\bar{\psi}\phi\psi, \tag{1.24}$$

with the gauge covariant derivative D_{μ}. Using the Euler-Lagrange mechanism, the Fermion-Higgs Lagrangian eq. (1.24), and left- and right-handed currents via $\psi = \psi_{\text{L}} + \psi_{\text{R}}$ [PS95] results in the equation of motion for a Higgs-field coupled fermion

$$\mathrm{i}\partial\!\!\!/\psi_{\text{L}} - \frac{G_{\psi}}{\sqrt{2}}\begin{pmatrix}0\\v\end{pmatrix}\psi_{\text{R}} = 0. \tag{1.25}$$

We can now identify the mass term by comparison with the Dirac equation

$$\left(\mathrm{i}\partial\!\!\!/ - m\right)\psi = 0, \tag{1.26}$$

where we see the maximum parity violation of the weak interaction. The neutrino oscillations results discussed in sec. 1.1.3 showed that neutrinos have mass. The simplest way to add a neutrino mass would be using an additional right-handed neutrino field ν_{R} which would not participate in the weak interaction. However, though this would give neutrinos mass in the same way as the charged leptons get their mass (Dirac mass), it would require an additional Yukawa coupling strength. The latter would need to be much smaller than the other particles Yukawa coupling to match the smallness of the neutrino mass.

As neutrinos are uncharged particles, a more elegant solution is the combination of the Majorana mechanism with the see-saw mechanism [Min77, GRS79, Yan80, MS80, SV80]. For reasons of simplicity, only the case of one neutrino flavour is considered. Decomposing the Dirac Lagrangian into its chiral components results in two Dirac equations, with the Majorana mass in the Lagrangian

$$\mathcal{L}^{\text{M}}_{\text{L/R}} = -\frac{1}{2}m_{\text{L/R}}\,\bar{\nu}^{\text{C}}_{\text{L/R}}\,\nu_{\text{L/R}}. \tag{1.27}$$

Together with the Dirac mass $\mathcal{L}^{\text{D}} = -m_{\text{D}}\bar{\nu}\nu$ ($\nu = \nu_{\text{L}} + \nu_{\text{R}}$), we have the overall mass term $\mathcal{L}^{\text{D+M}} = \mathcal{L}^{\text{D}} + \mathcal{L}^{\text{M}}_{\text{L}} + \mathcal{L}^{\text{M}}_{\text{R}}$, which can be shortened to

$$\mathcal{L}^{\text{D+M}} = -\frac{1}{2}N^{\text{T}}_{\text{L}}MN_{\text{L}} \qquad \text{with } N_{\text{L}} = \begin{pmatrix}\nu_{\text{L}}\\ \nu^{\text{C}}_{\text{R}}\end{pmatrix} \text{ and } M = \begin{pmatrix}m_{\text{L}} & m_{\text{D}}\\ m_{\text{D}} & m_{\text{R}}\end{pmatrix}. \tag{1.28}$$

The see-saw mechanism [Min77, GRS79, Yan80, MS80, SV80] now provides two essential ingredients for neutrino mass generation. First, it enables a small mixing angle between left- and right-handed neutrinos, which is needed since right-handed

(sterile) neutrinos have not been observed yet. Second, it enables small active neutrino masses, as we can choose $m_{\mathrm{L}} = 0$ [Min77, GRS79, Yan80, MS80, SV80] and $m_{\mathrm{D}} \ll m_{\mathrm{R}}$, so that the following masses are generated:

$$m_1 \approx \frac{m_{\mathrm{D}}^2}{m_{\mathrm{R}}} \text{ and } m_2 \approx m_{\mathrm{R}}. \tag{1.29}$$

Therefore, the neutrino mass m_1 can become small, and likewise the mixing angle $\tan 2\theta = 2m_{\mathrm{D}}/m_{\mathrm{R}}$. Accordingly, the active ν_{L} would mainly consist of the light ν_1 and the sterile ν_{R} of the heavy ν_2, which agrees with current observations in the neutrino sector.

1.3. Determination of the neutrino mass

Now that we have the reasoning for a non-zero neutrino mass from oscillation experiments, let us discuss some experiments that take on the challenge of determining the absolute mass scale of neutrinos. While some of them rely on underlying model-assumptions (sec. 1.3.1), the model-independent experiments rely on conservation of energy and momentum only (sec. 1.3.2).

1.3.1. Model-dependent determination

In this section, the model-dependent neutrino mass estimation methods based on observational cosmology, the search for $0\nu\beta\beta$-decay, and supernova neutrinos will be discussed. Note, that each of these methods makes some intrinsic (model) assumption to infer the neutrino mass. The discussion in this section follows the textbook by Perkins [Per09].

Cosmology Nowadays, the strongest claimed limits on the neutrino mass come from analyses of the Cosmic Microwave Background (CMB), with most recent measurements of the CMB by the Planck collaboration [Agh+18]. In the CMB spectrum, the cosmological fingerprint of massive neutrinos is a suppression of the power spectrum on small scales [Agh+18], linked to the relativistic free-streaming of neutrinos after their decoupling. Using the Λ-CDM model[2], the upper part of the multipole CMB spectrum, and constraints from baryonic acoustic oscillations [Beu+11, Ros+15, Ala+17], an upper limit on the sum of neutrino masses of

$$\sum_i m_i < 0.12\,\mathrm{eV} \quad (95\,\%\ \mathrm{C.L.}) \tag{1.30}$$

has been inferred. It has to be noted that, although this limit is quite stringent, it encompasses a dependence on the validity of the underlying Λ-CDM model, as well as on the different observational data sets combined to achieve the result. In the above-quoted paper [Agh+18], the Planck collaboration states limits which range up to 0.60 eV. A model-independent measurement of neutrino masses through a laboratory experiment would therefore ideally supplement cosmological observations.

[2] The Λ-CDM model uses a cosmological constant Λ for dark energy and cold dark matter (CDM) to describe the development of the universe after the Big Bang. Due to its good agreement with cosmological observations [Agh+18], it is often referred to as standard model of Big Bang cosmology.

Supernova neutrinos During the core-collapse of a supernova (type Ib, Ic, II), 99 % of the gravitational energy released is emitted in the form of neutrinos at MeV energies, with a burst length of about 10 s [Per09]. The observation of the neutrino burst signal of the supernova SN1987A enables to determine the the measured arrival time difference of two neutrinos ass

$$\Delta t = t_2 - t_1 = \Delta t_0 + \frac{Lc^3 m_\nu^2}{2}\left(\frac{1}{E_2^2} - \frac{1}{E_1^2}\right). \tag{1.31}$$

With the measured Δt, and the energies E_1, E_2 of the neutrinos, only the emission time difference $\Delta t_0 = t_{02} - t_{01}$ and the neutrino mass m_ν are unknown. Using a model for the neutrino emission in the core-collapse supernova, Δt_0 can be constrained, enabling an estimation of the neutrino mass. Loredo and Lamb derive an upper limit from the neutrino burst signal of SN1987A as [LL02]

$$m_\nu < 5.7\,\text{eV} \quad (95\,\%\ \text{C.L.}). \tag{1.32}$$

Neutrino-less double beta-decay As introduced in sec. 1.2.2, the see-saw mechanism provides a nice explanation for the smallness of the active neutrino mass. If neutrinos are their own anti-particles, so-called Majorana particles, this would enable a very rare decay, the double β-decay without emission of neutrinos [DKT85] ($0\nu\beta\beta$). Therein, a virtual neutrino is exchanged between the decaying nuclei which is possible due to the Majorana nature. From the observed half life of a $0\nu\beta\beta$-decay $T_{1/2}^{0\nu\beta\beta}$, the effective Majorana neutrino mass can be determined via (see e.g. ref. [EM17])

$$\langle m_{\beta\beta}\rangle^2 \leq \left|\sum_{i=1}^{3} U_{ei}^2 m_i\right|^2 = \frac{1}{G^{0\nu\beta\beta}\cdot\left|M^{0\nu\beta\beta}\right|^2 \cdot T_{1/2}^{0\nu\beta\beta}}, \tag{1.33}$$

with the phase space factor $G^{0\nu\beta\beta}$, and the nuclear matrix element $M^{0\nu\beta\beta}$. The estimated neutrino mass strongly depends on the uncertainty of the calculated nuclear matrix element. Most recent estimations of the effective Majorana mass by the Majorana [Aal+18], GERDA [Ago+18], EXO-200 [Alb+18], and CUORE [Ald+18] experiment result in values in the range

$$\langle m_{\beta\beta}\rangle < 0.11 - 0.52\,\text{eV} \quad (90\,\%\ \text{C.L.}). \tag{1.34}$$

The to date most stringent limit on on the effective Majorana neutrino mass is stated by the KamLAND-Zen collaboration [Gan+16] as

$$\langle m_{\beta\beta}\rangle < 0.061 - 0.165\,\text{eV} \quad (90\,\%\ \text{C.L.}). \tag{1.35}$$

It has to be noted that in the squared sum of the mixing matrix elements cancellations may occur due to the Majorana phases. This particular feature, in turn, may give access to the Majorana phases $\alpha_{1,2}$ by comparison of $\langle m_{\beta\beta}\rangle$ to a model-independent measurement.

1.3.2. Model-independent determination

In order to determine the neutrino mass in a direct, model-independent way, the most promising candidate today is investigating the kinematics of single β-decay.

Thereby, the only prerequisites are energy and momentum conservation, with no assumption made on the nature of the neutrinos. The neutrino mass manifests in form of missing energy in the β-decay

$$ {}^{A}_{Z}N \rightarrow {}^{A}_{Z+1}N' + \mathrm{e}^- + \bar{\nu}_\mathrm{e}. \tag{1.36} $$

Using Fermi's Golden Rule [Fer34], the β-decay rate can be derived [KAT05, Dre+13] (neglecting for now possible final states of the daughter molecule)

$$ \begin{aligned} \frac{\mathrm{d}\Gamma}{\mathrm{d}E} =& \frac{G_\mathrm{F}^2 \cdot \cos\theta_\mathrm{C} \cdot |M|^2}{2\pi^3} \cdot F(Z+1, E) \cdot p \cdot (E + m_\mathrm{e}) \\ & \cdot \sqrt{(E_0 - E)^2 - m_{\bar{\nu}_\mathrm{e}}^2} \cdot \Theta(E_0 - E - m_{\bar{\nu}_\mathrm{e}}), \end{aligned} \tag{1.37} $$

with Fermi's coupling constant G_F, Cabibbo angle θ_C, transition matrix element M, Fermi function $F(Z+1, E)$, kinetic energy and momentum of the electron E, p, mass of the electron m_e, endpoint of the β-decay spectrum $E_0 = Q - m_\mathrm{e}$, and the decay energy Q. An exemplary tritium β-decay spectrum and the effect of a non-zero neutrino mass are shown in fig. 1.7.

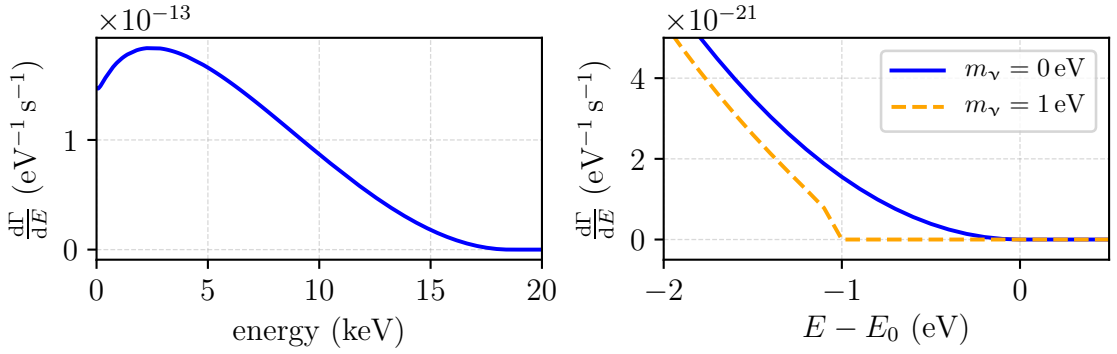

Figure 1.7.: **Tritium decay spectrum.** Left side shows the full-range tritium β-decay spectrum, right side an enlarged endpoint region.

Several experiments are currently in their commissioning phase or being set up in order to explore the kinematics of β-decay with unprecedented sensitivity. The most promising techniques are a calorimetric approach followed by the ECHo [Gas+17] and HOLMES [Nuc+18] collaborations, a cyclotron radiation approach followed by Project 8 [MF09] and the MAC-E filter approach [BPT80, KR83, LS85, Pic+92] followed by the Mainz [Kra+05], Troitsk [Ase+11], and KATRIN experiments [KAT05].

Calorimetric approach The ECHo [Gas+17] and HOLMES [Nuc+18] collaborations investigate the electron capture on ^{163}Ho, with a Q-value of 2.8 keV. Like for the β-decay spectrum, the rate close to the spectral endpoint depends on the neutrino mass squared [LV11]. Therefore, the ECHo and HOLMES collaborations aim for a high energy resolution combined with a detector read out by microwave SQUID multiplexing. The ECHo experiment determines the released energy via Metallic Magnetic Calorimeters, which are measuring the change in magnetisation due to the temperature increase of the detector [Bur+08]. With a projected energy resolution of $\Delta E < 3\,\mathrm{eV}$, and a set-up of up to 10^5 detectors, a sub-eV neutrino mass sensitivity may be reached [Dre+13]. For HOLMES, the Transition Edge Sensor (TES) technology is pursued [Nuc+18].

Cyclotron radiation approach The idea of the Project 8 experiment is to observe single electrons from tritium β-decay via their cyclotron radiation emitted in a magnetic field [MF09]. The power emitted by each electron depends on its relative velocity (and thereby the energy) as well as its pitch angle relative to the magnetic field. With a finite minimum observation time of 30 µs [MF09] as the minimum time between electron-gas scattering, the required long electron path length favours an electron trap configuration [MF09, Dre+13]. An obvious choice is a magnetic bottle with increased magnetic field at both ends of the tritium gas-filled tube. Microwave antenna arrays around the tube and at both ends can be used to detect the emitted cyclotron radiation and to reconstruct the electron's energy. In recent work, the Project 8 collaboration showed the promising detection technique to achieve energy resolutions of about 3 eV at energies of about 30 keV, achieved in the successful measurement of ^{83m}Kr-lines [Asn+15, Esf+17]. In a staged approach, the near-term aim of Project 8 is to achieve 2 eV sensitivity (90 % C.L.) with a molecular tritium source and to further explore a novel atomic tritium source technique to probe the inverted hierarchy mass scale on a longer perspective [Esf+17].

MAC-E filter approach The most recent model-independent limits on the neutrino mass come from the Mainz [Kra+05] and the Troitsk [Ase+11] experiment using the MAC-E filter technique to analyse the tritium β-decay spectrum. The MAC-E filter uses magnetic adiabatic collimation with electrostatic energy analysis, it is described in more detail in sec. 2.2.4. An ideal β-emitter for neutrino mass determination from kinematics is tritium, due to the following advantages:

- favourably low β-decay Q-value of 18.6 keV,
- super-allowed decay, so no energy dependence and corrections of the nuclear transition matrix element are needed,
- short half life of $T_{1/2} = 12.3$ yr (related to the previous item),
- mother and daughter nucleus have low Z values, leading to simple electron interactions and low inelastic scattering probability.

Note that β-decay spectroscopy estimates an effective neutrino mass as incoherent sum of the neutrino mass eigenstates

$$m^2_{\bar{\nu}_e} = \sum_{i=1}^{3} |U_{ei}|^2 \cdot m_i^2, \tag{1.38}$$

as present energy resolutions of spectroscopic experiments cannot resolve the different mass eigenstates. Combining the Mainz limit of 2.3 eV (95 % C.L.) [Kra+05] and the Troitsk limit of 2.05 eV (95 % C.L.) [Ase+11] for the effective electron (anti-)neutrino mass results in the currently most stringent model-independent limit [Tan+18] of

$$m_{\bar{\nu}_e} < 2.0\,\text{eV} \quad (95\,\%\ \text{C.L.}). \tag{1.39}$$

The KATRIN experiment is targeted to determine the neutrino mass with a one order of magnitude better sensitivity than the existing limit. KATRIN has successfully performed a sequence of dedicated commissioning phases, using electrons from a photo electron source, conversion electrons from ^{83m}Kr [Are+18b, Are+18a], and just recently first tritium β-decay data [Are+19]. Details about its experimental set-up are presented in the next chapter.

CHAPTER 2

THE KARLSRUHE TRITIUM NEUTRINO EXPERIMENT

The KArlsruhe TRItium Neutrino (KATRIN) Experiment is dedicated to determining the neutrino mass with an unprecedented sensitivity of 200 meV (90 % C.L.). Compared to the predecessor experiments at Mainz and Troitsk, this is a sensitivity gain of a factor of 10. Since the observable is the neutrino mass square, this requires an overall improvement of the neutrino mass square uncertainty of a factor of 100. In order to achieve this aspiring goal, KATRIN performs high precision spectroscopy of the tritium β-decay spectrum close to the endpoint at 18.6 keV.

This chapter gives an overview of the measuring principle of KATRIN (sec. 2.1), the set-up that allows to realise this measuring principle (sec. 2.2), and the analysis software used to access and analyse the produced data (sec. 2.4).

2.1. Neutrino mass from tritium β-decay

KATRIN investigates the β-decay of molecular tritium

$$\mathrm{T}_2 \rightarrow \left({}^3\mathrm{HeT}\right)^+ + \mathrm{e}^- + \bar{\nu}_\mathrm{e}. \tag{2.1}$$

The decay rate can be derived using Fermi's Golden Rule [Fer34]

$$\begin{aligned}\frac{\mathrm{d}\Gamma}{\mathrm{d}E} =& \frac{G_\mathrm{F}^2 \cdot \cos\theta_\mathrm{C} \cdot |M|^2}{2\pi^3} \cdot F(Z+1,E) \cdot p \cdot (E+m_\mathrm{e}) \\ & \cdot \sum_{fs} P_{fs} \cdot f_\mathrm{rad}(E-E_{fs}) \cdot \varepsilon_{fs} \cdot \sqrt{\varepsilon_{fs}^2 - m_{\bar{\nu}_\mathrm{e}}^2} \cdot \Theta(\varepsilon_{fs} - m_{\bar{\nu}_\mathrm{e}}),\end{aligned} \tag{2.2}$$

with the parameters G_F, θ_C, M, $F(Z,E)$, electron kinetic energy E, electron momentum p, electron mass m_e, and tritium endpoint E_0 defined according to eq. (1.37). As an extension to the single-nucleus treatment of eq. (1.37), this equation also considers molecular effects via the final states energy E_{fs}, resulting in a reduced endpoint energy of $\varepsilon_{fs} = E_0 - E - E_{fs}$. Due to interaction of the electron with virtual photons in the Coulomb field of the nucleus, the emitted electrons lose energy. This energy loss is implemented into the spectrum calculation as radiative corrections by the factor $f_\mathrm{rad}(E - E_{fs})$ according to the recommendations by Repko and Wu [RW83].

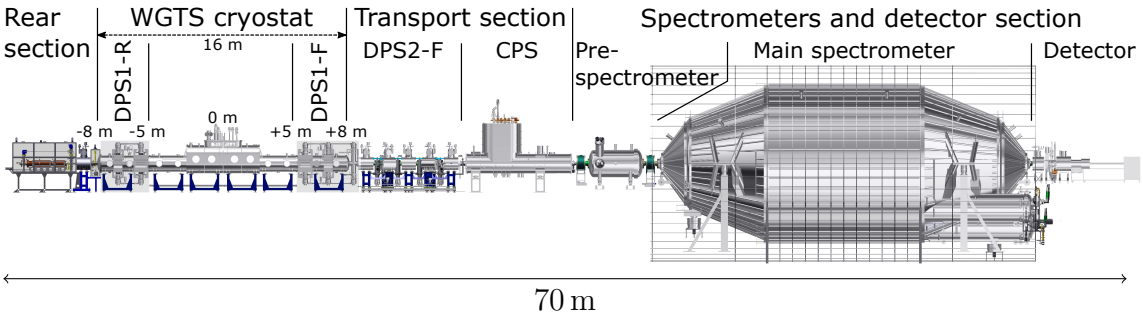

Figure 2.1.: **KATRIN set-up.** The individual components fulfil specific tasks to enable reaching the 200 meV sensitivity:

- Rear section - monitoring and calibration of the tritium source
- WGTS - providing a stable activity of $10^{11}\,\mathrm{s}^{-1}$
- DPS - tritium removal
- CPS - tritium removal
- Pre-spectrometer - pre-selection of the high-energy part of the β-decay spectrum
- Main spectrometer - high-resolution β-decay spectroscopy
- Detector - counting the transmitted electrons

KATRIN analyses the decay spectrum according to eq. (2.2) via the MAC-E filter principle [BPT80, KR83, LS85, Pic+92]. The (effective) neutrino mass is then extracted as a shape distortion close to the endpoint. The MAC-E filter acts as a high-pass filter, resulting in a measurement of an integrated spectrum by stepping the retardation potential [KAT05, Kle+18]. Using a response function to describe the electron transport through the experiment, this integrated spectrum reads [Kle+18]

$$\dot{N}(U) = \frac{1}{2} N_\mathrm{T} \int_{qU}^{E_0} \frac{\mathrm{d}\Gamma}{\mathrm{d}E} \cdot R(E,U)\,\mathrm{d}E. \tag{2.3}$$

Thereby, the signal rate depends on the number of tritium nuclei in the source N_T, the retarding voltage of the spectrometer U, and the response function $R(E,U)$ (only considering electrons emitted in direction of the detector, see sec. 2.2.4).

2.2. Components of the KATRIN experiment

The 70 m long set-up that KATRIN uses to measure the integrated count rates in eq. (2.3) is depicted in fig. 2.1. Electrons originating from β-decay in the ultra-luminous Windowless Gaseous Tritium Source (WGTS, sec. 2.2.1) are magnetically guided via the transport section (sec. 2.2.3) to the energy analysing spectrometer section (sec. 2.2.4). Those passing the spectrometers are finally counted at the detector (sec. 2.2.5). Several instruments monitor the activity, stability and composition

of the tritium gas (sec. 2.2.2), which is continuously injected into the WGTS and pumped out at both ends.

2.2.1. The Windowless Gaseous Tritium Source

In order to reach the unprecedented neutrino mass sensitivity of 200 meV, KATRIN makes use of a large β-decay rate of $10^{11}\,\mathrm{s}^{-1}$ provided by per-mille stable circulation of tritium gas in the Windowless Gaseous Tritium Source (WGTS) [Gro+08, Bab+12, PSB15, HS17]. A daily throughput of about 40 g of tritium in a closed gas loop system results in a longitudinally integrated gas column density in the WGTS beam tube of $\mathcal{N} = 5 \times 10^{21}\,\mathrm{m}^{-2}$ or roughly 300 µg of tritium. Tritium is injected with a pressure of about 3 µbar in the centre of the 10 m long beam tube and pumped out at both ends via turbomolecular pumps (TMPs). On their way to the pump ports, the tritium molecules may decay, leaving the daughter molecule in a possibly excited final state (see sec. 2.2.2). Electrons originating from the tritium decay are magnetically guided to both ends of the WGTS. The rear section uses the incoming electron flux for monitoring purposes (see sec. 2.2.2) while the other half of the electrons is used to perform neutrino mass spectroscopy with the spectrometers and detector section (sec. 2.2.4). In order to account for effects that affect the electron's energy on their way to the detector, the concept of a response function [KAT05, Kle+18] is introduced. The source-related quantities of interest are the energy loss ϵ of the electrons due to scattering on residual gas, which is described by the energy loss function $f(\epsilon)$ [KAT05, Kle+18], and the scattering probabilities for s-fold scattering, $P_s(z, \theta)$. The energy loss per scattering solely depends on the scattering cross section, as investigations by S. Groh showed the scattering attributed angular change to be negligible [Gro15]. The scattering probabilities $P_s(z, \theta)$ in general depend on the longitudinal density profile in the WGTS and the pitch angle of the electrons relative to the magnetic field lines.

Energy loss function The total scattering cross section consists of an elastic part and an inelastic part. In refs. [Gei64, Liu87], the elastic scattering cross section $\sigma_{\mathrm{el}} = 0.29 \times 10^{-22}\,\mathrm{m}^2$ was shown to be one order of magnitude smaller than the inelastic part, which is measured by Aseev et al. to $\sigma_{\mathrm{inel}} = (3.40 \pm 0.07) \cdot 10^{-22}\,\mathrm{m}^2$ [Ase+00]. As the neutrino mass uncertainty raised by neglecting the elastic scattering cross section is about $5 \times 10^{-5}\,\mathrm{eV}^2$, it is often neglected in the modelling of the β-decay spectrum. Aseev et al. determined the inelastic scattering cross section by fitting an empirical model to the energy loss function spectrum. The empirical model consists of a low-energy Gaussian describing the (discrete) excitation processes and a high-energy Lorentzian for the continuum due to ionisation of the tritium molecules

$$f(\epsilon) = \begin{cases} A_1 \cdot \mathrm{e}^{-2\left(\frac{\epsilon-\epsilon_1}{\omega_1}\right)^2} & , \epsilon < \epsilon_{\mathrm{c}} \\ A_2 \cdot \frac{\omega_2^2}{\omega_2^2 + 4(\epsilon-\epsilon_2)^2} & , \epsilon \geq \epsilon_{\mathrm{c}} \end{cases}, \tag{2.4}$$

with $A_1 = (0.204 \pm 0.001)\,\mathrm{eV}^{-1}$, $A_2 = (0.0556 \pm 0.0003)\,\mathrm{eV}^{-1}$, $\omega_1 = (1.85 \pm 0.02)\,\mathrm{eV}$, $\omega_2 = (12.5 \pm 0.1)\,\mathrm{eV}$, fixed $\epsilon_1 = 12.6\,\mathrm{eV}$, and $\epsilon_2 = (14.30 \pm 0.02)\,\mathrm{eV}$. The transition from one to the other part of the energy loss function eq. (2.4) is smooth due to the chosen critical energy of $\epsilon_{\mathrm{c}} = 14.09\,\mathrm{eV}$. Multiple scattering is accounted for via

convolving the energy loss function $f(\epsilon)$ with itself, compare the right-hand panel in fig. 2.2.

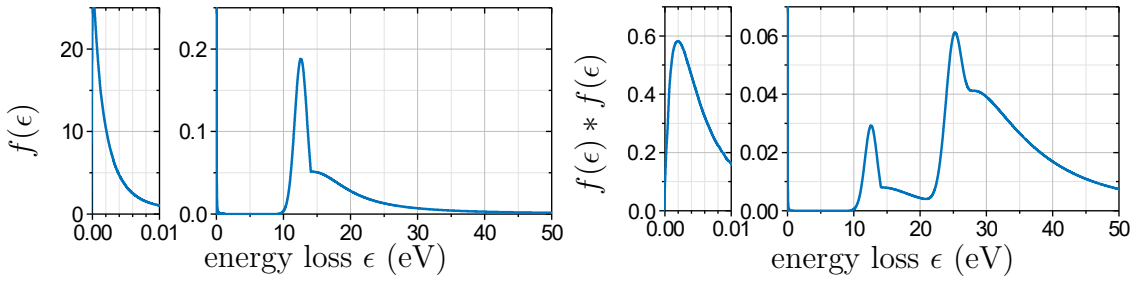

Figure 2.2.: **Energy loss function.** Left-hand side shows the energy loss for single scattering, right-hand side for two-fold scattering. The enlarged regions show the elastic scattering contribution. Figure adapted from [Kle+18].

Scattering probabilities In order to take into account spatial inhomogeneities of the magnetic field or the gas distribution in the source, the model partitions the source into so-called voxels (volume elements). The longitudinal extent of the voxels is given by the length of the source divided by the number of slices used, and the azimuthal and radial segmentation can be chosen as to magnetically map the pixels of the detector (see fig. 2.3). The probability for an electron to reach the detector

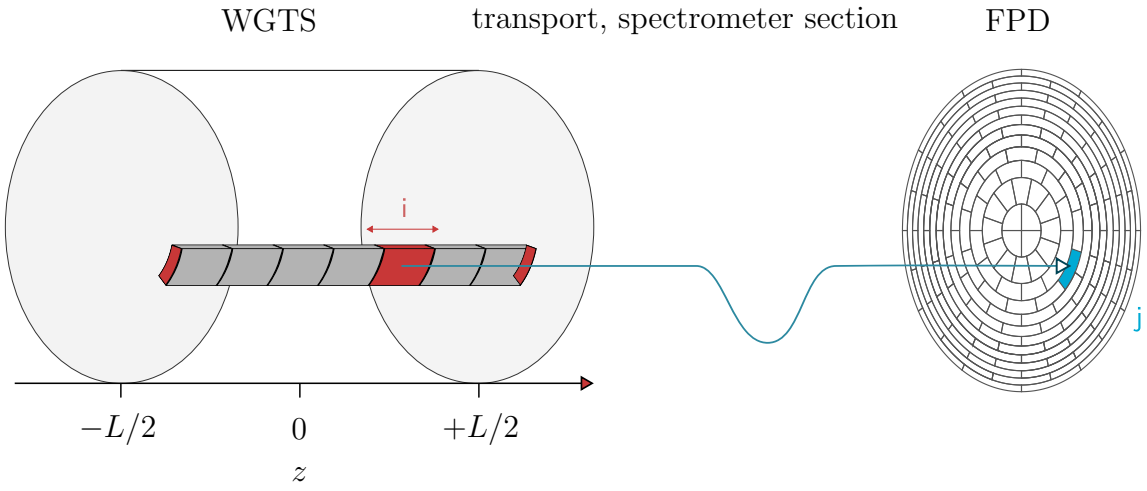

Figure 2.3.: **Voxelisation concept.** Each pixel j can be mapped onto corresponding voxels in the source. These voxels ares stacked longitudinally (index i) to calculate the rate for pixel j. Figure adapted from [Kle+18].

after undergoing s-fold scattering in the source depends on the total scattering cross section σ_{tot} and on the source geometry conditions, starting position and starting pitch angle θ (angle between electron momentum and magnetic field, $\theta = \angle(\boldsymbol{p}, \boldsymbol{B})$). Both source conditions define the effective column density $\mathcal{N}_{\text{eff}}$ that the electron has to pass. Electrons with a larger pitch angle take a longer path through the source and therefore "see" an increased effective column density. The effective column density

for an electron starting at longitudinal position z is

$$\mathcal{N}_{\text{eff}}(z,\theta) = \frac{1}{\cos\theta} \int_{z}^{L/2} n(z')\,\mathrm{d}z', \tag{2.5}$$

with the longitudinal density distribution $n(z)$ and the starting pitch angle θ. Using the effective column density, we can calculate the probability for this electron to leave the source after scattering s times according to a Poisson distribution[1] [KAT05, Kle+18]

$$P_s(z,\theta) = \frac{\left(\mathcal{N}_{\text{eff}}(z,\theta)\cdot\sigma\right)^s}{s!} \cdot \mathrm{e}^{-\mathcal{N}_{\text{eff}}(z,\theta)\cdot\sigma}. \tag{2.6}$$

Doppler effect The thermal motion of the tritium gas molecules combined with their bulk velocity due to the gas flow lead to a broadening of the electron energy. In ref. [Kle+18] it is shown that the resulting broadening (sigma) can be described by a Gaussian approximately centred[2] at 0 with a broadening of about 100 meV for a source temperature of 30 K and a molecular tritium source. From the modelling perspective, the Doppler broadening is accounted for as a convolution of the differential spectrum and the Gaussian described in ref. [Kle+18].

2.2.2. Monitoring of the source parameters

In order to ensure a stable source activity, several measuring instruments are dedicated to monitor the amount of gas in the source tube, its composition, and its activity.

Rear section The rear section closes off the WGTS and thereby the KATRIN experiment at the rear side. Two key parts of the rear section are the rear wall and the angular-selective, mono-energetic electron gun (e-gun). As the rear wall is enclosing the magnetic flux tube of the KATRIN experiment, its potential is designed to control the source plasma [KAT05, Kuc16]. Half of the β-decay electrons are guided from the WGTS to the gold-plated surface of the rear wall, where they produce X-rays which are detected by the BIXS detectors. Including the electrons that are reflected by the spectrometers or the strong magnetic field of the PCH magnet (see sec. 2.2.4), sufficiently intense X-ray emission is produced at the rear wall to be sensitive to activity fluctuations at the per-mille level [Röl15].

The e-gun of the rear section is a versatile tool to monitor and determine the total amount of gas in the beam tube (including the non-active parts). It is designed to reach electron energies up to about 30 keV with a small energy spread (0.2 eV) and angular distribution (4° at maximum pitch angle) [Bab14, Hei15]. Furthermore, count rates of 10^4 cps at minimum are required to enable fast determination of the column density (see sec. 4.3.4), and the energy loss function [Han+17].

[1] due to the low probability to scatter off a single gas molecule

[2] a small shift from 0 is due to the direction of the gas flow

Final states As introduced in eq. (2.2), we may find the daughter molecule of the molecular tritium β-decay in an excited state. The excitation of the daughter molecule can be of rotational, vibrational, and electronic nature. Each of the possible excited states has its own specific endpoint of $\varepsilon_{fs} = E_0 - E - E_{fs}$, compare eq. (2.2). As the final states energy is missing energy for the electron, it is crucial for a direct neutrino mass experiment like KATRIN to use highly accurate calculations of the final states distributions. About 57 % of the T_2-decays go into the rovibronically-broadened electronic ground state [JSF99]. As there are also other hydrogen isotopologues present in the source gas, each decaying species (T_2, DT, HT) needs to be weighted according to its abundance. Calculations for the final states of the different hydrogen isotopologues have been performed in refs. [SJF00, Dos+06, DT08] and give the excitation energy relative to the molecular recoil energy of $(HeT)^+$. The calculations also provide separate distributions for the different initial quantum state in terms of molecular angular momentum J. The J states are populated according to a temperature dependent Boltzmann distribution [Kle+18]

$$P_J(T) \propto g_s \cdot g_J \cdot \mathrm{e}^{-\frac{\Delta E_J}{k_\mathrm{B} T}}, \tag{2.7}$$

with k_B the Boltzmann constant, T the temperature, ΔE_J the energy difference to the electronic ground state, the rotational degeneracy of the distribution g_J, and the spin degeneracy of the nuclei g_s. The rotational degeneracy factor is given by $g_J = 2J + 1$, while $g_s = 1$ for the heteronuclear molecules DT and HT. For the spin-coupling T_2, g_s depends on the ortho-para ratio λ of the molecules [BPR15, Kle+18].

When comparing the overall decay energy (Q-value) to the maximum electron energy E_0, the molecular recoil energy $E_\mathrm{rec} \approx E \cdot \frac{m_\mathrm{e}}{m_{(^3\mathrm{HeT})^+}} \approx 1.7\,\mathrm{eV}$ needs to be taken into account. Over the last 50 eV of the electron spectrum, E_rec only changes by about 6 meV [KAT05].

LARA As outlined in the previous paragraph, it is very important to know the composition of the source gas at all times as it determines the mixing of the β-spectra from the different tritiated isotopologues: the final state distribution of the T_2, DT, and HT daughter molecule ions $^3HeT^+$, $^3HeD^+$, and $^3HeH^+$ differ substantially. In [Bab+12], a requirement on the precision of the tritium purity monitoring of 10^{-3} is derived from the argumentation that a precise monitoring of ϵ_T combined with a precise observation of the activity via the BIXS monitors at the rear wall enables conclusive monitoring of the column density. To reach the per-mille requirement, a dedicated LAser RAman (LARA) system was developed [Fis+11, Sch13, Fis14]. LARA uses the principle of Raman spectroscopy to determine the isotopic composition of the source gas. Photons from a laser with a wavelength of 532 nm scatter off gas molecules in an optical cell, which is part of the inner tritium circulation loop. The inelastically scattered (red-shifted) photons are spectroscopically analysed and recorded. Each of the six hydrogen isotopologues has a characteristic rotational-vibrational excitation which contributes to the resulting Raman spectrum. By taking into account an elaborate calibration method [Sch13, Zel17], the accurate gas composition can be extracted. An example of a LARA spectrum taken during the First Tritium campaign is shown in fig. 2.4. The ratios of the integrated intensities give the concentrations of the different isotopologues. Typical values during the

First Tritium campaign were a dominating D_2 concentration of about 93 %, an HD concentration of about 6 %, and a DT concentration of about 1 %. The other isotopologues are only present in negligible concentrations, as can be seen from fig. 2.4.

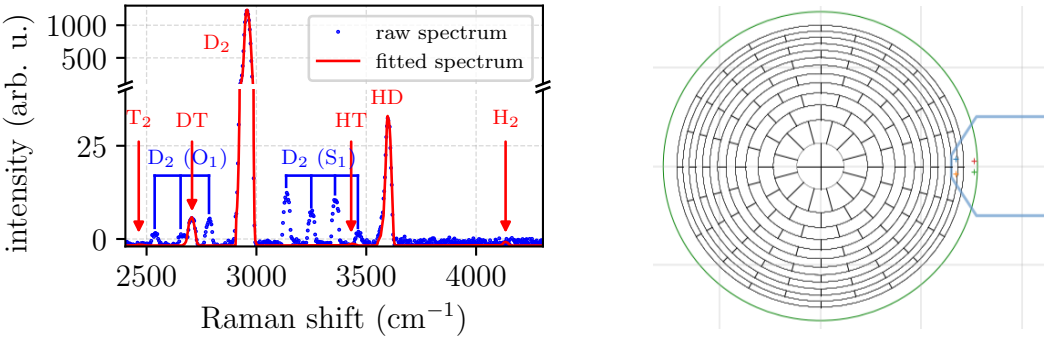

Figure 2.4.: **Monitoring instrumentation.** Left-hand side shows an example LARA spectrum from the First Tritium campaign. Right-hand side illustrates the measuring point of the FBM, projected onto the FPD. The blue cross is diode 1, the orange cross diode 2, red cross the Pt1000 sensor, and green cross the Hall probe.

Forward beam monitor The main purpose of the forward beam monitor is permille precision activity monitoring of the β-decay rate in the outer rim of the flux tube at the front pump port of the CPS (end of the transport section) [Bab+12, Hau18, Ell18]. Since it is mounted on a manipulator, the FBM detector board can be steered in azimuthal direction to scan the entire flux tube, enabling detection of column density and magnetic field inhomogeneities. For that purpose, the FBM detector board is equipped with two Si-pin diodes of type *S5971* [HAM18], a Pt1000 temperature sensor and a Hall sensor. The four components are marked by the crosses on the board in fig. 2.4. Later in this thesis, the FBM data will be used for an estimation of the column density from the active commissioning phase of the KATRIN experiment (First Tritium).

2.2.3. Transport section

The transport section of the KATRIN experiment has to fulfil several requirements. While ensuring collision-free and adiabatic transport of the electrons provided by the WGTS towards the spectrometer and detector section (SDS), the transport section has to prevent tritium from migrating into the SDS. The former is achieved via the guiding field of superconducting magnets, while the latter is achieved by applying staged mechanic and cryogenic pumping techniques.

Differential pumping section In the very same way as the WGTS reduces the gas flow with its TMPs, the differential pumping section (DPS) reduces the gas flow further by about seven orders of magnitude. For this purpose, the DPS uses a set of staged turbo-molecular pumps of type *Leybold Mag W 2800* [ide10], which

are installed at the pump ports between the beam tube elements. To prevent a "beaming effect" of the gas molecules [Luk+12, Kuc+18], the beam tube elements of the DPS are arranged in a 20° chicane (compare fig. 2.5). Since the superconducting magnets around the beam tube elements guide the charged electrons, the chicane increases the pumping efficiency without affecting the electrons. Another important task of the DPS is the removal of ions. The decay of a tritium molecule leaves behind a charged daughter molecule, which also follows the magnetic field lines. Furthermore, the high-energy β-electrons from the tritium decay increase the ion flux by another order of magnitude. In order to prevent this large ion flux from reaching the spectrometers, two ring electrodes are installed in the DPS. As ions can get trapped in between the ring electrodes on the one side and the incoming gas flow from the WGTS, they have to be removed [Kle18]. This task is accomplished by dipole electrodes, which drift the low-energy ions out of the flux tube due to the $\boldsymbol{E} \times \boldsymbol{B}$ drift [Kle18]. When the drifted ions hit a surface, they recombine to uncharged molecules and are then removed either at the DPS or latest at the CPS.

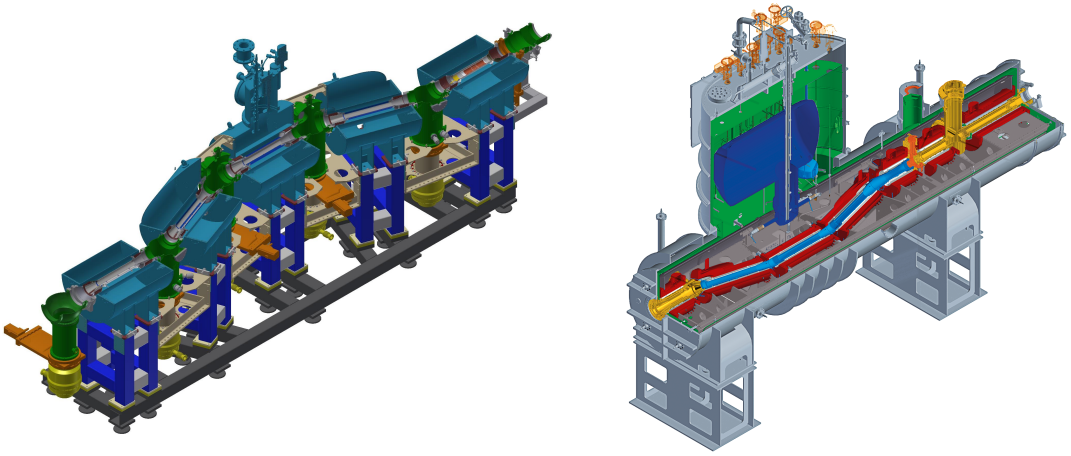

Figure 2.5.: **Transport section.** Left-hand side shows the DPS with beam tube (grey), surrounded by the magnets (blue) and connected via the pump ports (green). Right-hand side shows the CPS with beam tube (golden/blue, note the opposite direction of the chicane), and magnets (red). The elements of the CPS beam tube highlighted in blue mark the argon frost prepared section. Figure adapted from ref. [Fri+18].

Cryogenic pumping section At the end of the DPS, the gas flow is in a regime where further reduction of the flow rate by mechanical pumping is ineffective. Therefore, the DPS is complemented by a cryogenic pumping section (CPS). The CPS uses cryosorption of the remaining gas molecules to reduce the tritium flux by another seven orders of magnitude. Together with the DPS, this results in a reduction of the tritium flux from the WGTS towards the spectrometers by at least 14 orders of magnitude. Similar to the DPS, the CPS uses a chicane of the beam tube (though in opposite direction, compare fig. 2.5) to increase the pumping efficiency while the superconducting magnets ensure adiabatic transport of the signal electrons. The pumping efficiency via cryosorption is further increased by freezing an argon frost layer to the 3 K cold, gold-coated surface of the CPS beam tube elements 2-5 (highlighted in blue in fig. 2.5). Thereby, a cold trap is formed with an increased surface and sticking probability due to the argon frost. The argon frost requires a

few days of warming up the CPS in order to regenerate the frost layer about every 60 d [KAT05].

2.2.4. Spectrometers section

KATRIN makes use of a spectrometer tandem to perform high-precision β-decay spectroscopy of the electrons produced in the tritium source. The tandem consists of a pre-spectrometer to filter the low-energy electrons, followed by the main spectrometer to perform the high precision spectral analysis. One of the keys for the success of the KATRIN experiment is the ultra-high vacuum achieved in the spectrometers section, as low-energy electrons have a very large cross-section for scattering with residual gas. Both spectrometers are therefore operated at pressures below 10^{-11} mbar [Are+16].

Pre-spectrometer In order to enable the precision β-decay spectroscopy of the high-energy end of the β-spectrum with the main spectrometer, the pre-spectrometer uses an energy barrier up to a design value of 18.3 keV. This pre-filtering reduces the β-decay electron flux by seven orders of magnitude and thereby minimises background due to residual gas ionisation. Successful countermeasures to mitigate background caused by a Penning trap are e.g. the Penning wiper method [Pra11, Pra+12].

Main spectrometer After the pre-filtering in the pre-spectrometer, the electrons reach the main spectrometer. The task of this key component of the KATRIN experiment is to perform the high-precision spectroscopy of the tritium β-decay endpoint. In order to achieve the required superior energy resolution of 0.93 eV, the main spectrometer combines magnetic adiabatic collimation with electrostatic retardation, the so-called MAC-E filter principle [BPT80, KR83, LS85, Pic+92] which will be outlined in the following.

Magnetic adiabatic collimation The magnetic guiding field along the KATRIN beam line results in gyration of the electrons around the magnetic field lines due to the Lorentz force. The kinetic energy of the electrons is shared by the longitudinal and a transverse component relative to the magnetic field:

$$E_{\text{kin}} = E_{\parallel} + E_{\perp} = E\cos^2\theta + E\sin^2\theta, \tag{2.8}$$

with the pitch angle θ defined as the polar angle between the electron momentum and the magnetic field, $\theta = \angle(\boldsymbol{p}, \boldsymbol{B})$. The electrostatic retardation potential can only analyse the fraction of the energy that is parallel to the electric field direction ($E_{\parallel}$). Therefore, the momenta of the electrons need to be aligned as parallel as possible via the magnetic adiabatic collimation. This principle and further characteristics of the main spectrometer will now be discussed in detail:

- **Adiabatic guiding of the electrons.** With the minimised change of the magnetic field along one cyclotron cycle in the main spectrometer, adiabatic

guiding of the electrons is ensured. Then, the product $\gamma \cdot \mu$ of relativistic Lorentz factor γ and the magnetic moment μ is a constant of the motion [Jac99]: in the non-relativistic limit where $\gamma = 1$, this results in

$$\mu = \frac{E_\perp}{B} = \text{const.} \tag{2.9}$$

(Note that $\gamma = 1.04 \approx 1$ for electrons at the tritium endpoint energy of 18.6 keV.) As the electrostatic retarding potential only analyses the longitudinal part of the energy, the transverse part $E_\perp$ needs to be minimised in order to obtain a good energy resolution. This is achieved by two superconducting magnets at both ends of the spectrometer (with a distance of about 22 m in between, see fig. 2.6), resulting in a minimum magnetic (stray) field B_{min} in the middle of the spectrometer. As described by eq. (2.9), this drop of the magnetic field strength minimises the transverse energy accordingly, enabling the energy analysis in the so-called analysing plane via an electrostatic retarding potential.

- **Energy resolution.** The ratio of minimum and maximum magnetic field strength defines the fraction of transverse energy that cannot be analysed by the MAC-E filter, which is often referred to as energy resolution ΔE:

$$\frac{\Delta E}{E} = \frac{B_{\text{min}}}{B_{\text{max}}}. \tag{2.10}$$

For electron energies around the endpoint of $E = 18.6\,\text{keV}$, the design minimum magnetic field of $B_{\text{min}} = 0.3\,\text{mT}$, and the design maximum magnetic field of $B_{\text{max}} = 6\,\text{T}$, this results in a filter width of $\Delta E = 0.93\,\text{eV}$.

- **Conservation of magnetic flux.** In order to ensure transport of all signal electrons, the magnetic flux

$$\Phi = \int_A \boldsymbol{B}\,\mathrm{d}\boldsymbol{A}, \tag{2.11}$$

defined by the tritium source has to be conserved. With the low magnetic field of 0.3 mT in the analysing plane, this results in a diameter of the flux tube of about 10 m in the centre of the main spectrometer.

- **Magnetic mirror.** Adiabatic guiding of the electrons from the tritium source to the detector establishes a fixed relation between pitch angle and magnetic field. Two arbitrary points on the path of the electrons are related via

$$\frac{\sin^2\theta_1}{\sin^2\theta_2} = \frac{B_1}{B_2}. \tag{2.12}$$

The maximum pitch angle of tritium β-decay electrons is defined by the ratio of source magnetic field B_{S} and the maximum magnetic field along the beam line B_{max}, which usually is the PCH magnet on the detector side of the main spectrometer:

$$\theta_{\text{max}} = \arcsin\sqrt{\frac{B_{\text{S}}}{B_{\text{max}}}} = 50.8°, \tag{2.13}$$

with design values of $B_{\text{S}} = 3.6\,\text{T}$, and $B_{\text{max}} = 6\,\text{T}$.

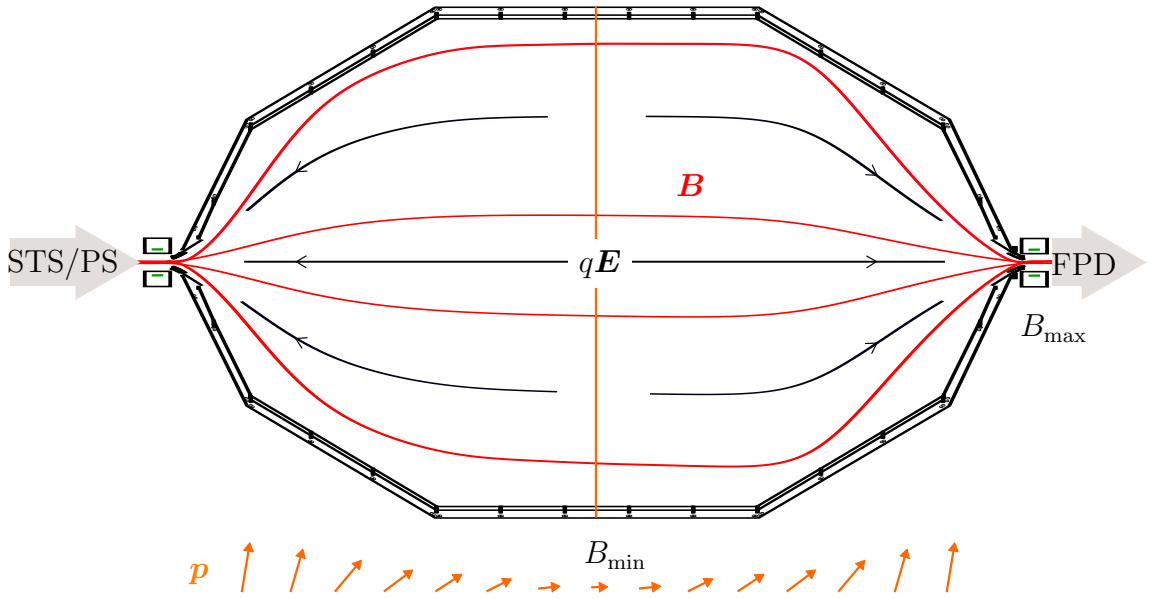

Figure 2.6.: **MAC-E filter principle.** The electron momentum is almost parallel to the minimum magnetic field in the centre of the main spectrometer (length of the arrows not to scale). Aligning minimum magnetic field and maximum retarding potential qU yields the unprecedented filter width of 0.93 eV. Figure adapted from ref. [Hac17].

Electrostatic retardation Using the principle of magnetic adiabatic collimation discussed above, the energy of the electrons can be studied via application of a (negative) electrostatic potential in the analysing plane. Only electrons with longitudinal energy larger than the electrostatic potential can pass the analysing plane and reach the detector. In that way, both spectrometers act as high-pass filters, resulting in the measurement of an integrated β-decay spectrum as indicated in eq. (2.3).

Transmission function Combining the above-mentioned MAC-E filter characteristics of magnetic adiabatic collimation and electrostatic retardation results in the transmission probability for electrons to pass the main spectrometer. It can be analytically described by the transmission function $T(E, qU)$ [KAT05, Kle+18]

$$T(E,U) = \begin{cases} 0 & \text{for } E < qU \\ \dfrac{1-\sqrt{1-\frac{E-qU}{E}\frac{B_\mathrm{S}}{B_\mathrm{min}}}}{1-\sqrt{1-\frac{B_\mathrm{S}}{B_\mathrm{max}}}} & \text{for } qU \leq E \leq qU+\Delta E\,. \\ 1 & \text{for } E > qU+\Delta E \end{cases} \tag{2.14}$$

Response function Combining all effects that influence the electrons on their way from their creation in the tritium source up to passing the analysing plane of the main spectrometer results in the aforementioned response function $R(E, U)$. It combines the transmission function of the main spectrometer $T(E, U)$ (see eq. (2.14)) with

the energy loss function of the source $f(\epsilon)$ (eq. (2.4)) as

$$R_{i,j}(E,U) = \int_{\epsilon=0}^{E-qU} \int_{\theta=0}^{\theta_{\max}} \sum_s T^{\mathrm{cycl}}_{s,i,j}(E-\epsilon,\theta,U) \cdot P_{s,i}(\theta) \cdot f_s(\epsilon)\,\mathrm{d}\epsilon\,\sin\theta\,\mathrm{d}\theta, \tag{2.15}$$

with the indices s, i, j denoting the number of scatterings s and the voxel i, j as previously introduced [KAT05, Kle14, Kle+18]. The label *cycl* indicates that the transmission function also needs to be corrected for energy loss due to cyclotron radiation [Kle+18].

2.2.5. Detector section

After passing the analysing plane of the main spectrometer, the signal electrons reach the detector section. A 148-pixel silicon pin diode wafer counts these signal electrons with high efficiency required as $\epsilon_{\mathrm{det},j} \geq 90\,\%$ [KAT05], which was confirmed in ref. [Ams+15] (the index j indicates the pixel of the detector). The signal electrons are guided to the focal plane detector (FPD) wafer by two superconducting magnets, the PCH magnet with the maximum magnetic field (6 T) of the KATRIN experiment and the detector magnet (3.6 T). In order to increase the detection efficiency and reduce backscattering effects, a post-acceleration electrode is used to add another constant 10 keV of energy to the signal electrons. At the port between the two magnets (compare fig. 2.7), calibration sources can be installed to determine the detection efficiency and energy calibration of each single pixel. One of these calibration sources is the Precision Ultra-Low Current Integrating Normalization Electrometer for Low-Level Analysis (PULCINELLA) [Ams+15], which can be used as a Faraday cup to detect an electron flux. This method will be used to estimate the column density from the active commissioning phase of the KATRIN experiment.

2.3. Modelled count rate

Now that all components of the KATRIN experiment were introduced and their respective importance for the measured spectrum described, the integrated count rate measured by the FPD pixel j for a given potential of the main spectrometer U can be written as [Kle+18]

$$\dot{N}_j(U) = \frac{1}{2}\,\epsilon_{\mathrm{det},j} \cdot \sum_i \cdot \int_{qU}^{\infty} \left(\frac{\mathrm{d}\Gamma}{\mathrm{d}E}\right)_{\mathrm{C,D}} (m_\nu^2, E_0) \cdot R_{i,j}(E,U)\,\mathrm{d}E, \tag{2.16}$$

with the indices C,D denoting theoretical corrections C, and the Doppler effect convolution D (see sec. 2.2.1) which both affect the differential spectrum of the tritium decay given in eq. (2.2). The response function $R_{i,j}(E,U)$ is given in eq. (2.15).

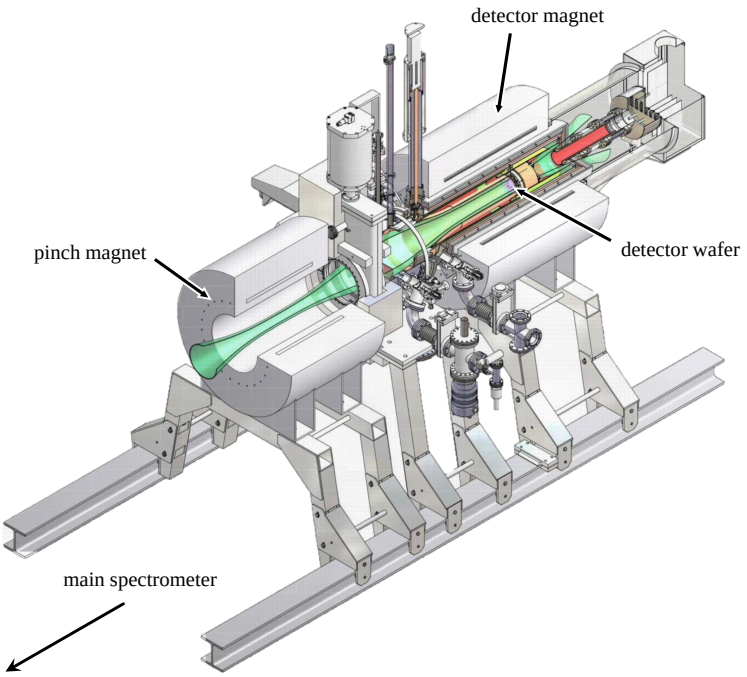

Figure 2.7.: **Detector section.** The magnetic flux tube is highlighted in green, while the orange part in front of the detector wafer depicts the post-acceleration electrode. At the port between the two magnets, calibration sources can be installed. Figure adapted from ref. [Ams+12].

2.4. Analysis tools and software at the KATRIN experiment

In order to enable the neutrino mass analysis of KATRIN data at the level of spectrum fitting, a number of successive data layers process the raw data acquired by various detectors (like FPD and FBM), and sensors (like Pt500 sensors of the WGTS). The first processing step of detector data is by a Detector Data Acquisition (DAQ) system based on Field Programmable Gate Array (FPGA) architecture. Operators usually interact with the detectors via the Object-oriented Real-time Control and Acquisition (ORCA) software [Phy18]. The various sensors and devices used to operate and control the beam line of the KATRIN experiment are referred to as *slow control* data. The slow control data consists of several different architectures like Siemens SIMATIC Process Control System 7 (PCS7) [Sie18] or LabVIEW [NI16]. The former is mainly used in safety-relevant systems as to control the magnets and cryostats inside the TLK (Tritium Laboratory Karlsruhe) while the latter is more common to readout sensors that e.g. measure the magnetic field.

The central connection to all KATRIN data is provided by the KDBServer logic [Kle14]. It provides user access to the slow control SQL database ADEI [Kle14] and the detector run data via KaLi [Kle14]. Another layer is currently in development, which is a quality cut database that enables automatic determination of the data quality of a KATRIN run. Originally designed to analyse detector data, the Building Elements for ANalysis Sequence (BEANS) package developed by S. Enomoto [Cen18] uses KaLi to access slow control data and is therefore an ideal candidate to implement

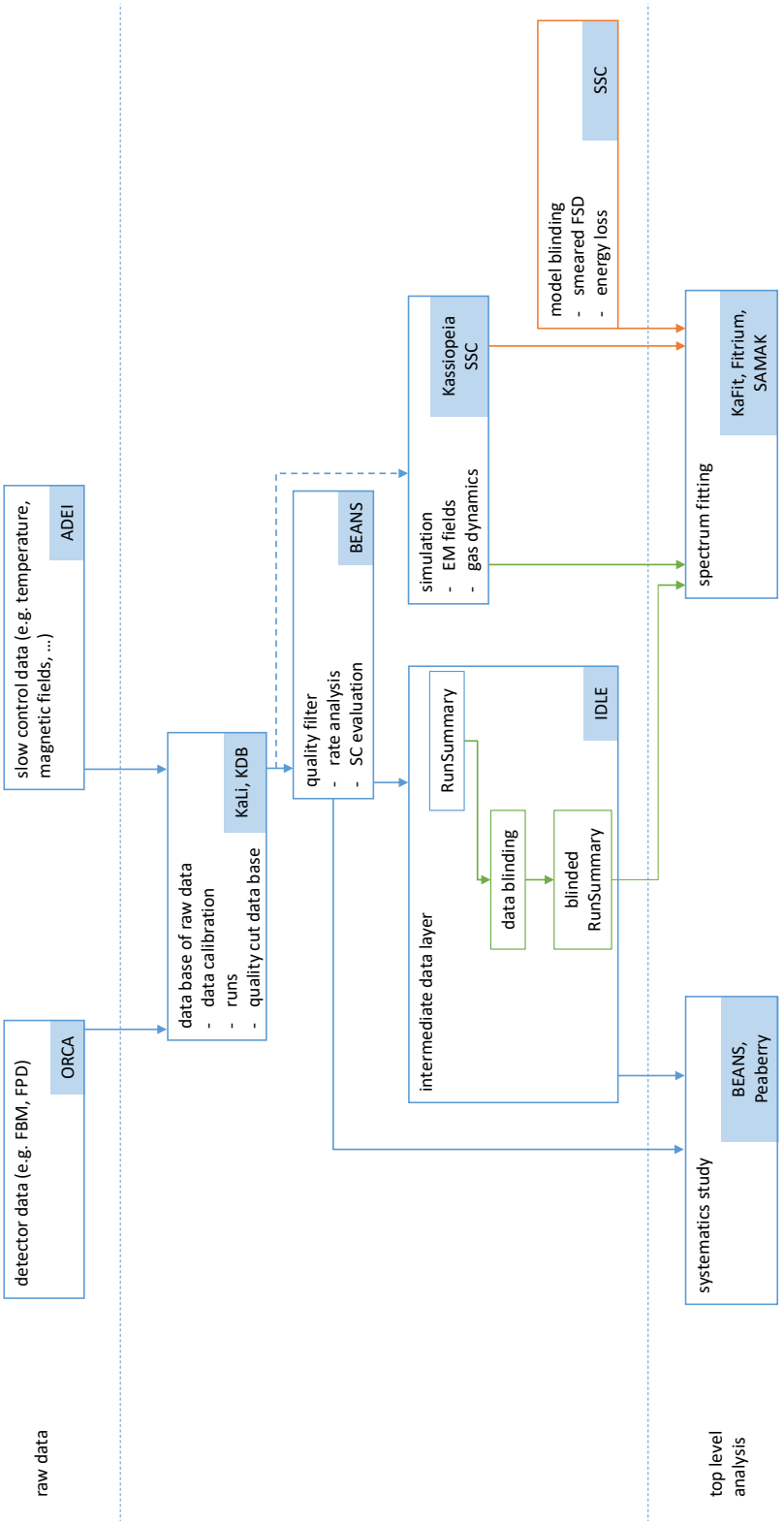

Figure 2.8.: **KATRIN data analysis structure.** Different levels and components of the KATRIN software which the user usually gets in contact with are depicted.

the quality cuts (see fig. 2.8). From the data processing side, the last step before the top-level spectrum analysis is the Intermediate Data LayEr (IDLE). It can provide a human-readable text file containing condensed information about, for example,

the number of counts per pixel for each high voltage of the main spectrometer, or the mean and stability of a temperature sensor of the WGTS. Thereby, this file summarises relevant data for each run into a so-called run summary. The run summary can then easily be accessed by the top-level analysis tools for spectrum fitting. Potential data blinding strategies will be integrated into the intermediate data layer.

Parallel to this data processing chain, the model building chain also uses sensor data, for instance, to calculate the magnetic fields using the measured currents of the superconducting magnets. The publicly available particle tracking software Kassiopeia [Fur+15, Fur+17] was developed specifically for the needs of the KATRIN experiment to precisely calculate particle tracks in complex electromagnetic field geometries. It can also model stochastic processes such as scattering, with an interface e.g. to use SSC-calculated density profiles in the WGTS. The Source and Spectrum Calculation (SSC) suite implements the calculation of differential and integrated tritium and krypton spectra, accounting for the KATRIN experiment characteristics. For that purpose, SSC needs to model the gas dynamical properties of the tritium source and the electromagnetic properties of the spectrometer part to calculate the response function. The development of SSC was started by W. Käfer [Käf12] and M. Hötzel [Höt12], followed by M. Kleesiek [Kle14, Kle+18], S.Groh [Gro15], and L. Kuckert [Kuc16]. In the course of this thesis, substantial extensions are implemented in the gas modelling part of SSC as well as in its spectral modelling with respect to physics beyond the neutrino mass.

The final step in KATRIN (tritium) spectrum data analysis as used in this work is then comparison of the SSC modelled spectrum to the run summaries produced by IDLE via KaFit [Kle14].

CHAPTER 3

THE WINDOWLESS GASEOUS TRITIUM SOURCE

The main task of the Windowless Gaseous Tritium Source (WGTS) is to provide a per-mille stable electron-rate originating from tritium β-decay. This can be split into two separate requirements: a stable magnetic field for stable transport of the electrons and a stable amount of tritium for a stable source activity. The chapter at hand gives an overview of the key parameters in sec. 3.1, the challenges that are imposed by the above requirements in sec. 3.2, and their technical implementation in the WGTS in sec. 3.3.

3.1. Key parameters

The key parameters defining the activity S provided by the WGTS and detected by the FPD are the amount of gas, represented by the column density $\mathcal{N}$, and the fraction of tritium therein, represented by the tritium purity ϵ_{T}. Therefore

$$S \propto \mathcal{N} \cdot A_{\mathrm{S}} \cdot \epsilon_{\mathrm{T}} \cdot a(\theta_{\mathrm{max}}), \tag{3.1}$$

with the source cross section A_{S} and a factor for the acceptance angle $a(\theta_{\mathrm{max}}) = a(B_{\mathrm{S}})$ which is related to the magnetic field in the source B_{S}.

3.1.1. Column density

The column density $\mathcal{N}$ is defined as the longitudinally integrated number density n of the gas molecules inside the beam tube

$$\mathcal{N}\left(p_{\mathrm{in}}, p_{\mathrm{out}}, T(\boldsymbol{r})\right) = \int_{-L_{\mathrm{rear}}}^{L_{\mathrm{front}}} n\left(\boldsymbol{r}, p_{\mathrm{in}}, p_{\mathrm{out}}, T(\boldsymbol{r})\right)\, \mathrm{d}z, \tag{3.2}$$

which in general depends on injection pressure p_{in}, outlet pressure p_{out}, and the beam tube temperature $T(\boldsymbol{r})$ at spatial coordinate $\boldsymbol{r}$. Obviously, the larger $\mathcal{N}$ is, the larger is the activity. However, larger $\mathcal{N}$ also means increased scattering probability for the signal electrons, leading to an increased systematic uncertainty for the neutrino mass, which will be discussed in the next sec. 3.2.

3.1.2. Temperature

The temperature T of the WGTS influences several effects which need to be accounted for in the modelling. On the one hand, a low temperature is favoured since it enables a high column density at relatively low injection pressures. Plus, a low temperature reduces broadening of the electron spectrum due to the Doppler effect though it can be modelled easily [Kle+18]. On the other hand, for temperatures below 27 K, tritium clusters form and gas freezes on the beam tube walls [KAT05]. Both latter effects cause complicated distortions to the electron spectrum and should therefore be avoided.

3.1.3. Tritium purity

In order to maximise the source activity in eq. (3.1), the tritium purity needs to be maximised. Pure tritium gas forms T_2 molecules, however due to exchange reactions the other hydrogen isotopologues (DT, HT, D_2, HD, and H_2) are also present in the source gas. The fraction of active gas, represented by the tritium nuclei, is defined as the tritium purity ϵ_T. Defining c_x as the concentration of isotopologue x in the source gas[1], we can calculate

$$\epsilon_T = c_{T_2} + \frac{c_{DT} + c_{HT}}{2}, \qquad \text{with} \quad \sum_x c_x = 1. \tag{3.3}$$

Though the fraction of non-T_2 isotopologues DT and HT is small, it needs to be included in the modelling of final states of the decaying molecules. Therefore, the concentrations of hydrogen isotopologues are monitored via the LARA system (see sec. 2.2.2).

3.1.4. Magnetic field

In order to transport the electrons from the source to the main spectrometer for the energy analysis, they need to be guided magnetically. Maximising the mapped flux tube, a strong magnetic field at the source B_S enables a relatively small cross-section of the source beam tube which is desired from gas dynamics considerations. Furthermore, a strong B_S increases the fraction of electrons that can surpass the magnetic mirror built by the PCH magnet (as the strongest magnet in the KATRIN set-up) and therefore increases the signal strength:

$$a(\theta_{max}) \propto (1 - \cos\theta_{max}), \qquad \text{with} \quad \theta_{max} = \arcsin\sqrt{\frac{B_S}{B_{PCH}}}. \tag{3.4}$$

For homogeneous starting conditions of the electrons, the source magnetic field needs to be as homogeneous as possible. The homogeneity of the source magnetic field directly influences the homogeneity of the path length and therefore the scattering probabilities of the electrons.

[1] Also compare ref. [Zel18].

3.1.5. Plasma potential

The longitudinal magnetic field of the WGTS confines any charged particles inside the beam tube. Together with the ionised daughter molecule from the β-decay and secondary ionisation processes, the β-decay electrons may form a cold plasma [KAT05]. The plasma potential distribution is influenced by space charges, the beam tube steel surface potential in radial direction, and the rear wall potential in longitudinal direction [Kuc16] because the magnetic field lines hit the rear wall surface. Since the rear wall surface is covered with gold, the work function difference between the rear wall gold surface and the beam tube stainless steel surface is about 1 eV, requiring the rear wall surface potential to be controlled [Kuc16].

3.2. Systematic uncertainties and requirements related to the WGTS

Already in the Design Report [KAT05], the KATRIN collaboration lists most of the largest identified sources of systematic uncertainty on the neutrino mass to be related with the WGTS. Any uncertainty related to the starting position of the β-decay electrons defined in the source causes a systematic difference between modelled and measured spectrum and thereby a systematic shift of the observable of interest, Δm_ν^2. The KATRIN systematics budget is currently undergoing a detailed re-evaluation

Table 3.1.: **Systematic uncertainties related to the WGTS.** This table lists the identified systematic uncertainties from the Design Report [KAT05], related to unaccounted for shifts of WGTS key parameters. Values given for one KATRIN run of 2 h [KAT05]. The systematics budget is currently undergoing a detailed re-evaluation by H. Seitz-Moskaliuk [Sei19] and can only serve as a guideline.

source of syst. uncertainty	syst. shift $\Delta m_\nu^2\,(10^{-3}\,\mathrm{eV}^2)$	requirement on the parameter	achieved
variations of $\mathcal{N}$	< 1.5	2×10^{-3}	see sec. 5.2
inlet pressure p_{in}		2×10^{-3}	see sec. 5.2
outlet pressure p_{out}		6×10^{-2}	see sec. 5.2
temperature T		2×10^{-3}	see sec. 5.2
tritium purity ϵ_{T}		2×10^{-3}	$< 10^{-3}$ [Sch13, Fis14]
magnetic field B_{S}	tbd [Sei19]		
inhomogeneity	< 2	2×10^{-3}	tbd
drift	tbd [Sei19]	$2 \times 10^{-3}/3\,\mathrm{months}$	$2 \times 10^{-4}/1\,\mathrm{month}$ [Are+18c]
fluctuations	tbd [Sei19]	2×10^{-3}	2×10^{-5} [Are+18c]

by H. Seitz-Moskaliuk [Sei19] as the first commissioning measurements [Are+18b,

Are+18a, Are+18c] increase the information on the system behaviour. Some of the systematic uncertainties listed in tab. 3.1 are also addressed in the course of this thesis, especially the stability of the source during the First Tritium campaign in sec. 5.2.

3.3. Technical realisation

In order to fulfil all the requirements described in sec. 3.2, a large 16 m long cryostat was custom-made for the KATRIN experiment. The cryostat consists of several insulation layers, shielding the 30 K cold beam tube and the 4.5 K cold superconducting magnets against the room temperature of the Tritium Laboratory Karlsruhe (TLK). The cryostat weighs 27 t including the magnets, and houses over 800 sensors and valves to control the different cooling circuits and ensure stable magnet and gas flow operation. A half-cut of the WGTS is shown in fig. 3.1 which gives an impression of the many layers inside the cryostat. The outer layer of the WGTS is the stainless

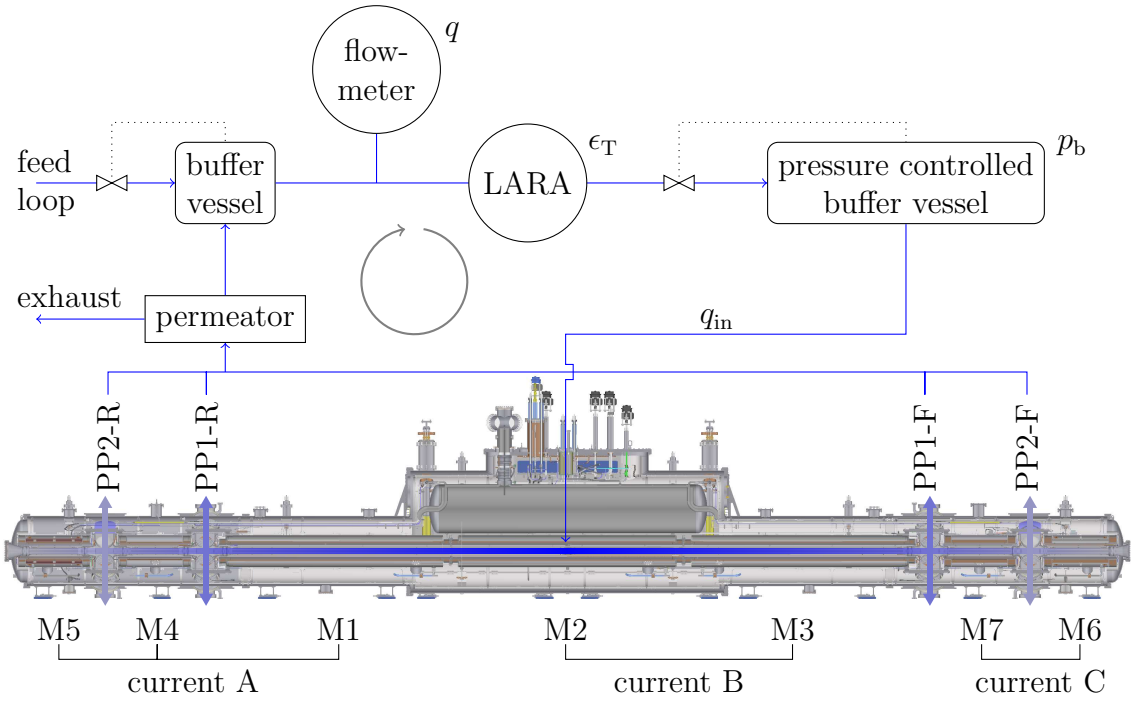

Figure 3.1.: **Half cut of the WGTS cryostat.** The CAD model shows the housing of the magnets, the position of the pump ports and a flow chart of the inner loop system. In blue, the gas distribution in the WGTS beam tube is illustrated. The currents defining the magnetic field are explained more in sec. 3.3.3.

steel cryostat hull, which is at room temperature (see fig. 3.2). In the insulation vacuum soon after, the outer shield represents the first cooled layer [Gro+08]. It is kept at liquid nitrogen (LN) temperature of about 80 K. The coldest layer inside the WGTS consists of the magnets, which are immersed in a liquid helium (LHe) bath at about 4.5 K. Since the beam tube should maintain a temperature of 30 K, it needs to be shielded against the colder magnets by the inner shield which is kept at

30 K by gaseous helium (GHe) cooling. The temperature control of the beam tube is the task of the 2-phase neon system, which is described in the next section.

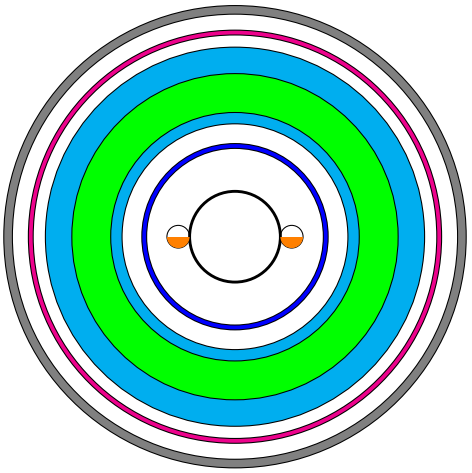

Figure 3.2.: **Layers of the WGTS cryostat.** The labelling from top to bottom represents the layers from outside to inside. The white spaces mark insulation vacuum with pressures below 10^{-5} mbar. For more explanations see text.

3.3.1. Temperature stabilisation and calibration

Temperature stabilisation In order to stabilise the temperature of the WGTS beam tube to the per-mille level, a dedicated cooling concept was developed [Gro09]. A closed neon cycle consisting of a thermo siphon and 2-phase tubes is used to define the beam tube temperature via the pressure of the gas phase. The 2-phase neon tubes are brazed on the sides of the beam tube (compare fig. 3.3) with included heaters to control the pressure of the gas phase. Gaseous neon flows back to the condenser in the thermo siphon, which is cooled by gaseous helium at about 25 K to liquefy the neon again. Fluctuations of the primary helium cycle are damped by the large heat capacity of the 3.7 kg lead condenser [Gro09]. Fine tuning of remaining fluctuations is done via automatically adjusting the heater power of the electrical heaters in the 2-phase neon tubes [Gro09]. In demonstrator measurements, the system was shown to beat the requirements by about one order of magnitude [Gro09, Gro+11, Gro+13].

Temperature calibration So far, only the stabilisation of the beam tube temperature was discussed. In this paragraph, the system to calibrate the temperature and thereby get an accurate estimation of the beam tube temperature will be introduced. The accurate measurement of temperature in the WGTS cryostat poses a challenge, since it has to face high magnetic fields of up to 3.6 T while providing precise and continuous monitoring of the temperature. Though they provide an accurate and magnetic field independent temperature value, vapour pressure sensors cannot be used for continuous monitoring. Vapour pressure sensors determine the temperature by measuring the saturation pressure of a small bulb filled with e.g.

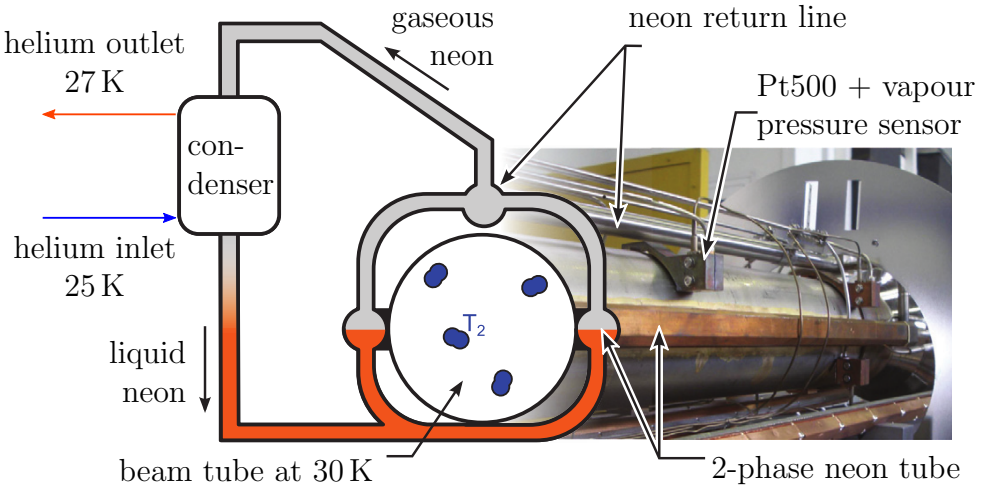

Figure 3.3.: **Beam tube cooling concept.** Neon is circulated in a closed cycle via a condenser. The vapour pressure defines the temperature of the beam tube and is controlled via heater wires. Adapted from ref. [Fis14].

neon. However, the fill-level of the vapour pressure sensors can neither be guaranteed nor tested during standard KATRIN operation, plus the filling of the vapour pressure sensors induces heat load onto the source tube due to the condensing neon. On the other hand, resistance sensors like the used Pt500 face a magnetic field dependence [Gro+11]. The solution therefore is to thermally couple a vapour pressure sensor and a Pt500 sensor to the beam tube [Gro09, Gro+11, Gro+13]. This combination enables calibration of the Pt500 sensors by the vapour pressure sensors once the magnetic field is set. After filling the vapour pressure sensor half with condensed neon, the thermalisation takes about 30 min [Mar17, Hac17]. Then the temperature of the Pt500 sensor can be calibrated to the vapour pressure sensor temperature. Afterwards, the vapour pressure sensor is emptied again, causing a local temperature drop of the beam tube.

The absolute accuracy on the temperature measurement by the Pt500 sensors after applying the calibration via the vapour pressure sensors was estimated by A. Marsteller to 8.27 mK [Mar17]. However, a careful re-evaluation became necessary due to changes in the readout procedure. H. Seitz-Moskaliuk estimates a new absolute accuracy of 159.77 mK for the currently used readout configuration, which can be improved to 82 mK if a larger current is used for the read out [Sei19]. Though a factor of 10 larger than in previous estimates, the 82 mK still meet the requirement of 150 mK for the final states distribution. Furthermore, the temperature homogeneity exceeds the required 30 mK from the Design Report with a value of about 500 mK, see sec. 4.2.3. In order to reasonably estimate the temperature profile with this larger inhomogeneity, a larger uncertainty on the accuracy of each sensor can be tolerated.

3.3.2. Gas flow (Inner loop system)

KATRIN relies on a per-mille stable (tritium) gas column density inside the WGTS beam tube. Gas is injected in the centre of the beam tube and pumped out at

both ends, compare fig. 3.1. Therefore, a stable column density – that is a stable amount of gas inside the beam tube – requires a stable injection and stable pumping. The stable circulation of gas is provided by the so-called inner loop system, which consists of more than 100 sensors and valves to control the gas flow [Bab+12]. A stable injection rate q_{in} and a stable inlet pressure p_{in} are achieved by a stable pressure in the pressure controlled buffer vessel and a stable temperature along the connection pipe. A stable pumping rate is achieved by a constant rotation speed[2] of the turbo molecular pumps (TMPs) attached to the four pump ports (PP) of the WGTS, compare fig. 3.1. There are 12 TMPs[3] of type *Oerlikon Leybold MAG W 2800* in total which have a pumping speed of about $2000\,\mathrm{l\,s^{-1}}$ for H_2 each [ide10]. The conductance of the tube between pump and pump port reduces the higher pumping speed of approximately $3000\,\mathrm{l\,s^{-1}}$ for T_2 [Mal07] to the same effective pumping speed as for hydrogen of about $2000\,\mathrm{l\,s^{-1}}$.

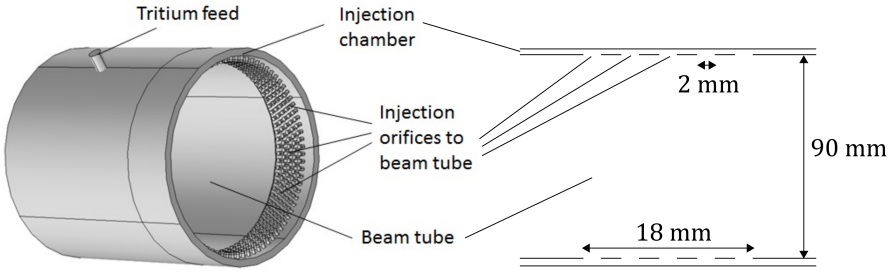

Figure 3.4.: **Injection chamber.** Left: a CAD model of the injection chamber showing the 415 orifices. Right: a sketch of the longitudinal cross section. Figure adapted from ref. [Kuc+18].

Tritium is injected at the centre of the beam tube through 415 2 mm orifices, see fig. 3.4. The dimensions of the orifices guarantee a shock-wave free injection without turbulences. Test measurements [Stu10, Pri13, PB13, PSB15] showed the pressure in the pressure controlled buffer vessel p_{b} and the pumping speed to exceed the requirements from the Design Report [KAT05].

In its design configuration, the inner loop system provides a per-mille stable tritium column density $\mathcal{N}$ of $5 \times 10^{21}\,\mathrm{m^{-2}}$ ($\equiv 300\,\mu\mathrm{g}$) by circulating a daily amount of about 40 g of tritium. This throughput requires buffering of about 15 g of tritium in several vessels. However, the inner loop system can also provide stable circulation of deuterium D_2 for commissioning and characterisation purposes. For the First Tritium campaign, the nominal gas throughput was achieved with the main gas constituent being D_2 with only trace amounts of tritium $\epsilon_{\mathrm{T}} \approx 0.5\,\%$ [Are+19].

3.3.3. Magnet set-up

The WGTS magnet system is housed inside a 16 m long cryostat, see fig. 3.1. Inside the cryostat, the magnets are cooled with liquid helium to a temperature of 4.5 K [Are+18c]. In total seven superconducting solenoids define the magnetic field

[2] stable on the 10^{-4} level
[3] four at each PP1 and two at each PP2

of the WGTS, plus the possibility of azimuthally steering the flux tube via four magnetic dipoles on both ends (dipoles mounted around M5 and M6). The three central magnet modules M1, M2, and M3 are each about 3 m long and provide an almost homogeneous field for the central beam tube by the help of two compensation coils at each end of the module. In order to reduce the stored magnetic energy of the current circuits, the seven modules are split into three circuits, current A (M5, M4, M1), current B (M1, M2), and current C (M7, M6) (compare fig. 3.1).

The magnetic field drift of the WGTS has to be smaller than 0.03 % per month [Are+18c] and fluctuations below 0.2 % per run [KAT05]. Since the magnets of the WGTS are operated in driven mode, the best precision in field monitoring can be reached via monitoring the current. Though there are current readouts before the current is fed into the cryostat, the most accurate and precise current sensors are inside the power supply with an accuracy better than 0.001 73 % [Are+18c, LEM18].

First commissioning measurements with the complete KATRIN beam line during the First Light campaign [Are+18b] revealed that lower magnetic fields of 70 % of the design values should be used in order to minimise the risk for a quench in the complex KATRIN magnet setup [Are+18c]. Thus, the magnetic field of the WGTS has a new set-point at 2.5 T instead of the nominal 3.6 T.

CHAPTER 4

SOURCE MODELLING

"I can never satisfy myself until I can make a mechanical model of a thing. If I can make a mechanical model, I can understand it."
– William Thomson, 1. Baron Kelvin, 1884 –

In order to reach the KATRIN design sensitivity for the effective neutrino mass of 200 meV (90 % C.L.), a cumulative amount of about 40 g of gaseous tritium is circulated daily in a windowless source section. As the gas flow through the Windowless Gaseous Tritium Source (WGTS) significantly influences the generation and transport of the β-decay electrons, an accurate gas model is of fundamental importance. The combination of gas model and magnetic field model enables fundamental understanding of the origin of the signal electrons that are detected by the FPD. This chapter presents the comprehensive gas model covering all regimes of rarefied gas dynamics and its first application to gas flow consisting of deuterium and trace amounts of tritium[1]. Furthermore, first results from commissioning measurements of a magnetic stray field measuring system developed for monitoring the magnetic field of the WGTS are presented and compared to simulations. Together, the gas model and the magnetic field model form the source model, defining the starting conditions for the β-decay electron spectroscopy used to determine the effective neutrino mass.

4.1. General concepts, notation

Let us start the source modelling with introducing some general concepts and notations which will be used throughout this chapter. The source model needs to describe the distribution of the gas inside the WGTS beam tube and the corresponding magnetic field. Gas is injected at the centre of the beam tube (defined as $z = 0$ in source model coordinates) and pumped out at both ends via turbomolecular pumps. Though the WGTS beam tube is 16 m long in total with a radius of $R = 4.5$ cm, 99 % of the gas is in the central 10 m of the beam tube. The corresponding magnetic field in the central beam tube is required to be homogeneous with a design value of 3.6 T.

[1] As used in the First Tritium campaign in May and June 2018.

The main task of the gas model is to estimate the gas column density $\mathcal{N}$ which is the longitudinally integrated[2] amount of gas in the beam tube

$$\mathcal{N} = \int_{-L_{\text{rear}}}^{L_{\text{front}}} n(z)\,\mathrm{d}z, \tag{4.1}$$

with $L_{\text{rear}} \approx L_{\text{front}}$ defining the length in backward (negative z) and forward (towards detector, positive z) longitudinal direction. In order to calculate the column density $\mathcal{N}$, the distribution of the molecules number density $n = N/V$ needs to be known. The number density is related to the pressure p via the volume V, the temperature T, the total number of molecules N, and the Boltzmann constant k_{B} in the ideal gas law

$$pV = Nk_{\text{B}}T. \tag{4.2}$$

One of the key parameters to derive the density distribution $n(z)$ is the mass flow rate $\dot{M}$. It is directly related to the throughput q, which can be derived by dividing eq. 4.2 by the time t

$$q = \frac{pV}{t} = \frac{k_{\text{B}}T}{m} \cdot \frac{N \cdot m}{t} = \frac{k_{\text{B}}T}{m} \cdot \dot{M} = \frac{v_{\text{m}}^2}{2} \cdot \dot{M}, \tag{4.3}$$

with the mass of the gas molecule m and the most probable speed[3] $v_{\text{m}} = \sqrt{2k_{\text{B}}T/m}$. If the gas flow is isothermal with a constant temperature along the beam tube, both $\dot{M}$ and q are constant along the beam tube. However, temperature variations along the beam tube cause throughput variations while the mass flow rate is always constant provided there is no additional source of gas.

A tube can also be characterised in terms of its conductivity C, which is the inverse of the resistance of the tube

$$C = \frac{q}{\Delta p}, \tag{4.4}$$

with the pressure difference $\Delta p = p_{\text{in}} - p_{\text{out}}$ between inlet and outlet. The WGTS gas dynamics covers the whole range of rarefied gases, which is usually characterised in terms of the rarefaction parameter δ

$$\delta = \frac{\sqrt{\pi}}{2}\frac{a}{\lambda} = \frac{\sqrt{\pi}}{2}\frac{1}{Kn}, \tag{4.5}$$

with the characteristic scale of the gas flow $a = R$, the mean free path λ, and the Knudsen number Kn. The mean free path

$$\lambda = \frac{\sqrt{\pi}\eta}{2p}\sqrt{\frac{2k_{\text{B}}T}{m}} = \frac{\sqrt{\pi}\eta}{2p}v_{\text{m}} \tag{4.6}$$

represents the average distance travelled by a gas molecule between collisions and is related to the shear stress viscosity of the gas η. We can differentiate between three gas flow regimes, which lead to different methods to calculate the gas flow:

[2] For this introduction, we will focus on one-dimensional gas flow since $L \gg R$, with L the length of the beam tube in the z-direction.

[3] Not to be confused with the average thermal speed $\bar{v} = \sqrt{8k_{\text{B}}T/(\pi m)}$ of the Boltzmann distributed velocities v.

- In the *hydrodynamic* or *viscous* regime ($\delta \gg 1$, $Kn \ll 1$), the mean free path is so small that intermolecular collisions occur more often than collisions between gas and tube wall. Therefore, the gas can be treated as a continuous medium and the hydrodynamic equations can be applied.
- In the *free-molecular* regime ($\delta \ll 1$, $Kn \gg 1$), the mean free path is so large that intermolecular collisions can be neglected. Therefore, the gas can be considered as free-flowing.
- In the *transitional* regime ($\delta \approx Kn \approx 1$), neither the intermolecular nor the gas-wall collisions can be neglected.

Another quantity that influences the distribution of the gas inside the WGTS beam tube is the accommodation coefficient α describing the interaction of the gas with the wall. Thereby, α defines the fraction of molecules that are reflected diffusely off the wall, while $(1 - \alpha)$ is the specular reflection part. Full accommodation ($\alpha = 1$) refers to full coverage of the tube walls with gas, leading to purely diffuse reflection.

The gas dynamics in the WGTS covers the whole range of rarefied gas flow, from viscous flow at the injection region over transitional flow around the first pump port to free molecular flow after the first pump port, see fig. 4.1.

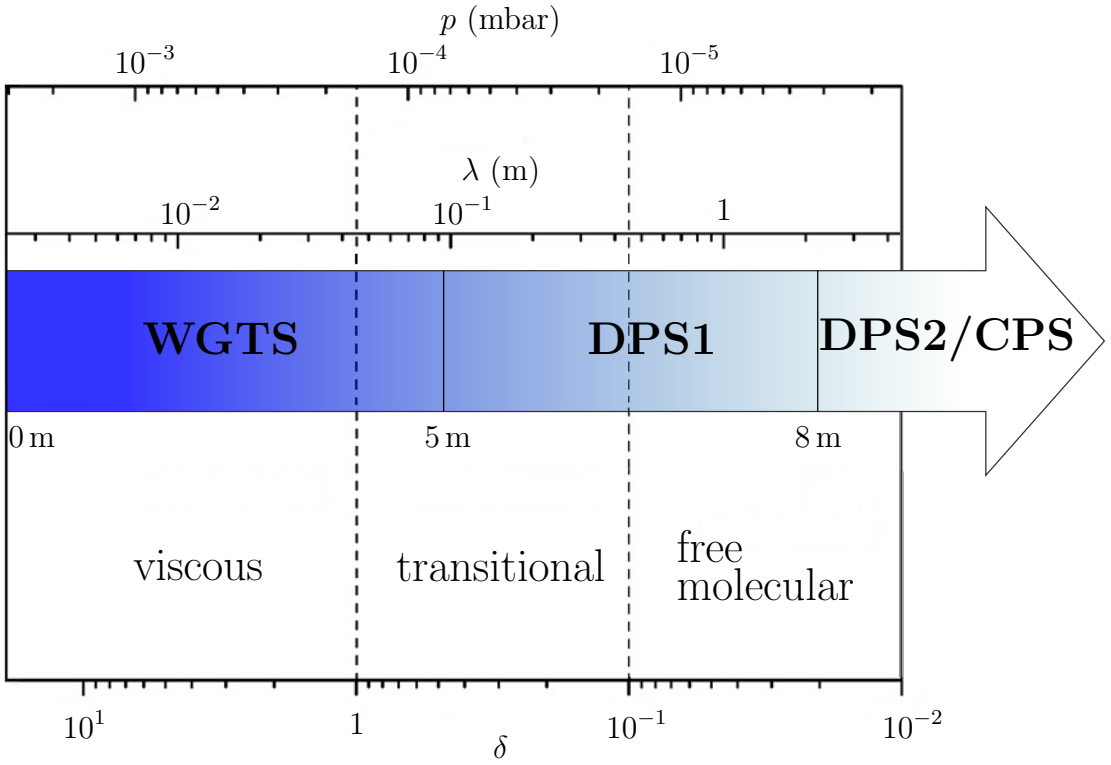

Figure 4.1.: **Pressure regimes.** The range of rarefaction parameter δ, the corresponding pressure p, and the equivalent free path λ are shown with associated gas flow regimes. Figure adapted from ref. [Kuc+18].

In order to accurately describe the gas dynamics inside the WGTS, the challenging part of the modelling is the transitional gas flow starting before the first pump port. In the following, two different methods will be introduced to solve the gas flow in the entire 10 m long central beam tube between the first pump ports. One is using a

phenomenological formula derived from measurements (intermediate Knudsen flow, sec. 4.1.1) and one is solving the Boltzmann equation (sec. 4.1.2), which is describing the theory of gas dynamics.

4.1.1. Intermediate Knudsen formula

In the limit of laminar viscous flow, the gas flow through a long tube can be described by Poiseuille's law. However, Kundt and Warburg [KW75] showed that Poiseuille's law has limited accuracy when the radius of the tube is of the order of the mean free path. Christiansen [Chr90] found that there is a smooth transition from Poiseuille flow to free molecular flow. By applying a series of measurements of the conductivity of tubes, Knudsen [Knu09] found a phenomenological relation which describes the measured conductivity for both extremes, viscous and molecular flow. Even more important for us, his formula can also describe the transitional regime by combining the viscous and molecular flow conductivities.

In eq. (13) [Knu09], Knudsen states the flow rate through cylindrical tubes. Converting to our naming scheme, we can rewrite his formula as [Glü03]

$$q = (D_{\mathrm{vis}}\, p + X\, D_{\mathrm{mol}})\, \frac{p_{\mathrm{in}} - p_{\mathrm{out}}}{L} = C_{\mathrm{Knudsen}} \cdot (p_{\mathrm{in}} - p_{\mathrm{out}}), \tag{4.7}$$

with p the pressure between p_{in} and p_{out}, $L = L_{\mathrm{rear}}, L_{\mathrm{front}}$ the length of the tube in rear and front direction[4], and D_{vis} and D_{mol} identified as the viscous and molecular flow rate coefficients

$$D_{\mathrm{vis}} = \frac{\pi R^4}{8\eta} \quad \text{and} \quad D_{\mathrm{mol}} = \frac{2}{3}\pi\, v_{\mathrm{m}}\, R^3. \tag{4.8}$$

These coefficients are pressure independent and determined by the geometry and temperature of the tube, as well as by the gas species. The coefficient X can be identified from Knudsen's formula as

$$X = \frac{1 + 2Y}{1 + 2.47Y}, \qquad \text{with } Y = \sqrt{\frac{m}{k_{\mathrm{B}}T}}\frac{R\bar{p}}{\eta}. \tag{4.9}$$

As the pressure ratio $p_{\mathrm{out}}/p_{\mathrm{in}}$ is expected to be small, the average pressure simplifies to $\bar{p} = p_{\mathrm{in}}/2$. From eq. (4.7), the differential equation for the pressure profile can be derived by $(p_{\mathrm{in}} - p_{\mathrm{out}})/L \to -\partial p/\partial z$ to [Glü03]

$$q = -D_{\mathrm{vis}}\, p\, \frac{\partial p}{\partial z} - X\, D_{\mathrm{mol}}\, \frac{\partial p}{\partial z}. \tag{4.10}$$

This differential equation can be solved by e.g. variable separation, enabling calculation of the inlet pressure and the pressure profile depending on the boundary conditions $p_{\mathrm{out}}/p_{\mathrm{in}}$, the throughput q, the temperature T, and the gas species. All other terms are set by the geometry of the WGTS. Note that this method of determining the pressure (or, equivalently, density) profile of the WGTS is purely based on the phenomenological formula of Knudsen. The conductance estimated with the intermediate Knudsen formula eq. (4.7) and his measured values for hydrogen at room temperature deviate by about $6 - 7\,\%$, which can be taken as the lower limit of the accuracy of the Knudsen formula. In order to get more accurate results, the Boltzmann equation needs to be solved (see sec. 4.1.2).

[4] Due to a slight longitudinal asymmetry caused by the injection chamber, L_{rear} and L_{front} differ by 7 cm.

4.1.2. Boltzmann equation and distribution function

The number of particles in the phase space volume $\mathrm{d}\boldsymbol{r}\,\mathrm{d}\boldsymbol{v}$ at time t is defined via $\mathrm{d}N = f(t,\boldsymbol{r},\boldsymbol{v})\mathrm{d}\boldsymbol{r}\,\mathrm{d}\boldsymbol{v}$ with spatial coordinate $\boldsymbol{r}$ and velocity $\boldsymbol{v}$. Therein, the one-particle velocity distribution function $f(t,\boldsymbol{r},\boldsymbol{v})$ solves the Boltzmann equation, which in absence of external forces can be written as

$$\frac{\partial f}{\partial t} + \boldsymbol{v}\cdot\frac{\partial f}{\partial \boldsymbol{r}} = Q(f,f_*), \tag{4.11}$$

with the collision integral $Q(f,f_*)$ describing the collision between two gas particles with distribution functions f and f_*. The Boltzmann equation eq.(4.11) can only be solved analytically with simplifications to the collision integral, and numerically only for simple cases [SS98].

Due to the large length-to-radius ratio L/R of about 100, we will consider the flow to be fully developed and reduce the calculation to one dimension for this introduction. In order to solve the Boltzmann equation, the key is the mass flow rate $\dot{M}$ since it is constant in absence of additional sources of gas. We will use the methods of F. Sharipov [Sha97, SS98] in the following, defining the mass flow rate through a cross-section of the tube as

$$\dot{M} = \frac{\pi R^3}{v_\mathrm{m}}\left(-G_\mathrm{P}(\delta)\,\frac{\mathrm{d}p}{\mathrm{d}z} + G_\mathrm{T}(\delta)\,\frac{p(z)}{T(z)}\,\frac{\mathrm{d}T}{\mathrm{d}z}\right), \tag{4.12}$$

with radius of the beam tube R, the local pressure $p(z)$, the local temperature $T(z)$ and the rarefaction parameter δ defined by eq. (4.5). The dimensionless reduced flow rates $G_\mathrm{P}(\delta)$ (Poiseuille flow) and $G_\mathrm{T}(\delta)$ (thermal creep) characterise the gas flow in terms of δ, so they are independent of the gas species. The gas species in turn influences δ, e.g. via its mass. Tabulated values as well as a parametrisation for G_P and G_T can be found in the literature as functions of the rarefaction parameter δ [SS98, Sha16]

$$G_\mathrm{P} = \frac{8}{3\sqrt{\pi}}\frac{1+0.04\,\delta^{0.7}\ln\delta}{1+0.78\,\delta^{0.8}} + \left(\frac{\delta}{4}+\sigma_\mathrm{P}(\alpha)\right)\frac{\delta}{1+\delta}, \tag{4.13}$$

$$G_\mathrm{T} = \begin{cases} \frac{4}{3\sqrt{\pi}} + 0.825(1+\ln\delta)\delta - (1.18-0.61\ln\delta)\delta^2 & \text{for } \delta \le 1, \\ \frac{\sigma_\mathrm{T}(\alpha)}{\delta} - \frac{1.75}{\delta^2} + \frac{1.47}{\delta^3} - \frac{0.5}{\delta^4} & \text{for } \delta > 1. \end{cases} \tag{4.14}$$

The interpolation formula for G_P, eq. (4.13), reproduces numerical results obtained with the S-model [Sha16] within 0.2 %. However, agreement between the numerical S-model results for G_P and results based on a hard-sphere model for the gas molecules [LH90] match within 2 % [Sha16], which also holds for comparisons to experimental data [Sha08]. Since the pressure profile in eq. (4.12) is mainly determined by G_P, the 2 % uncertainty also hold for the pressure profile. On the other hand this means that the column density determined via integration of the pressure equivalent density profile also has about 2 % uncertainty from the dimensionless flow rate coefficients.

In general, the reduced flow rates G_P and G_T depend on the gas-surface interaction which is described by the accommodation coefficient α, varying between 0 (no gas

on the beam tube wall) and 1 (full accommodation of the beam tube wall). The accommodation coefficient affects the viscous Poiseuille σ_P and thermal slip coefficients σ_T[5] which in term influence G_P and G_T [SS98]. However, it has to be noted that the dependence of σ_T on α is negligible compared to σ_P [Sha04b].

In the simple case of isothermal flow, the temperature gradient is zero and we can calculate the mass flow rate via z integration as

$$\dot{M} = \frac{\pi r_0^3 p_{\text{in}}}{v_m \delta_{\text{in}} L} \int_{\delta_{\text{out}}}^{\delta_{\text{in}}} G_P(\delta)\, \mathrm{d}\delta, \tag{4.15}$$

with the injection and outlet pressure equivalent rarefaction parameters δ_{in} and δ_{out}. In case of non-isothermal flow, the longitudinal distribution $\delta(z)$ has to be calculated by numerical finite difference schemes from eq. (4.12) as shown in [Sha96, Sha97, SS98].

4.2. Temperature model

The beam tube of the WGTS is designed to have a per-mille stable and homogeneous temperature. In order to control the temperature of the gas inside the WGTS, resistance sensors are brazed onto the beam tube. As 99 % of the gas column density are inside the central 10 m long beam tube between the first pump ports (compare fig. 3.1), this is the most important part for temperature modelling. This section presents commissioning results and the temperature distribution as it is used for the gas dynamics modelling.

4.2.1. Temperature sensors

At the central 10 m long beam tube, in total 24 Pt500 sensors measure the temperature distribution along the beam tube. As introduced in sec. 3.3.1, those sensors need to be calibrated by vapour pressure sensors to compensate for their magnetic field dependence. Once calibrated, the sensors have an accuracy of 159.77 mK in the worst case scenario [Sei19]. Most of the sensors sit on top (90°) and bottom (270°) of the beam tube (compare fig. 3.3 and fig. 4.2), with only two diagonal sensors at 45° and 225° at both ends of the beam tube. Two of the sensors (one of the front diagonal and one bottom in front side) cannot be used for analysis due to invalid temperature readings, see fig. 4.2. Not indicated on fig. 4.2 is the position of the temperature sensors relative to the beam tube cooling, the interested reader can find this information in the appendix in fig. A.1.

4.2.2. Temperature correlations

If the temperature of the beam tube is regulated via the 2-phase cooling system, the sensor readings should be correlated. In fact, investigations by A. Marsteller [Mar17] during commissioning measurements without gas in the beam tube showed perfect

[5] The slip coefficients influence the tangential velocity of the gas near the beam tube wall.

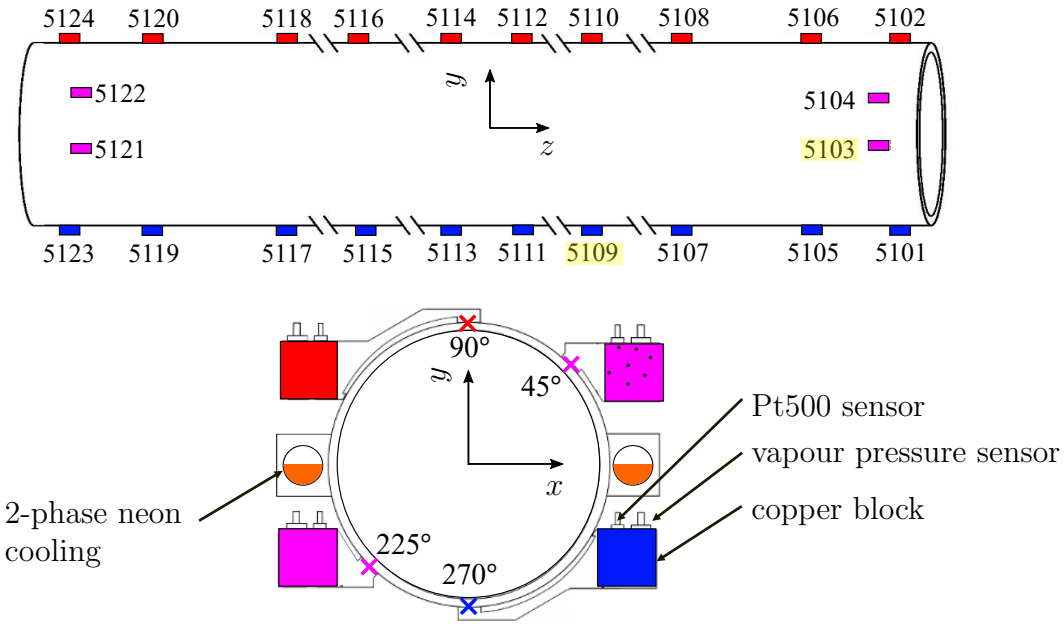

Figure 4.2.: **Temperature sensor positions.** The numbers indicate the sensor ID, malfunctioning sensors are highlighted in yellow. Schematic inspired by ref. [Höt12].

correlation with Pearson's r values of 1. The perfect correlation was obtained because the beam tube temperature was varied within 2 K over two days. During stable operation the readout fluctuations of about 0.5 mK prohibit correlation coefficients of 1 since the beam tube temperature is stable on the per-mille level, see sec. 5.2.1. This is confirmed by fig. 4.3, where some of the temperature sensors appear less correlated than others. However, it is concluded that this difference is due to the fact that readout fluctuations on the order 0.5 mK [Mar17] are dominating the temperature fluctuations, which are the same order of magnitude (see sec. 5.2.1).

4.2.3. Temperature homogeneity

In the Design Report [KAT05], the temperature homogeneity of the central 10 m long beam tube was specified to be better than 30 mK. This section will show that this requirement can not be met, however it will be shown, that the increased temperature at the rear side does not harm the estimation of the column density nor the neutrino mass sensitivity as it can be accounted for in the gas model.

Temperature simulations by L. Kuckert [Kuc16] showed, that the heat load from the pump ports via thermal radiation from the TMPs is the main source for temperature inhomogeneity of the beam tube. As the beam tube cooling ends about 25 cm before the pump port and the bellow connecting beam tube and pump port has no active cooling, it is expected that both ends of the WGTS might get warmer than the centre of the WGTS. Commissioning measurements with the Demonstrator set-up of the WGTS confirmed that expectation [Höt12]. Moreover, these commissioning measurements showed that there is a difference between the front side inhomogeneity and the rear side inhomogeneity of the temperature of the beam tube ends. As a conclusion, the beam tube was turned around to have the higher temperature

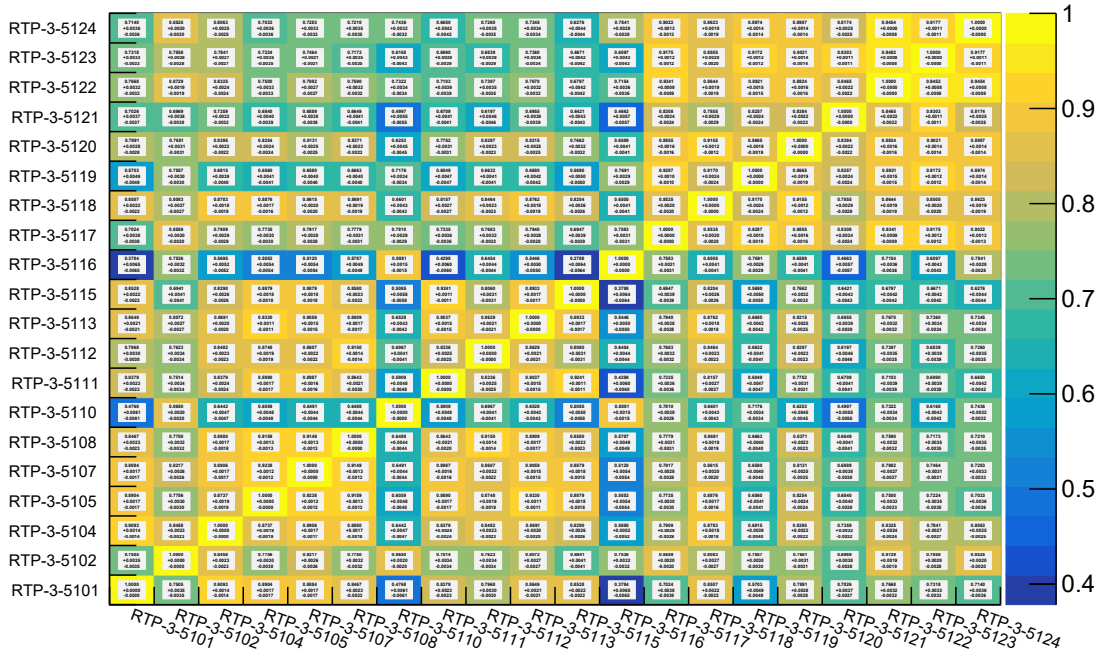

Figure 4.3.: **Temperature correlations.** As explained in the text, the reason for not having perfect correlation is the fluctuations of the readout.

at the rear side, due to electrons starting from the rear side contributing less to the measured β-decay spectrum[6]. Comparison of the simulated and the measured temperature increase showed that the simulation gives overstated values [Kuc16]. Furthermore, the simulations suggest that the azimuthal temperature profile at the end of the beam tube can be well described by a $\sin^2\phi$ relation with the temperature of the 2-phase neon cooling tube (at $\phi = 0, \pi$, compare fig. 3.3) as lower limit and the top/bottom temperature (at $\phi = \pi/2, 3\pi/2$) as upper limit. With this assumption the following azimuthal beam tube temperature profile $T(\phi, z)$ at longitudinal position z can be extrapolated

$$T(\phi, z) = T_0 + \Delta T_{\mathrm{t,b}}(z) \cdot \sin^2\phi, \tag{4.16}$$

with T_0 the temperature of the 2-phase neon cooling tube and $\Delta T_{\mathrm{t,b}}(z) = T_{\mathrm{t,b}}(z) - T_0$ the difference to the top/bottom temperature. As described in sec. 4.2.1, the majority of the temperature sensors sit symmetrically on the top and bottom of the beam tube, compare fig. 4.2. Therefore, the reading of the temperature sensors defines $T_{\mathrm{t,b}}(z)$, together with a splines interpolation [Gal+02]. It has to be noted that the top and bottom longitudinal temperature profile might be different, but the connection between top and bottom is smooth due to the 2-phase neon cooling tubes setting the reference temperature T_0, compare fig. 4.4. The figure shows the azimuthal temperature profile as expected at the position of the first and last top/bottom sensor pair. Furthermore, it reveals that diagonal sensors can not be directly compared to the azimuthal temperature profile at the position of the outermost top/bottom

[6] Electrons from the rear end have much higher probability to scatter out of the measuring window than electrons from the front end.

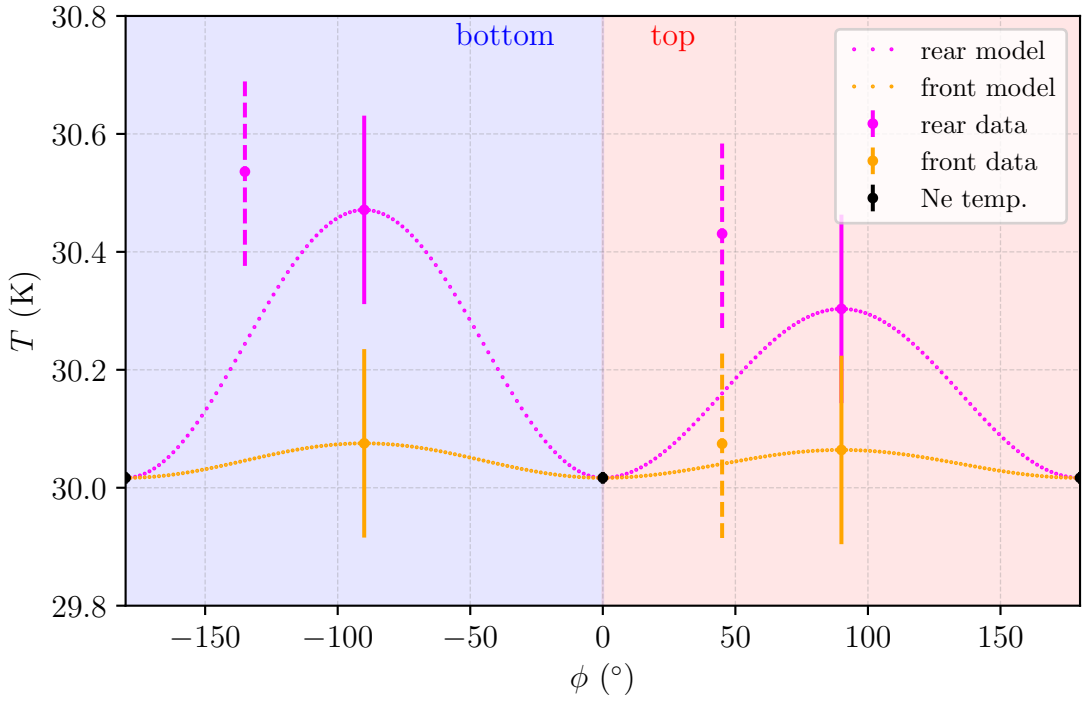

Figure 4.4.: **Azimuthal beam tube temperature distribution.** The figure shows the expected $\sin^2\phi$ temperature dependence, with sensor data from both ends of the beam tube. Background colours indicate the y position on the beam tube. The diagonal sensors visualised by dashed error bars are shifted 2 cm towards the centre compared to the top/bottom sensors which can explain the offset.

sensor pair. The reason might be that the true temperature maximum is between the last and second-to-last temperature sensor, which is not accessible via measurement. Also note that this discrepancy is within 2σ of the uncertainty on the sensor reading; plus the diagonal sensors only measure at the very end of the beam tube, where the effect on the column density is negligible. From fig. 4.5 it follows that the temperature has its maximum not at the last sensors as expected from temperature simulations of L. Kuckert [Kuc16], but presumably at the next pair, which is located 20 cm closer to the centre of the WGTS. The diagonal sensors show a higher temperature than the outer sensors, though they are only 2 cm closer to the centre. Therefore, the temperature simulations cannot be verified, which is the reason for using interpolation of sensor readings instead of a complete model. Furthermore it has to be noted that the gas dynamics uncertainty induced by a wrong temperature assumption in the outlet region will be shown to be negligible and the uncertainty on the β-decay spectrum modelling is even less.

In order to derive the temperature inside the beam tube, the gas distribution needs to be respected. This will be discussed in the next section, as well as the different components that combine to the gas dynamics model of the WGTS.

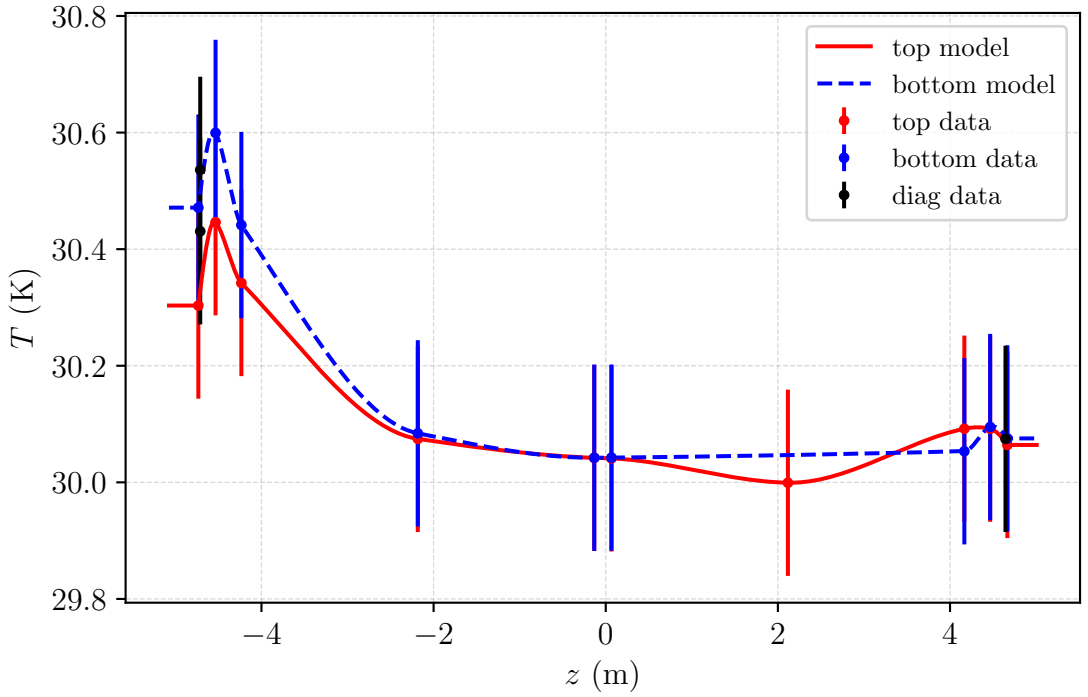

Figure 4.5.: **Longitudinal beam tube temperature distribution.** The figure shows sensor data as well as the splines-interpolated profile.

4.3. Gas dynamics model, nominal KATRIN set-up

As already introduced in sec. 4.1, the gas flow in the WGTS covers the whole range of rarefied gases. Starting in the viscous regime at the injection point (A1 in fig. 4.6), the gas reaches the transitional regime before the first pump port (PP1, region B1 in fig. 4.6). Before leaving the WGTS cryostat, the gas reaches the free molecular flow in the region around the second pump port (PP2, region B3 in fig. 4.6). Each rarefaction regime requires different modelling techniques in order to properly describe the gas flow, therefore the complete gas model of the WGTS consists of several different parts (compare fig. 4.6). These parts are connected via the condition of equal mass flow rate at their boundary.

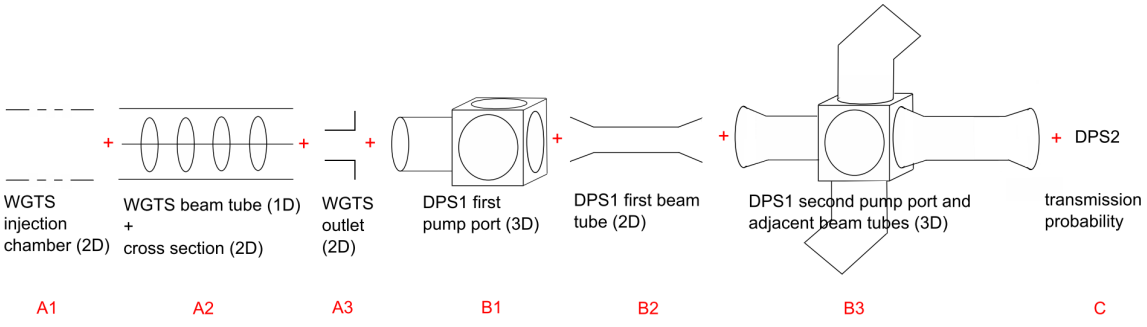

Figure 4.6.: **Scheme of the model geometries.** The schematic drawing visualises the different regions for the gas dynamics calculations and the respective dimensionality. Figure shows the scheme for front direction only, rear direction is symmetric with respect to the injection chamber. Figure adapted from ref. [Kuc+18].

The following section gives an overview of the applied techniques to describe the gas flow in the respective regime for the nominal KATRIN set-up. This refers to settings described in the Design Report [KAT05], treating the gas as pure molecular tritium with a column density of $5 \times 10^{21}\,\mathrm{m}^{-2}$. At the end of this section, an estimation of the total gas model related systematic neutrino mass uncertainty is given.

4.3.1. Gas flow in the central 10 m beam tube (A1-A3)

As about 99 % of the (tritium) gas is contained within the central 10 m long beam tube, this domain's gas flow needs more attention than the following regions. The large length-to-radius ratio L/R of about 100 enables the use of a one-dimensional fully developed flow for most of the beam tube. Only at the inlet and outlet regions, more dimensions have to be added. Following the introduction in sec. 4.1.2, the concept to derive the density profile is described in [Sha97, SS98]. The first to implement these concepts into the KATRIN source and spectrum calculation package SSC was M. Hötzel [Höt12], followed by L. Kuckert [Kuc16]. In order to derive the longitudinal density profile or pressure profile equivalent, eq. (4.12) needs to be solved for $\mathrm{d}p/\mathrm{d}z$ via the constant mass flow rate $\dot{M}$. Parameters influencing the derivation of the density profile are:

- Tabulated values for dimensionless G_P and G_T [Sha97, SS98].
- Inlet pressure p_in at the centre of the 10 m long beam tube, defined via the pressure controlled buffer vessel p_b (compare fig. 3.1).
- Outlet pressure p_out at both ends of the beam tube, defined via the pumping probability of the DPS1 (see fig. 4.6).
- Temperature profile of the beam tube $T(z)$, defined via the 2-phase neon cooling system described in sec. 3.3.1.
- Throughput q and mass flow rate $\dot{M}$, which are also related to the pressure controlled buffer vessel.
- Viscosity η, accommodation coefficient α, and mass m of the gas.

The best estimation of input parameters via sensor data can be given for the temperature profile (see sec. 4.2), all other sensors sit outside the WGTS cryostat and therefore the uncertainty on the corresponding input parameter of the gas dynamics simulation would exceed the 0.2 % requirement on the column density $\mathcal{N}$. Furthermore it needs to be stressed that the uncertainty on the dimensionless flow rate coefficients G_P and G_T is about 2 % [Sha97, SS98], already exceeding the column density uncertainty budget of 0.2 % [KAT05].

4.3.1.1. Gas and surface characteristics

In order to constrain the input parameters for the density profile calculation, let us start with the characteristics of the circulated gas, viscosity η, accommodation coefficient α and mass of the molecule m. The mass is determined by the circulated gas species and considered known. However, for tritium there is no data available for the accommodation coefficient α or the viscosity η at 30 K. These quantities

are estimated from either deuterium or helium data and therefore have quite large uncertainties as discussed in the following.

Accommodation coefficient As introduced in sec. 4.1.2, the accommodation coefficient α determines the viscous slip coefficient σ_P and the thermal slip coefficient σ_T [SS98]. However, the thermal slip coefficient σ_T can be treated as independent of α if compared to the viscous slip coefficient's $\sigma_P(\alpha)$ [Sha04b]. The physical meaning of α is the fraction of gas molecules that scatter diffusely off the beam tube wall. Consequently, $(1-\alpha)$ molecules undergo specular reflection. Diffuse scattering means that the gas particles lose all initial information. They are thermalised with the beam tube wall temperature and have velocities according to the Maxwell distribution. In contrast, specular reflection means that the gas molecules retain angular distribution and velocity of the gas molecules. The first to work out a model for the diffuse scattering was Knudsen [Knu09] who used the cosine law, nowadays known as Lamberts law, to describe the reflection of the gas molecules. Cercignani and Lampis [CL71] split up the accommodation coefficient into a perpendicular and a tangential part relative to the surface and thereby derived an improved version of Knudsen's scattering kernel. Recent measurements of the (tangential) accommodation coefficient of helium on stainless steel at room temperature resulted in a value of 0.912 ± 0.004 [Had+12]. Since the beam tube surface of the WGTS is also stainless steel but the temperature is one order of magnitude lower than in [Had+12], $\alpha = 0.9$ is taken as an extreme lower limit. It is considered safe to assume full accommodation, that is $\alpha = 1$, as standard value for tritium in the WGTS.

Viscosity Similar to the non-existing data for α, measured values for the tritium viscosity η_{T_2} at 30 K are also not available. Therefore it is derived from hydrogen and deuterium using the mass ratio of the isotopologues. Assael et al. relate the viscosities to the masses of the isotopologues hydrogen H_2 and deuterium D_2 as

$$\frac{\eta_{D_2}}{\eta_{H_2}} \sqrt{\frac{m_{H_2}}{m_{D_2}}} = 1. \tag{4.17}$$

However, they find that eq. (4.17) using hydrogen data from [AMW86] states a 7 % overstated value of η_{D_2} compared to measurements [AMW87]. Such an overstatement presumably exists also in the tritium-deuterium viscosity relation; however due to the smaller relative mass difference it is assumed to be below 7 %. It is therefore reasonable to estimate the overstatement of η_{T_2} by 5 %. The resulting tritium viscosity is then

$$\eta_{T_2} = 0.95 \sqrt{\frac{m_{T_2}}{m_{D_2}}} \cdot \eta_{D_2} \approx 2.425 \times 10^{-6}\,\mathrm{Pa\,s}. \tag{4.18}$$

Using the 7 % difference between deuterium data and estimation via eq. (4.17), the uncertainty on the estimated tritium viscosity eq. (4.18) is taken to be 10 %.

4.3.1.2. End effects (A1, A3)

Over a wide range, the gas flow in the WGTS tube can be considered a fully developed flow. However, in the inlet as well as in the outlet regions, local distortions from

the fully developed flow may occur. As 99 % of the gas is inside the central beam tube, one might consider using only the central beam tube calculation to estimate the column density. If doing so, the end effect correction can be used to account for the fact that the inlet and outlet should be modelled in 2D. Both end effects cause distortions on the order of cm [Kuc16, Kuc+18]. They can be accounted for using an effective length in solving eq. (4.12) [SS98, PVS14] which enables use of 1D calculations for the whole beam tube. The usage of the effective length causes differences in mass flow rate $\dot{M}$ and throughput q of up to 5 %. However the effective length causes opposite effects for inlet and outlet regions, leading to partial cancellation when integrating the density profile. Therefore, the column density is only affected to less than 1 % [Kuc+18].

4.3.1.3. Pseudo-3D profile

An inherent limitation of the 1D calculation is the non-treatment of an azimuthal temperature gradient. As shown in sec. 4.2.3, the heat load from the pump ports can cause a warming of the parts of the beam tube that are not in contact with the 2-phase neon cooling. Therefore, an azimuthal temperature gradient can cause radial and azimuthal flow and thereby change the density distribution. The maximum of the azimuthal temperature distribution is determined by the longitudinal temperature gradient, which was shown to be about 0.5 K between the centre and the end of the central beam tube (see sec. 4.2.3). Due to this limited gradient of $\Delta T/L \approx 0.1\,\mathrm{K/m}$, we can treat longitudinal and azimuthal flow separately [Sha09]. Assuming a maximal temperature deviation of 1 K, the resulting average column density difference compared to the 1D isothermal calculation is 0.15 % [Kuc+18]. Pre-calculated azimuthal density distributions can be used to correct for a given temperature profile by weighing them with the maximum temperature difference at a certain cross-section. Thereby, a pseudo-3D density profile can be derived, describing the density distribution at every point in the central WGTS beam tube [Höt12, Kuc16, Kuc+18].

4.3.2. Pumping section - DPS1 (B1-B3)

The density distribution in the pump ports defines the outlet pressure of the central beam tube. Due to the small rarefaction parameter $\delta \leq 0.5$ in the pumping section of the WGTS, the flow is no longer viscous and can therefore no longer be treated in 1D. Full 3D simulations are required to model the complex geometry of the pump ports (compare B1 and B3 in fig. 4.6) [Kuc+18].

4.3.2.1. First pump port (B1)

At the entrance of the first pump port, the gas is in the transitional regime with $\delta \approx 0.5$. A direct simulation Monte Carlo DSMC [Bir94] approach with 10^7 particles is chosen for numerical calculations of the density distribution. The geometry is simplified where possible to reduce computational costs. For example, the tubes connecting pump port and TMPs are replaced by pumping probabilities W_{pump}. A

pumping probability of 0.36 is estimated for these tubes, however their geometry might cause a reduced pumping probability. Therefore, calculations are carried out for $W_{\mathrm{pump}}^{\mathrm{B1}} = 0.2$ and 0.4 [Kuc16, Kuc+18]. Further input to the calculations is the density distribution at the end of the beam tube as expected from the 1D calculations described in sec. 4.3.1. In order to ensure a smooth transition, an overlapping region of 0.32 m length between the two geometries is used. Results for $W_{\mathrm{pump}}^{\mathrm{B1}} = 0.2\,(0.4)$ as well as the connection to the central beam tube calculation are shown in fig.4.7. From $W_{\mathrm{pump}}^{\mathrm{B1}} = 0.2\,(0.4)$, an outlet density at the end of the WGTS beam tube is estimated to 2 (1) % [Kuc16, Kuc+18] of the inlet density with a pump port column density contribution of about 0.01 %. The 2 (1) % outlet pressure estimates are considered the upper (lower) limit for nominal conditions.

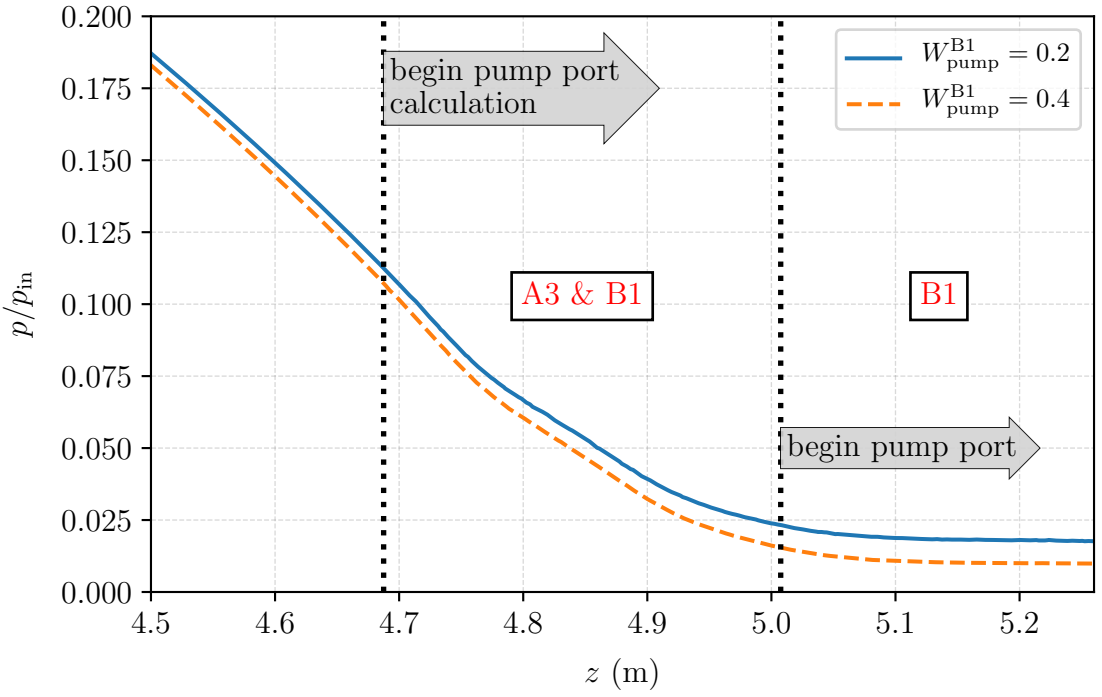

Figure 4.7.: **Transition between central tube and DPS1 PP1.** The start of the overlapping region is marked by *begin pump port calculation*. Figure adapted from ref. [Kuc+18].

4.3.2.2. Tube connecting the pump ports (B2)

The tube between the pump ports can be simulated in 2D by a transitional flow as $\mathcal{O}(\delta) \approx 10^{-1}$. Using the transitional flow interface of COMSOL Multiphysics (version 5.0) [COM14], an isothermal approach is applied to solve the Boltzmann equation. The isothermal approach is considered adequate since investigations with a temperature difference of 6 K [Kuc16] revealed pressure differences for this region of about 5 %. This has negligible impact on the global column density considering this region's column density of 0.3 % [Kuc16, Kuc+18]. It has to be noted that the uncertainty of the outlet pressure from PP1 (sec. 4.3.2.1) is propagated into this region, causing a larger uncertainty for the density distribution in B2 than the inherent 5 % of the B2 model.

4.3.2.3. Second pump port (B3)

Considering the small rarefaction parameter $\delta \approx 10^{-2}$, the last part of the WGTS gas model geometry can be modelled using a molecular flow approach. As the temperature changes significantly from about 30 K at the second pump port (PP2) to room temperature at the WGTS exit (connection to DPS2-F and rear section respectively), the 3D molecular flow interface of COMSOL [COM14] is applied [Kuc16, Kuc+18]. It has to be noted that the uncertainty of the outlet pressure of the central beam tube is propagated all the way to this domain, causing relatively large uncertainties on the density distribution. However, as this region contributes the least to the overall column density, its effect on the global column density can be neglected [Kuc16].

4.3.3. Complete gas model

The baseline to connect the different domains of the WGTS gas model is the calculation of the gas flow in the central 10 m long beam tube. Inlet and outlet regions are scaled accordingly, propagating uncertainties on the outlet pressure of the central beam tube all the way down to the global outlet pressure of the WGTS. The composite density distribution for the complete WGTS is shown in fig. 4.8. Overall reduction factors for gas flow and density are calculated to be about 400 and 2000 [Kuc+18].

Since the uncertainty of the pure simulation of the column density is exceeding the requirement of 0.2 % by one order of magnitude, it is necessary that a measurement of the column density is used as calibration for the overall column density. Once calibrated, the source model gives a precise prediction of column density changes considering changes of operating parameters such as temperature and inlet pressure [Kuc16, Kuc+18]. The following section gives an overview of such a calibration measurement, its requirements, and potential outcome.

4.3.4. Calibration of the column density

As outlined in the previous sections, the uncertainty on the column density due to uncertainties of the simulation parameters of the density profile exceeds the requirement of 0.2 % by about one order of magnitude. However, in terms of neutrino mass analysis, it is not the column density that enters the analysis, but the product of column density $\mathcal{N}$ and total inelastic electron-gas scattering cross section σ via calculation of the scattering probabilities (compare sec. 2.2.1) [Kuc16, Kuc+18, Kle+18]. This product needs to be known to

$$\frac{\Delta(\mathcal{N} \cdot \sigma)}{\mathcal{N} \cdot \sigma} \leq 0.2\,\%. \tag{4.19}$$

As the uncertainty on the inelastic scattering cross-section is stated with 2 % [Ase+00], it is absolutely necessary to determine $\mathcal{N} \cdot \sigma$ from a dedicated measurement to reach the 0.2 % requirement.

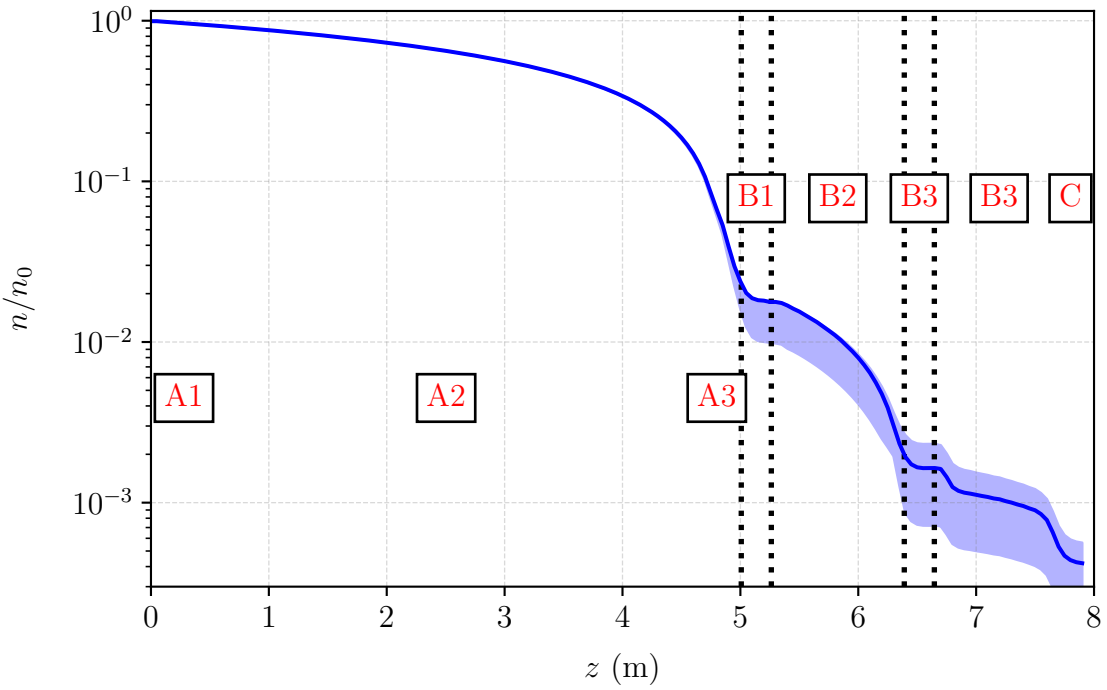

Figure 4.8.: **Longitudinal density distribution in the complete WGTS.** The uncertainty band arises from propagation of the uncertainty of the outlet pressure of the central beam tube. The vertical dotted black lines state the dimensions of the two pump ports. Figure adapted from ref. [Kuc+18].

For this dedicated measurement, an electron gun (e-gun) is used, which is installed at the rear section of the KATRIN experiment (compare sec. 2.2.2) [Bab14, Hei15]. The angular selective e-gun produces mono-energetic electrons of energy E_{e0} which are sent through the WGTS and detected with the focal plane detector (FPD) 70 m distant, at the other end of the KATRIN beam line (compare sec. 2.2). In order to determine the initial electron rate of the beam $\dot{N}_e(0)$, a reference measurement with evacuated WGTS (pressure below 10^{-6} mbar) is conducted before filling the WGTS with gas.

The product $\mathcal{N} \cdot \sigma$ determines the probability for e-gun electrons to cross the WGTS without scattering P_0, which can be calculated via

$$\dot{N}_e(\mathcal{N}) = P_0(\mathcal{N}) \cdot \dot{N}_e(0), \tag{4.20}$$

with $\dot{N}_e(\mathcal{N})$ the e-gun rate at filled WGTS. $\mathcal{N} \cdot \sigma$ is then linked by Poisson probability

$$\mathcal{N} \cdot \sigma = -\ln P_0, \tag{4.21}$$

for the case of zero pitch angle $\theta = 0$ electrons. With an e-gun rate of $10^5\,\mathrm{s}^{-1}$ stable on the per-mille level, a measurement time of about 3 min is required to reach 0.1 % precision at nominal column density $\mathcal{N} = 5 \times 10^{21}\,\mathrm{m}^{-2}$ [Kuc+18]. With the 0.1 % stable e-gun beam plus the finite angular resolution of the e-gun (simulated angular spread of 0.73° in 3.6 T WGTS field at zero e-gun tilt angle [Bab14]), a relative uncertainty of the e-gun determined $\mathcal{N} \cdot \sigma$ of

$$\frac{\Delta(\mathcal{N} \cdot \sigma)}{\mathcal{N} \cdot \sigma} \leq 0.15\,\% \tag{4.22}$$

is calculated [Kuc16]. The e-gun determined $\mathcal{N} \cdot \sigma$ can then be used to calibrate the density profile calculation. Though the uncertainty of the scattering cross-section σ prevents translation of $\mathcal{N} \cdot \sigma$ to $\mathcal{N}$ with the 0.15 % uncertainty, it enables use of the calibrated density profile for prediction of column density changes with the required uncertainty [Kuc16, Kuc+18]. Since changes of the column density can be modelled on the per-mille level or better [Kuc+18], the total uncertainty of the gas model is in fact determined by the measurement of the e-gun. The next section will present the neutrino mass uncertainty resulting from the accuracy of the e-gun measurement.

4.3.5. Neutrino mass uncertainty

With the product of column density and scattering cross-section $\mathcal{N} \cdot \sigma$ being constrained to 0.2 % by the measurement described in sec. 4.3.4, the resulting neutrino mass uncertainty can be estimated from ensemble tests [Kle14, Kle+18, Kuc+18]. The investigations were performed by L. Kuckert [Kuc16] and are briefly summarised below.

- The dominating effect is the first order effect of having a 0.2 % different $\mathcal{N} \cdot \sigma$ in the model and the generated data. It results in a neutrino mass squared shift (C in fig. 4.9) of

$$\Delta m_\nu^2\Big|_{\mathrm{C}} = (-2.62 \pm 0.25) \cdot 10^{-3}\,\mathrm{eV}^2. \tag{4.23}$$

- The second order effect of the accuracy of the gas density profile (difference of up to 5 % from two different models) for fixed column density yields a neutrino mass squared shift of (A in fig. 4.9)

$$\Delta m_\nu^2\Big|_{\mathrm{A}} = (-0.75 \pm 0.24) \cdot 10^{-3}\,\mathrm{eV}^2. \tag{4.24}$$

- Another second order effect is the limited column density accuracy of 2 % while $\mathcal{N} \cdot \sigma$ is assumed to be known precisely. This effect results in (B in fig. 4.9)

$$\Delta m_\nu^2\Big|_{\mathrm{B}} = (-0.26 \pm 0.25) \cdot 10^{-3}\,\mathrm{eV}^2. \tag{4.25}$$

- A combined ensemble test of all above mentioned effects yields the total gas model related uncertainty on the neutrino mass squared of (ABC in fig. 4.9)

$$\Delta m_\nu^2\Big|_{\mathrm{ABC}} = (-3.06 \pm 0.24) \cdot 10^{-3}\,\mathrm{eV}^2. \tag{4.26}$$

A summary of the outlined gas dynamics related systematic uncertainties on the neutrino mass is given in fig. 4.9 [Kuc+18]. It can be concluded that the Design Report estimated uncertainty can not be met if the Design Report requirement is interpreted as an accuracy requirement. However, it has been shown that relative changes can be modelled with an uncertainty well below the requirement [Kuc16, Kuc+18]. Furthermore, the estimated neutrino mass uncertainty from the accuracy of the gas model in combination with calibration by the RS e-gun is well below the limit of a single systematic uncertainty if assuming that the number of systematic uncertainties in the Design Report is complete. The overall KATRIN systematic uncertainty budget is currently undergoing a detailed revision [Sei19] which will reveal whether the uncertainty of the described e-gun measurement needs to be improved to reduce the systematic uncertainty related to the gas dynamics description.

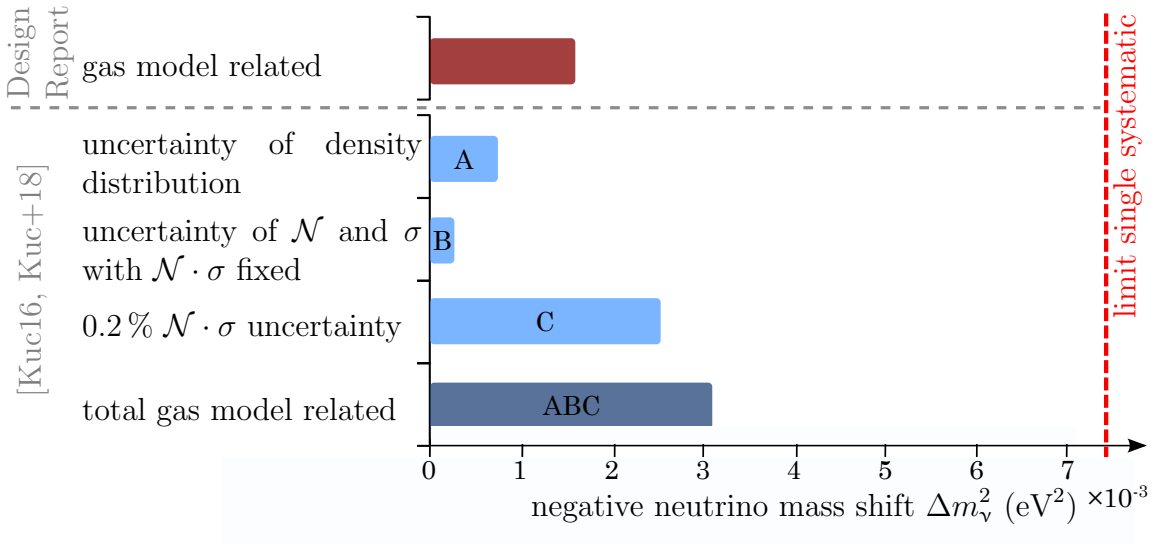

Figure 4.9.: **Gas dynamics related neutrino mass uncertainty.** The different effects investigated in [Kuc16, Kuc+18] and the requirement from the Design Report [KAT05] are shown. For further details, see text or [Kuc+18]. Figure adapted from ref. [Kuc+18].

4.4. Gas dynamics model, First Tritium set-up

In the last three years, KATRIN has achieved several commissioning milestones and will start neutrino mass data taking in early 2019. The first transmission of tritium β-decay electrons presents the latest major achievement towards long-term neutrino mass operation (compare chapter 5). For the first time, trace amounts of tritium were injected into the WGTS and the β-decay electrons were observed with the FPD detector on the other end of the KATRIN set-up.

This section will present the gas dynamics model developed from scratch specifically for the First Tritium campaign and discuss the uncertainty on the modelled gas distribution and consequently the uncertainty on the modelled column density.

4.4.1. Statement of the problem

The notation used throughout this section will be the same as in the introduction sec. 4.1 and the description of the gas dynamics for the nominal KATRIN set-up sec. 4.3, however the gas specific characteristics as viscosity will be used for deuterium. The major difference between the First Tritium setup and the nominal KATRIN operation was the tritium concentration ϵ_T. In nominal set-up, the tritium concentration will be $\epsilon_T \geq 0.95$ while in the First Tritium set-up trace amounts $\epsilon_T \approx 5 \times 10^{-3}$ were used with deuterium as carrier gas. A further difference to the nominal set-up arises from the non-availability of the e-gun during the First Tritium campaign. Since no e-gun means no possibility to calibrate the calculated column density as outlined in sec. 4.3.4, different procedures need to be used to estimate the input parameters for the gas profile calculation.

4.4.1.1. Choice of input parameters

As outlined in sec. 4.3, the dominant uncertainty in the calculation of the column density is the uncertainty on the pre-calculated dimensionless Poiseuille and thermal creep coefficients G_P and G_T of about 2 %. Since this presents the lower uncertainty limit of the column density $\mathcal{N}$ achievable from calculations, it was decided to perform calculations for the central beam tube only. Using the list of input parameters in sec. 4.3.1, two possibilities are left:

- Estimate the injection rate and therefore the throughput of the WGTS from the flow meter between the two buffer vessels of the inner loop (see fig. 3.1). Then use the throughput to calculate the mass flow rate and recursively estimate the density profile.
- Estimate the injection pressure from the measured pressure at the krypton capillary. The krypton capillary is used for the injection of krypton into the injection chamber (shown in fig. 3.4) in the high temperature mode of the WGTS and is equipped with a pressure sensor.

When operating the inner loop in a closed circle, there is no additional source of gas between pressure controlled buffer vessel at p_B and the injection chamber at p_{ch} which in turn defines the injection pressure into the beam tube, p_{in}. During the start-up of the gas circulation, gas might adsorb on the wall of the capillary feeding the injection chamber and thereby cause a reduction of the initial mass flow rate. However, once stable circulation is established in terms of buffer vessel pressure stability on the per-mille level, there is no decrease or increase of the mass flow rate between buffer vessel and injection chamber. This would enable estimation of the mass flow rate and thereby the throughput of the WGTS from the flow meter measurement.

Calculating the injection pressure from the pressure gauge at the krypton capillary on the other hand requires solving two differential equations, one to translate the pressure at the gauge (room temperature) into a pressure at the injection chamber (30 K) and one to translate the pressure from injection chamber to the inlet pressure in the beam tube itself.

It is therefore considered reasonable to use the flow meter and the pressure in the buffer vessel to estimate the injection rate into the WGTS source tube. Then one can apply a finite difference scheme to solve for the longitudinal density distribution and thereby estimate the column density. The pressure gauge at the krypton capillary will be used as a cross-check for the recursively calculated injection pressure.

4.4.1.2. Choice of methods to calculate the column density

Due to the importance of the column density for the modelling of the measured β-decay spectrum, two different methods are used to estimate the density profile from the injection rate. One is the phenomenological formula found by Knudsen [Knu09] (introduced in sec. 4.1.1) and the other one is solving the Boltzmann equation by applying a finite difference scheme [Sha97, SS98, Sha08, Sha16] (introduced in sec. 4.1.2). Integrating each density profile yields the respective column density estimate.

The calculations of the gas profile are done only for pure deuterium, as about 93 % of the circulated gas consists of D_2, about 5.5 % of HD, and about 1 % of DT (also compare sec. 5.1). Other isotopologues such as T_2 and H_2 are present in negligible amounts. Investigations by Sharipov and Kalempa on separation phenomena using 95 % T_2 and 5 % H_2 [SK05] revealed that separation phenomena for this extreme configuration can be neglected. They found a concentration column for H_2 of 4.94 %, which is very close to the injection concentration of 5 %. Therefrom, Sharipov and Kalempa concluded that separation phenomena for this most extreme configuration (H_2 is the lightest and T_2 the heaviest hydrogen isotopologue) are negligible and that the density distribution of T_2 is not affected by the 5 % H_2. Moreover, they also investigated separation phenomena for gas injected with 10 % DT concentration and 90 % T_2 [SK10], which is a mass configuration closer to the First Tritium set-up. Since the mass difference of these isotopologues is even smaller, they found the separation effects to be negligible and the column concentration of DT equal to the injection concentration. From the findings of Sharipov and Kalempa it is concluded that a treatment of the gas as pure deuterium D_2 is a valid assumption from the gas dynamics perspective.

4.4.2. Derivation of the injection rate

As outlined in sec. 4.4.1.1, the input of choice for the density profile derivation is the flow rate measured by the flow meter between the two buffer vessels. This section will now present the derivation of the mass flow rate that is injected into the WGTS beam tube and builds up the density profile.

Remembering the inner loop flow chart from fig. 3.1, the value measured by the flow meter between the buffer vessels is not exactly the injection rate. The valve between the two buffer vessels regulates the gas flow between the vessels in order to stabilise the pressure controlled buffer vessel. A stable buffer vessel in closed loop operation results in a stable injection rate, however the flow rate measured by the flow meter may undergo fluctuations due to the regulating valve. Therefore, a translation from pressure controlled buffer vessel to an injection rate is necessary. Using times of stable gas circulation, we can calibrate the injection rate into the WGTS q_{in} using the pressure in the pressure controlled buffer vessel p_{b}.

Since the gas starts in the viscous regime at the buffer vessel and reaches transitional flow at the injection chamber, the form for the fit function $q_{\mathrm{in}}(p_{\mathrm{b}})$ can be determined by Knudsen's intermediate flow formula [Knu09], given in eq. (4.7) to

$$q_{\mathrm{in}}(p_{\mathrm{b}}) = m \cdot p_{\mathrm{b}}^2 + c \cdot p_{\mathrm{b}}. \tag{4.27}$$

Unit conversion It needs to be stressed that the flow meter (see fig. 3.1) measures the gas flow q in sccm, while a conversion to $\mathrm{mbar\,l\,s^{-1}}$ is appropriate for the estimation of the injection rate. The conversion is done via a factor of 0.01689189 as recommended by NIST [RH09]. Furthermore, the zero offset of the flow meter needs to be considered, it shows about $-3\,\mathrm{sccm}$ for zero gas flow.

The time windows chosen to estimate the relation between pressure controlled buffer vessel and injection rate can be found in tab. A.1. Fig. 4.10 shows the retrieved

relation between pressure controlled buffer vessel and the injection rate. It can be seen that the fit formula fits the data well with resulting estimates of the fit parameters according to tab. 4.1.

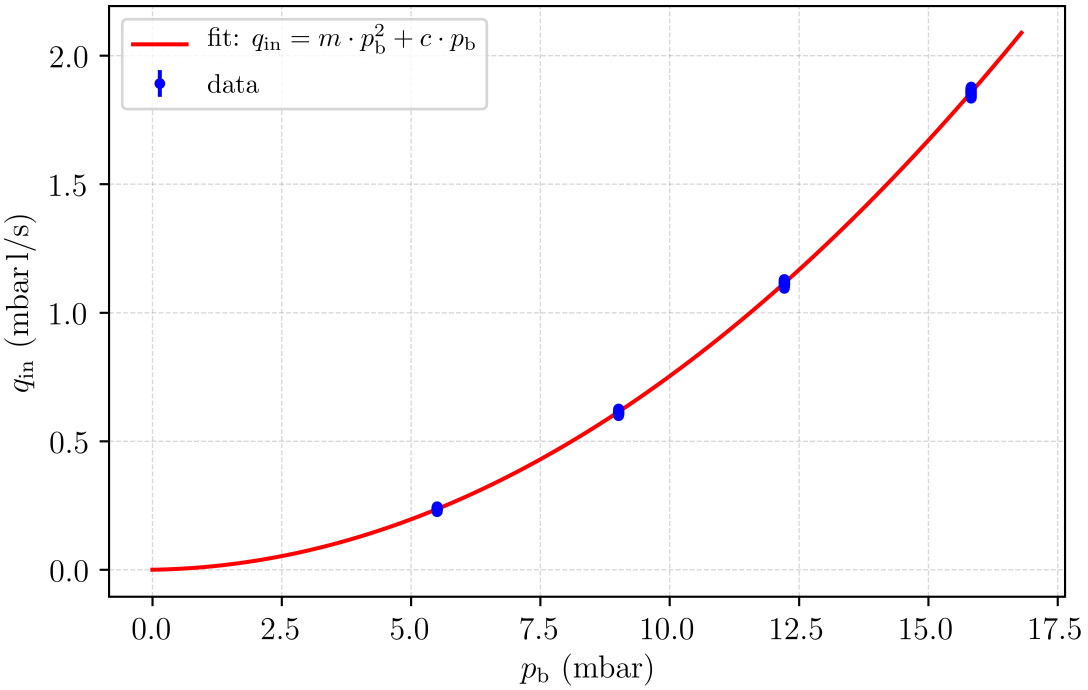

Figure 4.10.: **Relation between pressure controlled buffer vessel and injection rate.** The fit parabola from eq. (4.27) describes the relation well.

Table 4.1.: **Pressure to injection rate fit parameters.** Fit function according to eq. (4.27), $q_{in}(p_b) = m \cdot p_b^2 + c \cdot p_b$ (also see fig. 4.10).

parameter	estimate	uncertainty
m ($\mathrm{l\,s^{-1}\,mbar^{-1}}$)	7.2×10^{-3}	6.7×10^{-7}
c ($\mathrm{l\,s^{-1}}$)	3.2×10^{-3}	5.6×10^{-6}

The relation between buffer vessel pressure and injection rate is identified as the conductivity of the system. According to eq. (4.4) this is the ratio between the injection rate and the pressure controlled buffer vessel pressure (neglecting the injection pressure p_{in} which is four orders of magnitude lower than p_b).

4.4.3. Intermediate Knudsen flow

As introduced in sec. 4.1.1, the intermediate Knudsen formula [Knu09] can be used to get a fast and simple estimation of the density profile in the WGTS beam tube, depending on input parameters injection flow rate q_{in}, temperature T, and the pressure ratio p_{out}/p_{in}. The pressure profile $\partial p/\partial z$ can be derived by solving the differential equation eq. (4.10) and using the gas characteristics such as mass and viscosity [Glü03].

From eq. (4.10) (with $q = q_{\mathrm{in}}$), we can derive an equation for p_{in} by variable separation and integration. Using the boundary conditions $p(z = 0) = p_{\mathrm{in}}$ and a fixed pressure ratio $a_{\mathrm{p}} = p_{\mathrm{out}}/p_{\mathrm{in}} = \mathrm{const}$ yields

$$p_{\mathrm{in}} = \frac{-B \pm \sqrt{B^2 - 4\,A\,C}}{2\,A}, \tag{4.28}$$

with $A = 0.5\,D_{\mathrm{vis}} \cdot (1 - a_{\mathrm{p}}^2)$, $B = X\,D_{\mathrm{mol}} \cdot (1 - a_{\mathrm{p}})$ and $C = -q_{\mathrm{in}}\,L$. Iteratively solving eq. (4.28) for p_{in} until convergence[7] yields the inlet pressure p_{in}. Integrating eq. (4.7) from $z = 0$ to z enables a simple formula for the pressure profile, using the above calculated inlet pressure p_{in} as

$$p(z) = \frac{-B' \pm \sqrt{B'^2 - 4\,A'\,C'}}{2\,A'}, \tag{4.29}$$

with $A' = 0.5\,D_{\mathrm{vis}}$, $B' = X\,D_{\mathrm{mol}}$ and $C' = q_{\mathrm{in}}\,z - A'\,p_{\mathrm{in}}^2 - B'\,p_{\mathrm{in}}$. Obtaining the number density profile is then trivial via eq. (4.2).

4.4.3.1. Temperature dependence

It has to be stressed that the formula eq. (4.29) derived from [Knu09, Glü03] assumes constant temperature along the beam tube when solving for p_{in}. Calculating the column density for a beam tube temperature of $T = 30\,\mathrm{K}$ and $30.5\,\mathrm{K}$ yields a column density difference of 0.2 % when adapting the viscosity according to its temperature dependence stated in [AMW87]. Since the deuterium viscosity change from 30 K to 30.5 K is about 1.7 % and the quoted uncertainty on the viscosity is 2 %, we can also use the same viscosity for both temperatures, resulting in a column density difference of 0.8 %. This difference is the upper limit of the temperature related uncertainty to the Knudsen flow since it assumes 0.5 K temperature difference for the whole beam tube. As shown in sec. 4.2.3, the longitudinal temperature deviation only reaches 0.5 K at the rear end of the beam tube; therefore the realistic effect on the column density is even smaller.

4.4.3.2. Pure tritium

In order do get an estimate for the uncertainty of this alternative calculation of the column density, the result is compared to calculations by F. Sharipov for pure tritium [Sha04a]. Using the same conditions ($T = 27\,\mathrm{K}$, $q_{\mathrm{in}} = 1.853\,\mathrm{mbar\,l\,s^{-1}}$, $p_{\mathrm{out}} = 0$ and $L_{\mathrm{front}} = L_{\mathrm{rear}} = L = 5\,\mathrm{m}$, and viscosity according to eq. (4.18)[8]), the Knudsen flow results in a column density of $\mathcal{N} = 4.98 \times 10^{21}\,\mathrm{m^{-2}}$.

Compared to the $5 \times 10^{21}\,\mathrm{m^{-2}}$ estimate of Sharipov, this is a deviation of 0.4 %. As discussed in sec. 4.1.1, this is within the uncertainty of the intermediate Knudsen formula. It has to be noted that the estimate of Sharipov has a model-related uncertainty of 2 % [Sha04a], so it can be concluded that the Knudsen formula can be used as a simple cross-check of calculations based on solving the Boltzmann equation.

[7] Convergence here is defined as $\frac{p'_{\mathrm{in}} - p_{\mathrm{in}}}{p_{\mathrm{in}}} < 10^{-6}$.

[8] Including the temperature dependence of the deuterium viscosity according to [AMW87].

4.4.3.3. Pure deuterium

Repeating the calculations from sec. 4.4.3.2 with the same input parameters but with pure deuterium as gas (also adapting the viscosity) results in a column density of $4.48 \times 10^{21}\,\mathrm{m}^{-2}$. Due to the lighter mass of the deuterium, causing a larger most probable speed v_m at the same temperature, it is expected that the column density for deuterium compared to tritium is about 10 % lower.

For realistic input parameters ($T = 30\,\mathrm{K}$, $q_\mathrm{in} = 1.85\,\mathrm{mbar\,l\,s^{-1}}$, $p_\mathrm{out}/p_\mathrm{in} = 0.02$, $L_\mathrm{front} = 5.0075\,\mathrm{m}$, $L_\mathrm{rear} = 5.0745\,\mathrm{m}$), the Knudsen-based column density estimate is

$$\mathcal{N} = 4.52 \times 10^{21}\,\mathrm{m}^{-2}. \tag{4.30}$$

4.4.4. Boltzmann equation

As described in sec. 4.3.4, the nominal set-up requires a calibration of the column density in order to reach the necessary accuracy. The calibration by the e-gun enables one to find the input parameters for the density profile calculation such that the estimated column density and the WGTS flow rate match the e-gun measurement. However, as described in sec. 4.4.1, the e-gun was not available during the First Tritium campaign. Furthermore, the gas model before this thesis was only able to deal with pure tritium T_2. Therefore, in the course of this thesis, the intermediate Knudsen flow was implemented which can be used to calculate the density profile and column density for deuterium and tritium, directly using the injection rate. One drawback of the Knudsen implementation (compare sec. 4.4.3.1) is its lack of modelling temperature gradients. As introduced in sec. 4.1.2, solving the Boltzmann equation is one way to include temperature gradients. In contrast to the Knudsen formula, eq. (4.12) can deal with temperature driven flow. Therefore, another type of gas model was implemented, which is similar to the one described in sec. 4.3.1 but uses the WGTS flow rate as an input parameter instead of an output parameter. Furthermore, the new implementation is generalised for dealing with tritium and deuterium. Describing hydrogen gas dynamics would only require including the hydrogen viscosity from [AMW86].

4.4.4.1. Determining the density profile

The principle for deriving the density profile remains the same as in sec. 4.3.1. Converting the injection rate into a mass flow rate enables iterative calculation of the pressure profile using eq. (4.12) and the formulas for the dimensionless Poiseuille and thermal flow rates G_P (4.13) and G_T (4.14). The mass flow rate $\dot{M}$ can be obtained from the injection flow rate q_in from eq. (4.3) as

$$\dot{M} = \frac{m}{k_\mathrm{B} T} q_\mathrm{in}. \tag{4.31}$$

It has to be stressed that the gas flow q has to be scaled with the temperature, while the mass flow rate $\dot{M}$ is temperature independent and constant provided there is no additional source of gas. Knowing the mass flow rate, we can recursively calculate the pressure profile via a finite numerical difference scheme, which also

enables one to account for a longitudinal temperature gradient via G_T. In order to ensure the desired ratio of outlet to inlet pressure, this finite difference scheme is applied until $p_\mathrm{out}/p_\mathrm{in}$ converges while respecting the temperature profile. Similarly to the Knudsen flow, converting the converged pressure profile into a density profile is trivial via eq. (4.2) and integration of the latter yields the column density $\mathcal{N}$. Since the dimensionless flow rates G_P (4.13) and G_T (4.14) are parametrised in terms of the rarefaction parameter δ, they are gas species independent.

4.4.4.2. Pure tritium

Similarly to the intermediate Knudsen flow, an important cross-check for this new density profile implementation is the reproduction of the results from F. Sharipov for pure tritium [Sha04a]. Using the same settings ($T = 27\,\mathrm{K}$, $q_\mathrm{in} = 1.853\,\mathrm{mbar\,l\,s^{-1}}$, $p_\mathrm{out} = 0$ and $L_\mathrm{front} = L_\mathrm{rear} = L = 5\,\mathrm{m}$ and viscosity according to eq. (4.18)[9]), results in a column density of $\mathcal{N} = 4.95 \times 10^{21}\,\mathrm{m^{-2}}$.

Compared to the Sharipov estimation, this is a 1 % difference. However, this is within the modelling uncertainty and might well be due to the interpolation formulae used for G_P (see eq. (4.13)) and G_T (see eq. (4.14)).

4.4.4.3. Pure deuterium

Using the same settings as in sec. 4.4.4.2 but changing the gas species to D_2 yields a column density of $4.44 \times 10^{21}\,\mathrm{m^{-2}}$.

For realistic input parameters ($T = 30\,\mathrm{K}$, $q_\mathrm{in} = 1.85\,\mathrm{mbar\,l\,s^{-1}}$, $p_\mathrm{out}/p_\mathrm{in} = 0.02$, $L_\mathrm{front} = 5.0075\,\mathrm{m}$, $L_\mathrm{rear} = 5.0745\,\mathrm{m}$), the estimated column density is

$$\mathcal{N} = 4.49 \times 10^{21}\,\mathrm{m^{-2}}. \tag{4.32}$$

This agrees with the Knudsen estimate within 0.7 % and highlights the cross-check possibility of the two methods. Differences between the two methods are marginal, which can also be seen in fig. 4.11. Towards both ends, the density profile difference increases and reaches maximum at about 8 %. However, this difference in density profile only weakly affects the estimated column density: the column density difference is 0.7 %. The good agreement in column density though resulting in different density profiles also is shown in [Kuc+18]. There, we investigate whether a change in outlet pressure would change the column density and find the injection pressure to have a much stronger influence on the column density. Since the pressure sensors at the TMPs at PP1-F and PP1-R show the same pressure during stable gas circulation, the same pressure ratio is used for front and rear side.

4.4.5. Column density, injection rate and pressure controlled buffer vessel

During the First Tritium commissioning phase, several column densities were tested in order to show stable gas circulation and data taking at different column densities.

[9] Estimating the temperature dependence of the tritium viscosity from the deuterium viscosity according to Assael et al. [AMW87].

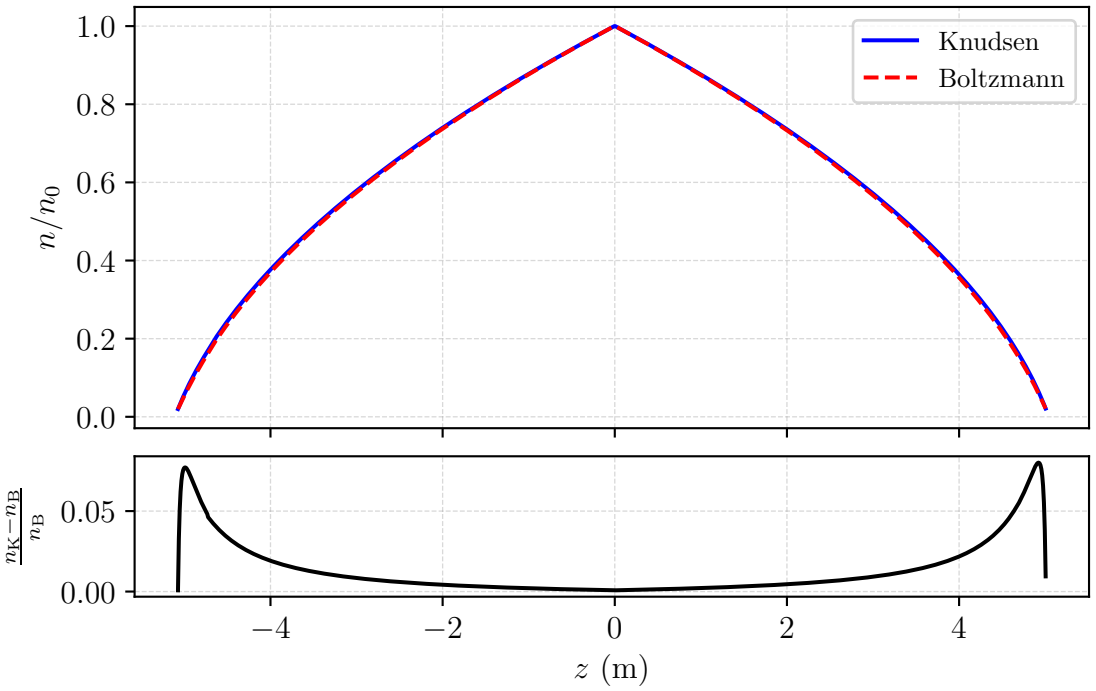

Figure 4.11.: **Realistic density profile for Knudsen and Boltzmann approaches.** The temperature distribution and injection rate $q_{in} = 1.85\,\mathrm{mbar\,l\,s^{-1}}$ are as during First Tritium (compare fig. 4.5). The upper plot shows the density distribution relative to the injection density, the lower plot the relative deviation between Knudsen (solid blue) and Boltzmann (dashed red) derived density profile.

The parameters of the inner loop system controlling the column density are the flow rate q between the buffer vessels and the pressure of the pressure controlled buffer vessel p_b. Using the conductivity calibration points from fig. 4.10, we can get the relations between calculated injection rate and column density (see fig. 4.12) as well as between pressure controlled buffer vessel and column density (see fig. 4.13). It can be seen from figs. 4.12 and 4.13 that the two estimations of the column density deviate with smaller injection rate, and that the column density depends almost linearly on the pressure in the pressure controlled buffer vessel over a wide pressure range.

4.4.6. Discussion of sources of uncertainties

In order to estimate the uncertainty on the calculated column density for both methods, Knudsen and solving the Boltzmann equation, the uncertainties of the input parameters need to be considered. For the total uncertainty, the model dependent uncertainty also has to be added, which is assumed to be uncorrelated with the input parameters. In the following the input parameters for the models plus their uncertainty will be discussed. Since the stability of the input parameters, such as outlet pressure or injection rate, are orders of magnitude better than the uncertainty on their absolute value, the column density uncertainty will only be evaluated for their systematic effect.

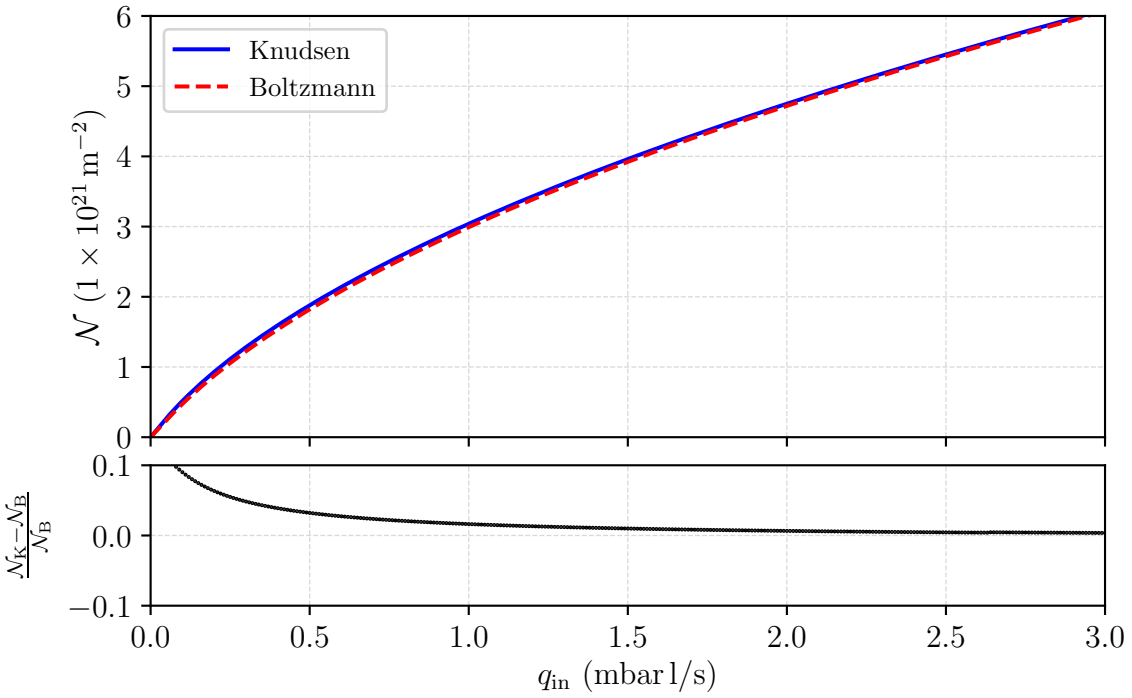

Figure 4.12.: **Relation between column density and injection rate.** Constant beam tube temperature of 30 K assumed. The upper plot shows the relation between column density and injection rate, while the lower plot states the relative difference between the Knudsen and Boltzmann based gas model.

Temperature The temperature along the beam tube has a small gradient of about $\Delta T = 0.5\,\mathrm{K}$ towards the rear side. Furthermore, the lowest temperature reading of a Pt500 sensor shows 30 K, which is taken as the lower limit. A conservative estimation assumes this temperature difference for the whole beam tube; as we will see the temperature related uncertainty on the column density is negligible compared to the other uncertainties.

Injection rate The flow meter has an accuracy of 1 %, communications with the operators however resulted in a conservative estimation of 2.5 % [Stu18]. This increased uncertainty also accounts for the fact that the flow meter calibration measurement described in sec. 4.4.2 is used to estimate the injection rate. To date, it is not clear whether the assumption of no additional gas source between pressure controlled buffer vessel and injection chamber fully describes the relation between pressure controlled buffer vessel and injection rate.

Outlet to inlet pressure ratio From the TMP pressure sensors we know that the ratio for front and rear side is the same. However its absolute value is not yet determined. Simulations by F. Sharipov with the nominal gas model showed a value between 1 % and 2 %; but higher or lower values are also possible. Therefore, a conservative lower value of 0 is assumed and an upper value of 5 %.

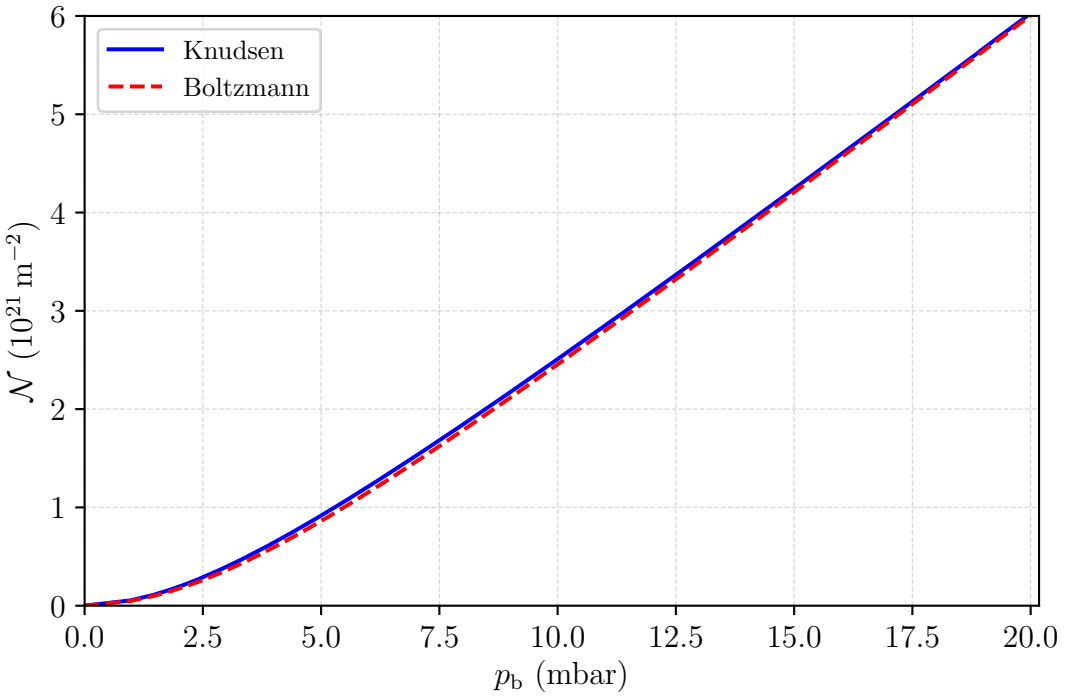

Figure 4.13.: **Relation between column density and pressure in the pressure controlled buffer vessel.** A constant beam tube temperature of 30 K is assumed.

Deuterium viscosity Assael et at. [AMW87] state a 2 % uncertainty on their estimated deuterium viscosity values.

Accommodation coefficient As outlined in sec. 4.3.1, there exist no measurements of the accommodation of deuterium or hydrogen in the temperature regime we are interested in. Hadj et al give a value of $\alpha = 0.912 \pm 0.004$ [Had+12] for the accommodation coefficient of helium on warm stainless steel. Therefore, a conservative value of $\alpha = 0.9$ is taken as lower limit of the accommodation coefficient of deuterium at 30 K, while the upper limit is 1 (full accommodation). It has to be noted that accounting for the accommodation coefficient is only possible in the 'Boltzmann' density model via the dimensionless flow rates G_P and G_T.

4.4.7. Estimation of the (deuterium) column density uncertainty

In order to see the effects of the uncertainties of the individual input parameters on the column density, each parameter is varied separately and the corresponding column density calculated. For example, the viscosity depends on the temperature, therefore changes in this one parameter propagate changes to all other parameters.

Input parameter effects on the column density estimate The result of deflecting one input parameter (which might influence others) is shown in fig. 4.14. For both simulation variants, we can see similar effects. We also see the previous statement, that the temperature dependence of the column density estimation is rather

Table 4.2.: **Column density input systematics.** The input parameters for the column density estimation according to sec. 4.4.3.3 and sec. 4.4.4.3. The values are drawn from these parameters assuming they are Gaussian distributed. Statistical variation of the parameters is ignored since the stability is orders of magnitude better than the accuracy.

quantity	estimate	uncertainty or range
T_{in} (K)	30.0168	0.5
q_{in} (mbar l s^{-1})	1.85	$0.025 \cdot 1.85$
$p_{\mathrm{out}}/p_{\mathrm{in}}$	0.02	$[0 - 0.05]$
$\eta_{\mathrm{D_2}}$ (10^{-6} Pa s)	2.084	$0.02 \cdot 2.084$
α	0.97	$[0.9 - 1.0]$

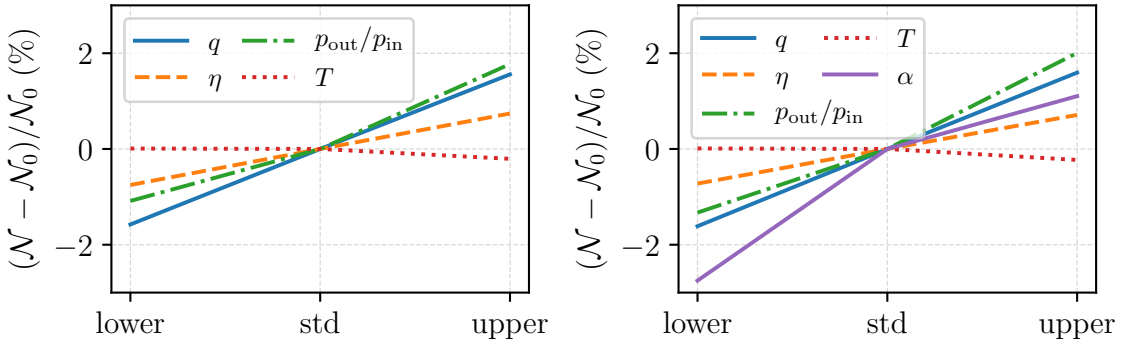

Figure 4.14.: **Input parameter effects on column density.** The left plot shows the effects on the Knudsen estimated column density, the right plot shows the effects on the Boltzmann equation estimated column density. The abscissa refers to the range between parameter's lower limit, standard value, and upper limit.

weak compared to the other effects, verified. The largest difference occurs due to the accommodation coefficient, which causes substantial changes to the Boltzmann estimated column density, but which is not included in the Knudsen model. On the other hand, none of the input parameter effects exceed the model uncertainty itself, which is about $6 - 7\,\%$ for the Knudsen model and (conservatively estimated), and $4\,\%$ for the Boltzmann model.

Column density distribution from uncorrelated input parameters As shown above, the dependence of the column density on the temperature is negligible compared to the other input parameters. Since the temperature is the only parameter that directly affects other parameters (namely the viscosity), neglecting temperature uncertainties enables uncorrelated treatment of the input parameters. We can now draw the individual parameters from a Gaussian distribution centred at the estimated value from tab. 4.2, with σ defined by the parameter's uncertainty. Some of the parameters face upper and lower limits such as the accommodation coefficient $\alpha \leq 1$ or the outlet to inlet pressure ratio $p_{\mathrm{out}}/p_{\mathrm{in}} \geq 0$. Those are considered in the

underlying distributions.

Drawing 10^4 times from these distributions and estimating the column density yields a distribution of the column density. From that distribution, we can estimate the lower and upper uncertainty of the column density related to input parameters. Using the column density calculated with best estimate input parameters as central value, searching the 1σ confidence interval yields the upper and lower uncertainty respectively.

Thereby, the column density for the Knudsen model is estimated to be

$$\mathcal{N}_{\mathrm{K,input}} = \left(4.5^{+0.1}_{-0.1}\right) \times 10^{21}\,\mathrm{m}^{-2}, \tag{4.33}$$

which evaluates to an input parameter related uncertainty on the column density of 2 %, compare fig. 4.15.

For the Boltzmann equation solving model, the column density distribution results in

$$\mathcal{N}_{\mathrm{B,input}} = \left(4.4^{+0.1}_{-0.2}\right) \times 10^{21}\,\mathrm{m}^{-2}, \tag{4.34}$$

which evaluates to an input parameter related uncertainty on the column density of $+3\,\%$ ($-4\,\%$). Note that the Boltzmann method has a larger uncertainty than the Knudsen model because of inclusion of variations on the accommodation coefficient α. This also explains why the distribution of the Boltzmann estimated column density is slightly skewed; it is because the input parameter α has a distribution cut-off at 1 (compare fig. 4.15).

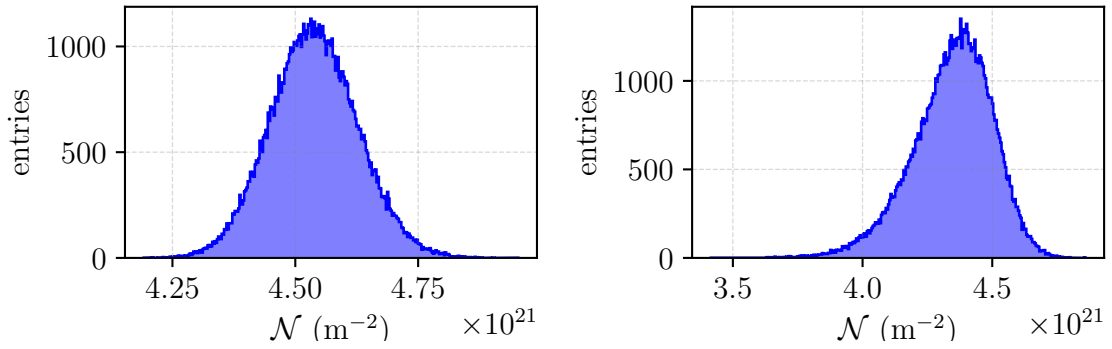

Figure 4.15.: **Systematic distribution of column density due to input parameters.** The left plot shows the effects on the Knudsen estimated column density, the right plot shows the effects on the Boltzmann equation estimated column density.

Total uncertainty on the column density In order to get the total column density uncertainty for the First Tritium set-up, the input parameter estimated uncertainty and the model dependent uncertainty have to be added. Since they are uncorrelated, we can use the square root of the squared sum.

For the Knudsen estimated uncertainty, this yields

$$\mathcal{N}_{\mathrm{K}} = \left(4.5^{+0.3}_{-0.3}\right) \times 10^{21}\,\mathrm{m}^{-2}, \tag{4.35}$$

which is a relative uncertainty of $\pm 7\,\%$. As expected, the model related uncertainty of 7 % dominates over the input related uncertainty of 2 %.

For the Boltzmann estimated total uncertainty is found to

$$\mathcal{N}_{\mathrm{B}} = \left(4.4^{+0.2}_{-0.3}\right) \times 10^{21}\,\mathrm{m}^{-2}, \tag{4.36}$$

which equals a relative uncertainty of $+5\,\%$ ($-6\,\%$). Here, the input parameters uncertainty cannot be neglected because it is comparable to the model related uncertainty of (conservatively estimated) $4\,\%$.

4.4.8. Estimation of injection pressure from krypton capillary pressure

Due to the non-availability of the e-gun during the First Tritium campaign, other methods have to be used to access the validity of the gas dynamics simulations. One of them is using the pressure measured in the krypton capillary, attached to the injection chamber. The krypton capillary is the analogue of the tritium capillary, and is used to inject krypton in the high temperature mode of the WGTS. During First Tritium, the injection chamber was filled via the tritium capillary while the valve after the krypton capillary pressure sensor was closed, compare fig. 4.16. The closed valve prevents a mass flow as through an open tube, however the temperature difference between injection chamber at 30 K and pressure sensor at room temperature requires solving a differential equation to translate the pressure sensor measurement into an injection chamber pressure. Furthermore, the injection pressure in the beam tube requires another differential equation to account for the gas flow through the injection capillaries (compare fig. 4.16 and fig. 3.4). The following section will deal with solving the two differential equations to estimate the injection pressure from the pressure measured at the pressure gauge at the krypton capillary.

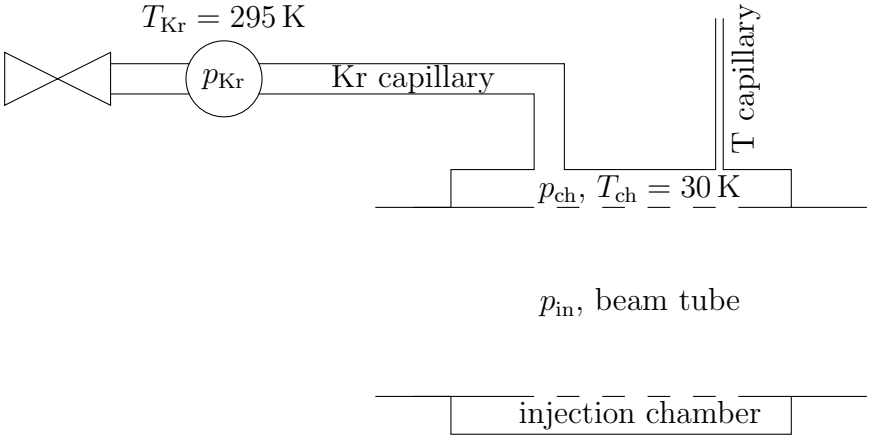

Figure 4.16.: **Sketch of the krypton capillary.** Geometry is not to scale. The distance between Kr pressure sensor and injection chamber is about 7 m. Gas inflow is through the T capillary.

4.4.8.1. Krypton capillary pressure to injection chamber pressure

Since the valve behind the pressure sensor of the krypton capillary was closed for the First Tritium measurements (compare fig. 4.16), the pressure gradient from

the pressure sensor to the injection chamber is caused by the temperature gradient. This leads to the so-called thermomolecular pressure effect. As shown by F. Sharipov [Sha96], we can relate the pressures at both ends of a long tube via their temperature ratio through a simple formula

$$\frac{p_{\mathrm{Kr}}}{p_{\mathrm{ch}}} = \left(\frac{T_{\mathrm{Kr}}}{T_{\mathrm{ch}}}\right)^{\gamma}, \tag{4.37}$$

if there is no gas flow between the two locations. The coefficient γ thereby depends on many factors such as tube geometry and gas species [Sha96]. To estimate γ, a differential equation needs to be solved [Sha96]

$$\frac{\mathrm{d}\mathcal{P}}{\mathrm{d}\mathcal{T}} = \frac{\mathcal{P}}{\mathcal{T}} \frac{Q_{\mathrm{P}}(\delta_{\mathrm{ch}}\mathcal{P}/\mathcal{T})}{Q_{\mathrm{T}}(\delta_{\mathrm{ch}}\mathcal{P}/\mathcal{T})}, \tag{4.38}$$

with dimensionless flow rates $Q_{\mathrm{P}}(\delta)$ and $Q_{\mathrm{T}}(\delta)$, $\delta = \delta_{\mathrm{ch}}\mathcal{P}/\mathcal{T}$, and dimensionless pressure $\mathcal{P} = p/p_{\mathrm{ch}}$ and temperature $\mathcal{T} = T/T_{\mathrm{ch}}$ relative to the injection chamber. The differential equation eq. (4.38) can be solved by applying a numerical difference scheme as outlined by Sharipov [Sha96]. This estimates the pressure at the position of the pressure gauge. However, we are interested in the other direction: we want to use the measured pressure at the gauge to estimate the injection chamber pressure. Therefore, a bisection search is applied until the estimated pressure at the gauge matches the measured value, the corresponding p_{ch} is then the pressure at the injection chamber. γ can also be estimated easily via eq. (4.37).

To solve the differential equation, we need the pre-calculated dimensionless flow rates from Sharipov [Sha96], temperatures according to the sketch in fig. 4.16, mass of deuterium, temperature dependent viscosity of deuterium [AMW87], $\alpha = 1$, and the diameter of the krypton capillary of 1 cm [Mar18]. Furthermore, the krypton pressure sensor showed a reading of $p_{\mathrm{Kr}} = 12.8 \times 10^{-3}$ mbar during the times used for comparison to simulations (10^{th} June 2018). Applying the iterative numerical difference scheme results in a pressure at the injection chamber of

$$p_{\mathrm{ch}} = 6.2 \times 10^{-3}\,\mathrm{mbar} \quad \text{and} \quad \gamma = 0.32. \tag{4.39}$$

4.4.8.2. Injection chamber to injection pressure

With the estimate of the injection chamber pressure from sec. 4.4.8.1, we can now calculate the injection pressure. Sharipov [Sha04a] calculated a relation between injection chamber pressure and injection pressure for tritium by assuming a free molecular regime. He argues that this is possible since the numerical calculations for a short channel presented in [SS98] showed the flow rate to be independent of the rarefaction parameter for small $\delta < 1$. Using the orifice geometry of 2 mm diameter and length, we can estimate the rarefaction parameter to about $\delta_{\mathrm{ch}} = 0.8 < 1$. Since the injection pressure is expected to be smaller than the chamber pressure, we can state that the relation $\delta < 1$ is satisfied and we may use the same principle as Sharipov [Sha04b].

With the dimensionless length $\mathcal{L} = l_{\text{orifice}}/r_{\text{orifice}} = 2$, we can calculate the transmission probability W through an orifice via [SS98]

$$W = 1 + \frac{\mathcal{L}^2}{4} - \frac{\mathcal{L}}{4} \cdot \sqrt{\mathcal{L}^2+4} - \frac{\left[(8-\mathcal{L}^2)\sqrt{\mathcal{L}^2+4} + \mathcal{L}^3 - 16\right]^2}{72\,\mathcal{L}\sqrt{\mathcal{L}^2+4} - 288\,\ln\left[\mathcal{L}/2 + \sqrt{\mathcal{L}^2/4+1}\right]}. \quad (4.40)$$

With the transmission probability W, we can relate the throughput $q_0 = q/415$ for one of the 415 orifice to the injection pressure p_{in} as [SS98, Sha04b]

$$p_{\text{in}} = \mathrm{p}_{\text{ch}} - q\frac{\sqrt{2\,T_{\text{ch}}\,m_{\mathrm{D}_2}/(\pi\,k_{\mathrm{B}})}}{273.15 \cdot 415\,r_{\text{orifice}}^2 \cdot W(\mathcal{L})}. \quad (4.41)$$

Using the pressure $p_{\text{ch}} = 6.2 \times 10^{-3}\,\text{mbar}$ estimated above, the injection pressure is estimated to be

$$p_{\text{in}} = 3.12 \times 10^{-3}\,\text{mbar}. \quad (4.42)$$

Comparing this to the injection pressure calculated from the density profile of the Knudsen model ($3.02 \times 10^{-3}\,\text{mbar}$) and the Boltzmann estimate ($2.99 \times 10^{-3}\,\text{mbar}$) yields a difference of 3 % and 4 %, respectively.

The agreement is remarkably good, despite the many assumptions that were made in the estimation of the injection pressure via the krypton pressure gauge. However, DSMC simulations for tritium by F. Sharipov [Sha10] of the ratio between injection chamber and injection pressure suggest a larger injection pressure than estimated via the method used in this section. Assuming that the ratio is the same for deuterium (1.8), the estimated injection pressure would be $3.4 \times 10^{-3}\,\text{mbar}$, which would yield a difference to the gas dynamics model estimated injection pressure of about 12 %.

4.4.9. Discussion

Since e-gun measurements of the column density were not yet available for the First Tritium campaign, a new way of modelling the column density was developed in this work. The most reliable input parameter for the calculations is estimation of the injection rate from a calibration of the pressure controlled buffer vessel. Furthermore, the dominating gas species in the First Tritium campaign was deuterium instead of tritium. Therefore, two new models were developed using the calculated injection rate as input parameter to estimate the density profile and thereby the column density. Both models are generalised for the gas species and therefore they are also valid for tritium. One model uses a phenomenological formula derived by Knudsen [Knu09] and the other is obtained from solving the Boltzmann equation [SS98]. In order to give a reliable estimation of the density profile, the temperature readings of the beam tube Pt500 sensors were implemented in the simulation framework. Both models agree within one percent in their estimated column density despite the difference in density profiles of up to 8 %.

A cross-check of the calculated injection pressure with an estimation from the pressure measured at the krypton capillary resulted in agreement with the two models within $5-6$ %. However, the uncertainty of this estimate is not yet determined and

may well be of the order of 10 % as shown in a comparative calculation by Sharipov. Further comparative measurements of the column density with two different detectors will be discussed in the First Tritium chapter in sec. 5.4.

In order to enable fast fitting of the measured tritium spectra, the calculations of the column density from the injection rate were included into the automatic run processing intermediate data layer IDLE (see sec. 2.4).

The uncertainties found for the column density estimate of the First Tritium non-standard set-up ($6 - 7\,\%$) are one order of magnitude larger than the required uncertainty in the nominal KATRIN set-up (0.2 %). Similarly to the nominal tritium operation gas model, a calibration measurement with the e-gun will decrease this uncertainty and enable an accurate estimation of the column density. It has to be noted that the gas model for the nominal tritium operation is ready to be used. With the e-gun calibration measurements foreseen to be available, the gas model related neutrino mass uncertainty is projected to stay within the budget for one single systematic [Kuc+18].

4.5. Magnetic field

The magnetic field of the WGTS B_S defines the starting magnetic field of the tritium β-decay electrons. As such, it defines the maximum acceptance angle via $\theta_{max} = \arcsin\sqrt{B_S/B_{max}}$ (compare eq. (2.13)). Electrons with initial polar angles larger than θ_{max} are magnetically reflected at the maximum magnetic field in the set-up, B_{max}[10]. A lower magnetic field in the source therefore increases the fraction of electrons reaching the detector without undergoing scattering processes. This would increase the number of electrons in the endpoint region. Besides, the synchrotron radiation emitted by the electrons is also related to the source magnetic field, it decreases the kinetic energy of the electrons.

Monte Carlo investigations with a global KATRIN model by S. Groh [Gro15] revealed that the required accuracy on the source magnetic field is below 1 %. Groh gives an allowed relative deviation range of $[-8.3, 6.4] \times 10^{-3}$ for the absolute value of the source magnetic field for Design Report settings [KAT05]. This section will introduce the most recent source model and compare it with stray field measurements before closing with a discussion of the results.

4.5.1. Magnetic field model

As introduced in sec. 3.3.3, the magnetic field of the WGTS is defined by seven superconducting magnets with two booster coils each. The field inside the central 10 m long beam tube is homogeneous with a slight unavoidable drop between the long modules M1, M2, and M3 (see fig. 3.1). Fig. 4.17 shows the model of the superconducting magnets, with the resulting nominal 3.6 T field. Since the magnets shrink during cool down, a cooling factor of 0.997 for the length of the modules is assumed in the model, estimated from the linear expansion coefficient of $\approx 10\,\mu m\,m^{-1}\,K^{-1}$ and

[10] In the nominal set-up, the maximum magnetic field is at the PCH magnet.

a temperature difference of $\approx 300\,\mathrm{K}$ compared to room temperature. The shrinking is considered to be symmetric to the centre of the WGTS, thus the positions of M1 and M3 change slightly compared to the warm WGTS. Since the superconducting coils have axial symmetry, the resulting magnetic field is calculated via the zonal harmonics field solver in Kassiopeia [Fur+17] (also see sec. 2.4).

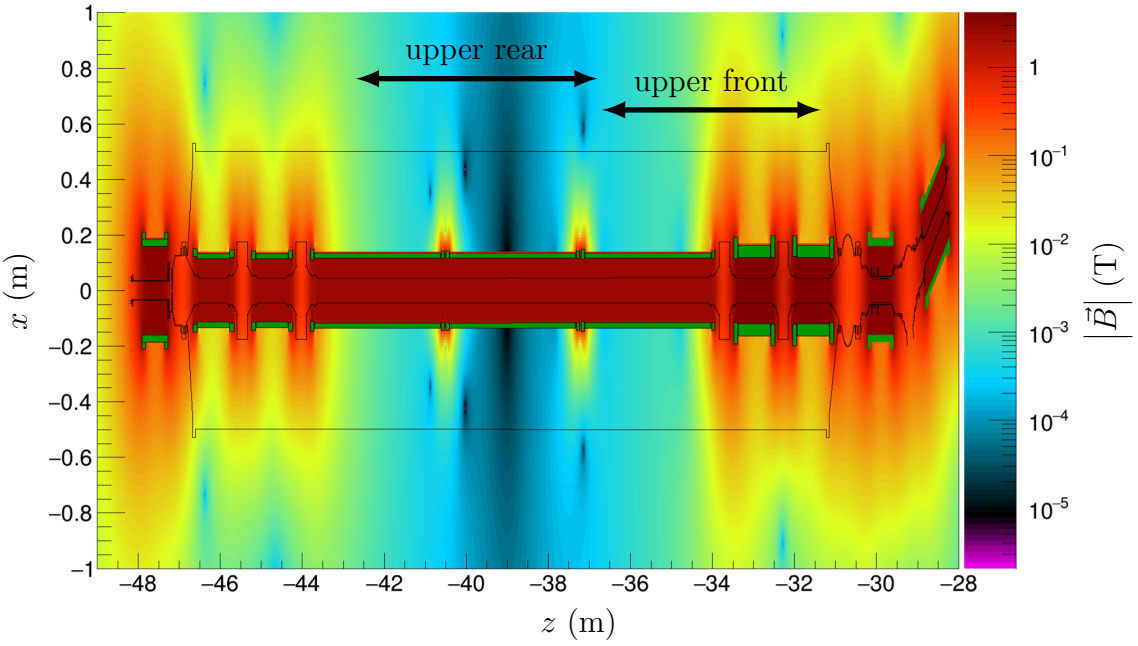

Figure 4.17.: **Magnetic field map.** The map shows the expected magnetic field distribution in the $x - z$ plane for design WGTS field (without the earth magnetic field). The rail positions of the magnetic field measuring system are indicated by the black arrows.

The input variables defining the modelled magnetic field are the currents (and the number of turns). Since the WGTS magnets are operated in driven mode [Are+18c], the currents are known at all times. The most precise and accurate measurement of the currents is available from sensors inside the power supplies, as outlined in sec. 3.3.3, this readout is used as input for magnetic field simulations.

4.5.2. Magnetic field measurement system

The calculation of the magnetic field of an axial symmetric, long coil is less challenging than verifying these calculations via measurements of the WGTS magnetic field. An accuracy of better than 1 % is needed [Gro15] to be within the requirements. Due to the technically challenging environmental conditions inside the beam tube of the WGTS (30 K, radioactive tritium), we can not use a Hall probe to measure the field inside. The only way into the WGTS are the outer pump ports of the WGTS (PP2-F/R), where there are only two pumps mounted. However, the measurement device would have to pass the tube and the first pump port (PP1-F/R) before reaching the central magnetic field. In contrast to the inside, environmental conditions are less harmful outside the WGTS, which is why it was decided to measure the stray field of the WGTS and compare it to simulations to derive the field inside.

In order to reach the required accuracy with stray field measurements, positioning of the measurement device is crucial. Simulations showed that the position has to be known to the order of 1 mm to reach an accuracy below 0.5 % when comparing the measured to the simulated magnetic field.

To meet this requirement, a system of well-defined position measurement and accurate and precise magnetic field measurement was developed. The position is constrained to only one degree of freedom, which is longitudinal movement along the cryostat of the WGTS, measured by a rope sensor. The magnetic field is determined via a three-axis Hall probe with well defined magnetic field sensitive volume.

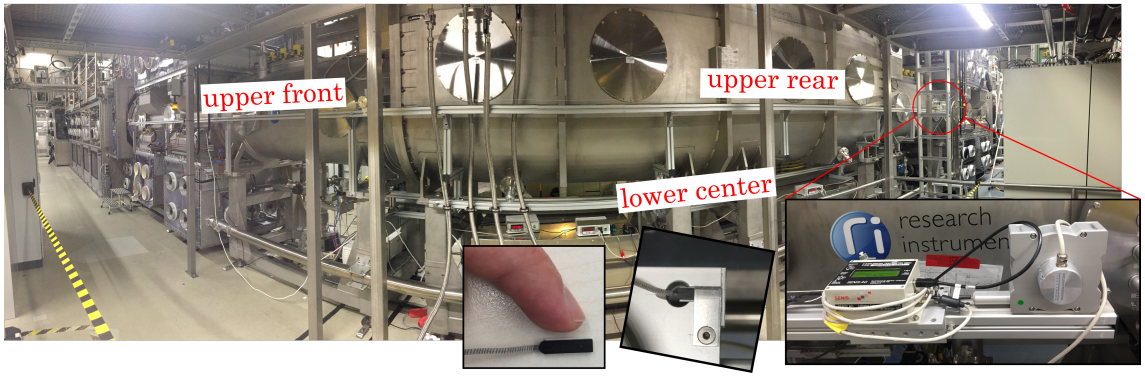

Figure 4.18.: **Magnetic field measuring setup.** The panorama includes all three rails (*upper front*, *upper rear*, and *lower center*) used for the measurements. The inlets show the mounting of the Hall probe and the readout unit on top of the Bosch EcoSlide© [Bos18], plus the mounting of the rope sensor (lower right picture).

Hall probe The magnetic field measurement device which fulfils the requirement of an accuracy better than 0.5 % plus a well-defined and accurately known magnetic field sensitive volume is an integrated three axis Hall probe in a SENIS *3-Axis Digital Teslameter 3MH3A-0.1%-200mT* [SEN18]. For the measured magnetic field, the producer lists an accuracy of better 0.1 % of full range (200 mT) and resolution of 0.02 mT.

The Hall probe and its readout are mounted onto a 45 × 45 × 160 mm aluminium Bosch EcoSlide© [Bos18], which can move 5-6 m along the 45 × 45 mm aluminium rails. Fig. 4.18 shows the mounting of the Hall probe and its readout as well as the assembled slide. It has to be noted that special care was taken to have only non-magnetic materials in the set-up in order not to disturb the measurements.

Rope sensor As outlined before, the position of the Hall probe has to be known to sub-mm precision. Since the assembly has only one degree of freedom, the parameter of interest here is the longitudinal position of the slide. The chosen WayCon rope sensors *SX80* [Way18b] and *SX135* [Way18a] have a linearity deviation of less than 0.02 % over the full measurement range. Linearity here describes the relation between

rotation of the slit disk inside the rope sensor and the length of the rope, representing the measured distance. When the slide with the Hall probe moves, the rope is pulled out of the rope sensor and the slit disk inside of the rope sensor is turned. With an optical system, the number of slits is counted and transformed into a distance resulting in a linear relation.

Though the 0.02 % linearity uncertainty would result in 1 mm uncertainty at a distance of 5 m, a calibration reveals two points to keep the requirement:

- The deviation from linearity is not linear on the distance but rather an upper limit. Calibration curves for the deviation of the measured distance from the linear relationship reveal that the deviation is maximum 0.002 % (the interested reader finds an example table in fig. A.2 in app. A.3), which adhers the sub-mm requirement.

- Given the linearity deviation is larger than the requirement, the calibration table enables compensation of the deviation which in turn decreases the uncertainty on the distance.

Combining magnetic field and position measurement In order to compare the measured magnetic field to simulations, position and magnetic field need to be read out at the same time. The developed LabVIEW [NI16] programme (see fig. 4.19) enables the position and measured magnetic field to be written to a text file in different modes.

In the *manual* mode, the user can decide the step width of the longitudinal positions and use the average of a defined number of points as the magnetic field at that position. Thereby, the step width can be adjusted to the gradient of the magnetic field and the averaging smooths fluctuations of the Hall probe. Furthermore, the continuous monitoring of the magnetic field in the lower right plot of the measuring programme (fig. 4.19) enables the user to start the measurement when the Hall probe has adjusted to the new magnetic field.

In the *fixed time* mode the position and magnetic field are read out every t-th second, resulting most likely in more measurement points than in the manual mode. This mode enables faster scanning of the longitudinal distance, decreasing the required measurement time for one scan to the order of minutes compared to the manual scan of the complete rail. However it needs to be verified that the moving Hall probe does not face any hysteresis effects or similar, which can be done with the manual mode.

4.5.3. Magnetic field measurements

After introducing the set-up and the methods to measure the magnetic stray field of the WGTS in sec. 4.5.2, this section presents results from commissioning measurements and first comparisons to simulations.

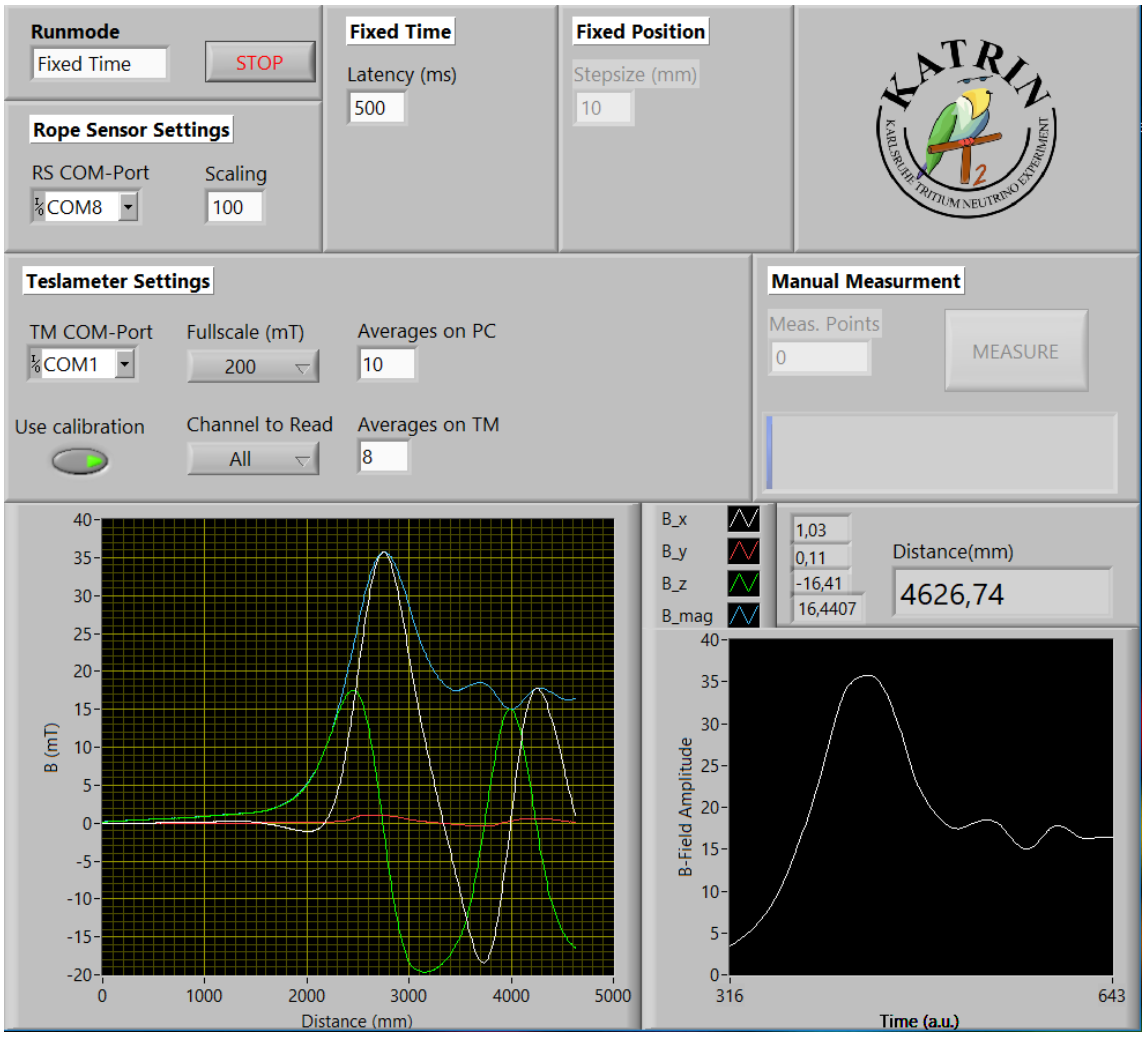

Figure 4.19.: **Magnetic field measuring programme.** The screen shot shows the user interface of the developed LabVIEW [NI16] programme.

4.5.3.1. Manual versus fixed time mode

Before comparing the measurements to simulations, it needs to be verified that the fixed time mode does not introduce any bias and the maximum possible velocity needs to be obtained. A comparison between a scan with fixed time mode and with manual mode is shown on fig. 4.20. The figure shows a scan of the *upper front* rail, which is mounted along M3, M7, and M6 (compare fig. 4.17). Fig. 4.20 reveals that for a driving velocity below $0.01\,\mathrm{m\,s^{-1}}$ (lower plot), the magnetic field inside the strong stray field region above 10 mT matches better than 0.5 % between manual and fixed time mode (middle plot). The time for completing the fixed time scan is 20 min, which is half the time for completing the manual scan (40 min).

4.5.3.2. Forward versus backward scan

During the measurements it was discovered that for the upper front rail (in direction of DPS2-F), the scan in backwards direction ran more smoothly than the one in forward direction. The reason for this is in the movement of the slide. In forward

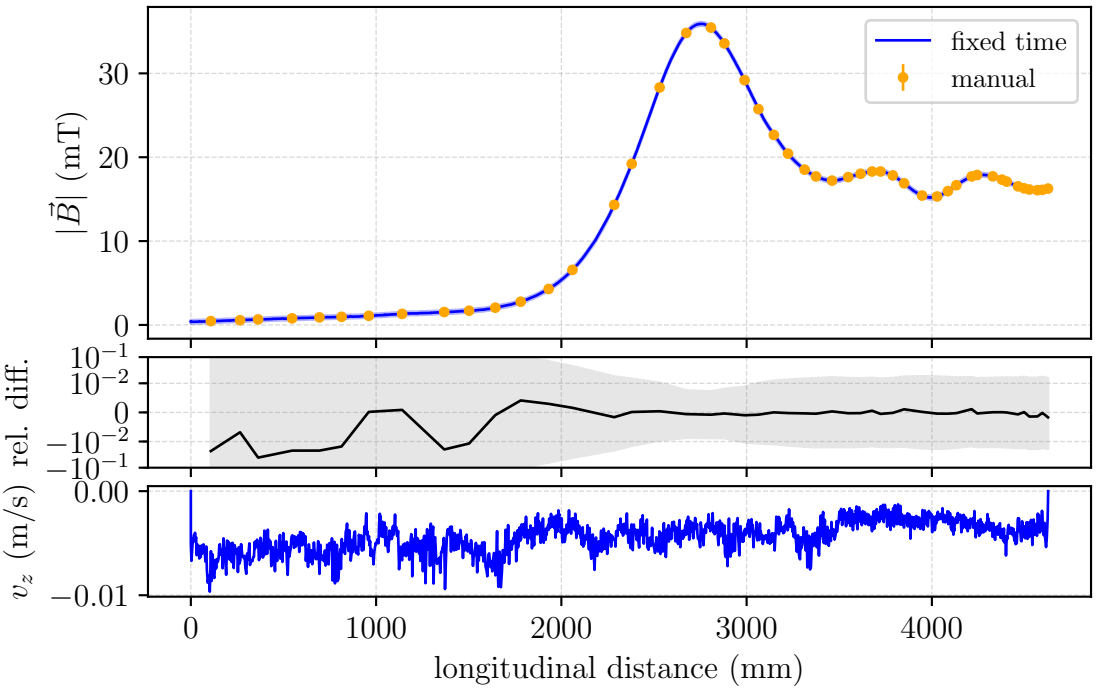

Figure 4.20.: **Magnetic field measuring modes.** The data was taken directly after the ramp of the WGTS magnets on 8$^{\text{th}}$ September 2018. Both modes in the upper plot have uncertainty bands/bars, though they are too small to be visible. The middle plot shows the relative deviation $(B_\text{f} - B_\text{m})/B_\text{m}$ and the lower plot shows the velocity of the fixed time mode in the longitudinal direction.

direction the operator has to turn a crank, while in backward direction the pulling force of the rope sensor moves the slide. As mentioned in sec. 4.5.3.1, there must be an upper limit of velocity in the fixed time mode which causes a hysteresis of the Hall probe. This was tested with a fast forward and backward scan of the upper front rail, see fig. 4.21. Figure 4.21b shows forward and backward scans with a velocity one order of magnitude larger than on fig. 4.21a. This results in a hysteresis effect of the measured magnetic field difference on the %-level which would not fulfil the requirements. However, the standard scan velocity shown in fig. 4.21a shows no such hysteresis effect, favouring a velocity of about 0.01 m s^{-1}. It has to be noted that the velocity should be constant over the whole range, even short deviations are directly visible in the middle relative difference plot (see e.g. the peak around 3100 mm). Therefore, the backwards scans are compared to simulations since they have a much smoother velocity profile than the forward scans.

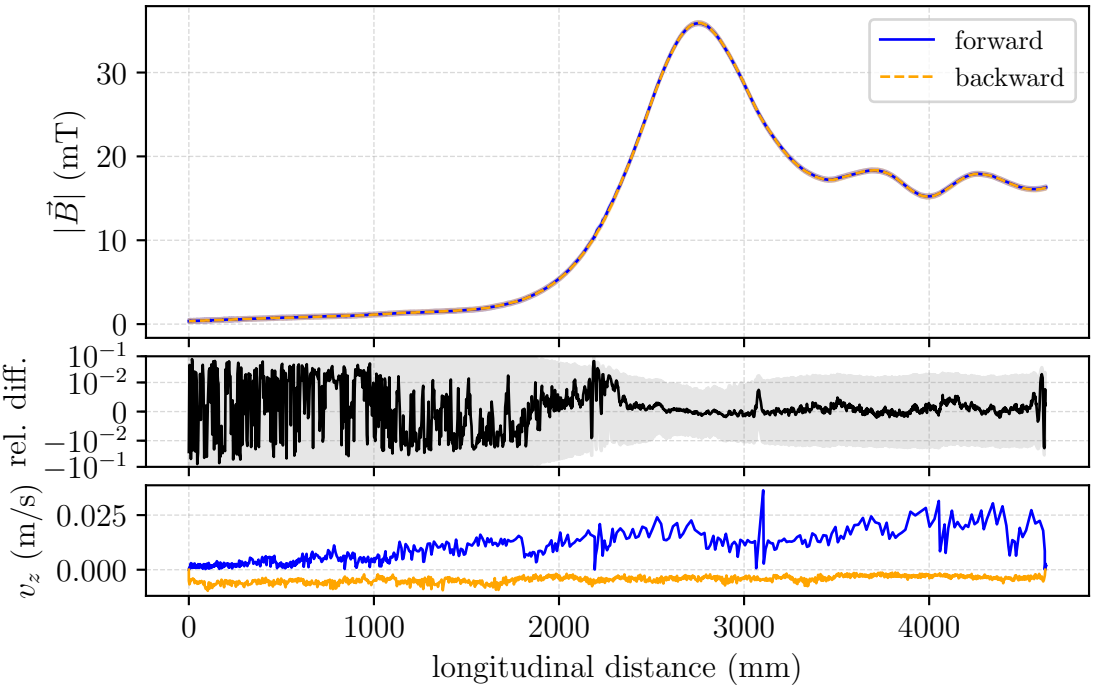

(a) **Magnetic field, standard measurement.**

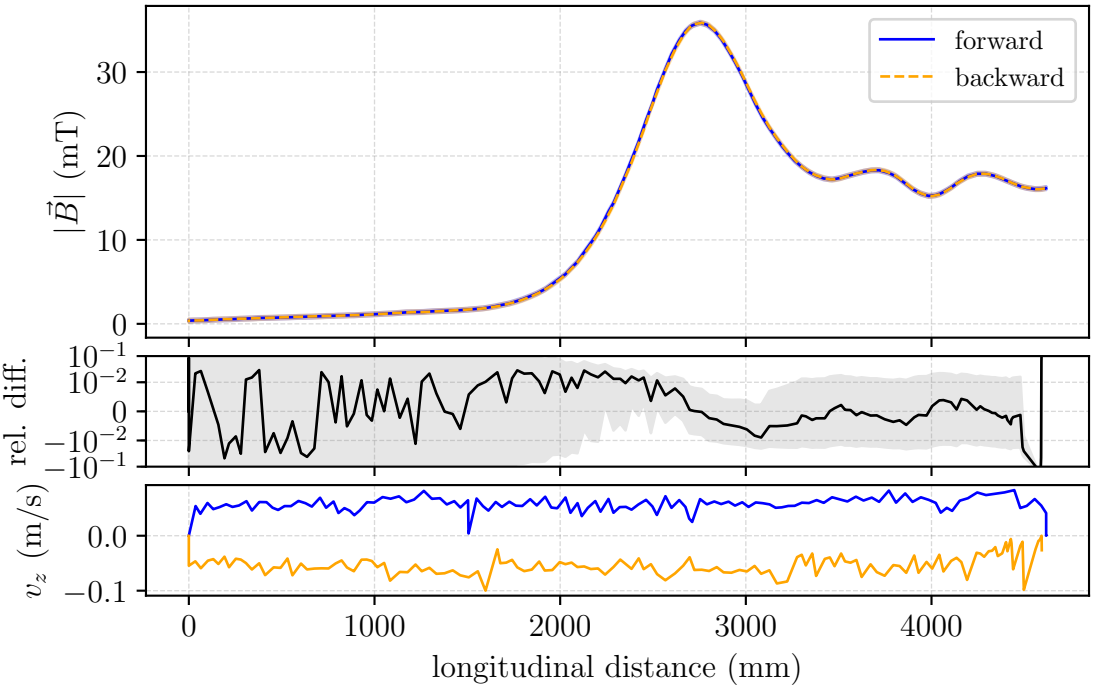

(b) **Magnetic field, fast measurement.**

Figure 4.21.: **Magnetic field measuring directions.** Figure a (b): The data was taken on 8$^{\text{th}}$ (13$^{\text{th}}$) September 2018. Both directions in the upper plots have uncertainty bands, though they are too small to be visible. The middle plots show the relative deviation $(B_{\text{fw}} - B_{\text{bw}})/B_{\text{bw}}$ and the lower plots show the longitudinal velocity. The lower figure (b) shows scans with a much higher velocity, resulting in a hysteresis curve.

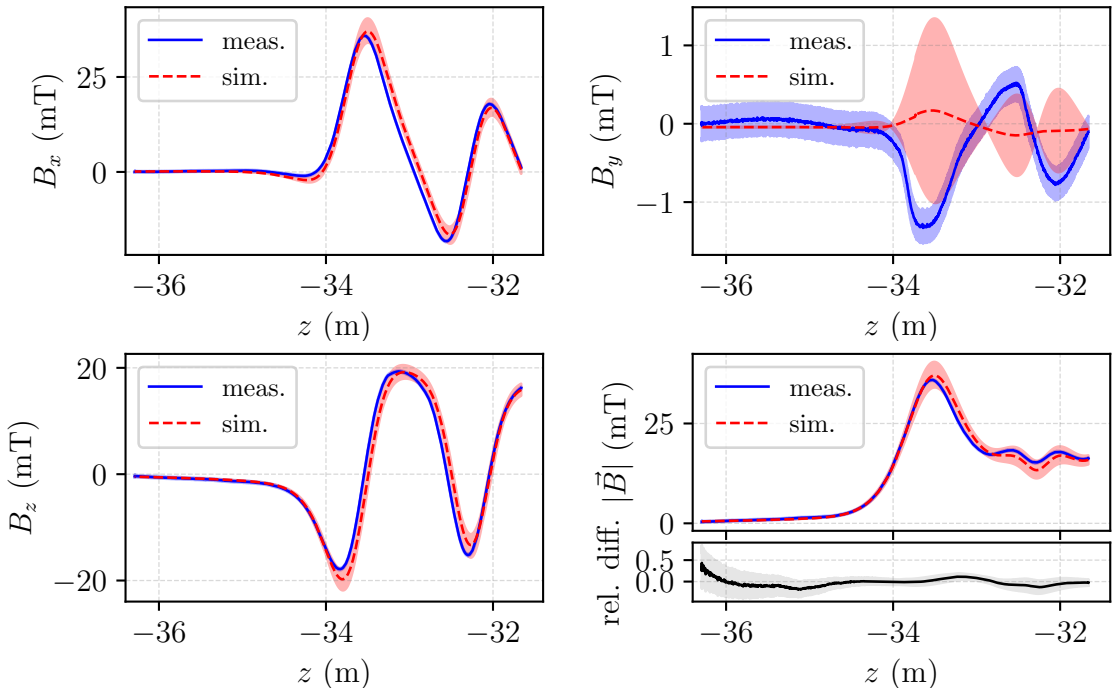

Figure 4.22.: **Comparison of measured to simulated magnetic field.** The data was taken on 8$^{\text{th}}$ September 2018. Upper left, upper right, and lower left plots show the component-wise comparison of the measured magnetic field to simulations. The lower right plot shows the comparison of the magnetic field magnitudes, including the relative deviation $(B_{\text{sim}} - B_{\text{meas}})/B_{\text{meas}}$. Simulation and measurement agree mostly within the uncertainty bands.

4.5.3.3. Comparison to simulations

Since the field configuration could not be optimised for the stray field measurements, only the measurements of the upper front rail will be compared to simulations because those reach stray fields larger than 30 mT. As discussed in sec. 4.5.3.2, the backward direction has a much smoother velocity profile and is therefore used for the comparisons. Data was taken on 8$^{\text{th}}$ September 2018, after the ramp of the WGTS magnets to 2.5 T. Simulation to measurement comparisons of the magnetic field components, as well as of the magnitude, are visualised in fig. 4.22. The large uncertainty band on the simulation originates from the poorly known positioning of the rail, which could only be determined to about 2 cm accuracy. Despite that the measurement and simulation agree within the estimated uncertainty, it can clearly be seen that the positioning has a large influence on the simulated magnetic field. In particular, for the B_{y}-component, ± 2 cm makes a large difference. Therefore, no conclusions can be drawn yet as to measurement and simulation agree within the required 0.5 %.

4.5.4. Discussion

A dedicated stray field measuring system was developed to determine the magnetic field of the WGTS to an accuracy better than 0.5 %. The measuring system consists

of a three-axis Hall probe mounted onto a rail parallel to the WGTS cryostat axis with a rope sensor to determine the longitudinal distance. Two different measuring modes were developed for the readout, an all-manual mode with manual selection of the distances and a fixed time mode which automatically measures the magnetic field and position every t-th second. Both modes were found to produce the same results if the velocity of the moving Hall probe is below $0.01\,\mathrm{m\,s^{-1}}$. For larger velocities the results between forward and backward scan show a hysteresis effect.

No conclusive argument could be found from comparison to simulations because the uncertainty on the positioning of the rail (not the longitudinal distance of the Hall probe) is about 2 cm, which is one order of magnitude above the sub-mm requirements found in sec. 4.5.2. However, the measuring system will remain in place, allowing the sub-mm accurate determination of its positioning via combined laser tracker and FaroArm® [FAR18] measurements. Using this knowledge, the data can either be re-analysed or new data will be acquired to get more conclusive insights into the magnetic field of the WGTS. Another improvement would be a stepper motor which guarantees smooth movement of the Hall probe in both directions for a more accurate determination of the stray field in the fixed time mode.

Concerning additional measurements, dedicated settings for the magnetic field should be considered. An asymmetric setting with only one of the three WGTS current circuits active (and no other field on e.g. DPS2-F or CPS) would allow determination of the positioning of the coils inside the cryostat if the positioning of the rail is known to sub-mm accuracy. The increase of the stray field caused by that asymmetric setting would furthermore decrease the uncertainty on the measurement in the high-field region and also allow for reliable comparisons with simulations for the other two rails (upper rear and lower center).

The ultimate determination of the magnetic field inside the WGTS however can be done via the angular-selective electron gun (e-gun) installed at the rear section. Using a well-characterised superconducting magnet such as the PCH magnet, the transmission edge of the e-gun at an arbitrary pitch angle can be found by varying the magnetic field of the PCH until all e-gun electrons are magnetically reflected. Thereby, the pitch angle of the e-gun is calibrated against the magnetic field of the PCH and can then be used to calibrate the magnetic field of the WGTS in the same way. The accuracy of this measurement is determined by the knowledge of the magnetic field of the PCH magnet (0.2 %[11]) since the angular resolution of the e-gun is constant for both measurements.

[11] This value is estimated from the 6.01 T NMR measurement by C. Schönfeld [Sch15] and the 6.00 T simulated field using the measured current of 86.98 A.

4.6. Conclusion

An accurate modelling of the electron spectrum of tritium β-decay requires accurate knowledge of the processes in the windowless gaseous tritium source. One of the major systematic effects arises from the description of the energy loss processes due to inelastic electron-gas scattering. Closely linked to that is the modelling of the gas flow and the magnetic field in the source section.

In order to reach the required accuracy of the description of gas flow, the temperature distribution in the central source tube needs to be included in the gas model. In sec. 4.2, recent commissioning measurement data is used to derive a sensor based yet model motivated temperature profile of the beam tube. Towards the rear end, the homogeneity criterion of the beam tube temperature can not be maintained because the temperature increase is about 0.5 K. Since the temperature profile is stable on the per-mille level, this temperature increase can be accounted for in the modelling of the gas dynamics and does therefore not impact the neutrino mass sensitivity.

The comprehensive gas dynamics model developed over the course of several theses (notably, [Höt12, Kuc16] and the thesis at hand) is presented in sec. 4.3. In order to describe the gas flow through the whole WGTS, several modelling techniques need to be applied and smoothly connected to provide the density distribution $n(z)$ and thereby the column density $\mathcal{N}$ in the 16 m long beam tube. Furthermore, a calibration measurement by an angular selective, mono-energetic e-gun is discussed which is necessary to reach the required 0.2 % accuracy on the parameter of interest for the scattering model, $\mathcal{N} \cdot \sigma$. With this calibration measurement it is possible to keep the neutrino mass uncertainty related to the description of gas dynamics at $3.06 \times 10^{-3}\,\mathrm{eV}^2$, which is below the limit of a single systematic derived from the Design Report [KAT05, Kuc+18].

In May and June 2018, the first spectra of electrons stemming from tritium β-decay were recorded by the KATRIN experiment. For the data analysis of that major commissioning milestone, two dedicated gas models were derived. This was necessary, because the carrier gas for the trace amounts of tritium was deuterium and the above mentioned e-gun calibration measurements had not yet been carried out. Therefore, a calibration of the pressure controlled buffer vessel is used to estimate the injection rate into the WGTS and therefrom recursively calculate the deuterium density profile. Calculations were restricted to the central 10 m long beam tube which contains 99 % of the gas column. The dominant uncertainty for the phenomenological Knudsen formula is the model related uncertainty while for the model derived from solving the Boltzmann equation the input parameter uncertainties are also significant. As deuterium has a smaller mass than tritium, the same throughput causes an about 10 % lower column density. For most of the tritium spectrum scans, the deuterium column density is estimated to be about $4.5 \times 10^{21}\,\mathrm{m}^{-2}$, with a total uncertainty of 5(7) % for Boltzmann (Knudsen) based flow.
A cross-check of the amount of gas in the injection region estimated by the discussed gas models was performed by translating the pressure gauge measurement at the krypton capillary into an injection pressure. Agreement was found within $3 - 4$ %, depending on the model. However, it has to be noted that the uncertainty of this comparative calculation might well be of the order of 10 % when assuming the same relative difference for tritium obtained by a DSMC [Bir94] simulation by

F. Sharipov [Sha10].

Besides the distribution of the gas inside the source, the magnetic field of the source is very important for modelling the electron-gas scattering as it determines the path length of the electrons through the gas. Since measurements inside the beam tube are not possible, a stray field measurement system was designed, developed, and successfully commissioned. Several readout configurations were tested in order to find the most suitable compromise between speed and accuracy of the measurement. The approach by constantly moving a Hall probe along a rail is considered to be a good compromise, provided the driving speed is below $0.01\,\mathrm{m\,s^{-1}}$. Comparison between simulation and measurement does not reveal a disagreement. However, the global position of the rails needs to be measured by means of laser tracker or FaroArm® [FAR18], which can be done after the current measurement phase. This accurate determination of the position will enable a conclusive comparison of measurement and simulation.

Experimental verification of the overall source model requires the RS e-gun, which is currently in its commissioning phase. Measurement strategies have been proposed on procedures to use the e-gun for an accurate determination of the column density $\mathcal{N}$ and the magnetic field. With the comprehensive gas model and the magnetic field calibrated or verified by the e-gun, the source model is ready to be used in the analysis of the upcoming neutrino mass data.

CHAPTER 5

ANALYSIS OF FIRST TRITIUM DATA

"In the fields of observation, chance favours only the prepared mind."
– Louis Pasteur, 1854 –

KATRIN aims to determine the effective electron neutrino mass by analysis of the β-decay spectrum of tritium. On the road to neutrino mass data taking, several major milestones were completed during the past two years. After the first transmission of electrons throughout the complete KATRIN set-up in 2016 [Are+18b] and the successful spectroscopy of ^{83m}Kr-lines in 2017 [Are+18b, Are+18a], first tritium spectra were recorded in spring 2018. This chapter will present results from these commissioning measurements with regard to experiment characterisation and comparisons to the modelled tritium spectrum.

5.1. Experimental set-up

For the first detection of tritium β-decay electrons in the spring 2018 engineering run, the KATRIN experiment used slightly different settings than will be used for the neutrino mass data taking. Tritium was only present in the WGTS in trace amounts, with the main constituent of the gas being D_2. The resulting tritium purity of about 0.5 % reduces the activity by about a factor of 200 compared to nominal neutrino mass operations with a tritium purity of $\epsilon_T > 95\,\%$. Due to the different gas content in the WGTS, a different gas dynamics model was developed and used for the estimation of the gas distribution in the source tube (compare sec. 4.4). Besides this difference, all major components of the set-up are in their final configuration.

The (molecular) gas column density of the runs analysed in this chapter is estimated from the gas model to be about $\mathcal{N} = 4.5 \times 10^{21}\ \mathrm{m}^{-2}$, with the tritium column density scaled by the tritium purity and accounting for the number of atoms in the gas molecules. Due to the low concentrations of tritium, almost all tritium is present as DT.

Further important settings to be accounted for during analysis are the slightly inhomogeneous magnetic and electric fields in the analysing plane of the main spectrometer, which is shown in fig. 5.1. It has to be noted that the measurements were performed with a factor three worse energy resolution than the designed 0.93 eV to mitigate the volume effect of the background rate [Har15, Tro18]. For a retarding energy of 18 600 eV, the resulting width of the transmission function is

$$\Delta E = \frac{0.63\,\mathrm{mT}}{4.2\,\mathrm{T}} \cdot 18\,600\,\mathrm{eV} = 2.8\,\mathrm{eV}. \tag{5.1}$$

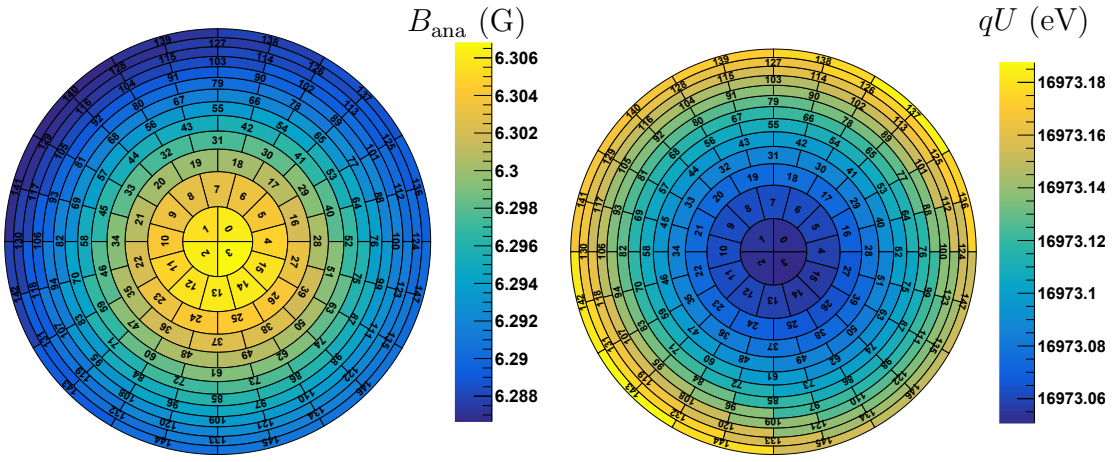

Figure 5.1.: **Analysing plane.** The left side shows the magnetic field in the analysing plane mapped onto the FPD. The right side shows the mapped retarding potential (using a low retarding energy of 16 975 eV as example).

The overall magnetic field setting of the KATRIN experiment was at 70 % of its design value, so therefore the WGTS and FPD were at about 2.5 T instead of the designed 3.6 T.

In order to account for the expected low statistics in the endpoint region due to the low tritium concentrations, a measuring time distribution was chosen over a wider energy interval than the 30 eV from the Design Report [KAT05]. With closer spaced and longer measuring time at points close to the endpoint and wider spaced and shorter measuring time at points far away from the endpoint, the resulting measuring time distribution (MTD) is shown in fig. 5.2. In the endpoint region $qU \in [18555, 18615]$ eV, the sub runs were spaced in 10 eV steps with 900 s per sub run. The least measuring time was spent in the high statistics region, for $qU \in [16975, 18175]$ eV each sub run was 100 s long.

As outlined in sec. 2.2.4, the calculation of the expected rate requires the usage of a response function [KAT05, Kle+18] which accounts for all effects the electron may face on its way to the detector. Amongst those the most significant are the scattering off gas molecules in the source tube and the magnetic field and analysing potential in the main spectrometer. For an example retarding energy of 16 975 eV of the example run 40667, the model based response function is shown in fig. 5.3. Note that the width of the transmission step and the height of the zero-scattering

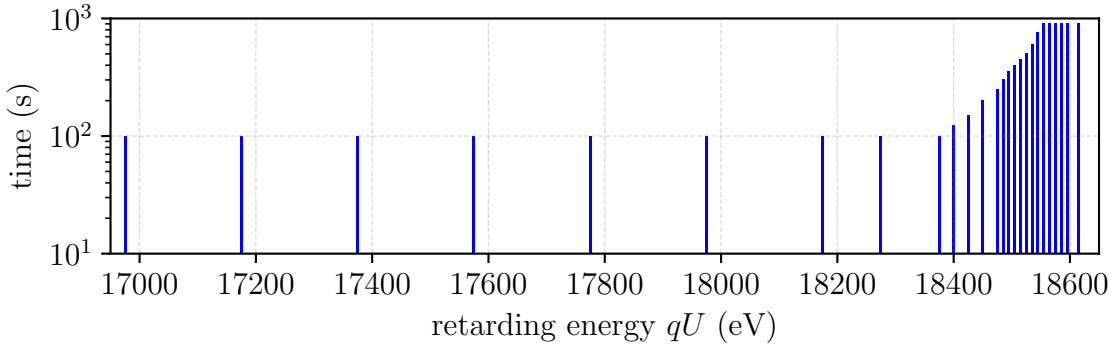

Figure 5.2.: **Measuring time distribution for a single 3 h run.** More measuring time is spent at retarding energies closer to the endpoint.

plateau are different from the design settings due to different experimental settings as described above. Furthermore, it has to be noted that the response function is purely model based since the e-gun was not yet available at this time.

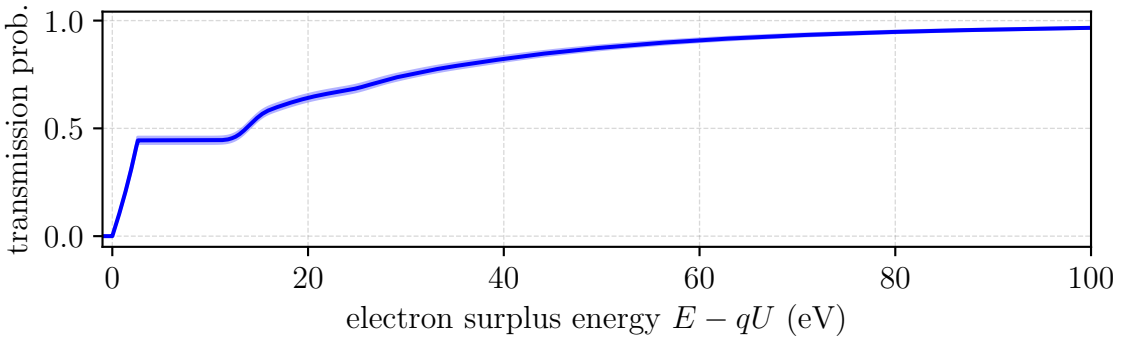

Figure 5.3.: **Modelled response function.** Abscissa shows the electron surplus energy over the retarding energy and ordinate the corresponding probability to reach the detector. This example is for a retarding energy of 16 975 eV during run 40667, using a uniform detector model. The shaded band includes 5 % uncertainty on the column density.

5.2. Operating conditions

As the overall stability of the tritium source is essential for KATRIN, the commissioning measurements from the First Tritium phase also reveal important information about the source operation. This section gives an overview of the most important source parameter stability and compares the achievements with the requirements listed in tab. 3.1. In the following, relative fluctuations are defined as the deviation from the mean of a specific time period,

$$\frac{x - \bar{x}}{\bar{x}}. \tag{5.2}$$

Relative stability is defined as the standard deviation over the mean of a specific time period,

$$\frac{\sigma_x}{\bar{x}}. \tag{5.3}$$

An overview of the estimated run-averaged relative stabilities as well as the mean and standard deviation of the source parameters over all runs is given in tab. 5.1. Note that the requirements of the experimental conditions are mostly valid for one single run, which is why the stability will be evaluated run-wise.

5.2.1. Temperature stability

In order to characterise the achieved temperature stability of the WGTS beam tube, the sensor with the worst stability over the complete analysed time interval is taken as a conservative estimate. Even at a relative stability of 8.5×10^{-5}, the sensor *200-RTP-3-5104* still surpasses the requirement for one run by almost two orders of magnitude, calculated for the time span of about four days. The relative fluctuations as defined in eq. (5.2) are shown for the example run 40667 on the left side of fig. 5.4, while the right side shows the histogram of the relative stabilities for all runs. Comparing to the requirement of 2×10^{-3} relative stability per run in the Design Report [KAT05], we can conclude that the average relative stability of $(6.4 \pm 0.5) \times 10^{-5}$ exceeds this requirement by almost two orders of magnitude.

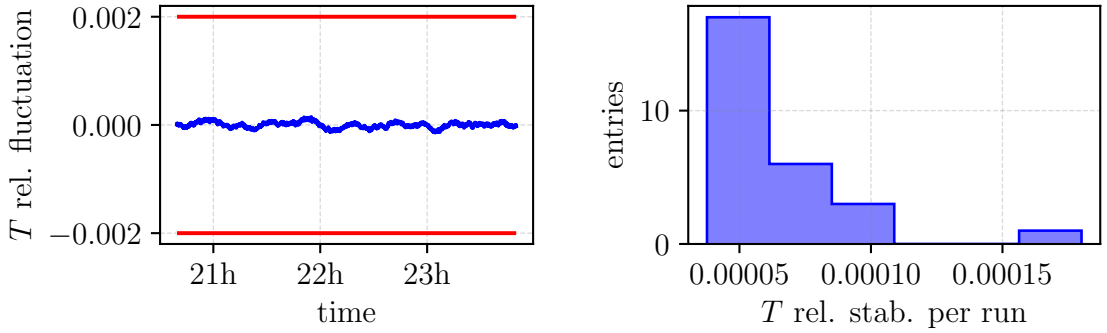

Figure 5.4.: **Temperature stability.** The left side shows the temperature fluctuations in run 40667 (7^{th} June 2018), with the requirements as red horizontal lines. The right side shows the histogram of the run-wise relative stability values.

5.2.2. Gas circulation stability

As the temperature of the WGTS beam tube exceeds its stability requirements, the column density stability is mainly determined through the stability of the injection rate and the outlet pressure, both related to the inner loop system. The corresponding sensors measure the pressure controlled buffer vessel p_{b}, the pressure in the krypton capillary looking at the injection chamber p_{Kr}, and the outlet pressure p_{out} represented by the pressure at the TMPs of the pump ports (compare fig. 3.1). As for the temperature stability, the inner loop parameters also exceed the requirements (compare fig. 5.5):

- p_{b}: achieved average relative stability per run of $(9.8 \pm 0.005) \times 10^{-5}$, required 2×10^{-3} per run

- p_{Kr}: achieved average relative stability per run of $(3.2 \pm 0.2) \times 10^{-4}$, required 2×10^{-3} per run

- p_{out}: achieved average relative stability per run of $(1.7 \pm 0.3) \times 10^{-3}$ at PP1-R and $(2.0 \pm 1.9) \times 10^{-4}$ at PP1-F, required 6×10^{-2} per run

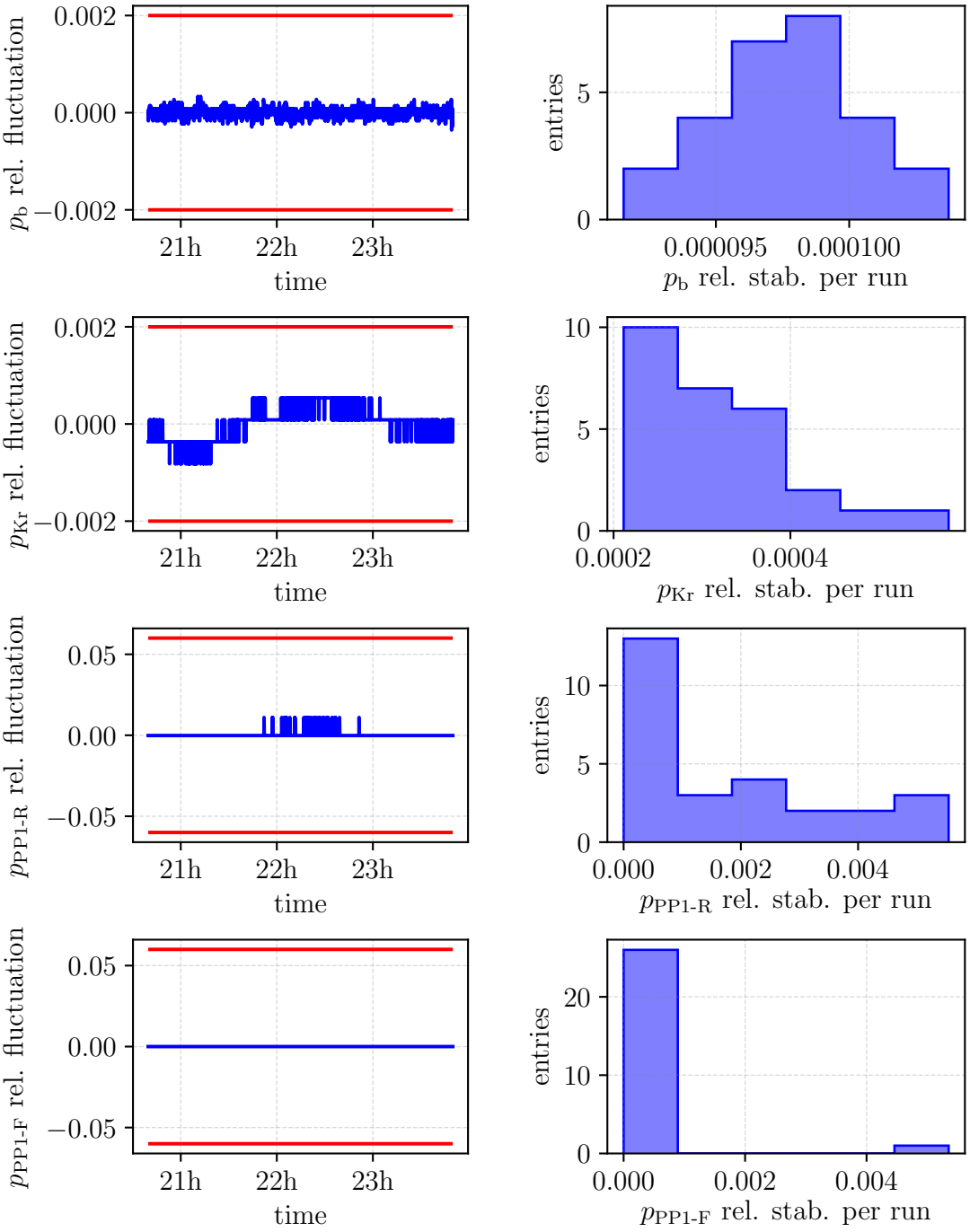

Figure 5.5.: **Gas circulation stability.** The left side shows the fluctuations in run 40667 (7^{th} June 2018), with the requirements as red horizontal lines. The right side shows the histogram of the run-wise relative stability values.

5.2.3. Tritium concentration stability

Due to the trace amounts of tritium used in the First Tritium campaign, the precision per single LARA measurement (60 s) is not expected to be within the specifications of 1×10^{-3} as required for the nominal tritium purity $\epsilon_T > 0.95$. The average relative stability per run determined from LARA data is found to be $(4.48 \pm 0.05) \times 10^{-2}$, which exceeds 1×10^{-3}. However, it has to be noted that the design operation of the tritium source will have tritium as the main constituent of the source gas, which will enable LARA to monitor the tritium purity with a precision on the per-mille level. When using the stability of the (dominant) D_2 concentration as an estimate for the stability of the tritium concentration, an average relative stability per run of $(6.9 \pm 0.1) \times 10^{-4}$ is obtained, which would fulfil the 10^{-3} requirement (see fig. 5.6). Furthermore, the LARA group presented updated analysis results for the isotopologue concentrations with about a factor of three improved uncertainty on the DT concentration [KZ18]. Thus, also the precision on the tritium purity will improve when using this re-analysed data.

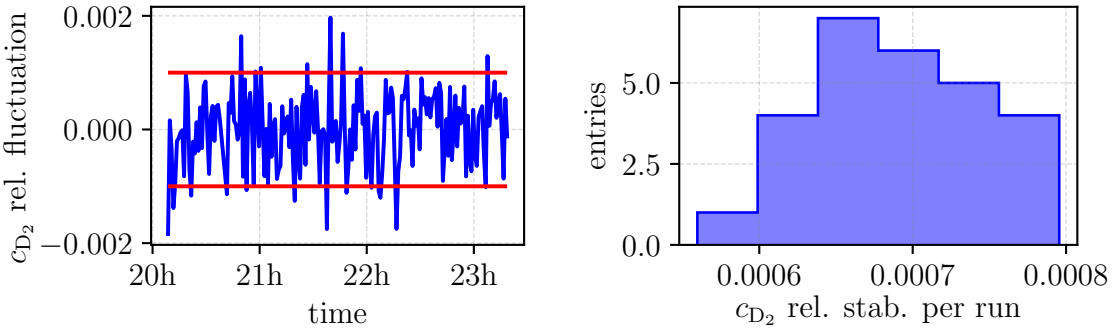

Figure 5.6.: **LARA determined D_2 concentration stability.** The left side shows the fluctuations in run 40667 (7^{th} June 2018), with the requirements as red horizontal lines. The right side shows the histogram of the run-wise relative stability values.

5.2.4. Magnetic field stability

As already demonstrated in [Are+18c], the magnetic field of the WGTS fulfils its requirements. This is also confirmed from the relative stability during the First Tritium campaign, which is found to be $(2.3 \pm 0.6) \times 10^{-6}$ averaged over all runs (required 2×10^{-3}).

5.3. Analysis of tritium β-decay spectra

After introducing the operating conditions of the experiment during the First Tritium campaign, this section will now cover inference of the parameters of interest (effective endpoint $E_{0,\mathrm{eff}}$, amplitude Amp and background rate Bg). The endpoint is always referred to as effective, since the work function difference between main spectrometer and source is not yet known.

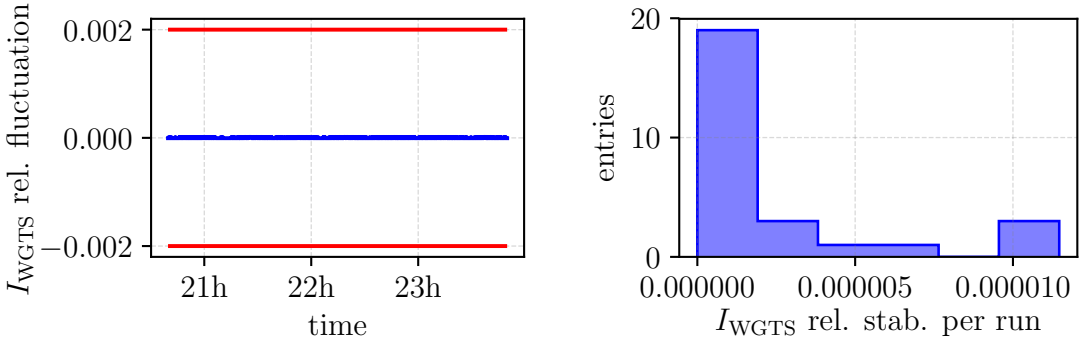

Figure 5.7.: **Magnetic field current stability.** The left side shows the fluctuations in run 40667 (7^{th} June 2018), with the requirements as red horizontal lines. The right side shows the histogram of the run-wise relative stability values.

Table 5.1.: **Source parameters overview.** Note that the mean μ and standard deviation σ are given for the whole data taking period analysed, while the relative stability per run is the run-averaged relative stability, which needs to fulfil the requirements stated in sec. 3.2.

parameter	mean μ	sigma σ	rel. stab. per run	requirement
T	30.076 K	2.5 mK	$(6.4 \pm 0.5)\,10^{-5}$	2×10^{-3}
p_{b}	15.8 mbar	0.002 mbar	$(9.8 \pm 0.05)\,10^{-5}$	2×10^{-3}
p_{Kr}	12.8×10^{-3} mbar	0.002×10^{-3} mbar	$(3.2 \pm 0.2)\,10^{-4}$	2×10^{-3}
p_{out} PP1-R	3.1×10^{-5} mbar	1.7×10^{-7} mbar	$(1.7 \pm 0.3)\,10^{-3}$	6×10^{-2}
p_{out} PP1-R	3.1×10^{-5} mbar	0.4×10^{-7} mbar	$(2.0 \pm 1.9)\,10^{-4}$	6×10^{-2}
I_{WGTS}	215.9 A	0.001 mA	$(2.3 \pm 0.6)\,10^{-6}$	2×10^{-3}
ϵ_{T}	0.56 %	0.03 %	$(4.48 \pm 0.05)\,10^{-2}$	1×10^{-3}
$c_{\mathrm{D_2}}$	93.44 %	0.14 %	$(6.9 \pm 0.1)\,10^{-4}$	-

After introducing the analysis cuts used for this section, comparisons of model and data from the Very First Tritium campaign will be shown in sec. 5.3.2. The pixel distribution of the fit parameters will be shown in sec. 5.3.3 before investigating the fit parameter stability from the First Tritium campaign in sec. 5.3.4. One of the major systematic uncertainties in the First Tritium set-up was the column density $\mathcal{N}$ [Are+19], its impact on the analysis is discussed in sec. 5.3.5 in order to enable a more sound estimate of the fit parameters. It needs to be stressed here that the column density is certainly not the only systematic uncertainty. For a complete estimate of the effective endpoint, other systematic effects also need to be taken into account, however in this thesis the focus is on the column density and its uncertainty as estimated in sec. 4.4.7.

5.3.1. Analysis cuts

Though the tritium spectrum was scanned over a wide energy range of about 1.6 keV, the focus of this thesis is on analysis of the last 400 eV. Notably, thefit model is optimised for fitting in a narrow energy window around the endpoint (i.e. an energy dependence of the inelastic scattering cross section is not taken into account). Moreover, the onset of electronic final states and the uncertainty of their excitation probabilities will play a role for larger analysis windows deeper into the spectrum. Hence, stronger systematic effects are expected when fitting data from a wider energy range. If not mentioned otherwise, the lower limit of the energy analysing window is at $E_0 - 400\,\mathrm{eV}$ (that is including the data point taken at 18 175 eV). The last data point was taken at 18 615 eV.

Concerning the pixel related cuts, we have to account for an imperfect mapping of the geometrical source cross section onto the detector, as can be seen from fig. 5.8. Therefore the two outermost rings are excluded from the analysis, as well as the pixels shadowed by the FBM which was in monitoring position throughout First Tritium. It needs to be stressed that when not using all pixels for the fit, amplitude and background are not scaled accordingly. That means that the estimated amplitude and background are not valid for the whole detector but only for the analysed part.

The term *uniform detector* refers to using the detector as one single pixel with rate equal to the sum of all pixels, except for the removed pixels. This is the standard form of fitting used in the following. For pixel-wise fitting, the energy width of the analysing window has to be doubled to 0.9 keV in order to get enough statistics for a reasonable estimate of the fit parameters.

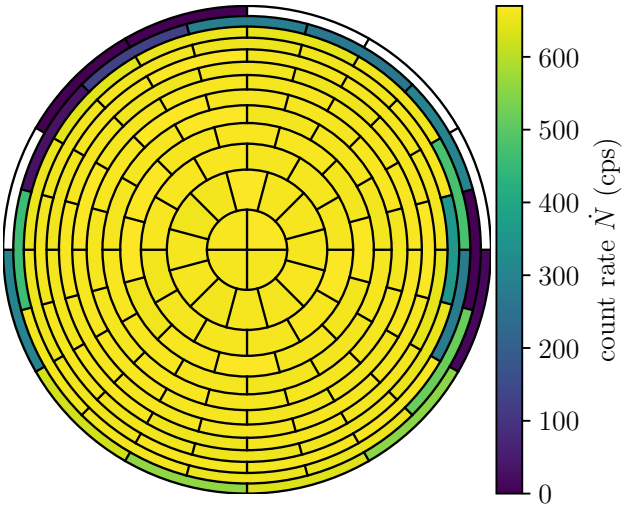

Figure 5.8.: **High rate pixel distribution.** Example run 40667, for a retarding energy of $qU = 16\,975\,\mathrm{eV}$.

5.3.1.1. Parameter inference

A central role in parameter inference is assigned to the likelihood function L. It defines the probability for an observation given a specific model. The KATRIN like-

lihood function for a standard four parameter (m_ν^2, $E_{0,\mathrm{eff}}$, Amp, Bg) fit is given as [Kle14]

$$L(m_\nu^2, E_{0,\mathrm{eff}}, Amp, Bg|\mathbf{N}_{\mathrm{obs}}) = \prod_i p\left(N_{\mathrm{obs},i}|N_{\mathrm{theo},i}(qU_i, m_\nu^2, E_{0,\mathrm{eff}}, Amp, Bg)\right), \quad (5.4)$$

with the retarding potentials qU_i denoting the high voltage corresponding to the observed events $N_{\mathrm{obs},i}$. The expected number of events $N_{\mathrm{theo},i}$ is calculated accordingly, depending on the neutrino mass squared m_ν^2, the effective endpoint of the tritium spectrum[1] $E_{0,\mathrm{eff}}$, the signal amplitude Amp, and the background rate Bg. $p(N_{\mathrm{obs},i}|N_{\mathrm{theo},i})$ defines the probability for a single observation $N_{\mathrm{obs},i}$ given an assumption $N_{\mathrm{theo},i}$. The best-fit parameters are defined as maximising the likelihood function L and are found by evaluating the likelihood function for various different input parameters. When analysing for the neutrino mass as parameter of interest, the so-called nuisance parameters effective endpoint, amplitude, and background rate are of secondary interest. In general it is numerically more convenient to minimise the negative log likelihood function $-\ln L$ instead of maximising the likelihood function L:

$$-\ln L = -\sum_i \ln p\left(N_{\mathrm{obs},i}|N_{\mathrm{theo},i}(qU_i, m_\nu^2, E_{0,\mathrm{eff}}, Amp, Bg)\right). \quad (5.5)$$

In case the probability distribution p can be approximated by a Gaussian distribution, the negative log likelihood function converges to a χ^2 function[2]

$$-2\ln L = \sum_i \left(\frac{N_{\mathrm{obs},i} - N_{\mathrm{theo},i}(qU_i, m_\nu^2, E_{0,\mathrm{eff}}, Amp, Bg)}{\sigma_i}\right)^2 + \text{const.},$$

with the statistical uncertainty σ_i of an observation $N_{\mathrm{obs},i}$. Since in particular the β-decay electrons obey Poisson statistics, a Poisson likelihood statistic $\chi^2_{\lambda,p}$ is implemented [BC84] as

$$\chi^2_{\lambda,p} = 2\sum_i N_{\mathrm{theo},i}(qU_i, m_\nu^2, E_{0,\mathrm{eff}}, Amp, Bg) - N_{\mathrm{obs},i} + N_{\mathrm{obs},i}\cdot\ln\left(\frac{N_{\mathrm{obs},i}}{N_{\mathrm{theo},i}(qU_i, m_\nu^2, E_{0,\mathrm{eff}}, Amp, Bg)}\right). \quad (5.6)$$

This statistic yields the same parameter and uncertainty estimates as the maximum likelihood method [BC84, Kle14], and additionally enables goodness-of-fit estimation as it asymptotically obeys a χ^2 distribution.

One way to include systematic uncertainties of the model into the fit procedure is introducing another fit parameter $\hat{\xi}$ for each systematic uncertainty ξ. Knowledge about the systematic uncertainty (for example from calibration measurements or simulations) can be incorporated into the likelihood as a penalty term (pull method) [Kle14]

$$\chi^2(m_\nu^2, E_{0,\mathrm{eff}}, Amp, Bg, \xi|\mathbf{N}_{\mathrm{obs}}) = \chi^2(m_\nu^2, E_{0,\mathrm{eff}}, Amp, Bg|\mathbf{N}_{\mathrm{obs}}) + \left(\frac{\hat{\xi} - \xi}{\sigma_\xi}\right)^2, \quad (5.7)$$

[1] KATRIN will determine an effective endpoint, which amongst others is influenced by the work function difference between WGTS and main spectrometer.

[2] This is also valid for a Poisson distribution with expectation value $\mu \leq 25$.

with the estimated uncertainty σ_ξ of the systematic effect ξ. This method will be used to include the uncertainty of the simulated column density into the uncertainty of the best-fit effective endpoint (see sec. 5.3.5.2). Note that no neutrino mass analysis is performed on the First Tritium data, i.e. the neutrino mass is set to zero in all fits. This leaves the effective endpoint as parameter of interest to test the different analysis methods presented in the following.

5.3.2. Agreement between model and data

The very first injection of tritium into the WGTS (in the following referred to as *Very First Tritium*) was achieved through the controlled gas release from a total number of four sample cylinders.

Very first tritium Instead of continuously supporting the inner loop with a constant amount of tritium via the feed loop (see fig. 3.1), this set-up used sample cylinders filled with tritium which were attached to the permeator. Via a hand valve, the cylinder was emptied and filled into the inner loop system. At some point, the valve regulating the flow between buffer vessel and pressure controlled buffer vessel fully opened in order to keep the pressure stable. At this point, the buffer vessel ran empty as did the activity injected into the source (see fig. 5.9). Therefore the activity during the Very First Tritium runs remained stable only over limited periods of time, despite all other parameters such as source temperature being within their specifications. The Very First Tritium spectra taken with this set-up show very good agreement with the prediction by the model, as can be seen from fig. 5.10.

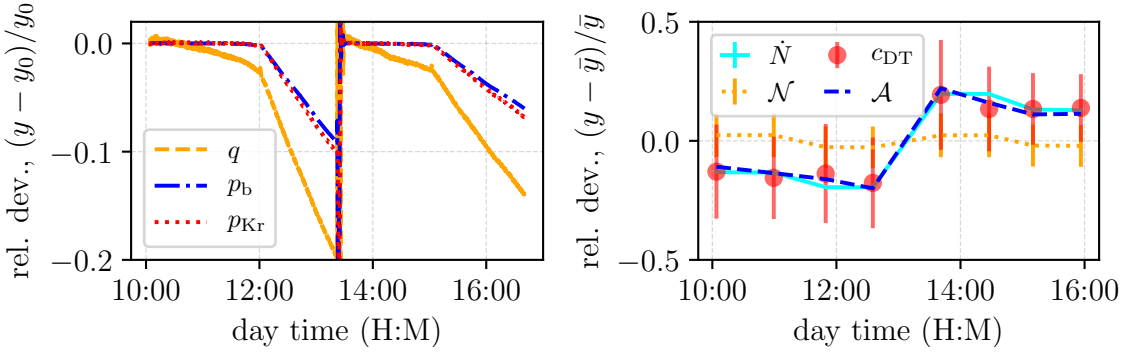

Figure 5.9.: **Decrease of activity.** The reconstructed activity $\mathcal{A}$ (right) decreases due to gas circulation based on sample cylinders for the Very First Tritium set-up (left). Data from 19$^{\text{th}}$ May 2018.

5.3.3. Fit parameter pixel distribution

As the FPD measures the incoming electron flux with 148 pixels, each pixel measures its own β-spectrum. Correcting for the radial and azimuthal dependence of the magnetic and electric field in the analysing plane (compare fig. 5.1), we can fit each pixel separately. The resulting run-averaged distribution of the fit parameters

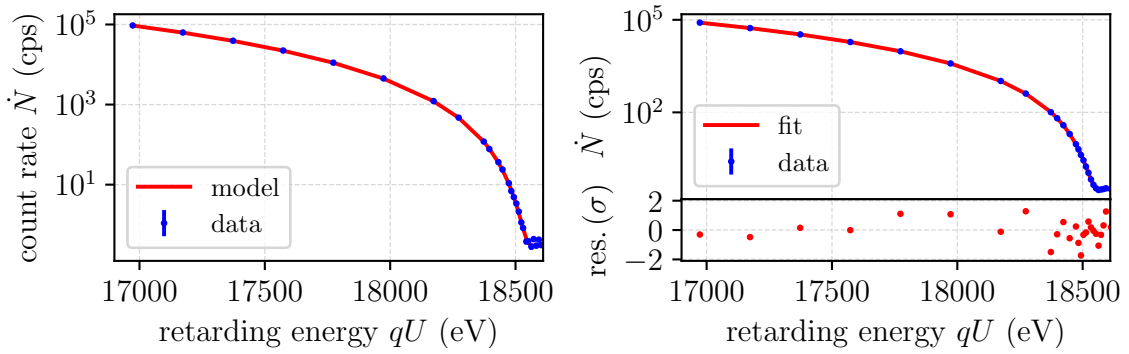

Figure 5.10.: **Model to data comparison.** Data from an initial scan with tritium data, run 40263. Left: model with initial values only, no fit. Right: model with fit parameters $E_{0,\mathrm{eff}}$, Amp, and Bg. Data from 19$^{\mathrm{th}}$ May 2018.

is shown in fig. 5.11. In order to enable pixel-wise fitting per run, the energy window was increased to 0.9 keV below the endpoint. This appears justified, since here we are only interested in the relative pixel-based trend of the fit parameters instead of their absolute accuracy. From the segmented figure, we can see that the effective endpoint and amplitude parameters show no structure over the detector. However, the background rate has the same radial and azimuthal structure as found in previous background investigations [Sch14, Har15]. From the centre to the outside, the background rate increases due to the volume effect of the main spectrometer [Sch14, Har15, Tro18]. The top-bottom asymmetry might be explained by a misalignment between detector and main spectrometer [Blo18].

5.3.4. Fit parameter stability

As shown in sec. 5.2, the KATRIN experiment was running with stable conditions during the First Tritium measurement phase with the design gas circulation. Data from the First Tritium campaign is used in this section to investigate the fit parameter stability. From fig. 5.12 it can be seen that this also holds for the fit parameters. Effective endpoint $E_{0,\mathrm{eff}}$, amplitude Amp, and background Bg vary within their statistical uncertainty, with one outlier marked for the amplitude. The deviation is shown relative to the mean and the error bars reflect the statistical uncertainty only. The binned distribution of the minimised chi-squared, normalised to the number of degrees of freedom, is shown in fig. 5.13. Due to the small number of runs, the resulting distribution is rather flat. An example correlation matrix for a three-parameter fit ($E_{0,\mathrm{eff}}$, Amp, Bg) can be found in the appendix in fig. B.3.

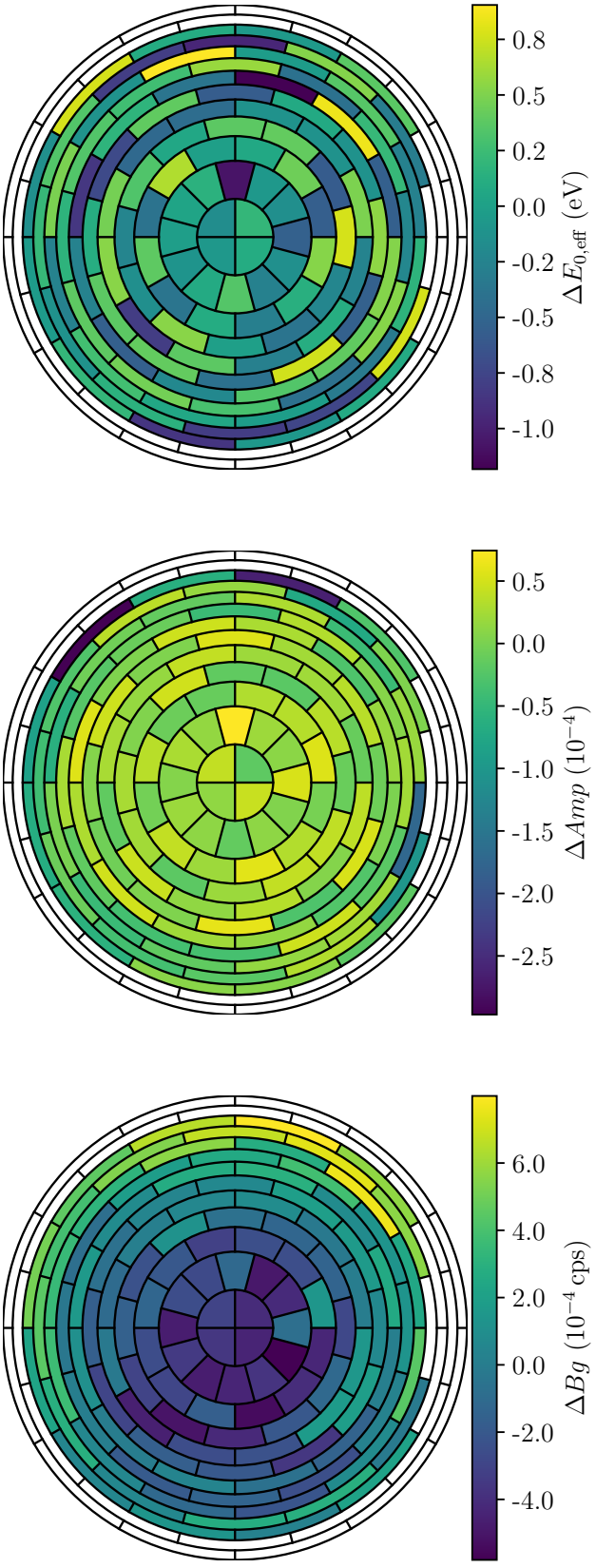

Figure 5.11.: **Fit parameter pixel distribution.** The pixel-wise deviation from the mean is shown, averaged over all runs. The energy interval was widened to 0.9 keV to enable pixel-wise fitting per run.

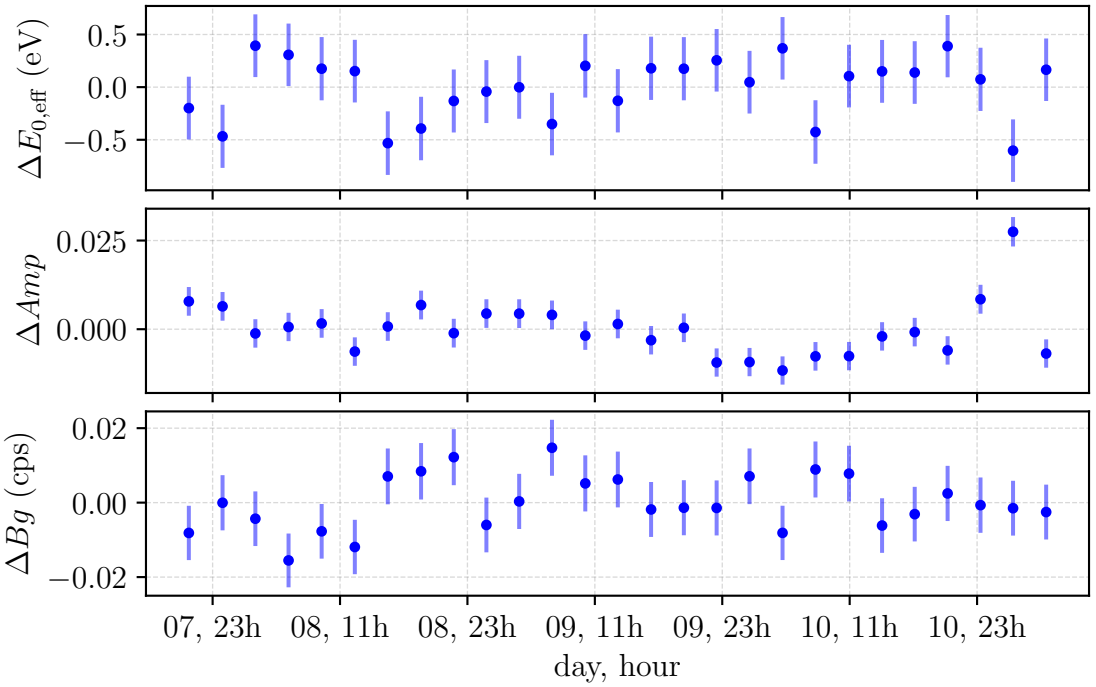

Figure 5.12.: **Fit parameter stability**. The time span is about four days in June 2018, the deviation of the parameters is shown relative to the mean ($\langle E_{0,\mathrm{eff}} \rangle = 18573.72 \pm 0.056\,\mathrm{eV}$, $\langle Amp \rangle = 0.929 \pm 0.0015$, and $\langle Bg \rangle = 0.324 \pm 0.0014\,\mathrm{cps}$).

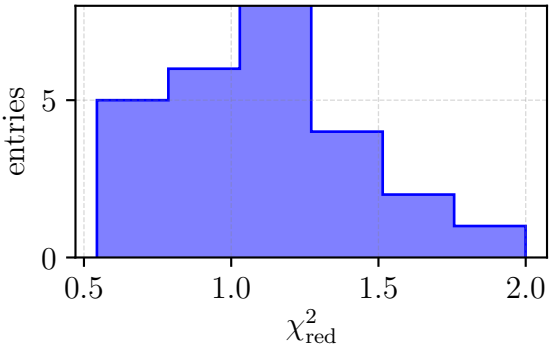

Figure 5.13.: **Chi squared distribution.** The distribution of the reduced χ^2_{red} for the fits from fig. 5.12 is shown.

5.3.5. Systematic effects due to column density uncertainty

One of the major systematic effects [Are+19] when analysing spectra from the First Tritium measurement phase arises from the uncertainty on the column density. As outlined in sec. 4.4.7, the uncertainty on the simulated column density for the First Tritium set-up is 5 %. In the following, different approaches will be used in order to propagate that uncertainty into the parameters of interest $E_{0,\mathrm{eff}}$, Amp, and Bg.

1. The ensemble test method is used to perform several fits, using column density values as sampled from a Gaussian distribution with sigma equal to 5 % of the estimated column density.
2. The column density is treated as a nuisance parameter, using the 5 % uncertainty as width of a Gaussian pull-term in the likelihood.
3. The pull term is removed from the likelihood and the column density is used as a free fit parameter, potentially leading to increased fluctuations of the inferred parameters.

5.3.5.1. Column density distribution as input parameter, ensemble testing

The "brute force" method of ensemble testing ensures propagation of input parameter uncertainty into the inferred parameters. In our case, we want to investigate the impact of a 5 % uncertainty in column density. Therefore, the column density used to fit the measured spectrum is varied according to a Gaussian distribution with sigma equal to 5 % of the simulated value. For each sampled column density, a three-parameter fit is performed. Executing 5000 uniform fits results in the distributions shown in fig. 5.14 (in this example run 40667). We can see that the column density affects all of the three parameters, with the strongest impact on the amplitude. In order to estimate the systematic uncertainty on the effective endpoint, for example, the standard deviation of the fits' effective endpoints is used. A table listing the broadening of the inferred parameter distribution is shown in tab. 5.2.

Table 5.2.: **Ensemble test results.** Note that the amplitude and background are scaled due to the pixel cut. Results are for run 40667.

parameter	mean μ	sigma σ_{sys} due to $\mathcal{N}$	σ_{stat}	total unc.
$E_{0,\mathrm{eff}}$ (eV)	18573.52	0.46	0.30	0.55
Amp	0.94	0.04	0.004	0.04
Bg (cps)	0.316	0.001	0.007	0.007

Assuming that the statistical uncertainty and the systematic uncertainty estimated by the ensemble test method are uncorrelated, we can take the square sum of the two uncertainties to obtain the total uncertainty. Performing that calculation for every run yields the increased uncertainties on the parameters as shown in fig. 5.15.

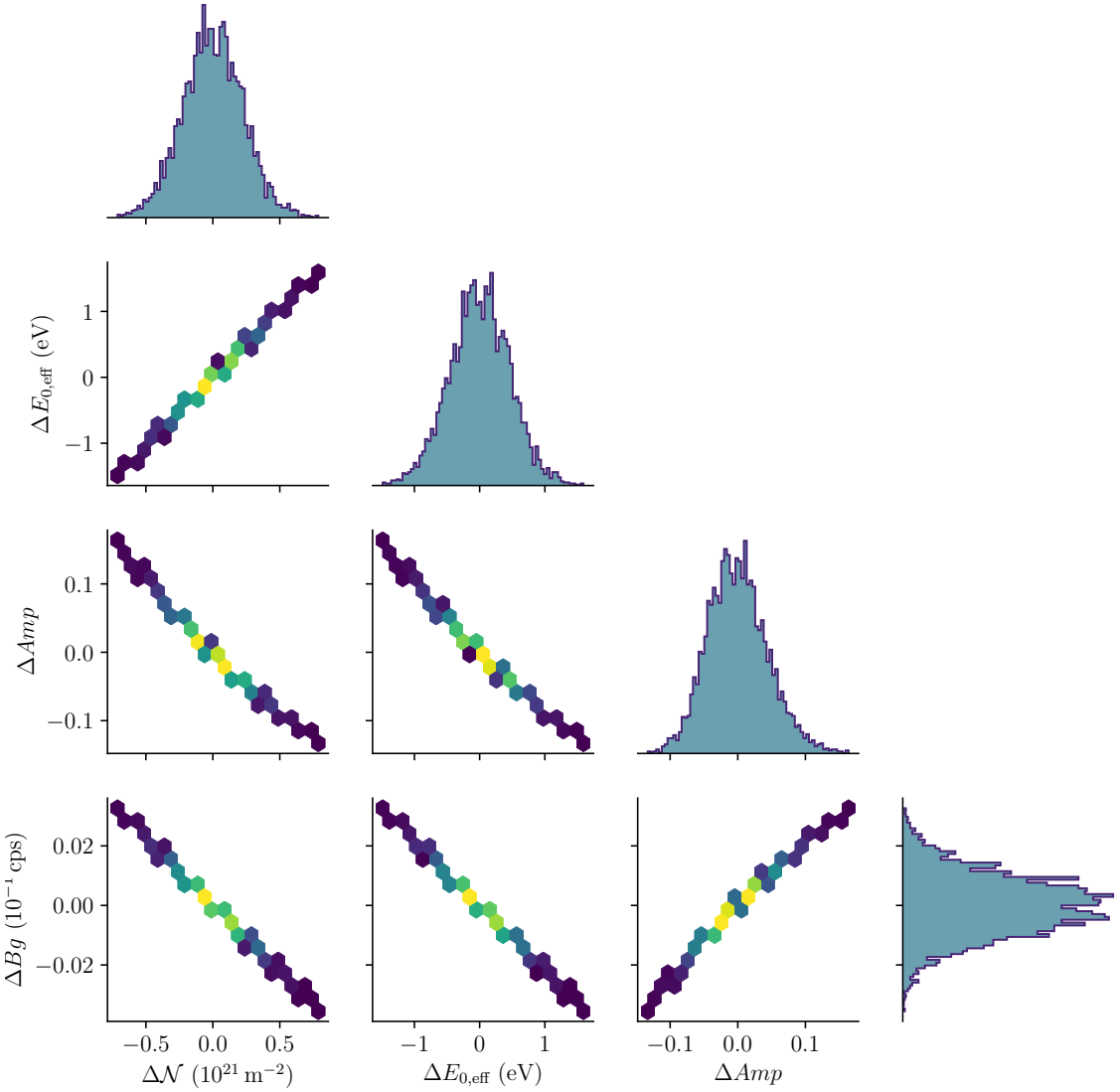

Figure 5.14.: **Parameter distribution from ensemble test.** 5000 fits were performed for run 40667 with fit parameters $E_{0,\mathrm{eff}}$, Amp, and Bg.

5.3.5.2. Column density as constrained parameter

In addition to the powerful but costly ensemble test method, we can also use the pull method (see sec. 5.3.1.1) to introduce the column density as an additional parameter to the fit model. For the fitting, we use the knowledge we have about that parameter, which is its central value and its uncertainty estimated from simulations (see sec. 4.4.7). The additional degree of freedom broadens the likelihood and therefore increases the uncertainty on the estimated parameters of interest. The results are shown for the run 40667 in tab. 5.3. Using the pull method for all runs leads to the run-wise variation of the fit parameters as shown in fig. 5.16. Most significantly, the outlier in the statistical only evolution of the amplitude in fig. 5.12 disappeared. Furthermore, the estimated uncertainties and inferred parameters are compatible with the estimates of the ensemble test method.

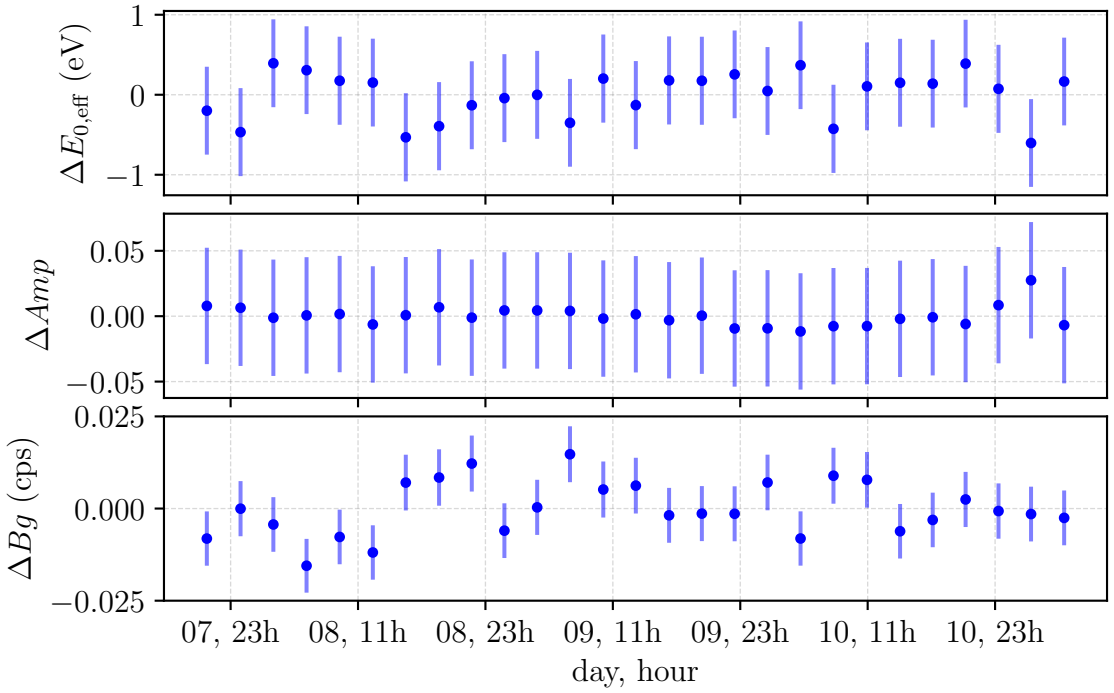

Figure 5.15.: **Fit parameter stability, including systematic uncertainty found by ensemble testing.** Used data is identical to fig. 5.12.

Table 5.3.: **Pull term results.** Note that the amplitude and background are scaled due to the pixel cut. Results are for run 40667.

parameter	estimate	total unc.
$E_{0,\mathrm{eff}}$ (eV)	18573.51	0.52
Amp	0.94	0.04
Bg (cps)	0.316	0.007

5.3.5.3. Column density as free parameter

In order to test the estimation of the column density as well as its uncertainty, we can remove the pull term on the column density in the fit model and treat it as a free fit parameter. Though this provides an estimation of the column density, it needs to be kept in mind that we are only using the column density as additional free parameter. Therefore, potential compensations as for fitting the inelastic scattering cross section at the same time are not respected in this case. Removing the pull term gives rise to an increased broadening of the likelihood due to the additional fit parameter, which results in larger uncertainties as shown in tab. 5.4. Applying this additional free fit parameter to all runs yields the increased fluctuations and uncertainties on the parameters of interest, as shown in fig. 5.17. As expected from the ensemble tests, the largest effect of the column density is on the amplitude, its uncertainty is increased by two orders of magnitude compared to the statistical only derivation.

Having the column density as a free parameter also enables comparison of its best

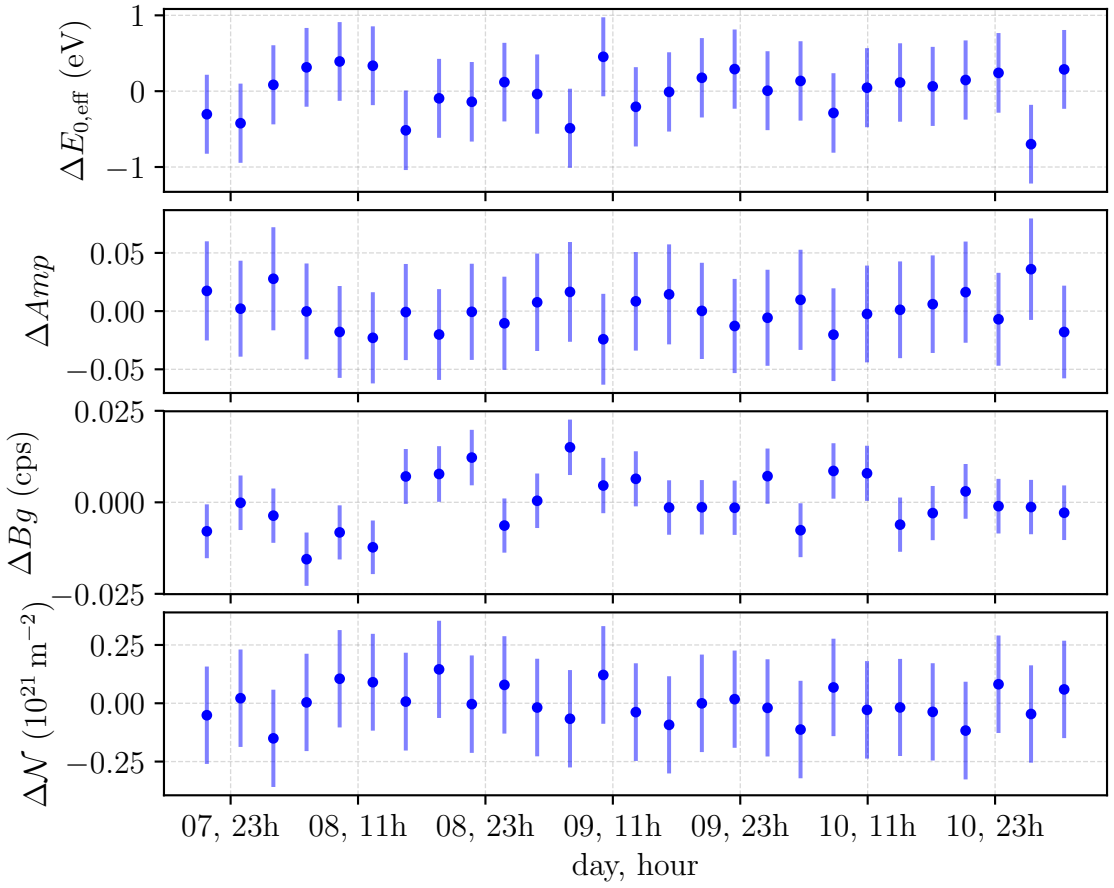

Figure 5.16.: **Fit parameter stability, including systematic uncertainty found by pull method.** The data used is identical to fig. 5.12.

fit value to other column density estimates. For example for run 40667, the best fit is at $4.41 \times 10^{21}\,\mathrm{m}^{-2}$ and the uncertainty found by profiling the likelihood function is $0.59 \times 10^{21}\,\mathrm{m}^{-2}$, which is a relative uncertainty of 13 %. Furthermore, for this example run the fitted and the estimated ($4.46 \times 10^{21}\,\mathrm{m}^{-2}$) column density agree very well.

5.3.6. Appended runs

In contrast to averaging the fit results of each run which is fit separately, this analysis method appends all the runs and fits them together. This results in multiple data points for one retarding energy. In order to have a reasonable estimate of the experiment's condition over this longer time period, the mean value of each sensor is used, justified by the stable conditions of the KATRIN experiment (see sec. 5.2). Appending the runs and including the column density as systematic uncertainty via the above mentioned pull-method results in

$$E_{0,\mathrm{eff}}^{\mathrm{multi,pull}} = 18574.34 \pm 0.22\,\mathrm{eV}, \tag{5.8}$$

while the free column density result gives

$$E_{0,\mathrm{eff}}^{\mathrm{multi,free}} = 18574.40 \pm 0.24\,\mathrm{eV}. \tag{5.9}$$

Table 5.4.: **Free fit parameter results.** Note that the amplitude and background are scaled due to the pixel cut. Results are for run 40667.

parameter	estimate	total unc.
$E_{0,\mathrm{eff}}$ (eV)	18573.43	1.23
Amp	0.95	0.13
Bg (cps)	0.316	0.008
$\mathcal{N}$ ($10^{21}\,\mathrm{m}^{-2}$)	4.41	0.59

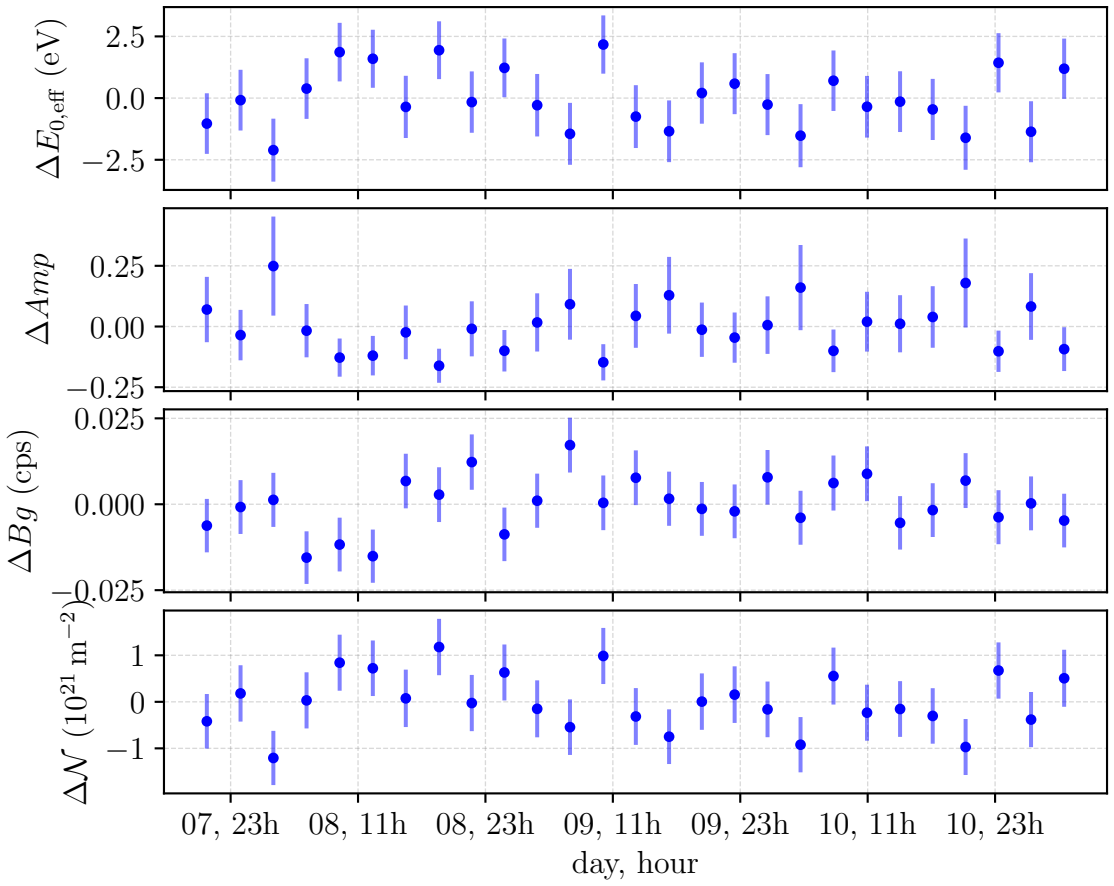

Figure 5.17.: **Fit parameter stability, including systematic uncertainty found by free parameter.** The data used is identical to fig. 5.12.

Note that the quoted values do not include a sizeable systematic uncertainty due to work function effects for example. In order to access the absolute endpoint, those need to be considered. The free column density estimate with this method is

$$\mathcal{N}^{\mathrm{multi,free}} = (4.6 \pm 0.12) \times 10^{21}\,\mathrm{m}^{-2}, \tag{5.10}$$

with statistical uncertainty only.

5.3.7. Overview of the effective endpoint estimates

This section summarises the different estimates of the effective endpoint displayed in fig. 5.18.

For comparison, the expected value of the effective endpoint estimated from T-^{3}He atomic mass difference measurements is shown. Following the discussion of Otten and Weinheimer [OW08], the mass difference needs to be "[...] corrected for the difference in the electronic binding energy ΔE_B between the *atomic mother/daughter pair* and the *actual mother/daughter systems* of the experiment [...]" [OW08]. With the T-^{3}He atomic mass difference $\Delta M(^3\mathrm{He}, \mathrm{T}) = 18592.01 \pm 0.07\,\mathrm{eV}$ as determined by Myers et al. [Mye+15], the electronic binding energy difference $\Delta E_\mathrm{B} = 16.3\,\mathrm{eV}$ [Sou86, OW08], the T_2 recoil energy $E_\mathrm{rec} = 1.7\,\mathrm{eV}$ (see sec. 2.2.2), and the work function difference $\Delta\phi = 0.3 \pm 0.5\,\mathrm{eV}$ [Sle17] between main spectrometer and tritium source, the expected effective endpoint is estimated to

$$E_{0,\mathrm{eff}} = \Delta M(^3\mathrm{He}, \mathrm{T}) - \Delta E_\mathrm{B} - E_\mathrm{rec} - \Delta\phi \tag{5.11}$$

$$= 18\,592.0\,\mathrm{eV} - 16.3\,\mathrm{eV} - 1.7\,\mathrm{eV} - 0.3\,\mathrm{eV} = 18\,573.7\,\mathrm{eV}. \tag{5.12}$$

In order to fit one common endpoint, the energies of the modelled final states distributions of the different hydrogen isotopologues are shifted such that the common modelled endpoint (used to fit) is the one of T_2 [Dos07]. Therefore, the T_2 values of ΔE_B and E_rec are used to calculate the expected effective endpoint though the most abundant tritium gas species during First Tritium was DT.
The main uncertainty of the expected effective endpoint is due to the uncertainty of the work function difference $\Delta\phi$. In the preliminary analysis of gaseous $^{83\mathrm{m}}$Kr measurements by M. Slezák, the 0.5 eV uncertainty on the work function difference is dominated by the uncertainty of the gamma-ray energy [Sle17]. An additional uncertainty has to be added when using work function analysis results from gaseous $^{83\mathrm{m}}$Kr measurements for the analysis of tritium measurements, as the two measurements use different gas temperatures (about 100 K for $^{83\mathrm{m}}$Kr mode, but 30 K for tritium mode) and different gas species[3]. This difference in set-up could be expected to affect the work function of the source beam tube differently, through adsorption. In order to account for this extra uncertainty, the KATRIN effective endpoint is conservatively estimated to be within a 1 eV interval around 18 573.7 eV [WVH].

Figure 5.18 shows that all effective endpoint estimates presented in this thesis lie inside this interval. The estimates labelled "mean" denote the mean over all runs and the uncertainty is the error of the mean. For comparison, the single run estimate of run 40667 is also shown. The estimates labelled "multi" are obtained from fitting all runs together as described in sec. 5.3.6. The inclusion of the column density as a systematic effect results in larger estimates of the effective endpoint, which underlines the importance of treating systematic effects.

Furthermore, it has to be stressed that the estimates shown in fig. 5.18 only include the column density as a systematic effect. Further systematic uncertainties arise from the 2 % uncertainty on the inelastic scattering cross section, the absolute value

[3] Additionally, there was a short venting of the WGTS beam tube, exposing the beam tube surface to laboratory air in July 2017 [Jan17]. This eventual change in surface conditions translates to an uncertainty on the work function difference development between the $^{83\mathrm{m}}$Kr and the First Tritium campaign.

of the magnetic fields, and the tritium purity, to name only a few. This section only gives the effects related to the column density, detailed investigations for the other input parameters are also required in order to get the complete picture.

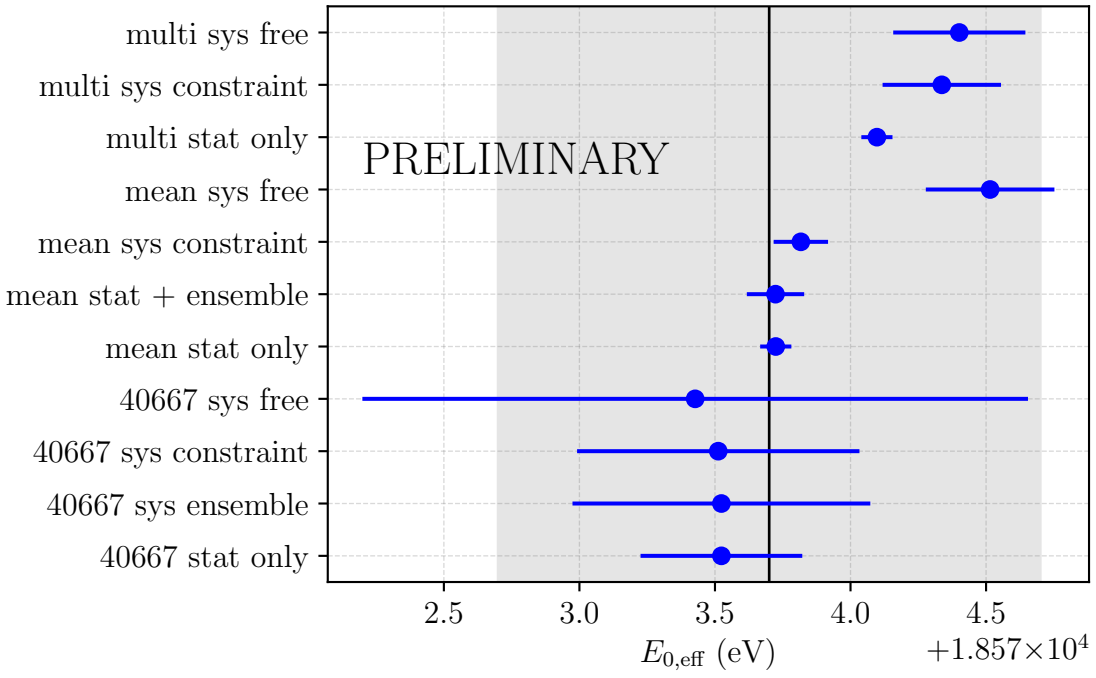

Figure 5.18.: **Overview of the effective endpoint estimates.** The black line shows the expected value as determined from the T-^{3}He mass difference and the relevant binding energies. The grey band represents a 1 eV estimated uncertainty range of the expected KATRIN effective endpoint. An important role therein is attributed to the uncertainty of the work function difference between main spectrometer and WGTS beam tube. Note that the only systematic uncertainty for which the impact on the endpoint measurement is investigated here in detail is the column density.

5.3.8. Systematic effects due to slicing the WGTS

In the fits presented so far, an average column density was assumed along the WGTS beam tube to calculate average scattering probabilities [Kuc+18, Kle+18]. If we now want to respect the longitudinal density profile and also include the small magnetic field inhomogeneities in the central source tube due to the gaps existing between the 3 m long coils (compare fig. 4.17), we have to divide the 10 m long beam tube into lateral slices. Each slice is calculated to contain the same magnetic flux mapped from the detector, so the radius of a slice close to a pump port is larger than in the centre due to the lower magnetic field. S. Groh investigated the effect of the slicing on the neutrino mass [Gro15] and recommended a number of 200 slices. However, as each slice has its own β-spectrum and response function accounting for the integrated density in front of that particular slice, fitting with slicing is very

costly in computation time. For the First Tritium settings, the effect of the number of slices is investigated using the effective endpoint, and results are shown in fig. 5.19. We can see that the change in effective endpoint estimate levels off for increasing number of slices, as expected. The more slices, the better the sliced density profile follows the unbinned density profile. For the low statistics of the First Tritium data the slicing does not appear to have a strong effect compared to the final set-up. If using a sliced WGTS for fitting, it is recommended to use at least 50 slices. A larger number of slices does not significantly affect the estimation of the effective endpoint, but is very costly in computation time.

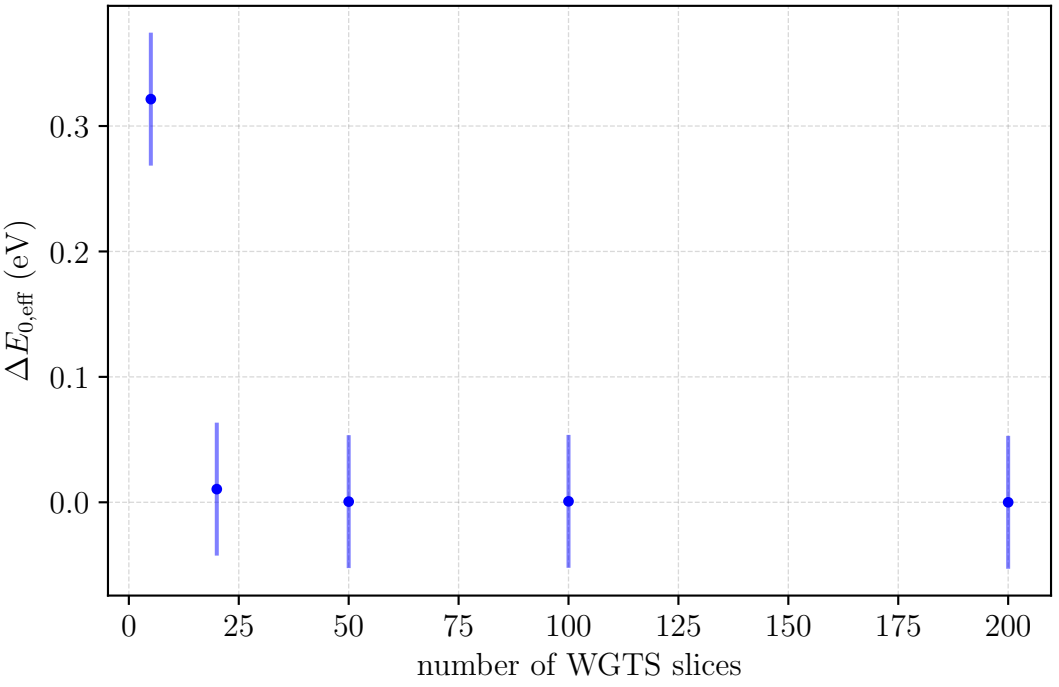

Figure 5.19.: **Effect of WGTS slicing.** The shift of the effective endpoint relative to the 200 slices estimate is shown, averaged over all runs.

5.3.9. Test of the scattering implementation

Close to the endpoint of the tritium spectrum, the signal rate $S = \dot{N} - Bg$ is proportional to the zero-scattering probability P_0 and the number of tritium atoms seen by the detector, represented by the column density $\mathcal{N}$ times the tritium purity ϵ_T:

$$S \propto P_0 \cdot \epsilon_\mathrm{T} \cdot \mathcal{N}. \tag{5.13}$$

Assuming a constant tritium purity, the signal ratio of two different column densities can be used to investigate the scattering implementation in the spectrum model. Scaling the signal ratio with the inverse of the column density ratio yields the ratio of the zero-scattering probabilities at e.g. 10 eV below the endpoint:

$$\frac{P_0}{P_{0_0}} = \frac{S}{S_0} \cdot \frac{\mathcal{N}_0}{\mathcal{N}}, \tag{5.14}$$

with the index 0 indicating the reference measurement. Due to the low statistics in the endpoint region, the uncertainties will be large even without including systematic uncertainties on e.g. the column densities. In fig. 5.20, the ratio of the signal rates scaled with the column density ratio is displayed for two column densities $\mathcal{N} = 1.09 \times 10^{21}\,\mathrm{m}^{-2}$ and $\mathcal{N}_0 = 4.46 \times 10^{21}\,\mathrm{m}^{-2}$. The corresponding zero-scattering probability ratio is 1.8, shown as the black line in the endpoint region. It can be seen that indeed, the statistical uncertainties are sizeable – and within these uncertainties the model matches the data. No conclusions on the zero-scattering probabilities can be drawn as the statistical uncertainties are already too large.

The scattering investigations will be simplified and much more detailed once the e-gun of the rear section starts operating. As mentioned in sec. 4.3.4, it will be used to accurately determine the product of column density and inelastic scattering cross section, which in turn enables determining the zero-scattering probability.

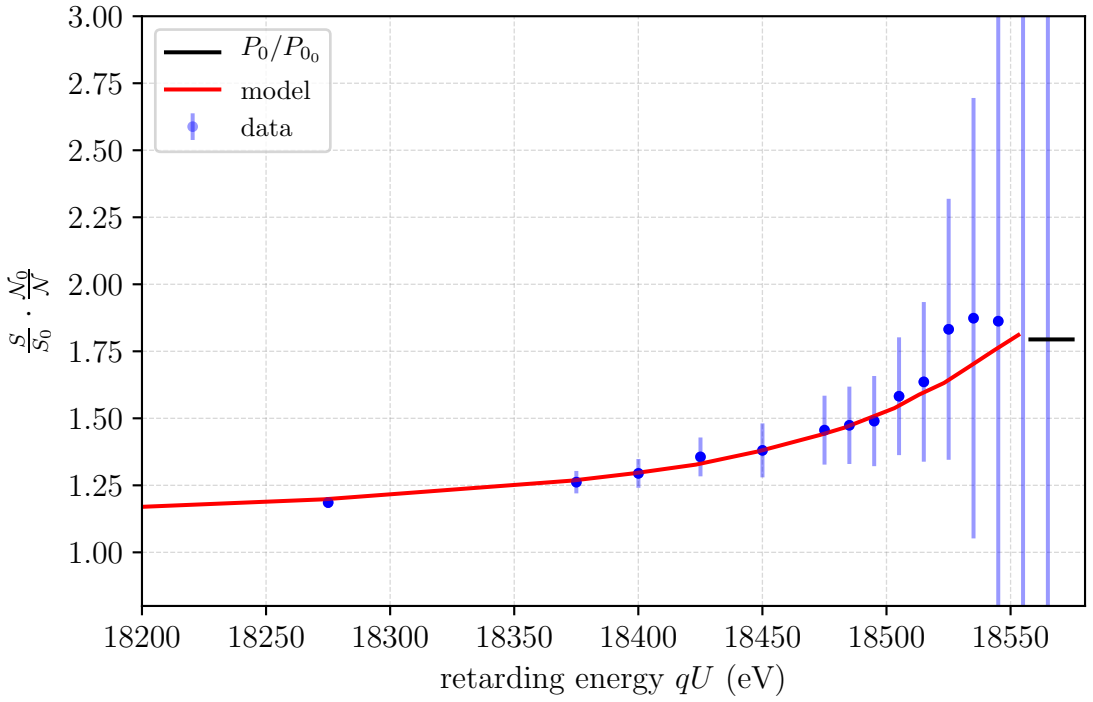

Figure 5.20.: **Test of scattering implementation.** The signal ratio of the $\mathcal{N} = 1.09 \times 10^{21}\,\mathrm{m}^{-2}$ column density runs and the $\mathcal{N}_0 = 4.46 \times 10^{21}\,\mathrm{m}^{-2}$ column density runs, scaled by the respective column densities, statistical uncertainty only, is shown. The red line is using the fit result from the spectra and the black line illustrates the expected zero scattering probability ratio.

5.4. Estimation of the column density via additional detectors

This section presents ways to estimate and cross-check the column density simulations by using data from the active commissioning of KATRIN. The data available during First Tritium stems from the Forward Beam Monitor (FBM), the PULCINELLA disk in front of the Focal Plane Detector (FPD) and from the FPD itself. Each of the methods faces different challenges, which will be addressed in detail in this section.

5.4.1. Estimation of the column density via the FBM

In order to compare the simulated value of the column density to measured data, one possibility is using the FBM. Comparing its integrated rate $\dot{N}_{\mathrm{FBM}}$ (above some energy threshold E_{th}) to the theoretical decay rate $\dot{N}_{\mathrm{theo}}$ (also integrated from E_{th}) yields information about the number of active gas atoms and thereby about the column density. The rate is proportional to the activity in the source, which itself depends on the number of tritium atoms:

$$\dot{N}_{\mathrm{FBM}}\Big|_{E\geq E_{\mathrm{th}}} = \dot{N}_{\mathrm{theo}}\Big|_{E\geq E_{\mathrm{th}}} \cdot \epsilon_{\mathrm{det}} \cdot n_{\mathrm{T}} \cdot a(\theta_{\mathrm{max}}), \tag{5.15}$$

with the FBM detection efficiency ϵ_{det}, the number of tritium atoms mapped onto the FBM n_{T} and the maximum acceptance angle θ_{max} defining the fraction of electrons that can arrive at the FBM, $a(\theta_{\mathrm{max}})$. The column density enters through the number of tritium atoms (see sec. 5.4.1.2), enabling estimation of the column density from a rearranged form of eq. (5.15) as

$$\mathcal{N} = \frac{\dot{N}_{\mathrm{FBM}}\Big|_{E\geq E_{\mathrm{th}}}}{\dot{N}_{\mathrm{theo}}\Big|_{E\geq E_{\mathrm{th}}} \cdot \epsilon_{\mathrm{det}} \cdot c_{\mathrm{DT}} \cdot A_{\mathrm{WGTS}} \cdot (1-\cos\theta_{\mathrm{max}}) \cdot 0.5}. \tag{5.16}$$

In the following, the factors of eq. (5.15) (or eq. (5.16) equivalently) will be discussed individually.

An overview of the runs used is given in tab. 5.5. All runs were taken in June 2018.

Table 5.5.: **FBM run overview.**

run	purpose	duration
145-147	100 % $\mathcal{N}$	2:14 h
247	FBM background	1 h
272-274	50 % $\mathcal{N}$	3 h
278-280	25 % $\mathcal{N}$	3 h
331-333	75 % $\mathcal{N}$	3 h

5.4.1.1. Maximum acceptance angle

In contrast to the usual θ_{max} being defined by the relation between source and PCH magnetic field, at the location of the FBM θ_{max} is defined by the relation between source $B_{\text{S}} = 2.5\,\text{T}$ and CPS magnetic field B_{CPS} since the maximum magnetic field between WGTS and the FBM is $B_{\text{CPS}} = 4\,\text{T}$:

$$\theta_{\text{max}} = \arcsin\sqrt{\frac{B_{\text{S}}}{B_{\text{CPS}}}} = 52.5°. \tag{5.17}$$

The maximum acceptance angle defines the fraction of electrons arriving at the FBM:

$$a\left(\theta_{\text{max}}\right) = \frac{\int_0^{\theta_{\text{max}}} \sin\theta\,\mathrm{d}\theta}{\int_0^{\pi} \sin\theta\,\mathrm{d}\theta} = \frac{1-\cos\theta_{\text{max}}}{2}. \tag{5.18}$$

The uncertainty on the maximum acceptance angle is determined by the uncertainty on the magnetic fields. In sec. 5.2.4 it was shown that the relative stability of the magnetic fields is better than 1×10^{-5}, leaving the systematic uncertainty of 1 % as dominant uncertainty of the magnetic fields.

5.4.1.2. Number of tritium atoms

The number of tritium atoms in the cross-section A in the WGTS can be estimated via

$$n_{\text{T}} = 2 \cdot \mathcal{N} \cdot A \cdot \epsilon_{\text{T}}, \tag{5.19}$$

with $\mathcal{N}$ being the total column density and $\epsilon_{\text{T}} \approx 0.56\%$ the tritium purity. Due to the low tritium concentration in the First Tritium campaign of KATRIN, almost all of the tritium occurs in form of DT. Therefore, the number of tritium atoms can also be estimated via

$$n_{\text{T}} = \mathcal{N} \cdot A \cdot c_{\text{DT}}, \tag{5.20}$$

with $c_{\text{DT}} \approx 1.04\,\%$ being the DT concentration in the gas inside WGTS. During the 1 h time scale of a FBM run, the fluctuation of the DT concentration was 0.02 %. For the systematic uncertainty of the DT concentration in First Tritium data, LARA gives an absolute number of about 0.16 %. Re-analysed LARA data yields a factor three improved uncertainty on the estimated DT concentration [KZ18]. To ensure consistency with the spectral analysis results presented in this chapter, it was decided to not use this updated LARA data for the column density estimation.

5.4.1.3. Fluxtube mapping

In order to compare the predicted to the measured FBM rate, the effective WGTS cross-section and therefore the flux tube seen by the each of the two FBM diodes needs to be determined. The magnetic field at the position of the FBM diodes is $B_{\text{FBM}} = 0.8\,\text{T}$, while the source is at $B_{\text{S}} = 2.5\,\text{T}$. This means that the FBM sees

fewer electrons as if it was located at B_S. The result is a lower effective detection area of the FBM diodes, estimated from conservation of the magnetic flux ϕ:

$$\phi_\mathrm{FBM} = \phi_\mathrm{WGTS} \rightarrow A_{\mathrm{WGTS}_{1,2}} = A_\mathrm{FBM} \cdot \frac{B_\mathrm{FBM}}{B_\mathrm{WGTS}} = 1.35\,\mathrm{mm}^2 \cdot B_{\mathrm{FBM}_{1,2}}/B_\mathrm{S}, \tag{5.21}$$

with $B_{\mathrm{FBM}_{1,2}}$ the magnetic field at the position of diode 1 and 2, $(B_{\mathrm{FBM}_1}, B_{\mathrm{FBM}_2}) = (0.8191, 0.8197)\,\mathrm{T}$ and the photosensitive area of $A_\mathrm{FBM} = 1.35 \pm 0.05\,\mathrm{mm}^2$ [Hau18]. Using $B_\mathrm{S} = 2.5\,\mathrm{T}$ results in $(A_{\mathrm{WGTS}_1}, A_{\mathrm{WGTS}_2}) = (0.44, 0.44)\,\mathrm{mm}^2$.

Though the Hall sensor of the FBM board can determine the magnetic field of the FBM, it is positioned a small distance away from the two diodes on the FBM board (compare fig. 2.4). Including an offset of the whole FBM detector board of $(x, y) = (0.26, 2.7)\,\mathrm{mm}$ [Ell18], the author found a z component of the magnetic field at the position of the Hall probe from Kassiopeia simulations of $-0.8029 \pm 0.0005\,\mathrm{T}$. The Hall probe measured a magnetic field of $-0.7973\,\mathrm{T}$, which yields a difference to the simulation corresponding to 0.7 %. Together with the 1 % general uncertainty on magnetic fields, this amounts to a systematic uncertainty of 1.2 % on the magnetic field at the position of the diodes. The magnetic field of the WGTS has the 1 % systematic uncertainty estimated for the First Tritium settings [Are+19]. The uncertainty on the effective WGTS cross-section is then determined via bootstrapping, considering the uncertainties on the individual factors of eq. (5.21).

5.4.1.4. FBM rate prediction

Since the FBM diodes are of Si-pin type, the FBM has some intrinsic energy resolution $\Delta E_\mathrm{FWHM} = 2.4\,\mathrm{keV}$. The theoretical β-spectrum needs to be convolved with the detector resolution function in order to estimate the column density. The effect of the FBM energy resolution is shown in fig. 5.21: as expected, it smears the theoretical spectrum to both sides, at lower and higher energies. The FBM rate

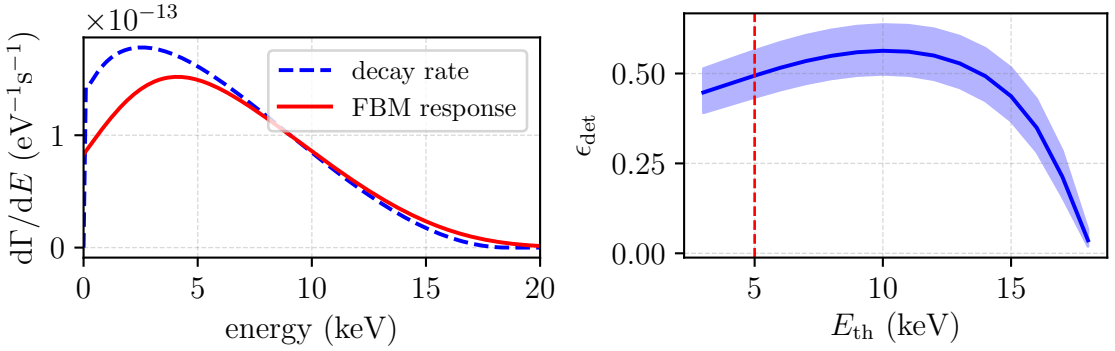

Figure 5.21.: **FBM rate prediction**. Left: we see the smearing towards lower and higher energies caused by the intrinsic FBM energy resolution. Right: the energy threshold dependent detection efficiency is shown. Data kindly provided by N. Haußmann [Hau18].

per tritium atom is estimated as the sum over all final states, convolved with the detector resolution $G(E, \epsilon)$:

$$\dot{N}_\mathrm{theo}\Big|_{E \geq E_\mathrm{th}} = \int_{E_\mathrm{th}}^{\infty} \int_{-\infty}^{\infty} G(E - \epsilon) \cdot \sum_{fs} P_{fs} \cdot \frac{\mathrm{d}\Gamma(\epsilon)}{\mathrm{d}E}\bigg|_{fs} \mathrm{d}\epsilon\,\mathrm{d}E \tag{5.22}$$

Besides the energy resolution of the FBM, there are various other effects to be taken into account. One of them is the backscattering of electrons off the surface of the FBM, causing a reduction of the estimated rate. Since the FBM diodes are of Si-pin type [HAM18], they have a non-zero dead layer. If electrons deposit energy in this region, the deposited energy cannot be detected by the FBM. Such dead layer effects were investigated by N. Haußmann [Hau18] and E. Ellinger [Ell18] via measurements and KESS[4] simulations. Using dead layer measurements by E. Ellinger [Ell18], N. Haußmann finds energy threshold dependent upper and lower limits for the FBM detection efficiency ϵ_{det}. The results for ϵ_{det} are shown in fig. 5.21 and yield for the threshold energy $E_{\text{th}} = 5\,\text{keV}$ used in

$$\epsilon_{\text{det}} = 0.49\ ^{+0.07}_{-0.06}. \tag{5.23}$$

In fig. 5.21, the uncertainty band represents the dead layer thickness estimate of $350 \pm 50\,\text{nm}$ with lower dead layer thickness resulting in higher detection efficiency. The estimation of the detection efficiency also includes backscattering onto the FBM due to the magnetic mirror effect.

5.4.1.5. FBM rate estimation

The measured rate at the FBM is estimated via integration of the measured spectrum above some threshold E_{th}. Since the energy estimation of the FBM for electrons with energies below 5 keV is not reliable, we set $E_{\text{th}} = 5\,\text{keV}$. Also note that the cut was done on the ADC equivalent (166) instead of the calibrated energy (5 keV).

The applied calibration is of the form

$$E = 31.747\,\text{eV/channel} \cdot \text{ADC} - 241.357\,\text{eV} \qquad \text{channel 1} \tag{5.24}$$

$$E = 31.892\,\text{eV/channel} \cdot \text{ADC} - 262.987\,\text{eV} \qquad \text{channel 2} \tag{5.25}$$

The rate estimation is then the integration of the ADC spectrum from 166 ADC (the interested reader can find the spectrum plots in app. B.1); the time dependence is shown in fig. 5.22 for a sampling time of 60 s. A horizontal line is fit in fig. 5.22

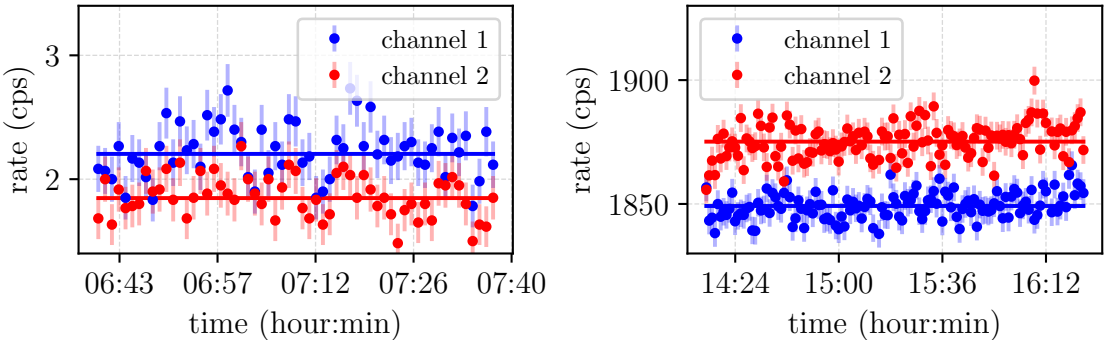

Figure 5.22.: **FBM estimated rate**. Left side: background run 247 (11th June 2018). Right side: signal runs 145-147 (6th June 2018).

which enables estimation of the rate in a specific time interval. In order to estimate

[4] KATRIN Electron Scattering in Silicon Simulation (KESS) package developed by P. Renschler [Ren11].

the signal rate, the background rate needs to be subtracted. The signal rates were determined from runs 145-147, while run 247 was taken as background run when the FBM was outside the active flux tube (compare tab. 5.6). The systematic uncertainty

Table 5.6.: **FBM fitted rate.**

quantity		fit value	fit uncertainty
$\dot{N}_{\mathrm{FBM,tot,1}}\big\vert_{E\geq E_{\mathrm{th}}}$	(cps)	1849.2	0.5
$\dot{N}_{\mathrm{FBM,tot,2}}\big\vert_{E\geq E_{\mathrm{th}}}$	(cps)	1875.2	0.5
$\dot{N}_{\mathrm{FBM,bg,1}}\big\vert_{E\geq E_{\mathrm{th}}}$	(cps)	2.2	0.03
$\dot{N}_{\mathrm{FBM,bg,2}}\big\vert_{E\geq E_{\mathrm{th}}}$	(cps)	1.8	0.02
$\dot{N}_{\mathrm{FBM,sig,1}}\big\vert_{E\geq E_{\mathrm{th}}}$	(cps)	1847.0	0.5
$\dot{N}_{\mathrm{FBM,sig,2}}\big\vert_{E\geq E_{\mathrm{th}}}$	(cps)	1873.3	0.5

assigned to the two rates is estimated as the distance to the mean, resulting in $\sigma_{\dot{N}_{\mathrm{FBM,sys}}} = 13.0\,\mathrm{cps}$.

5.4.1.6. Uncertainty estimation

The uncertainties of the factors of eq. (5.16) are propagated to an uncertainty on the estimated column density via ensemble testing. A summary of the uncertainties is given in tab. 5.7; note that the systematic uncertainties are given in relative percentage values. In order to estimate the column density uncertainty, each item of tab. 5.7 is sampled from a Gaussian distribution centred at the estimated value with σ being the estimated uncertainty. With a number of 10^5 samples, the statistical and systematic distribution of the column density can be estimated with a precision of 0.3 %, yielding the statistical and systematic uncertainty of the column density estimate via the FBM. Lower and upper uncertainties are estimated as the column density representing a cumulative 34 % below and above the column density estimate, comparable to a 1σ interval of a Gaussian distribution. The resulting statistical and systematic distributions of the column density are shown in fig. 5.23 and listed in tab. 5.7.

5.4.1.7. Column density

Ignoring energy loss processes in the source, one can rearrange eq. (5.15) in order to estimate the column density with eq. (5.16). Combining the estimates of the factors as listed in tab. 5.7 results in an estimate of the column density from the measured FBM rate of (estimate ± stat. ± sys.)

$$\mathcal{N}_{\mathrm{FBM}} = \left(4.59\ {}^{+0.07}_{-0.06}\ {}^{+1.14}_{-0.93}\right) \times 10^{21}\,\mathrm{m}^2. \tag{5.26}$$

Compared to the expected value from gas dynamic simulations of $4.46 \times 10^{21}\,\mathrm{m}^{-2}$, this is a deviation of 3 % which presents good agreement within the estimated uncertainty. It has to be noted that one of the main uncertainties of the column density

Table 5.7.: **FBM column density uncertainty.** Note that the systematic uncertainties are given in relative values. Magnetic fields are stable to the 10^{-5} level, therefore their statistical uncertainty is neglected.

quantity	estimate	stat. unc.	sys. unc.
measured rate 1 $\dot{N}_{\mathrm{FBM},1}\big\vert_{E\geq E_{\mathrm{th}}}$	1849.2 cps	0.5 cps	0.7 %
measured rate 2 $\dot{N}_{\mathrm{FBM},2}\big\vert_{E\geq E_{\mathrm{th}}}$	1875.2 cps	0.5 cps	0.7 %
DT concentration c_{DT}	1.04 %	0.02 %	16.3 %
B_{FBM}	0.8 T	–	1.2 %
B_{WGTS}	2.5 T	–	1 %
B_{PCH}	4.2 T	–	1 %
FBM cross-section A_{FBM}	1.35 mm^2	–	3.7 %
detection efficiency ϵ_{det}	0.4941	–	14 %
column density $\mathcal{N}$ (10^{21} m^{-2})	4.59	$^{+0.07}_{-0.06}$	$^{+1.14}_{-0.93}$

determination via the FBM is the detection efficiency. Also the photosensitive area of the diode measured by N. Haußmann (1.35 ± 0.05 mm^2) deviates from the size listed by Hamamatsu specifications (1.1 ± 0.03 mm^2) [HAM18]. Using the Hamamatsu given area would result in an estimate of the column density of 5.6×10^{21} m^{-2}, which would be a 20 % difference.

Different column densities In order to test whether neglecting the scattering in eq. (5.16) has an effect on the estimated column density, we can compare simulated column densities to the FBM-based ones from eq. (5.16) for various column densities. The different column densities arise from the change in injection rate shown in the top part of fig. 5.24. As can be seen, the FBM rate scales perfectly with the column density (plot shows relative deviation to the start of the shown measuring period). On the lower plot, we can see that the change in column density does not cause a change in the difference between gas dynamics simulated and FBM determined column density. Though the tritium concentration increases because of gas exchange reactions due to the different pressures, the difference between the gas dynamics estimated column density and the FBM estimated column density does not change significantly. Therefore it can be concluded that the effect of the scattering can indeed be neglected for the estimation of the column density via the FBM.

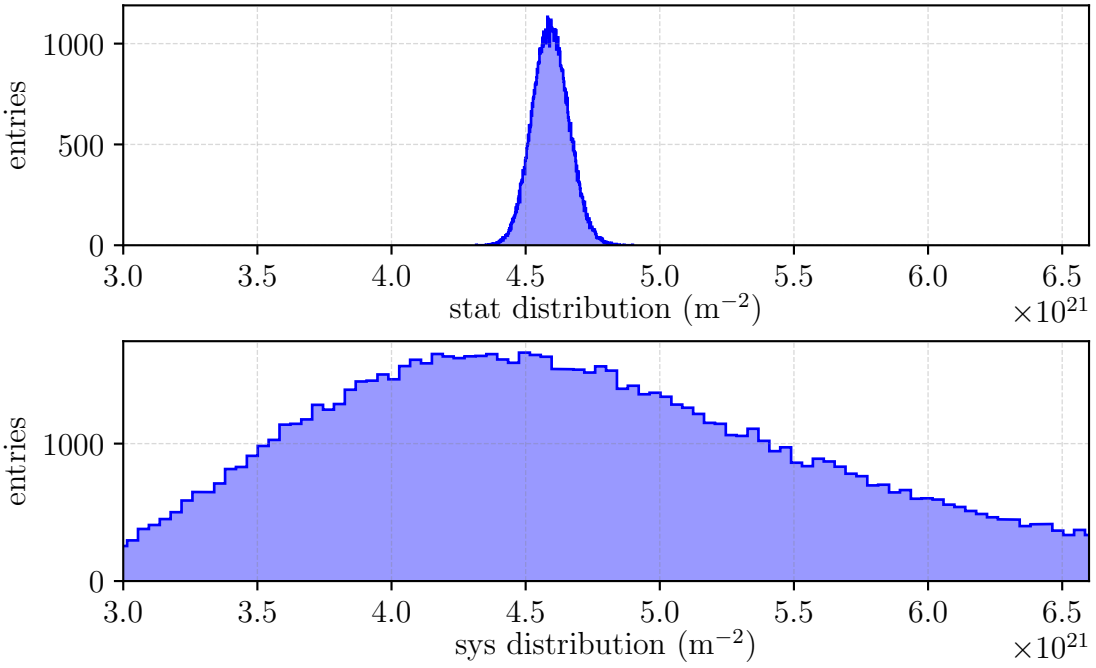

Figure 5.23.: **FBM determined column density uncertainty.** The upper panel shows the statistical distribution, while the lower one shows the systematic distribution. 10^5 samples were diced.

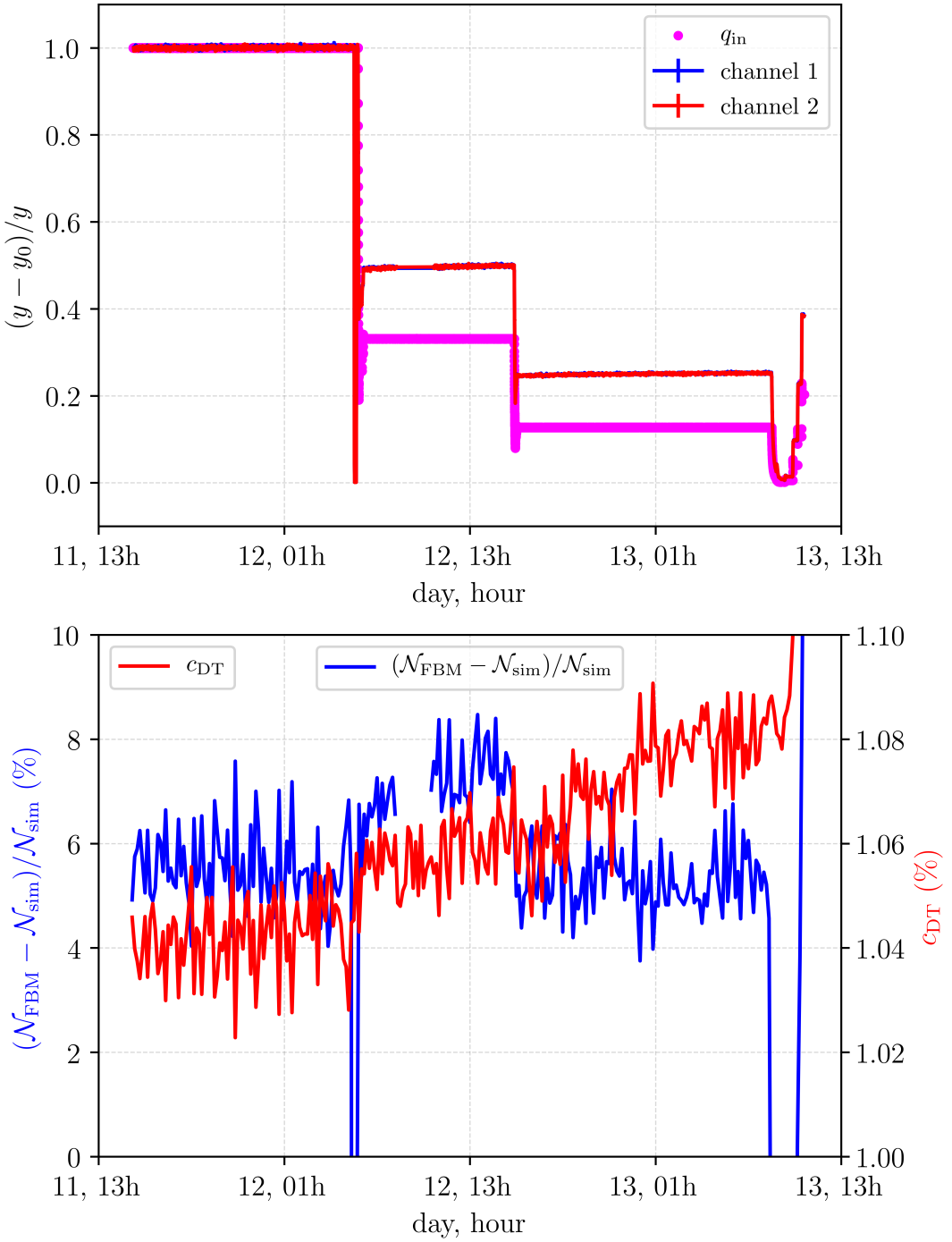

Figure 5.24.: **FBM estimate of different column densities.** Upper plot shows the variation of the injection rate and the FBM rate. Lower plot shows the difference between simulated and FBM determined column density (left ordinate), and the DT concentration (right ordinate). Data from 11^{th} June to 13^{th} June 2018.

5.4.2. Estimation of the column density via PULCINELLA

The main purpose of PULCINELLA is calibration of the FPD [Ams+15]. However, the measured electron flux of PULCINELLA can also be used to estimate the column density. PULCINELLA is a titanium disk in front of the FPD, equipped with a pico ammeter. The idea for connecting the measured current (converted into an electron rate) to the theoretical prediction is the same as for the FBM as described in sec. 5.4.1:

$$\dot{N}_{\mathrm{PULCINELLA}}\Big|_{E\geq E_{\mathrm{th}}} = \dot{N}_{\mathrm{theo}}\Big|_{E\geq E_{\mathrm{th}}} \cdot \epsilon_{\mathrm{det}} \cdot n_{\mathrm{T}} \cdot a(\theta_{\mathrm{max}}), \tag{5.27}$$

with the detection efficiency ϵ_{det}, the number of tritium atoms visible by PULCINELLA n_{T} and the maximum acceptance angle θ_{max}. The maximum acceptance angle and the detection area will be different, though, from sec. 5.4.1 since the PULCINELLA disk is positioned at a different magnetic field than the FBM. In the following only the coefficients which are different from the column density estimation via FBM in sec. 5.4.1 are discussed. An overview of the runs used is given in tab. 5.8; all runs were taken on 5$^{\mathrm{th}}$ June 2018.

Table 5.8.: **PULCINELLA run overview.**

run	purpose	duration
40495	position determination	first 130 s
40498	tritium signal	1 min
40500	PULCINELLA background	10 min

5.4.2.1. Maximum acceptance angle

The PULCINELLA disc is located in front of the FPD in the pump port between PCH and detector magnet. Therefore, the relevant maximum magnetic field is the 4.2 T magnetic field of the PCH magnet:

$$\theta_{\mathrm{max}} = \arcsin\sqrt{\frac{B_{\mathrm{S}}}{B_{\mathrm{PCH}}}} = 50.8°, \tag{5.28}$$

which defines the fraction of detectable electrons according to eq. (5.18).

The uncertainty on the maximum acceptance angle is determined by the uncertainty on the magnetic fields. In sec. 5.2.4 it was shown that the relative stability of the magnetic fields is better than 1×10^{-5}, leaving the systematic uncertainty of 1 % as dominant uncertainty of the magnetic fields.

5.4.2.2. Flux tube mapping

In order to compare the predicted to the measured PULCINELLA rate, the WGTS flux tube seen by PULCINELLA needs to be determined accurately. Since the main focus of the PULCINELLA measurements was not on determining the column density, the PULCINELLA position was not well-determined in advance.

Determining the position of PULCINELLA The only way to determine the position of the PULCINELLA disk in the KATRIN global coordinate system is to use its shadow on the FPD. Usually, PULCINELLA covers the entire FPD, during the measurements discussed in this section however there was a slight offset, compare fig. 5.25 (from run 40495, see tab. 5.8). This offset can be estimated using the shadow of PULCINELLA on the FPD. Due to the crescent-shaped form of the shadow, a ring can be fit onto the FPD in order to determine the origin of PULCINELLA.

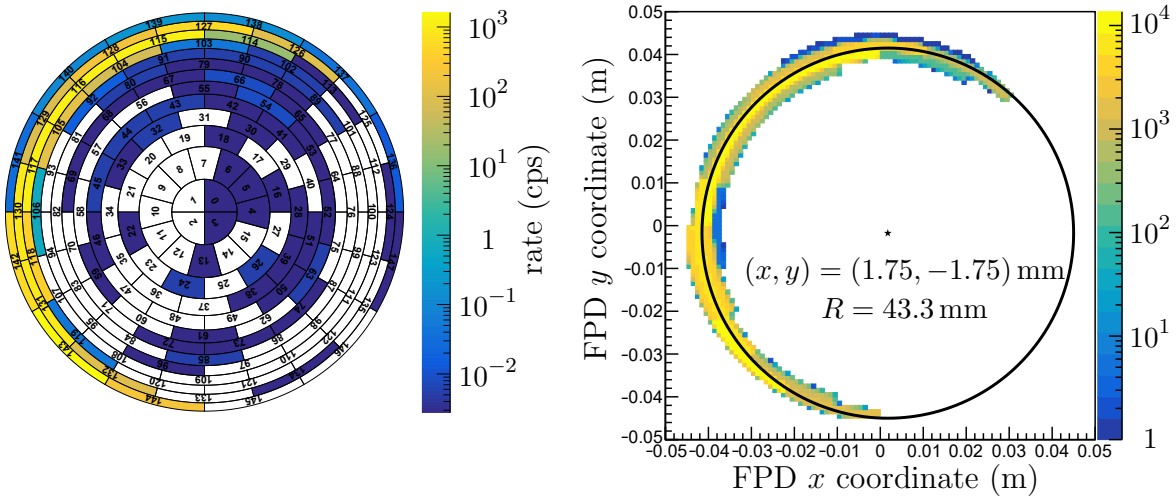

Figure 5.25.: **PULCINELLA shadow on FPD**. Run number 40495, compare tab. 5.8. The left side shows the pixel mapping of the shadow, the colour scale denotes the measured rate (cps). The right side shows the fit ring representing the PULCINELLA position. Note the pixel weighting of the electron hits.

The fit ring can then be used to track electrons from the FPD to the PULCINELLA disk in order to get the image of the ring on PULCINELLA[5]. The fit PULCINELLA radius is 2.6 mm larger than the nominal 110.5 mm PULCINELLA radius. This is expected since the origin of the electrons is the ring fit onto the FPD; this ring is larger than the mapped PULCINELLA radius due to pixels being half-shadowed. From the position of the ring on PULCINELLA, the relative shift of PULCINELLA in KATRIN global coordinates can be obtained, see tab. 5.9.

Determining the WGTS cross-section seen by PULCINELLA The cross-section of the WGTS seen by PULCINELLA can be determined by tracking simulations of electrons from PULCINELLA to the center of the WGTS. In the simulation, 30×10^3 electrons were created uniformly distributed across the PULCINELLA surface and then tracked towards the WGTS (see fig. 5.26). Binning the final azimuthal position in the WGTS enables numerical determination of the cross-section. A grid of 48×48 bins for the $0.045 \times 0.045\,\mathrm{m}^2$ area of interest yields an area per bin of $3.516\,\mathrm{mm}^2$. The effective cross-section of the WGTS seen by PULCINELLA is then determined by multiplying the number of bins, 1482, with non-zero entries with the area per

[5]This was done using a disk with a larger diameter than PULCINELLA in order to ensure that the electrons are terminated correctly.

Table 5.9.: **PULCINELLA position determination.**

position	KATRIN coordinates (mm)	FPD coordinates (mm)
origin FPD	$(-0.96, 3.29)$	$(0, 0)$
origin PULCINELLA	$(1.40, 8.55)$	–
ring FPD	$(0.79, 1.54)$	$(1.75, -1.75)$
ring PULCINELLA	$(5.89, 4.05)$	–
shift of PULCINELLA	$(4.50, -4.50)$	–

bin:

$$A_{\mathrm{WGTS}} = 1482 \cdot 3.516\,\mathrm{mm}^2 = 52.1\,\mathrm{cm}^2 \tag{5.29}$$

A visualisation of the effective cross-section of the WGTS is shown in fig. 5.26 on the right side. Note the cut-out there due to the shadow of the FBM board, caused by the monitoring position of the FBM.

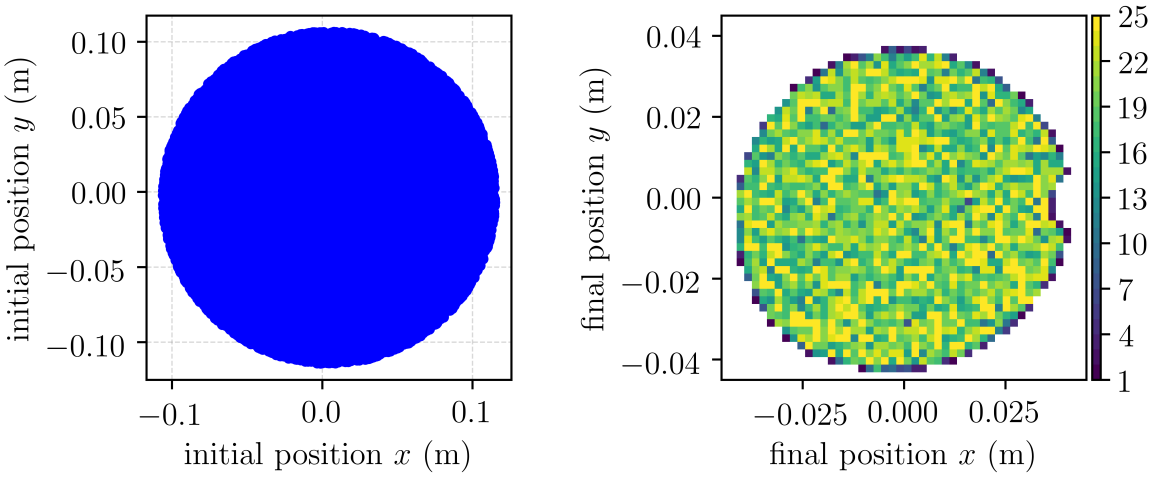

Figure 5.26.: **PULCINELLA to WGTS mapping**. Left side shows the 30×10^3 simulated electrons created on the PULCINELLA surface. Right side shows those electrons reaching the centre of the WGTS, the colour scale denotes the number of entries. Bin size is $3.516\,\mathrm{mm}^2$. Note the cut-out due to the FBM shadow.

The systematic uncertainty of the determination of the effective cross-section of the WGTS is conservatively estimated to 5 %, which includes uncertainty due to wrongly accounted misalignments and an uncertainty on the determination of the area itself.

5.4.2.3. PULCINELLA rate prediction

The rate prediction for PULCINELLA is less complicated than for the FBM because PULCINELLA does not have an intrinsic energy resolution. This leaves us with

$$\dot{N}_{\text{theo}}\Big|_{E\geq E_{\text{th}}} = \int_{E_{\text{th}}}^{\infty} \sum_{fs} P_{fs} \cdot \frac{\mathrm{d}\Gamma(\epsilon)}{\mathrm{d}E}\Big|_{fs} \mathrm{d}E. \tag{5.30}$$

This time the threshold energy is given by the highest blocking potential between WGTS and PULCINELLA, which is the high voltage at the pre-spectrometer (PS): the inner electrode of the PS was set to $E_{\text{th}} = -500\,\text{V}$. This gives

$$\dot{N}_{\text{theo}}\Big|_{E\geq E_{\text{th}}} = 1.66 \times 10^{-9}\,\text{cps}. \tag{5.31}$$

Besides the "threshold", the detection efficiency also needs to be taken into account. GEANT4 simulations by E. Förstner [FG18] showed a backscattering probability for electrons from the disk of 2.06 % for zero-degree incident electrons, with PULCINELLA at 0 V and including the magnetic mirror effect. During the measurements discussed in this section, the PULCINELLA disk was at 200 V positive potential, thereby increasing the detection efficiency for electrons. The detection efficiency at 200 V is estimated by fitting a straight line to the simulated $\epsilon_{\text{det}}(U) = 1 - P_{\text{backscatter}}(U)$ by E. Förstner, see fig. 5.28:

$$\epsilon_{\text{det}}(200\,\text{V}) = 0.9795. \tag{5.32}$$

The systematic uncertainty related to the detection efficiency is estimated to be 5 %. This is a rather conservative value, which accounts for the simulations of E. Förstner being done only for zero incident angle; the magnetic mirror effects for electrons with larger impinging angle is even larger than for zero incident angle.

5.4.2.4. PULCINELLA rate estimation

The PULCINELLA disk acts as a Faraday cup: it measures a continuous current of electrons with a pico-amperemeter. The measured current can be translated into an electron rate via

$$\dot{N}_{\text{PULCINELLA}}\Big|_{E\geq E_{\text{th}}} = -\frac{I}{e}. \tag{5.33}$$

During the First Tritium campaign, there was one 1 min signal (40498) and one 10 min background (40500) run with PULCINELLA at stable column density (compare tab. 5.8). The corresponding currents are shown in fig. 5.27. Fit results of a constant as well as the corresponding uncertainty are shown in tab. 5.10, along with the converted electron rate $\dot{N}$.

Note that the positive background current leads to a negative electron rate. Since the background run showed a positive current, its deduction leads to a more negative signal current resulting in the measured electron rate

$$\dot{N}_{\text{PULCINELLA}}\Big|_{E\geq E_{\text{th}}} = 8.13 \times 10^{7}\,\text{cps}. \tag{5.34}$$

Besides the statistical uncertainty of the measured rate listed in tab. 5.10, the systematic uncertainty on the measured rate is 3 %, as shown by Amsbaugh et al. [Ams+15].

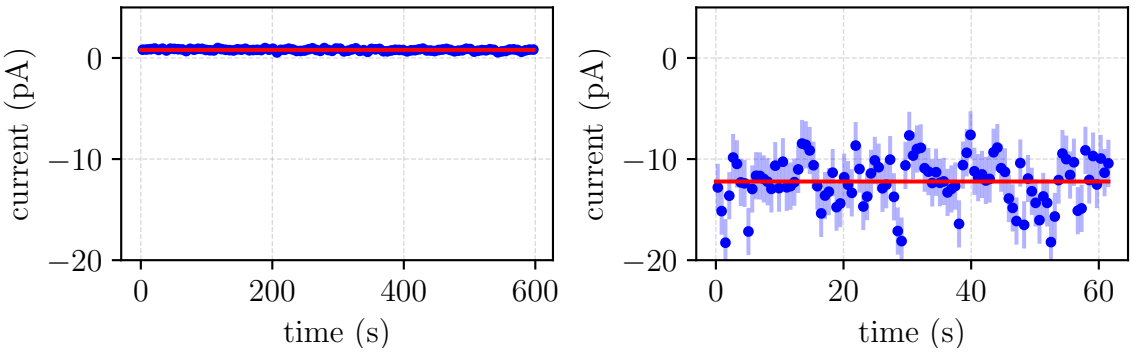

Figure 5.27.: **PULCINELLA measured current**. Left: FPD run 40500 (5^{th} June 2018), PULCINELLA background. Right: FPD run 40498 (5^{th} June 2018), PULCINELLA signal.

Table 5.10.: **PULCINELLA fit current and electron rate.**

quantity	fit value	fit error
I_{tot} (pA)	-12.22	0.23
$\dot{N}_{\text{tot}}$ (cps)	7.63×10^7	0.14×10^7
I_{bg} (pA)	0.80	0.01
$\dot{N}_{\text{bg}}$ (cps)	-0.50×10^7	0.01×10^7
I_{sig} (pA)	-13.02	0.23
$\dot{N}_{\text{sig}}$ (cps)	8.13×10^7	0.14×10^7

5.4.2.5. Uncertainty estimation

An overview of the estimated uncertainties of the factors of eq. (5.27) is given in tab. 5.11. Note that the systematic uncertainties are given in relative percentage values. The uncertainty on the column density is estimated via ensemble testing. Each item of tab. 5.11 is sampled from a Gaussian distribution centred at the estimated value with σ being the estimated uncertainty. Some of the distributions have lower and upper limits, for example the detection efficiency cannot be larger than 1. The distribution of the detection efficiency is shown as an example in fig. 5.28.

Using 10^5 samples from the distributions of the factors of eq. (5.27), the distribution of the estimated column density can be determined with a precision of 0.3 %. From the statistical and systematic distribution of the column density, the statistical and systematic uncertainties are determined as the ±34 % interval around the estimated value. The resulting statistical and systematic distributions of the column density are shown in fig. 5.29 and listed in tab. 5.11.

5.4.2.6. Column density

Combining the estimates of the factors as listed in tab. 5.11 and discussed in this section results in an estimate of the column density from the measured PULCINELLA

Table 5.11.: **PULCINELLA column density uncertainty.** Note that the systematic uncertainties are given in relative values. Magnetic fields are stable to the 10^{-5} level, therefore their statistical uncertainty is neglected.

quantity	estimate	stat. unc.	sys. unc.
measured rate $\dot{N}_{\text{PULCINELLA}}\big\vert_{E\geq E_{\text{th}}}$	8.13×10^7 cps	0.14×10^7 cps	3 %
DT concentration c_{DT}	1.07 %	–	14 %
B_{WGTS}	2.5 T	–	1 %
B_{PCH}	4.2 T	–	1 %
eff. WGTS cross-section A_{WGTS}	52.1 cm^2	–	5 %
detection efficiency ϵ_{det}	0.9795	–	5 %
column density $\mathcal{N}$ ($10^{21}\,\text{m}^{-2}$)	4.92	$^{+0.09}_{-0.09}$	$^{+0.78}_{-0.79}$

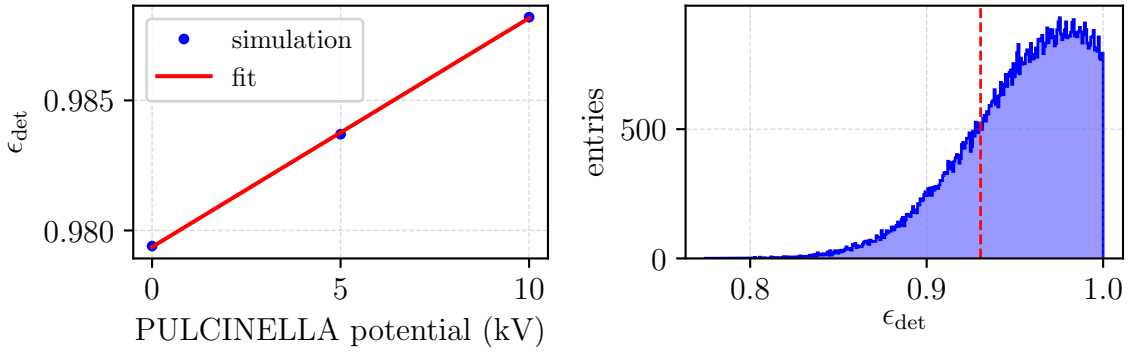

Figure 5.28.: **PULCINELLA detection efficiency.** Left: A straight line is fit to the simulation by E. Förstner [FG18]. Right: Possible detection efficiency distribution. Note the upper limit of 1. The dotted red line denotes the 1σ lower systematic uncertainty. 10^5 samples were diced.

current of (estimate ± stat. ± sys.)

$$\mathcal{N}_{\text{PULCINELLA}} = \left(4.92\ ^{+0.09}_{-0.09}\ ^{+0.78}_{-0.79}\right) \times 10^{21}\,\text{m}^2. \tag{5.35}$$

Compared to the expected value from gas dynamic simulations of $4.46 \times 10^{21}\,\text{m}^{-2}$, this is a deviation of 9 % which is in agreement within the estimated uncertainty of the PULCINELLA determination.

5.4.3. Discussion

Three different methods have been presented in this chapter to estimate the column density from the data. One is fitting the column density as an additional fit parameter, another one is using the FBM detector, and the last one is using the PULCINELLA disk in front of the FPD. The best agreement with the simulated column density can be found for one single run fit (e.g. 40667) and for fitting multiple runs together (appended runs). Good agreement is also given between simulation

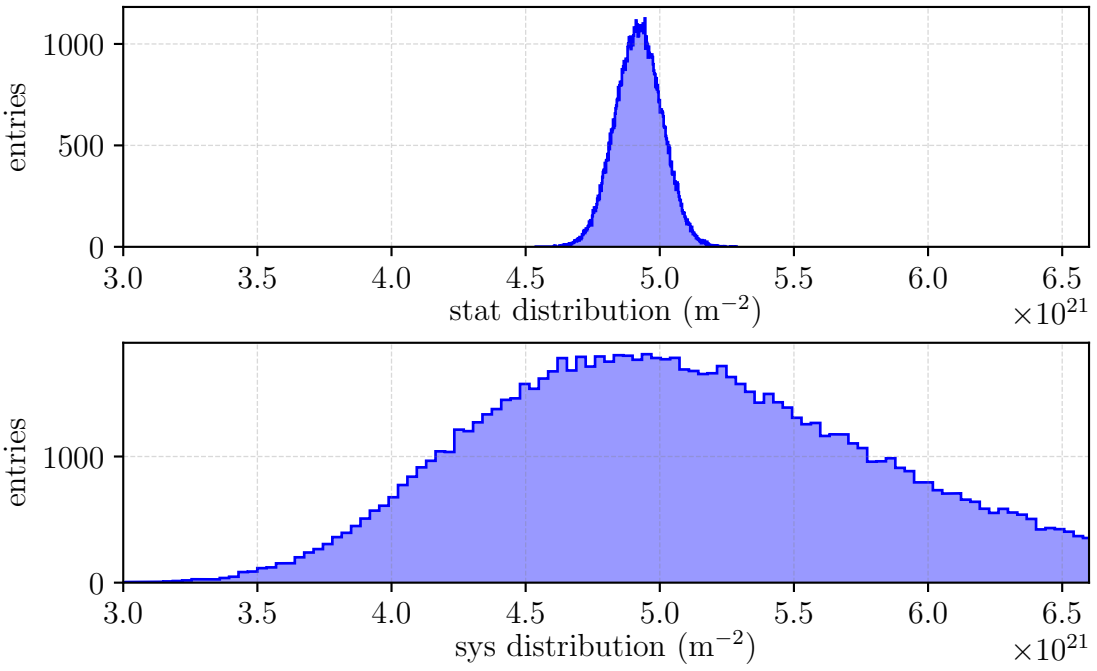

Figure 5.29.: **PULCINELLA determined column density uncertainty.** The upper panel shows the statistical distribution, while the lower one shows the systematic distribution. 10^5 samples were diced.

and measurement by the PULCINELLA disk, as well as the FBM estimate. Furthermore, the previous chapter includes an estimation of the inlet pressure by the measured pressure at the krypton capillary, see sec. 4.4.8. Calculating the column density corresponding to the estimated inlet pressure of 0.3115 µbar yields a column density of $4.65 \times 10^{21}\,\mathrm{m}^{-2}$ from the pressure at the krypton capillary, which is in good agreement with the simulated column density.

An overview of the discussed column density estimates is given in fig. 5.30. It can be seen that all estimates agree within their uncertainties. However, the simulated column density seems to be underestimated as most other estimates result in larger values. In order to match the measured and the simulated column density estimation, the input parameters of the simulation might be varied inside their uncertainties estimated in sec. 4.4.7. Using input parameters $\alpha = 1$ (instead of $\alpha = 0.97$), and an outlet to inlet pressure ratio of 0.05 (instead of 0.02) results in perfect agreement between the Boltzmann based simulation and the values determined by the different measurements, with a column density value of $4.6 \times 10^{21}\,\mathrm{m}^{-2}$ (see the dotted black line in fig. 5.30). With the Knudsen based simulation and an outlet to inlet pressure of 0.05, the same column density is estimated $(4.6 \times 10^{21}\,\mathrm{m}^{-2})$[6]. These are strong hints that the input parameters $\alpha = 1$ and $p_{\mathrm{out}}/p_{\mathrm{in}} = 0.05$ describe the D_2 dominated gas dynamics better than $\alpha = 0.97$ and $p_{\mathrm{out}}/p_{\mathrm{in}} = 0.02$. However, no decisive conclusion can be drawn as the uncertainties of all measurements are larger than the ones of the simulation. Column density estimates via fitting the spectrum currently only include the 2 % uncertainty on the inelastic scattering cross-section [Ase+00]. As mentioned before, the re-analysed LARA data results in a factor three decreased

[6]Note that the Knudsen flow has no accommodation coefficient parameter α.

uncertainty [KZ18] on the deuterium concentration, which will reduce the FBM and PULCINELLA column density uncertainty by a similar factor. This holds especially for the PULCINELLA determination, as here the LARA related systematic uncertainty of the DT concentration is the largest contribution to the overall PULCINELLA uncertainty. The final answer on the column density will be given by the e-gun of the RS, which is currently in its commissioning phase and will set the reference measurement of the column density at an accuracy of 0.1 % [Kuc+18].

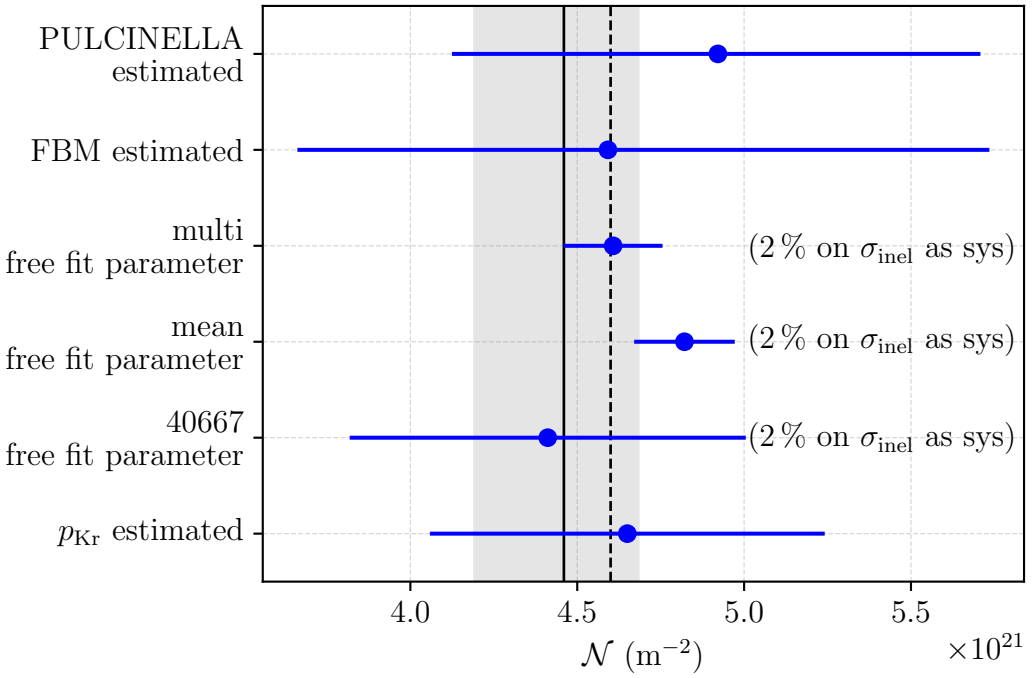

Figure 5.30.: **Overview of column density estimates.** The black line with grey shaded area marks the estimation from initial gas dynamics simulations, the dotted black one is for adapted input parameters. Note that the treatment of $\mathcal{N}$ as free fit parameter considers only the 2 % uncertainty on the inelastic scattering cross section [Ase+00] as systematic uncertainty.

5.5. Conclusion

In this chapter, results from the first injection of tritium into the WGTS were presented. The stability of the source related components was shown to exceed the respective requirements, with one exception: the stability of the tritium concentration. The out-of-specification trace amounts of tritium were a factor 200 below the concentration that will be used for neutrino mass measurements. It was shown that the LARA-determined stability of the dominant gas species (D_2) is within its requirements which is promising for neutrino mass data taking when T_2 will be the dominant gas species.

First comparisons between the spectral model and the data showed excellent agreement, enabling the testing of different analysis techniques to extract the parameters

of interest $E_{0,\mathrm{eff}}$, Amp, and Bg. Estimates of the effective endpoint $E_{0,\mathrm{eff}}$ were presented including the systematics due to the column density uncertainty, amongst these treating the column density as nuisance parameter via a pull term, as a free fit parameter, or using ensemble testing of the column density. All estimates of $E_{0,\mathrm{eff}}$ are within the assumed spread of $E_{0,\mathrm{eff}}$ due to the unknown work function difference.

In order to test the column density simulations from sec. 4.4, estimations of the column density via the additional detectors FBM and PULCINELLA were given. The free spectrum parameter estimate, the FBM estimate, the PULCINELLA estimate, the krypton capillary estimate, and the simulation estimate of the column density were found to agree within their respective uncertainties. From comparisons of the simulated column density estimate and the one obtained from various other methods, it seems as if the best agreement is found for an accommodation coefficient $\alpha = 1$ and an outlet to inlet pressure ratio of $p_{\mathrm{out}}/p_{\mathrm{in}} = 0.05$, resulting in a column density of $\mathcal{N} = 4.6 \times 10^{21}\,\mathrm{m}^{-2}$ for Boltzmann and Knudsen based flow. With the tritium purity increased by a factor of 200 for the neutrino mass data taking, the LARA determined ϵ_{T} will have an accuracy on the order of 1 %. With all other uncertainties reduced, this will enable a PULCINELLA-based estimation of the column density with uncertainty also on the percent level. In order to further decrease uncertainties on the column density determination, a cross-check between e-gun, FBM, and PULCINELLA measurements with active source gas is recommended.

Dedicated measurements with the RS e-gun to determine the column density and to test the gas dynamics model of the source are an integral part of the STS-IIIa measurement programme (autumn 2018). As the KATRIN experiment was shown to be stable well within its requirements, the start of neutrino mass data taking with increased tritium concentration is planned for spring 2019 after a maintenance break, with final hardware works, during the winter 2018/19.

CHAPTER 6

BLIND ANALYSIS AND METHODS

"It is also desirable to emphasize the importance of the human equation in accurate measurements such as these. It is easier than is generally realized to unconsciously work toward a certain value."
– Frank Dunnington, 1933 –

The goal of the KATRIN experiment is to determine the (effective) neutrino mass by analysis of the tritium β-decay spectrum. In order to reduce the influence of human observer's bias, a blind analysis can be performed. In this chapter, several methods for blind neutrino mass analysis of KATRIN-data will be presented and their effect will be tested on simulated data as well as ^{83m}Kr-data and T-data from the First Tritium campaign of the KATRIN experiment.

6.1. Motivation

The requirement to apply blind analysis techniques arises from the observer's bias: in general, data analysts have expectations of what the result should be, which may cause them to unconsciously work toward that expected value. One way to prevent this observer's bias is by performing a blind analysis of the data. This blinding requires obscuring of some part of the physics results until such a time that they cannot influence subsequent analysis steps. In KATRIN, our observable of interest is the neutrino mass squared m_ν^2 which we obtain by comparing a measured integrated tritium β-spectrum to a model prediction. In order to worsen the neutrino mass sensitivity and thereby hide the observable of interest, two blinding paths can be followed: either we hide some physics details of our model, resulting in model blinding, or we artificially modify the analysed data set, in a well-controlled and strictly-reversible way, resulting in data blinding. This chapter will present and discuss adequate methods for a blind analysis of KATRIN data.

6.1.1. Observer's bias

One of the most famous examples of an observer's bias is the story of Clever Hans [Pfu07]. In 1904, Wilhelm von Osten claimed that Hans could perform arith-

metic and other intellectual tasks such as adding numbers. The issue was that Hans was a horse. Wilhelm von Osten – a retired teacher confident in his methods – argued that he taught Hans to answer his questions by tapping his hoof. No tricks could be found at first and after this miracle of a horse received worldwide attention [Hey04, The04], the founder and director of the Psychological Institute of Berlin, Prof. Dr. Carl Stumpf, was officially asked to investigate the Clever Hans phenomenon. Together with his student, Oskar Stumpf, they could prove that Clever Hans was not able to perform arithmetic operations but was indeed very clever: Hans could only answer those questions where the questioner knew the result and where Hans could see the questioner's face although it did not matter who asked the questions [Pfu07]. This lead to the conclusion that Hans could detect tiny changes in the facial expression of the questioner and stopped tapping as soon as the number of hoof taps reached the correct number. This Clever Hans effect was not only a major breakthrough in psychology but also shows a clear observer's bias: Hans answered the questions such that the result matched the expectation of the questioner.

But it is not only this kind of observer's bias that threatens accurate results: as shown by Klein and Roodman from speed of light measurements published over an entire century [KR05], researchers are rather conservative about their estimated results if they disagree with previous measurements of that quantity. Even though they used different techniques, four experiments in a row stated a value that was $17\,\mathrm{km\,s^{-1}}$ off previous and following experiments. The reason for this may have been that the experiments compared their estimated value to the most recent published. If their value was off, they would search for a source causing such systematic shift until their value matched the previous result. This is only one example for scientists stopping to search for systematic uncertainties when their result matches a certain outcome.

The systematic uncertainty caused by the observer's bias cannot be estimated when publishing the results, but only in a historic view, as shown by Klein and Roodman [KR05]. This is a fundamental difference between observer's bias and any other kind of bias in a measurement, requiring a kind of analysis that prohibits the observer's bias. In the following, this kind of analysis is called *blind analysis*, because the analyst does not know the final answer or initial trend (the neutrino mass m_ν) of his experiment before the analysis is complete.

6.1.2. Goal of blind analysis in KATRIN

As concluded in sec. 6.1.1, the general goal of blind analysis is to avoid biases in data analysis. With this kind of analysis technique, the data is analysed in a way that the final answer remains unknown before the analysis is complete, preventing the analyst from tuning intermediate results and cuts to arrive at the expected answer. On the other hand with the decision to perform a blind analysis, there is the commitment beforehand to publish the result when unblinding, barring all consequences. One of the first to apply blind analysis techniques in physics was F. Dunnington in his measurement of e/m [Dun33]. His estimation of e/m was directly proportional to the angle between electron source and detector. Therefore Dunnington had his machinist select angles close to but not exactly at the optimal value and keeping these angles secret. This hiding of the angles made Dunnington blind to the final

answer and therefore unable to tune his analysis towards an expected value. Only after Dunnington finished his analysis, he had his machinist reveal the angles used, enabling Dunnington to calculate the final answer. The example of Dunnington cannot be easily translated to KATRIN, since the measuring concepts are fundamentally different with the neutrino mass manifesting as a shape distortion close to the endpoint of the β-decay spectrum.

In general, however, performing a blind analysis does not mean

- that you never look at the data,
- that you are not allowed to correct for a mistake once you find one,
- that your analysis is inevitably correct, or
- that a non-blind analysis is necessarily wrong.

In KATRIN, the main physics goal is to extract the value or limit on the neutrino mass. Though there will be other types of analyses such as searches for sterile neutrinos, right handed currents, light bosons, or relic neutrinos, all of which require different blinding techniques, focus will be on developing blind analysis techniques for neutrino mass analysis in the following. This implies hiding the value or limit on the neutrino mass from the analyst. The most stringent limit on the neutrino mass is currently the limit obtained from the analysis of Mainz and Troitsk data [Tan+18]:

$$m_\nu \leq 2.0\,\mathrm{eV}. \tag{6.1}$$

In order to be conservative and to circumvent problems like those in the speed of light measurements mentioned in sec. 6.1.1, the requirement for each blinding technique for KATRIN neutrino mass analysis is defined to prevent intermediate neutrino mass sensitivities any better than

$$m_\nu \leq 2.0\,\mathrm{eV}\,(90\,\%\ \mathrm{C.L.})\ \text{before unblinding}, \tag{6.2}$$

(that is, any better than what is already established empirical knowledge). Unblinding will then yield the full sensitivity.

6.2. Sensitivity definition and derivation

KATRIN will measure an integrated tritium β-decay spectrum [KAT05]. In the standard KATRIN neutrino mass analysis, the spectrum will be compared to a model containing four variable fit parameters [KAT05, Kle14]:

1. (effective) neutrino mass squared m_ν^2,
2. endpoint E_0,
3. signal amplitude Amp,
4. background rate Bg.

First a definition of the sensitivity for the neutrino mass needs to be derived to be able to compare the different blinding methods. The sensitivity will be defined in terms of discovery potential, expressed in terms of standard deviations, and the corresponding total uncertainty. Then the methodology on how to derive the necessary level of blinding to prevent sensitivities better than eq. (6.2) will be defined.

6.2.1. Sensitivity as discovery potential

In the KATRIN Design Report [KAT05], the sensitivity for the neutrino mass is seen as the neutrino mass which can be determined at a significance of 1.645σ. Assuming normal distribution of the best fit estimate $\hat{m}^2_\nu$, this translates into a 90 % C.L. upper limit. In other words, the sensitivity is the discovery potential representing a 1.645σ distance of the best fit estimate $\hat{m}^2_\nu$ to the null-hypothesis 0:

$$\text{discovery potential} = \frac{\hat{m}^2_\nu - 0}{\sigma_{m^2_{\nu\,\text{tot}}}} \tag{6.3}$$

requiring the sensitivity to fulfil the following relation:

$$1.645 = \frac{\hat{m}^2_\nu - 0}{\sigma_{m^2_{\nu\,\text{tot}}}}. \tag{6.4}$$

6.2.2. Adaption of the total neutrino mass uncertainty

In the KATRIN Design Report [KAT05], the total uncertainty $\sigma_{m^2_{\nu\,\text{tot}}}$ is composed of the uncorrelated statistical ($\sigma_{m^2_{\nu\,\text{stat}}}$) and systematic ($\sigma_{m^2_{\nu\,\text{sys}}}$) uncertainties:

$$\sigma^{\text{DR}}_{m^2_{\nu\,\text{tot}}} = \sqrt{{\sigma_{m^2_{\nu\,\text{stat}}}}^2 + {\sigma_{m^2_{\nu\,\text{sys}}}}^2}. \tag{6.5}$$

The different blinding methods are expected to result in two different effects on the estimated neutrino mass squared: either in an increased statistical uncertainty $\sigma_{m^2_{\nu\,\text{stat}}}$ or in a systematic shift $\delta_{m^2_\nu}$ of the estimated neutrino mass squared $\hat{m}^2_\nu$ with respect to the true neutrino mass squared $m^2_{\nu\,\text{true}}$:

$$\delta_{m^2_\nu} = \hat{m}^2_\nu - m^2_{\nu\,\text{true}}. \tag{6.6}$$

In order to be able to compare the different blinding methods, one common definition of the total uncertainty is needed. For this work it was decided to adapt eq. (6.5) to include the systematic neutrino mass shift into the sensitivity calculations as follows:

$$\sigma_{m^2_{\nu\,\text{tot}}} = \sqrt{{\sigma_{m^2_{\nu\,\text{stat}}}}^2 + {\sigma_{m^2_{\nu\,\text{sys}}}}^2 + {\delta_{m^2_\nu}}^2}. \tag{6.7}$$

This implementation treats the introduced neutrino mass shift as new, unknown systematic uncertainty uncorrelated to all others.

6.2.3. Methodology to derive the necessary level of blinding

Using eq. (6.2), eq. (6.4), and eq. (6.7), the methodology to derive the necessary level of blinding can be described:

1. for the blinding parameters of each blinding method (smearing values, measuring times, window widths, et cetera), calculate the total uncertainty $\sigma_{m^2_{\nu\,\text{tot}}}$ from eq. (6.7) for various true neutrino masses,

2. use this to find the intersection points between the 1.645σ discovery potential (6.4) and the lines for the various blinding parameters: the abscissa of these intersection points is the sensitivity,
3. plot the sensitivity against the various blinding parameters to obtain the blinding parameter required to not exceed a certain sensitivity limit,
   e.g. 2 eV (90 % C.L.) for the first KATRIN neutrino mass analysis.

6.3. Blind analysis methods

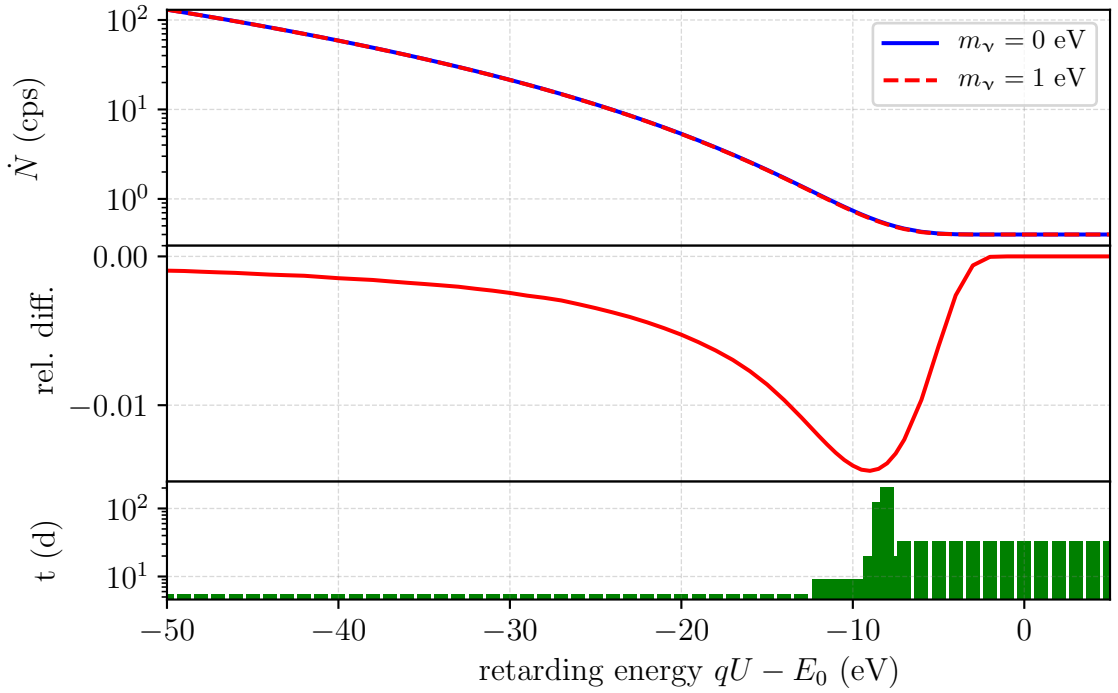

Figure 6.1.: **Integrated spectrum with MTD.** The neutrino mass sensitive region is shown by comparing a spectrum with neutrino mass $m_\nu = 1$ eV (red) to a spectrum without neutrino mass $m_\nu = 0$ eV (blue). The peak of the measuring time distribution (MTD) sits in the region where the neutrino mass has the largest distortion relative to the zero mass spectrum.

In order to establish useful blinding and unblinding strategies, the effect and signature of a non-zero neutrino mass in the tritium spectrum needs to be understood. Figure 6.1 shows the effect of two different neutrino masses: a non-zero neutrino mass results in a shape distortion of the β-spectrum close to the endpoint, with position and relative strength of the distortion depending on the neutrino mass. Since the neutrino mass in KATRIN is determined via a four-parameter (see sec. 6.2) fit to the measured data, blinding can be performed in two ways: either blind the fit model (*model blinding*) or blind the measured data (*data blinding*). From fig. 6.1, an obvious way to hide the neutrino mass signature is to decrease the significance of a hypothetical signal by increasing the statistical uncertainty (*reduced statistics*). This implies, for example, using only one run (scan) of the tritium β-spectrum at a time, that is, at typically only a few hours. It has to be noted that all runs can be analysed and inspected individually, just not combined. Another possibility would

be to apply a blinding method mostly used in rare-decay searches, such as $0\nu\beta\beta$-decays (e.g. GERDA blind analysis [Ago+13]): the region where a potential signal is expected to show up remains hidden from the analysts. Only after the complete analysis chain is developed and fixed, the signal region is opened. Applying this method to the KATRIN neutrino mass analysis (*window blinding*) may require hiding a broad energy window from the analysts: fig. 6.1 shows that a 2 eV neutrino mass, for example, would require a window width of about 20 eV, in the range of $[E_0 - 20\,\text{eV},\ E_0]$ to successfully hide the signal of the neutrino mass, which will be shown in sec. 6.4.1.2. Another method discussed in the following is an artificial smearing of the neutrino mass signal by convolving the β-spectrum with a Gaussian. This may be performed in different ways: either in terms of data blinding acting directly on the measured spectrum (*energy smearing*) or in terms of model blinding, either smearing the distribution of the modelled final states (*FSD smearing*) or smearing the energy loss function of the electrons (*energy loss smearing*). All of these blinding methods will be described in more detail and results from their test on commissioning measurements will be presented.

6.3.1. Data blinding

The most powerful way to perform a blind analysis is blinding the data. This gives maximum control over which data is released and which not: if the neutrino mass is hidden by blinded data, the analysts can not get access to the original data for neutrino mass analysis development and thereby can not tune any cut towards expected neutrino masses. However, data blinding introduces the risk that the original data contains unexpected features as reported by Lobashev et al. [Lob+99a].

In the following, three different methods leading to blinded data sets will be presented. For each of the methods, ensemble tests were performed on simulated data in order to inspect the effect of the blinding method on the parameter of interest, the neutrino mass. The settings for these simulations can be found in tab. C.2. Most important is to note that a larger magnetic field in the analysing plane together with an increased background (225 mcps, a factor of 23 higher compared to the design reference background level of 10 mcps [KAT05]). These settings were assumed, since all measurements with the KATRIN set-up so far showed an increased and volume dependent background rate [Har15, Blo18, Tro18]. A total of 10^4 fits were performed per setting for each blinding method.

6.3.1.1. Reduced statistics

In the starting phase of the initial neutrino-mass runs, the neutrino mass sensitivity of KATRIN will be driven by the statistical uncertainty. Due to the unprecedented activity of the KATRIN tritium source, the statistical uncertainty will decrease fast: In this section it is investigated by ensemble testing how many hours of measuring time can be allowed to be analysed in order to not exceed the 2 eV sensitivity. The outcome will not only be useful to determine the maximum length of one spectral scan at KATRIN, but also for determining the time intervals in which unblinded KATRIN data will be released.

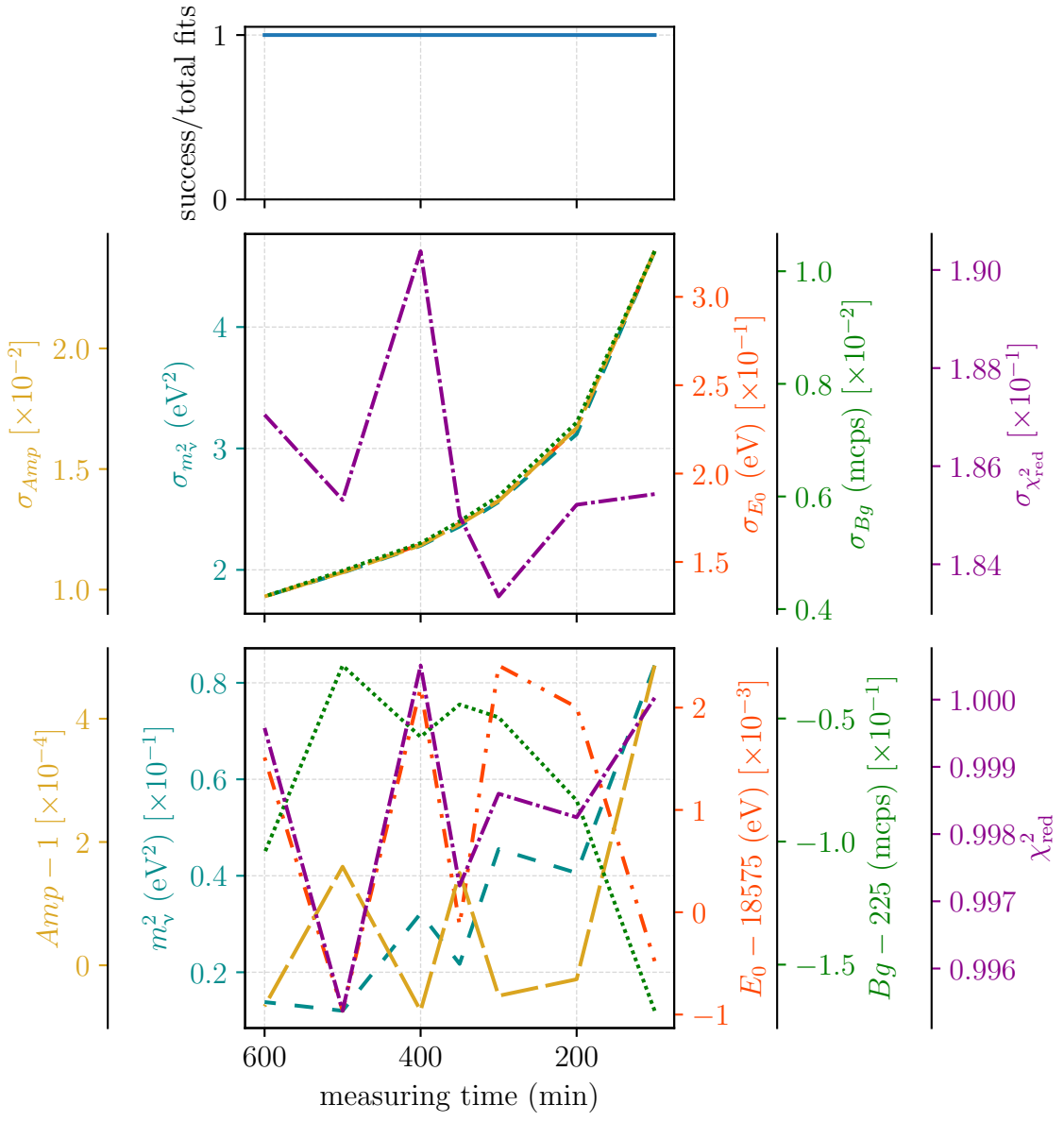

Figure 6.2.: **Measuring time dependence of fit parameters**. Plots share the x-axis. All fits were successful (upper plot). A clear dependence of the standard deviation of the best fit values (middle plot) on the measuring time can be seen. There is no clear dependence of the best fit mean values (lower plot) on the measuring time.

First it is tested whether the reduced statistics method causes other effects besides increasing the statistical uncertainty on the neutrino mass. Such effects may be a systematic shift of one of the four standard fit parameters, a substantial increase of the χ^2 or a decrease in number of successful fits. A good indicator to investigate these effects is the live time dependent distribution of the best fit estimates for a

true value $m^2_{\nu_{\text{true}}} = 0$, which is shown in fig. 6.2. The middle plot clearly shows an increase of the standard deviation of all best fit estimates, while the lower plot has no such clear structure. Therefore, it can be deduced that limiting the statistics does not imply a systematic shift on the best fit estimates, and does not cause fewer successful fits (upper plot) or an increase in χ^2. It can be concluded that the reduced statistics method is a promising candidate in terms of blinding by increased statistical uncertainty. However, the allowed measuring time for this blinding method is short compared to the overall three-year measuring time of KATRIN.

6.3.1.2. Window blinding

The signal in direct neutrino mass searches with tritium β-decay experiments is most pronounced in the region close to the endpoint, as shown in fig. 6.1. Compared to 0νββ-decay or dark matter experiments, neutrino mass analysis in KATRIN goes beyond counting events in a specific signal region: the neutrino mass mainly manifests in a shape distortion of the integrated spectrum, causing blinding to be challenging. Blinding by removing data from some energy region will not make the neutrino mass analysis with blinded data impossible but it is expected to increase the statistical uncertainty as desired. A sketch of the removal of data from a specific energy

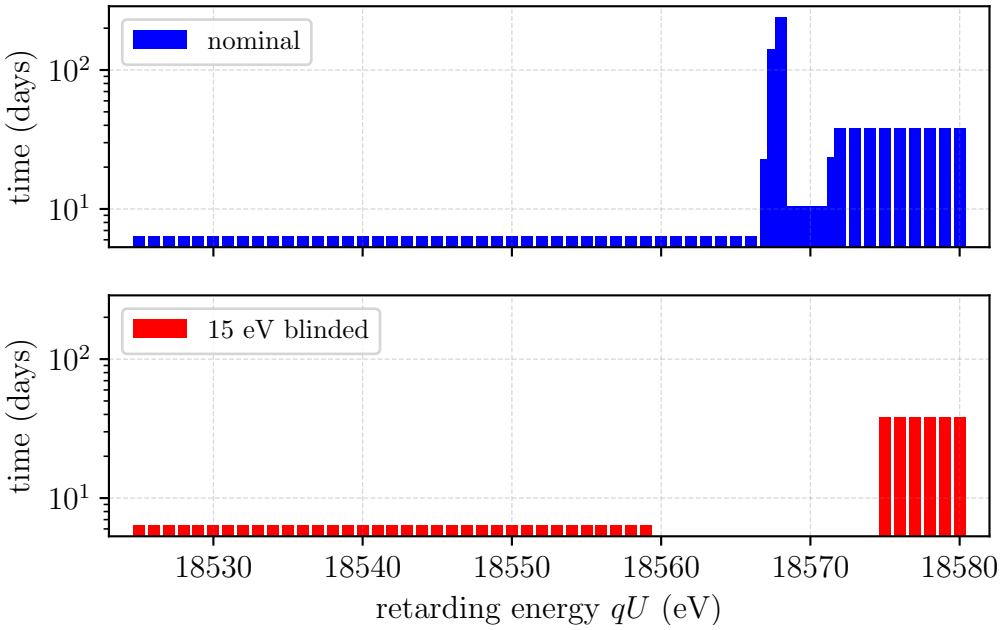

Figure 6.3.: **Window example**. The upper plot shows the unblinded measuring time distribution, the lower illustrates a 15 eV blinded window, from which the data is completely removed for neutrino mass purposes.

window for neutrino mass analysis is shown in fig. 6.3, for an example window size of 15 eV. For convenience, the upper end of the blinding window is kept fixed at the estimated endpoint of 18 575 eV equivalent. The lower end is extended into the spectrum towards lower energies. Other versions of this blinding method have also been investigated, but were discarded after detailed studies. The discarded methods will be described here for completeness:

- **Removing the background region**: this blinding method would be based on the blinding of data at energies beyond the endpoint. The idea was that this removal would increase the uncertainty on the background such that the neutrino mass is hidden. However, tests with Design Report settings [KAT05] showed that even removing all data beyond the endpoint only results in a deterioration of the neutrino mass sensitivity from 0.2 eV (90 % C.L.) to 0.35 eV (90 % C.L.). This would not be sufficient to hide a 2 eV neutrino mass.
- **Removing endpoint and high statistics region**: here the idea is that a two-window removal approach successfully blinds the neutrino mass. Indeed, studies with Design Report settings [KAT05] showed a (sufficiently) degraded neutrino mass sensitivity. For a removal of $[E_0 - 30\,\text{eV}, E_0 - 23\,\text{eV}] \wedge [E_0 - 19\,\text{eV}, E_0]$, the sensitivity on the neutrino mass is decreased to 2.12 eV (90 % C.L.). However, the data from the high statistics region is precious in terms of monitoring the stability of the source or testing the fit routines. Since it also does not yield a better blinding result than blinding only one window[1], this method is not considered for further studies.
- **Removing only parts of the window**: this version of the window blinding has the same principle as shown in fig. 6.3, with one difference. Here, not all of the data is removed but a small amount, e.g. 0.1 % or 1 %, is kept in the blinded window region. However keeping only 0.1 % of the data in this region is enough for the fitter to estimate the neutrino mass with a sensitivity better than allowed: for Design Report settings [KAT05], keeping 0.1% of a window of 21 eV width below the endpoint results in a sensitivity of 0.69 eV (90 % C.L.). Keeping 1 % of the same window, the sensitivity is 0.40 eV, compared to 2.09 eV if the data of that window is completely removed. Therefore, window blinding while keeping some percentage of the data is regarded inferior to completely removing the data.

Since none of the itemised versions of the window blinding is superior to the window blinding described in the beginning of this section (complete removal, blinding the endpoint region), they are not pursued as candidates for KATRIN blind analysis methods.

To test the effect of increasing the window width on the best fit estimates of the four fit parameters, the same procedure as in sec. 6.3.1.1 is followed. The distribution of the four fit parameters after performing 10^4 fits for $m^2_{\nu_{\text{true}}} = 0$ per chosen window width can be seen from fig. 6.4. As for the reduced statistics method, all fits were successful and the expected effect on the parameter uncertainty can be seen: the most prominent uncertainty increasing with extended window width is the neutrino mass uncertainty. The standard deviation of the neutrino mass squared increases by more than one order of magnitude, while the relative increase in the other parameters uncertainty remains minor. In contrast to the reduced statistics method, the window blinding causes a systematic shift of the best fit estimates for large windows. However this shift is several orders of magnitude lower than the increase in uncertainty, so it is neglected. This is also confirmed by the reduced χ^2, which does not show a clear increase or decrease for the larger windows. With these findings in mind, it can be concluded that the window blinding[2] is also a promising candidate in terms

[1] This window is of same size as the two windows combined.

[2] Note that only the complete removal is considered as an option.

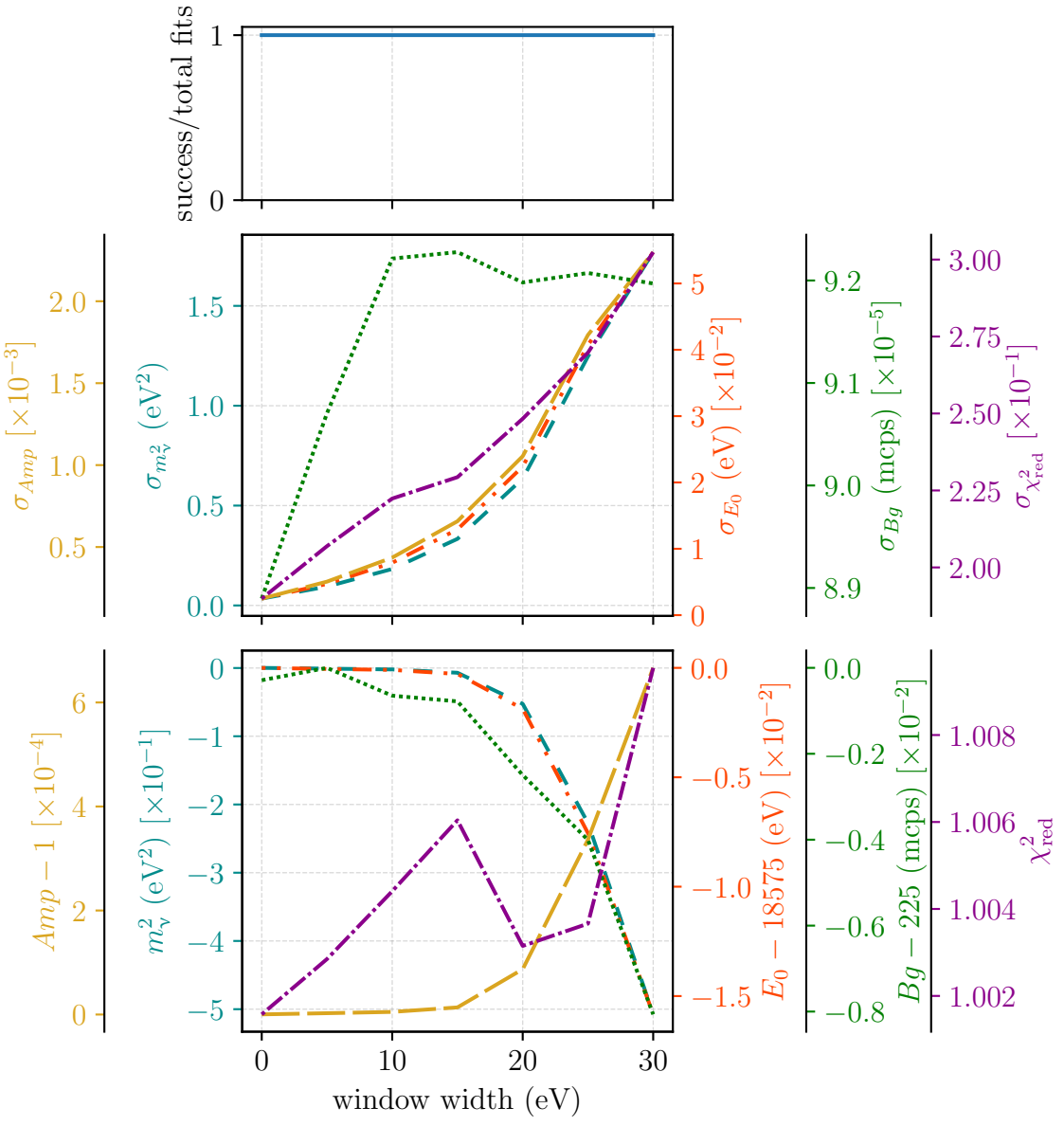

Figure 6.4.: **Window width dependence of fit parameters**. Plots share the x-axis, results are shown for three years of data. All fits were successful (upper plot). A clear dependence of the standard deviation of the best fit values (middle plot) on the window width can be seen. There is a minor dependence of the best fit mean values (lower plot) on the window width.

of blinding by increased statistical uncertainty.

6.3.1.3. Energy smearing

Another blinding method aims to hide the neutrino mass by smearing the energy of the measured spectrum. Thereby the neutrino mass shape distortion of the integrated spectrum should be hidden and the neutrino mass sensitivity deteriorated. In contrast to the two data blinding methods mentioned so far (see sec. 6.3.1.1, 6.3.1.2), the energy smearing of the measured spectrum is not expected to increase the statistical uncertainty on the neutrino mass but to give a shifted neutrino mass as the best fit. This would have the advantage that fits to the blinded data could be used as a stability criterion for data quality checks on blinded data with the same statistical precision as the unblinded data.

A common way to introduce a smearing to data is by convolution with a Gaussian. One example is including a finite energy resolution to model the detector response function of a Si-pin diode[3] or including the Doppler broadening in the spectrum calculation [Kle+18] (also see sec. 2.2.1). The intuitive approach is to smear the energy of each single electron and then move it from its original energy bin to a new one. This strict implementation would require smearing the differential spectrum to get a smeared integrated spectrum. Though this single-event smearing was dropped in favour of a spectrum-wide smearing, the energy smearing is still a smearing of the differential spectrum.

Methodology In the following, a run is defined as one scan over the whole measurement range. Each run contains subruns with index i representing the electron counts N_i from measuring at the respective entry (U_i, t_i). Since the high-voltage at the spectrometer represents a high-pass filter, the counts N_i are the number of electrons with energies $E \geq qU_i$. The energy smearing will be applied run-wise, meaning each scan is smeared independently from the other scans. Since the run will contain a non-uniform distribution of measuring times t_i (compare fig. 6.3), we use the integrated rates spectrum as

$$\dot{N}_i = \frac{N_i}{t_i}. \tag{6.8}$$

From the integrated rate spectrum $\dot{N}_i$, a differential rate spectrum $\mathrm{d}\dot{N}_i/\mathrm{d}E$ is derived by applying a spline interpolation. In order to enable universal usage of this smearing method independent of the underlying measuring time distribution, splines interpolation was chosen[4]: the interpolation enables differentiation and evaluation at intermediate steps $\Delta U_j < \Delta U_i$, making the method independent of the high-voltage steps ΔU_i of the spectrum scan. In the following, the evaluation step width ΔU_j is chosen to be $\Delta U_j = 5\,\mathrm{mV}$, a value which is a good compromise between fast computation and accuracy of the result. The differential spectrum to be smeared is

$$\frac{\mathrm{d}\dot{N}_j}{\mathrm{d}E}. \tag{6.9}$$

[3] For example the FBM, see sec. 5.4.1.4 or the FPD, see sec. 2.2.5.

[4] The gsl_splines package of the GNU scientific library [Gal+02] was used.

Rate difference spectrum Since the integrated rate is monotonously decreasing for larger energies, the direct differentiation of the integrated spectrum leads to negative values. This is expected because the differentiation describes the slope of the integrated spectrum. Numerical differentiation yields the rate difference in the interval $[U_{j-1}, U_j)$

$$\Delta\dot{N}_j = \dot{N}_j - \dot{N}_{j-1} = \frac{\mathrm{d}\dot{N}_j}{\mathrm{d}E} \cdot \Delta E_j, \tag{6.10}$$

with $\Delta E_j = q\Delta U_j$. This is the spectrum we want to smear. The smearing by a convolution with a Gaussian $G_{j,k}$ changes the rates $\Delta\dot{N}_j$ at voltage U_j according to their neighbouring points k on both sides of j. Let the Gaussian function be

$$G_{j,k}(E_j, E_k, \sigma_{\mathrm{blind}}) = \frac{1}{\sqrt{2\sigma^2_{\mathrm{blind}}}} \cdot \exp\left(-\frac{(E_j - E_k)^2}{2\sigma^2_{\mathrm{blind}}}\right). \tag{6.11}$$

Let the convolution $\Delta\dot{N}_j * G_{j,k} = \Delta\dot{N}'_j$ define the smeared rate differences and let $C_j^{-1} = \sum_k G_{j,k}$ be a normalisation factor. The smeared rate differences are then defined as

$$\Delta\dot{N}'_j = \Delta\dot{N}_j * G_{j,k} = C_j \sum_k \Delta\dot{N}_k \cdot G_{j,k} = C_j \sum_k \frac{\mathrm{d}\dot{N}_k}{\mathrm{d}E} \cdot \Delta U_k \cdot G_{j,k}. \tag{6.12}$$

$\Delta\dot{N}'_j$ now describes the smeared rate changes in the interval $[U_{j-1}, U_j)$.

Smeared integrated rate spectrum Until this point, the steps to derive the smeared rate difference spectrum to base j (representing the finer interpolation steps) have been outlined. In order to get the smeared integrated rate spectrum to base i (representing the measured high-voltage steps ΔU_i), the interpolated $\Delta\dot{N}'_j$ need to be summed up:

$$\Delta\dot{N}'_i = \sum_{U_{i-1} \le U_j < U_i} \Delta\dot{N}'_j. \tag{6.13}$$

In fig. 6.5, the effects of two extreme smearing values are shown: one small 0.1 eV and one large 3 eV smearing. From smearing the rate difference spectrum, it is expected that the small smearing follows the rate fluctuations while the large smearing smoothes the rate difference spectrum. Indeed, the large smearing cancels the Poisson fluctuations and smoothes the spectrum, while for a small smearing the estimated smeared rate difference spectrum matches the original one.

Calculating the smeared integrated rates can now be done recursively,

$$\dot{N}'_{i-1} = \dot{N}'_i - \Delta\dot{N}'_i, \tag{6.14}$$

which reveals a requirement of this algorithm: the measuring points need to be sorted in i in increasing energies qU_i. Since random scanning strategies are also under consideration, this will require an intermediate sorting step in the processing chain. Further constraints are due to the recursive calculation: on both sides of the measured spectrum, measuring points within a $5\sigma_{\mathrm{blind}}$ range are to be removed from the smeared spectrum since there are not enough smearing contributions from points beyond the measurement range. However this is a minor concern, since there will be enough points on both sides of the spectrum. This behaviour is also a reason why a 20 eV wider scan range was utilised for the simulations used here.

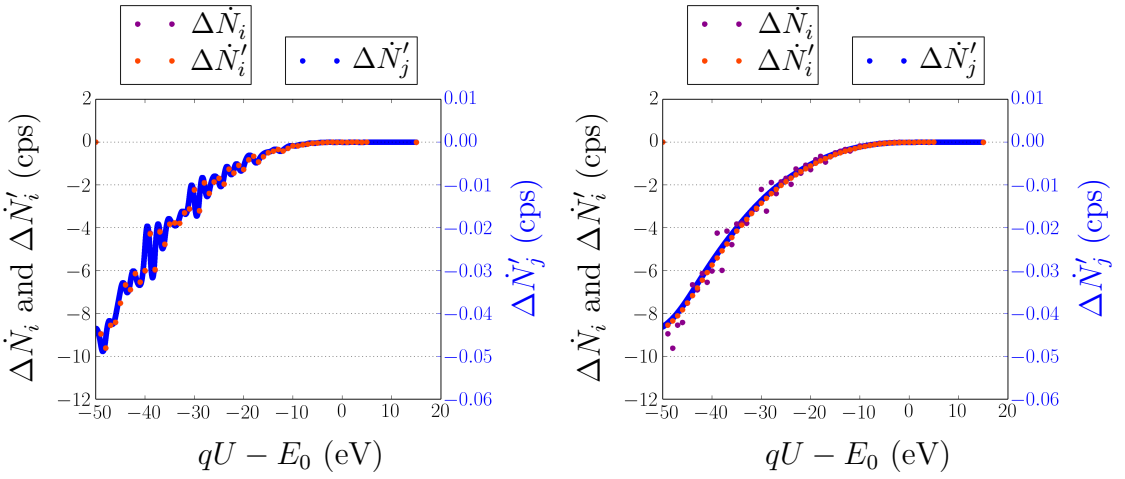

(a) Smearing of 0.1 eV.

(b) Smearing of 3 eV.

Figure 6.5.: **Rate difference spectra.** Smearing of (a) 0.1 eV and (b) 3 eV. The small smearing clearly represents the fluctuations of the randomised original spectrum ($\Delta\dot{N}_i$ below $\Delta\dot{N}'_i$), while the larger smearing smoothes any such fluctuations.

From the relative difference of the original integrated spectrum $\dot{N}_i$ and the smeared integrated spectrum $\dot{N}'_i$, the sign of the estimated neutrino mass squared shift can be estimated. A decrease of the smeared spectrum in the signal region would prefer a positive neutrino mass squared while an increase prefers a negative neutrino mass squared as best fit estimates. Choosing the recursive calculation as defined in eq. (6.14) prefers a negative neutrino mass squared as shown in fig. 6.6. The effect of the smearing on the integrated spectrum is exactly opposite to the one of a positive neutrino mass squared: the smearing increases the rate at the position of the neutrino mass signal, whereas a positive m_ν^2 would lead to a rate decrease (compare fig. 6.1). Thereby, it is expected that the energy smearing causes unidirectional shifts of the best fit neutrino mass squared in negative direction, which would mimic an unaccounted systematic effect.

As shown by Robertson et al. [RK88], an unaccounted systematic effect caused by an energy broadening is expected to result in a shift towards negative neutrino mass squared values which can be approximated as[5] of $\delta_{m_\nu^2} \approx -2\sigma^2$. Indeed, this behaviour can be seen in fig. 6.7. χ^2_{red} has a minimum around $\sigma_{\text{blind}} = 1\,\text{eV}$ (lower plot) while the uncertainties of the fit parameters – represented by the standard deviations of the best fit values (middle plot) – do not show a significant increase. Most prominent is the negative parabola describing the shift of the best fit neutrino mass squared: the true neutrino mass was $m_{\text{true}} = 0$ for all fits, but the estimated best fit neutrino mass squared follows the estimated $-2\sigma^2_{\text{blind}}$ relation. The fact that the energy smearing of the measured spectrum in simulations only affects the neutrino mass makes this blinding method a very promising candidate. It would allow testing of the fitting algorithms on the (nearly) complete measured spectrum, enabling the run-wise fit parameter estimation (e.g., endpoint or neutrino mass squared) as an

[5] This approximation is derived from Taylor expansion for zero-limit. Therefore, large smearing values may cause neutrino mass squared shifts deviating from that approximation.

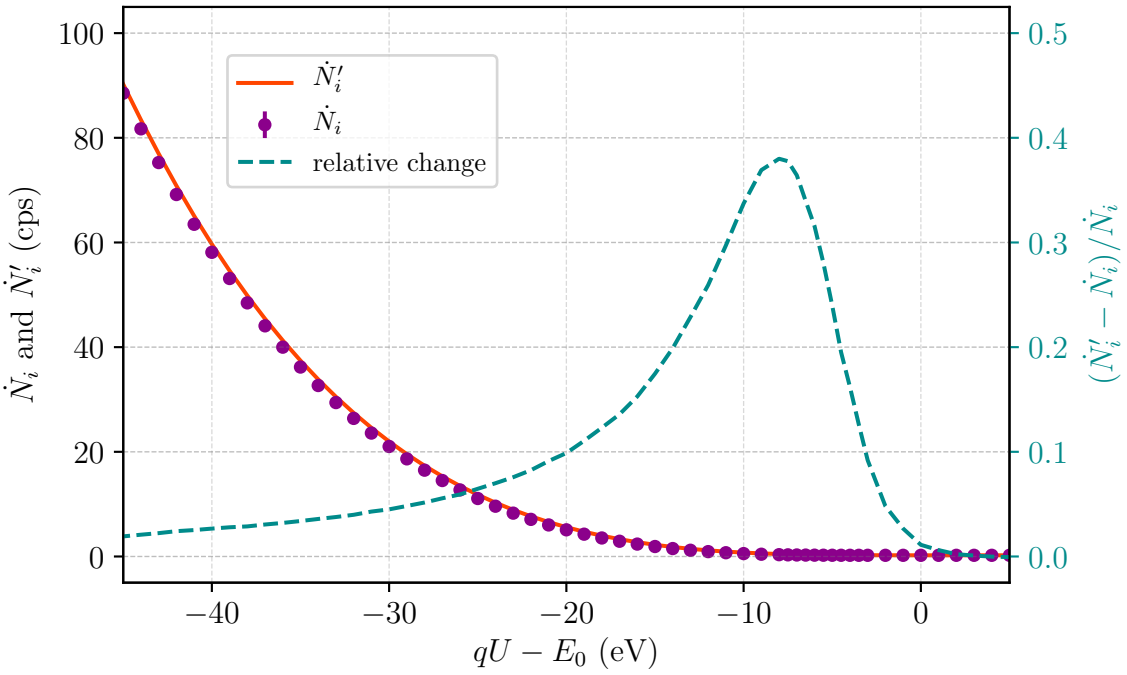

Figure 6.6.: **3 eV energy smearing effect on the integrated spectrum**. The shape distortion mimics a negative neutrino mass squared: it increases the rate in the endpoint region (also compare fig. 6.1).

experiment stability diagnostic: concerning the stability, the interest is not on the absolute value but on the relative change, reflected by the statistical uncertainty on the parameter estimates.

6.3.2. Model blinding

So far, data blinding methods have been discussed; this section will now cover two model blinding methods. In both cases, an imperfect model is used to ensure that the estimated neutrino mass is not the final answer. It has to be noted that every model blinding method requires awareness of the analysts; it may easily happen that the "correct" model is used before unblinding, revealing possibilities for experimenter's bias. However, the model blinding intrinsically does not require any changes to the measured data, making it less pervasive for the analysis chain.

The two model blinding methods discussed in the following both are based on smearing some essential parts of the model. One is based on smearing the distribution of final states (*FSD smearing*) while the other is based on smearing the energy loss function (*energy loss smearing*).

It has to be noted that the model blinding methods results presented in the following and in sec. 6.4 were obtained not by ensemble testing but by comparing spectra without any Poisson randomisation. Thereby, a systematic shift is also expected for the smearing of the final states and for using an imperfect energy loss model; both of which will degrade the sensitivity on the neutrino mass as will be discussed in sec. 6.4.

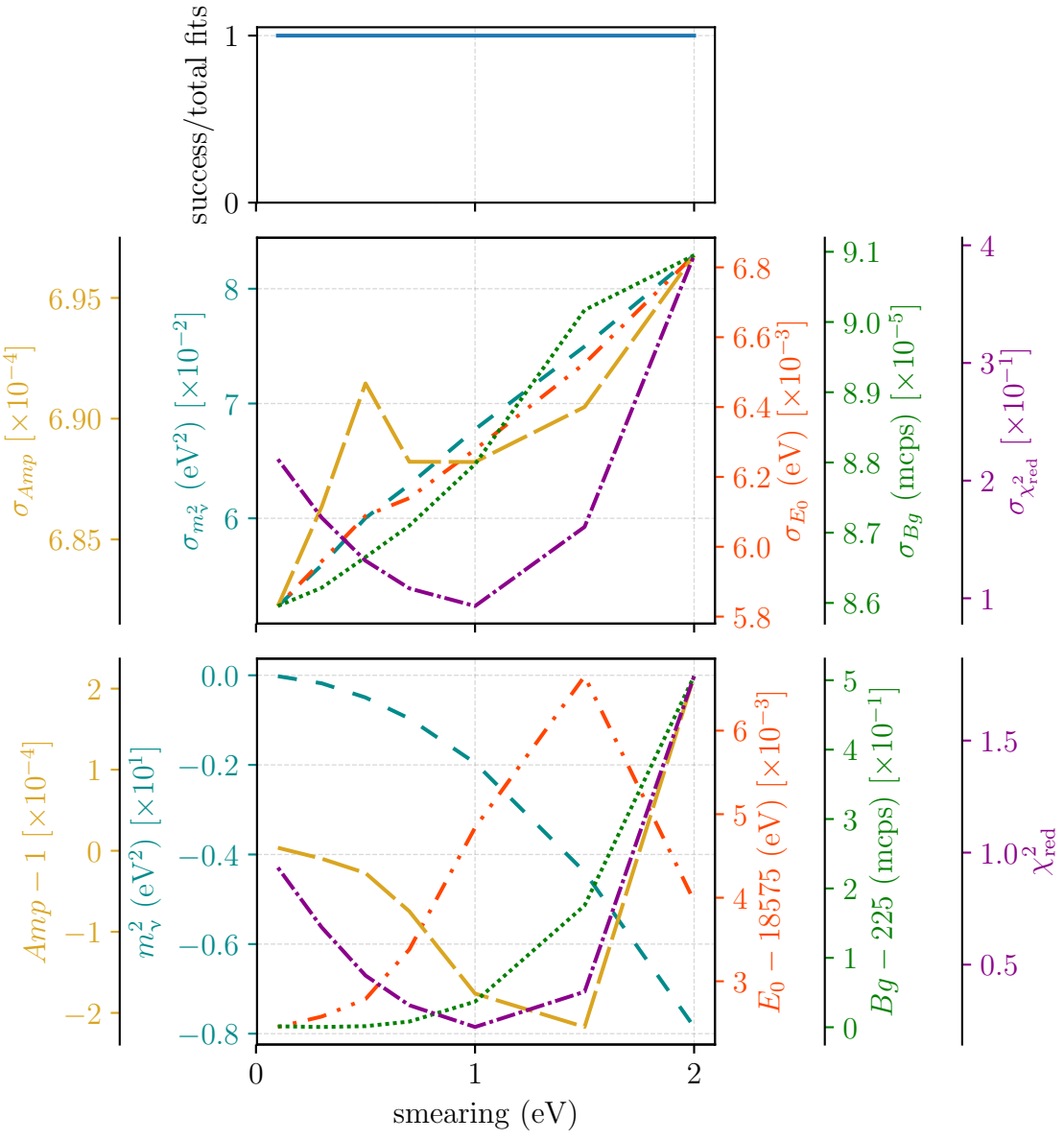

Figure 6.7.: **Energy smearing dependence of fit parameters**. Plots share the x-axis, results are shown for three years of data. All fits were successful (upper plot). There is a minor dependence of the standard deviation of the best fit values (middle plot) on the smearing value. There is a clear dependence of the mean of the best fit neutrino mass (lower plot) on the smearing value: it follows the $-2\sigma^2$ expectation. Minor shifts of the other mean best fit values can also be observed, in hand with an increasing χ^2_{red} for large smearings.

6.3.2.1. Final states distribution smearing

The FSD smearing method is based on the idea that the sensitivity for the neutrino mass is worsened by using a smeared final states distribution (FSD). If this blinding method is used, all members of the analysis team have to use a smeared version of the FSD until the collaboration decides that all analysis steps are approved and all cuts are fixed. Only then, after unblinding, the original unsmeared FSD set may be used to perform the final fit on the data.

The FSD defines the probability of the daughter molecule to decay into a given final state fs with some excitation energy E_{fs} after the β-decay (see sec. 2.2.2). Since there are no precise measurements of the FSD of the hydrogen isotopologues, KATRIN analysis relies on precise theoretical calculations. Several groups have calculated the FSD with slightly different results (for example, [SF97a, SF97b, SJF00], and [Dos+06, DT08]). The final states have discrete energies, which may be subject to rebinning in order to reduce computation time. This chapter will deal with the final states for T_2 as calculated in [SJF00]. Though the gas composition in the source will also contain DT and HT as tritiated molecules, the focus here is on showing the principal understanding of the effect of smeared final states. It should also be noted that for a tritium purity $\epsilon_T > 95\%$ as required in the Design Report [KAT05], the T_2 fraction is more than 90% of all the gas in the source and therefore dominates over other tritiated molecules.

Smeared distribution In the source and spectrum calculation (SSC) package of the KATRIN simulation and analysis framework KASPER, the final states distribution is accounted for by a summation over all possible final states of the daughter molecule for a certain electron energy, see sec. 2.2.2. The final states fs reduce the phase space $\varphi_\nu(E)$ of the neutrino at a certain electron kinetic energy E:

$$\varphi_\nu(E) = \sum_{fs} P_{fs} \cdot \left(E_0 - E - E_{fs}\right) \cdot \sqrt{\left(E_0 - E - E_{fs}\right)^2 - m_\nu^2}, \qquad (6.15)$$
$$\forall \left(E_0 - E - E_{fs}\right)^2 \leq m_\nu^2.$$

Smearing of the final states distribution is considered in a similar way to the energy smearing of the spectrum: a suitable discretisation of the FSD needs to be found which is convolved with a Gaussian of a certain σ_{blind}, representing the smearing of the FSD. The binning $\Delta E_{fs,i}$ of the smeared FSD is constrained such that it should be smaller than the aimed σ_{blind}. Reasonable values for σ_{blind} are values larger than 0.1 eV which is the lower limit set by the Doppler broadening. Similar to eq. (6.12), the smeared probabilities are then defined via

$$P'_{fs,i} = C \cdot \sum_{E_{fs,j} \in E_{fs,i} \pm 5\sigma_{\text{blind}}} G_j(E_{fs,j}, E_{fs,i}, \sigma_{\text{blind}}) \cdot P_{fs,j}, \qquad (6.16)$$

with j denoting the unbinned final states distribution, G the Gaussian function being defined according to eq. (6.11), and the normalisation factor C taking into account the binning effect and ensuring probability conservation:

$$C = \frac{\sum_j P_{fs,j}}{\sum_i P'_{fs,i}}. \qquad (6.17)$$

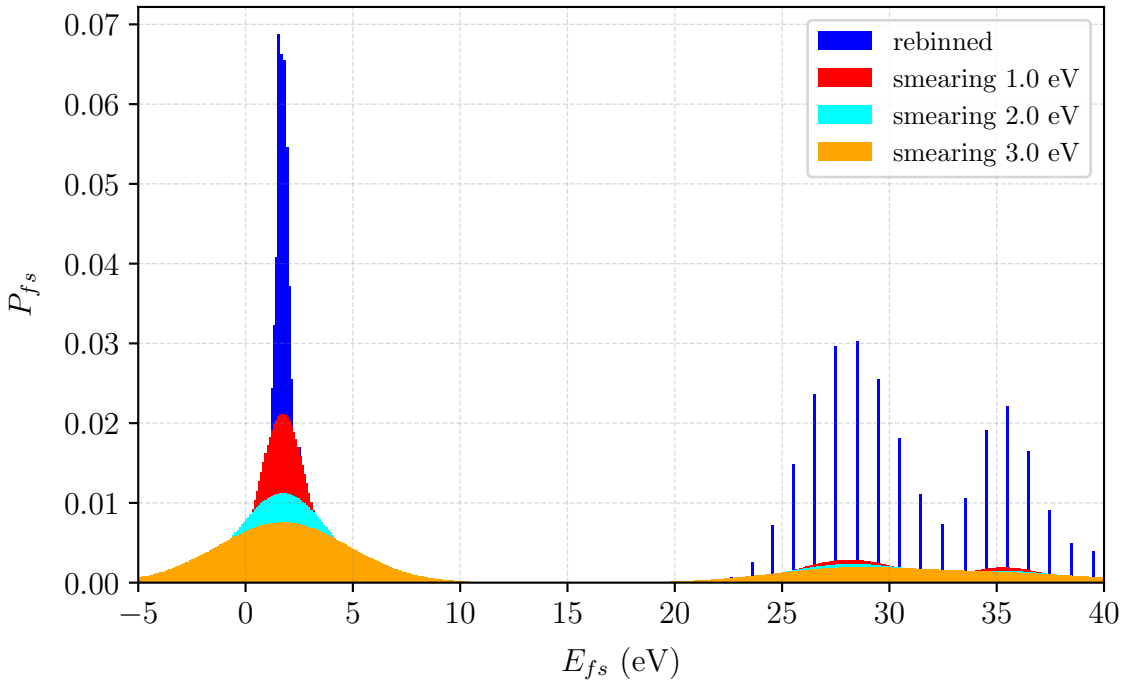

Figure 6.8.: **FSD smearing effect.** Smeared and unsmeared (T_2) excitation probabilities as a function of excitation energy E_{fs}. The rebinned final states in blue have the same binning ($\Delta E_{fs,i} = 0.1\,\text{eV}$) as the smeared final states.

The result of a smearing value of $\sigma_{\text{blind}} = 1, 2, 3\,\text{eV}$ on the final states distribution is shown in fig. 6.8. Note that the larger smearing values result in smearing an increasing amount of the probabilities into negative final states energies. The effect of the FSD smearing on the integrated spectrum is shown in fig. 6.9 for an example smearing of 3 eV. Note the opposite effect compared to energy smearing: the FSD smearing mimics a positive neutrino mass squared because it decreases the rate in the endpoint region. Therefore it is expected that the FSD smearing results in a unidirectional positive shift of the neutrino mass squared. Also note the difference in notation of the relative change compared to energy smearing; this is due to energy smearing acting on data while FSD smearing acts on the model side.

Probability conservation The smearing of the final states by construction conserves the probability due to the normalisation factor C. Negative final states energies are to be expected for large smearing values $\mathcal{O}(1\,\text{eV})$, since the smeared ground state extends until negative energies. Negative final states energies can easily be absorbed into the estimated endpoint, see eq. (6.15). The lower bound of the final states energies was set to $-\Delta E_{fs,i} - 5\sigma_{\text{blind}}$, thereby ensuring that the tails of the smeared ground state $J = 0$ are included.

6.3.2.2. Imperfect energy loss

The principle of using an artificial imperfect energy loss function is similar to the FSD smearing discussed in sec. 6.3.2.1: the model fit to the data is worsened on purpose in order to reduce sensitivity for the neutrino mass.

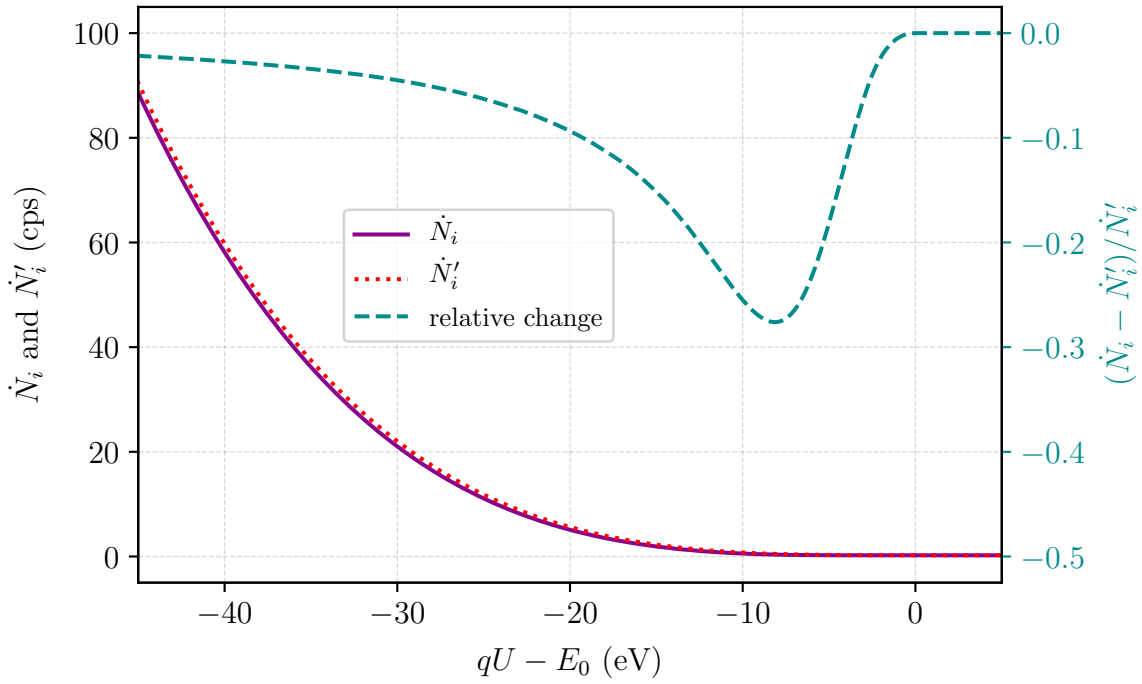

Figure 6.9.: **3 eV FSD smearing effect on the integrated spectrum.** The shape distortion mimics a positive neutrino mass squared: it decreases the rate in the endpoint region. Note the difference in notation of the relative change compared to energy smearing (fig. 6.6).

Besides the final states of the daughter molecule, another important ingredient of the spectral analysis is the energy loss function [KAT05, Kle+18]. The energy loss function $f(\epsilon)$ describes the probability for an electron to lose an amount of energy ϵ due to inelastic scattering on residual gas molecules in the tritium source. It is accounted for via an s-fold convolution for s-times scattering [Kle+18] (also compare sec. 2.2.1) in the response function.

Base energy loss function In the following, the empirical energy loss function measured by Aseev et al. [Ase+00] will be used as reference energy loss function. Aseev et al. find the energy loss function to be a superposition of a Gaussian function describing the excitation of bound states up to the ionisation energy of about 15 eV and a Lorentzian function for the ionisation continuum (also see sec. 2.2.1):

$$f(\epsilon) = \begin{cases} A_1 \cdot \exp\left(-\frac{2(\epsilon-\epsilon_1)^2}{w_1^2}\right) & \text{for } \epsilon < \epsilon_c \\ A_2 \cdot \frac{w_2^2}{w_2^2+4(\epsilon-\epsilon_2)^2} & \text{for } \epsilon \geq \epsilon_c \end{cases}, \tag{6.18}$$

with the critical energy ϵ_c defining the smooth transition between the two parts of the energy loss function. The values of the energy loss function parameters A_1, A_2, ϵ_1, ϵ_2, ω_1, ω_2 are chosen according to the findings of Aseev et al. [Ase+00] (compare sec. 2.2.1).

In the source and transport section characterisation measurements, there are dedicated time slots to determine the energy loss function in deuterium with an angular-selective, mono-energetic electron gun installed at the rear section of the KATRIN experiment (see sec. 2.2.2). Though the energy loss function will be slightly different

in tritium, its result is expected to be representative. This enables use of the deuterium energy loss function for a blind analysis of upcoming tritium data. However, since the result will be so similar, it is not expected to have a sufficient blinding effect. Therefore, this section will discuss modifications of the energy loss function by means of using wrong excitation/ionisation ratios. The ratio is defined via the two amplitudes A_1 and A_2. When this ratio is changed, also the critical energy has to be adapted in order to ensure a smooth transition.

Definition of imperfect energy loss Let the artificially distorted amplitudes be

$$A_1'(\eta) = A_1 \cdot (1 - \eta), \tag{6.19}$$
$$A_2'(\eta) = A_2 \cdot (1 + \eta), \tag{6.20}$$

then the critical energy is obtained via solving

$$A_1 \cdot \exp\left(-\frac{2(\epsilon - \epsilon_1)^2}{w_1^2}\right) = A_2 \cdot \frac{w_2^2}{w_2^2 + 4(\epsilon - \epsilon_2)^2}. \tag{6.21}$$

Analytical solutions can be obtained by a Taylor expansion. The interested reader can find the result for ϵ_c for different η in app. C.3.

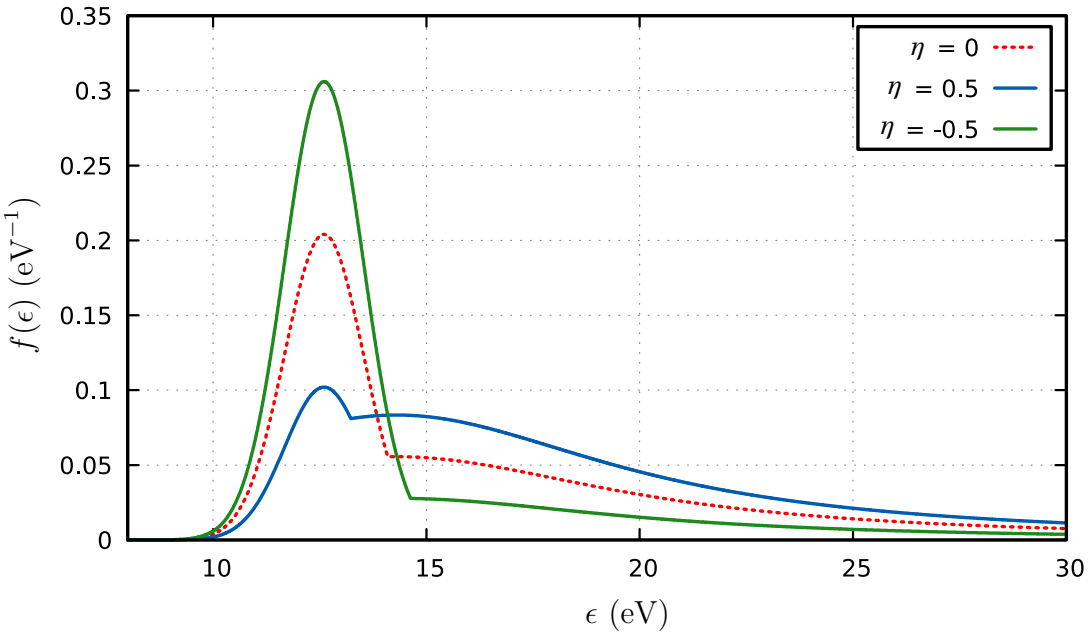

Figure 6.10.: **Imperfect energy loss function**. Results shown for several excitation/ionisation share changes. The transition from excitation to ionisation remains smooth; ϵ_+ and ϵ_- merge as $\eta \to \eta_{\max}$. Credits V. Sibille.

The effect of the changed excitation/ionisation ratio defined via η can be studied in fig. 6.10. The transition between excitation and ionisation remains smooth even for large ratio changes. As $\eta \to \eta_{\max}$ (the maximum ratio change[6]), the ionisation threshold changes and the two roots ϵ_+ and ϵ_- merge towards a single value. Also note that the sign of η matters; this enables positive or negative shifts of the neutrino mass [Hei+18].

[6]Defined by requiring the root of the solution of eq. (6.21) to be positive.

6.4. Sensitivity estimates

After having introduced the blinding methods (sec. 6.3) and the derivation of the respective sensitivity (sec. 6.2), this section will cover the sensitivity estimates for each of the blinding methods. First results of the data blinding methods will be presented, then results of the model blinding methods.

A difference worth mentioning is the way the sensitivity is calculated: for the data blinding methods, full ensemble tests were performed with 10^4 fits per blinding setting, while for the model blinding, only fits to spectra without Poisson randomisation (so no ensemble testing) were applied. Nonetheless, the result is comparable since the likelihood of the neutrino mass squared is extended towards negative values in a way that it has a parabolic shape [Kle+18]. This extension is especially important for maximising the likelihood function at neutrino masses around zero. Since both model blinding methods are based on introducing a systematic shift of the neutrino mass squared, the results will also hold for ensemble tests.

6.4.1. Data blinding

As described in sec. 6.3.1, the data blinding sensitivity estimates are based on ensemble tests with settings according to tab. C.2. The steps followed in this section are defined in sec. 6.2.3.

6.4.1.1. Reduced statistics

To derive the sensitivity in dependence of the measuring time according to the steps outlined in sec. 6.2.3, ensemble tests were performed for true neutrino mass squared

$$m^2_{\nu,\mathrm{true}} \in [0.00, 0.04, 0.25, 0.64, 1.00, 2.25, 4.00]\,\mathrm{eV}^2. \tag{6.22}$$

Discovery potential The estimation of the discovery potential contains steps 1 and 2 of sec. 6.2.3. First the total uncertainty on the neutrino mass squared $\sigma_{m^2_\nu}$ for each true neutrino mass and each measuring time is calculated. Initially, rough estimates of the measuring time dependence of the sensitivity revealed that a 2 eV (90% C.L.) sensitivity will be achieved after a measuring time of ≈ 400 min. Therefore, measuring times of

$$[100, 200, 300, 350, 400, 500, 600]\,\mathrm{min} \tag{6.23}$$

were chosen. The resulting discovery potential is shown in fig. 6.11 for true neutrino mass values up to 2 eV. From the figure, the expected behaviour can be drawn: increased measuring time results in stronger discovery potential values.

Sensitivity To then estimate the sensitivity, the intersection of the discovery potential curves for the different measuring times and the horizontal line defining 1.645σ is determined (step 3 from sec. 6.2.3): in fig. 6.11, the x-values of the intersection points

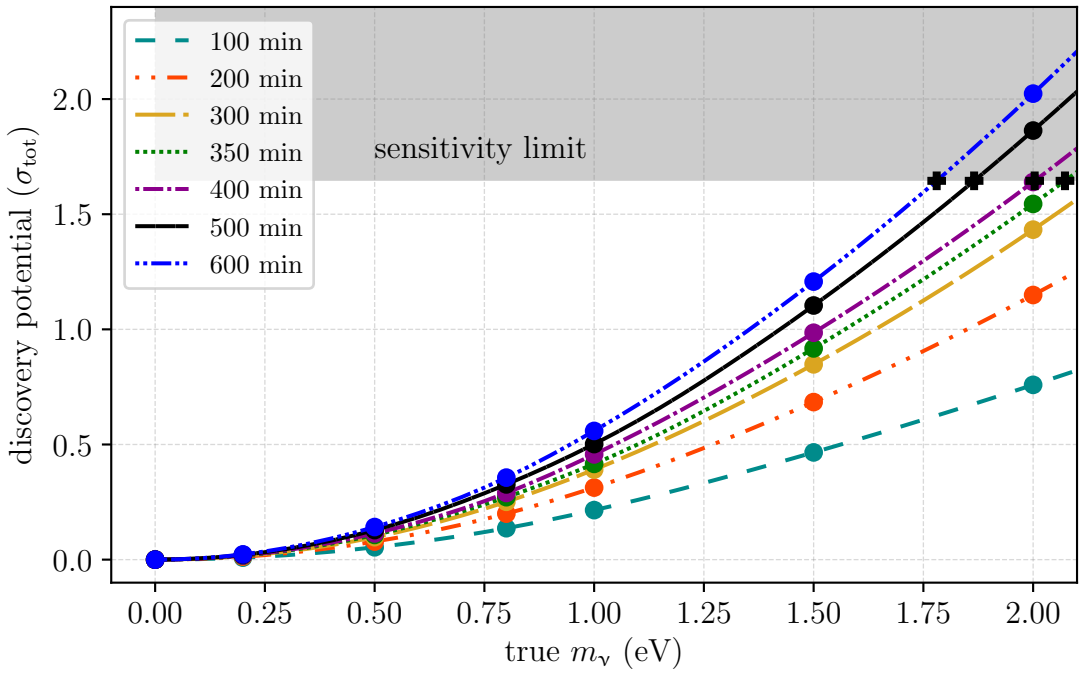

Figure 6.11.: **Discovery potential for reduced statistics blinding**. Different colours/line styles show the duration of the analysed run. Sensitivities are defined by the intersection with the greyed 1.645σ region.

with the greyed $1.645\sigma_{\mathrm{tot}}$ region define the sensitivity. Figure 6.12 shows the sensitivity dependent on the measuring time. We can read off that after 400 min $\approx$ 6.5 h the 2 eV current limit will be exceeded. Though this is plenty of time for one run to be completed, this is a short time interval considering that KATRIN is looking at data taking periods of several years.

6.4.1.2. Window blinding

To derive the sensitivity in dependence of the window blinding width, again the steps outlined in sec. 6.2.3 are carried out. As in sec. 6.4.1.1, the sensitivity estimates are performed for true neutrino mass squared values of

$$m^2_{\nu,\mathrm{true}} \in [0.00, 0.04, 0.25, 0.64, 1.00, 2.25, 4.00]\,\mathrm{eV}^2. \tag{6.24}$$

Section 6.4.1.1 showed that KATRIN will have a measuring time dependent sensitivity on the neutrino mass. Therefore, the different intervals in which KATRIN might publish results require different blinding configurations. For the window blinding and the energy smearing method, neutrino mass data equivalent to 30 days, one year, and three years of pure measuring time is investigated. In the hypothetical scenario where KATRIN may publish data according to these intervals, this also will mean that the 2 eV sensitivity is only relevant for the first blinded data. The result of these first 30 days of data can then be used as a new lower limit for the blinded sensitivity of the next data taking period. Thereby, the window width may stay constant if the increase in statistics due to increased measuring time matches the limit obtained from analysis of the previous data set.

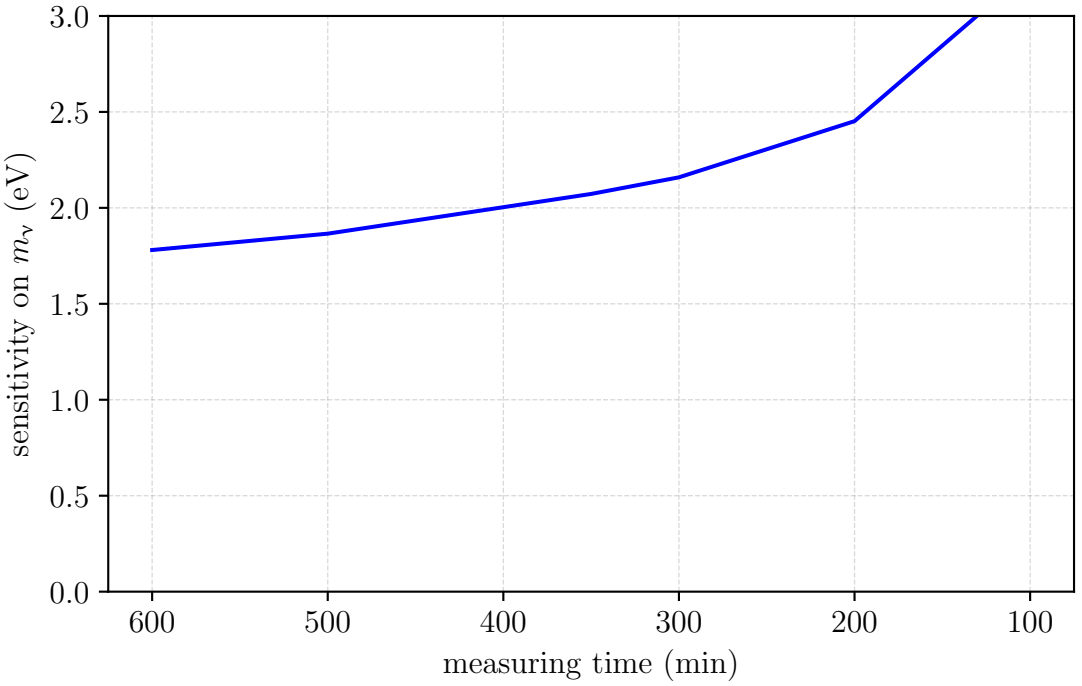

Figure 6.12.: **Sensitivity for reduced statistics blinding**. The 2 eV current limit will be exceeded after 400 min measuring time.

Discovery potential, 30 days of data A window width of about 16 eV below the endpoint is required in order to constrain the sensitivity to neutrino mass values up to 2 eV. For the first 30 days of KATRIN data a sensitivity of about $0.7 - 0.8$ eV can be expected after unblinding, which can be used as new sensitivity limit for the analysis of the one year blinded data, for instance.

Discovery potential, one year of data A window width larger than 20 V is required in order to constrain the sensitivity to neutrino mass values up to 2 eV for the first year of KATRIN data. This larger window width compared to 30 days of data was expected, and, consequently, the three years of data will even require a broader window in order not to break the 2 eV limit. However, the unblinded 30 days of data will have a sensitivity of about $0.7 - 0.8$ eV: taking this value as the new blinding requirement for the one year of KATRIN data reduces the required window width down to about 7 V. After unblinding, the first one year of KATRIN data will have a sensitivity of about $0.3 - 0.4$ eV, which can be used as new sensitivity limit for the neutrino mass analysis of the three years blinded data.

Discovery potential, three years of data A window width larger than 25 V is required in order to constrain the sensitivity to neutrino mass values up to 2 eV for the intended duration of KATRIN data. This larger window width compared to 30 days or one year of data was expected and is now confirmed. However, the unblinded one year of data will have a sensitivity of about $0.3 - 0.4$ eV: taking this value as the new blinding requirement for the three years of KATRIN data reduces the required window width down to about $2 - 3$ V. After final unblinding of the entire data set, KATRIN will reach its full sensitivity.

Sensitivity To estimate the sensitivities for the three data sets mentioned in this section, the intersection points of the discovery potentials with the 1.645σ greyed region are found. Plotting these as a function of the window width yields the blinded sensitivity curves shown in fig. 6.13. It can be seen that the first KATRIN neutrino mass data would require a blinding window width of 16 V in order to constrain the sensitivity to neutrino mass values up to 2 eV. 30 days of KATRIN data is expected to have a sensitivity of about $0.7 - 0.8$ eV, which taken as new blinding limit would yield a window width of about 7 V for the first year of KATRIN neutrino mass data. Again, taking the upper limit derived from the first year (about $0.3 - 0.4$ eV) as the new blinding limit yields a required window of at least $2 - 3$ V for the blind analysis of the full three years of KATRIN data. If this step-wise approach is not followed, it has to be noted that the 2 eV limit requires much larger windows for the one year and three years of KATRIN data.

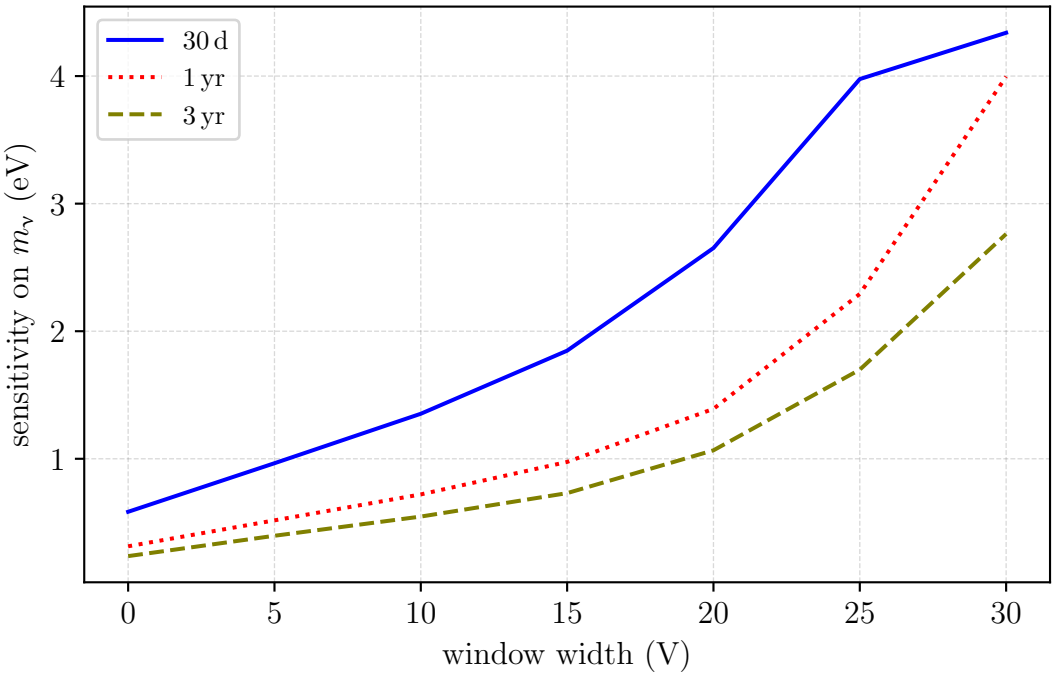

Figure 6.13.: **Sensitivity for window blinding**. In this scenario, the 2 eV limit can be met with different window widths for the different data sets. The upper limit derived from the shorter data taking period will serve as blinding limit for the next longer data taking period. Window widths larger than 25 V lead to fitting problems for the 30 days of data.

6.4.1.3. Energy smearing

As for the window blinding method, different measuring times are also worth investigating for the energy smearing method. This is because less measuring time results in larger statistical fluctuations, which might be diluted by large smearing values. It is expected that at some point, the increased smearing outweighs the statistical fluctuations and thereby worsens the sensitivity beyond the statistical uncertainty. Furthermore, it is expected that the neutrino mass squared shift induced by the

energy smearing follows a $-2\sigma^2_{\text{smear}}$ relation [RK88], resulting in a parabola for the total uncertainty eq. (6.7).

Discovery potential A smearing of about 1 eV is required for the first 30 days of data. This matches the expectation of $\delta_{m_\nu^2} \approx -2\sigma^2_{\text{smear}}$ and confirms that the statistical uncertainty of the first 30 days will have to be compensated for by a large artificial systematic effect to reach sufficient blinding. The same smearing is required for one year and three years of data, which confirms that the sensitivity needs to be decreased by the systematic effect caused by the smearing.

Sensitivity As for the window blinding, the sensitivity for each of the three data sets (30 days, one year, three years) is evaluated separately and shown in one plot. The intersection points of the discovery potentials with the 1.645σ greyed region are found and the results shown as a function of the energy smearing. Fig. 6.14 confirms the expectation from the discovery potential plots, in that the sensitivity is independent of the statistics above smearing values of $\sigma_{\text{smear}} \approx 0.75\,\text{eV}$ since this is where the smearing starts to dominate over statistics. Similar to the window blinding, different smearing values can be chosen for the different data sets, respecting the fact that the upper limit from the last analysed data set can be taken as new blinding limit.

If the step-wise data approach is not followed, the energy smearing - in contrast to the window blinding methods - does not require larger smearing values for the longer data periods, due to the method being based on a deliberate systematic influence rather than worse statistics.

Knowledge of the analysts So far, no assumptions have been made concerning the analysis of the energy smeared KATRIN data. The estimation of the total uncertainty via eq. (6.7) assumes that the analysts know the systematic uncertainty caused by the blinding. However the approximate relation of $\delta_{m_\nu^2} \approx -2\sigma^2_{\text{smear}}$ enables analysts to estimate the level of smearing used and in theory correct for the smearing effect. Therefore it is foreseen to hide the smearing value and only reveal to the analysts that the smearing was chosen from some interval. For now, let us assume we chose from a uniform distribution of the smearing values in the interval $[a, b]$. This would require the analysts to make assumptions about the smearing. One natural assumption would be using the mean of the uniform distribution to estimate the smearing related neutrino mass shift and account for it in the analysis. However, this would require inclusion of the distribution of all possible neutrino mass shifts as an uncertainty; the neutrino mass shift $\delta_{m_\nu^2}$ in eq. (6.7) becomes the standard deviation of a uniform distribution:

$$\delta_{m_\nu^2} \to \sigma^2_{\text{blind}} = \frac{(\beta - \alpha)^2}{12}, \tag{6.25}$$

with $\alpha \approx -2a^2$ and $\beta \approx -2b^2$ representing the minimum and maximum neutrino mass squared shift. If we sample the smearing from the maximum interval $[0, b]$, this will become

$$\sigma^2_{\text{blind}} = \frac{\beta^2}{12}, \tag{6.26}$$

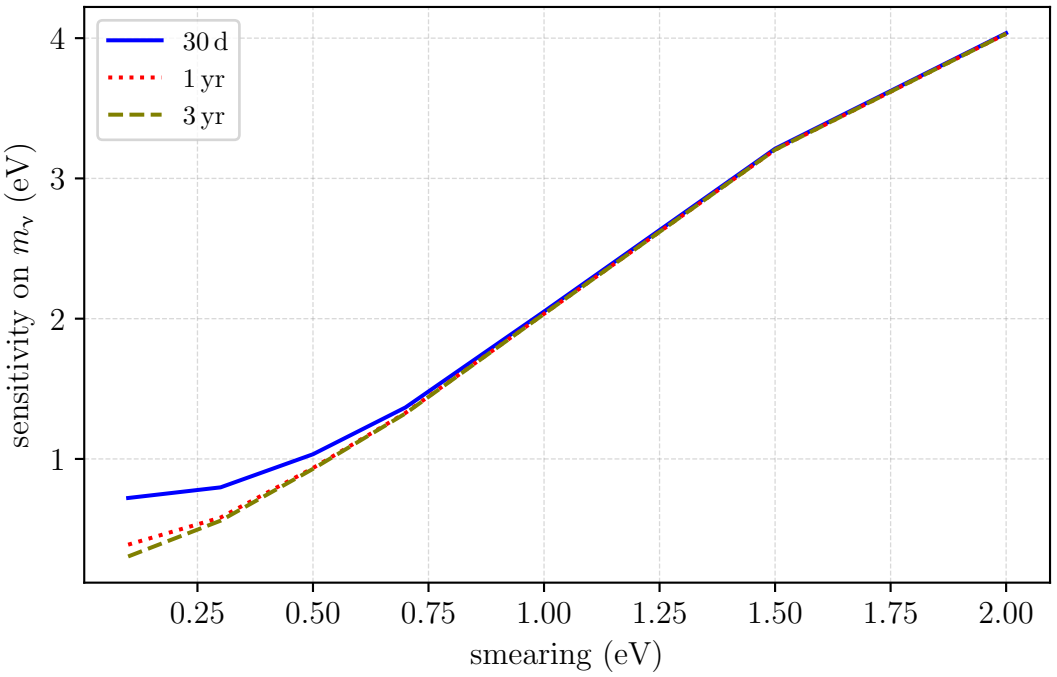

Figure 6.14.: **Sensitivity for energy smearing**. The 2 eV limit can be upheld with the same smearing for all three data sets. If the limit obtained from the shorter data taking periods is used as upper limit for the longer data taking periods, smaller smearings can be used for the longer data taking period.

with β the maximum neutrino mass squared shift obtained if smearing b is used. Therefore we can redefine eq. (6.7):

$$\sigma_{m^2_{\nu\,\mathrm{tot}}} = \sqrt{{\sigma_{m^2_{\nu\,\mathrm{stat}}}}^2 + {\sigma_{m^2_{\nu\,\mathrm{sys}}}}^2 + \frac{\beta^2}{12}}. \tag{6.27}$$

This definition of the total uncertainty includes some minimum assumptions as an analyst and will require larger smearings to get the same decreased sensitivity as with eq. (6.7). We see the effect when comparing fig. 6.15 to fig. 6.14: a smearing of 2 eV gives a sensitivity of 4 eV for the worst case scenario with no information for the analysts. If the analysts know that the smearing was chosen from a certain window starting at 0, the resulting blinded sensitivity is better because the analysts can use that information.

6.4.2. Model blinding

In contrast to the data blinding methods, the model blinding results presented in this section are based solely on fits without Poisson randomisation, since its purpose is to show that blinding may be achieved through smearing of the final states or an imperfect energy loss function. Further differences are a slightly altered experiment configuration: the model blinding results were obtained from assuming Design Report characteristics.

Since there were no ensemble tests performed, the discovery potential was estimated for various smearing or ratio changes in 0.01 eV^2 steps in true neutrino mass squared

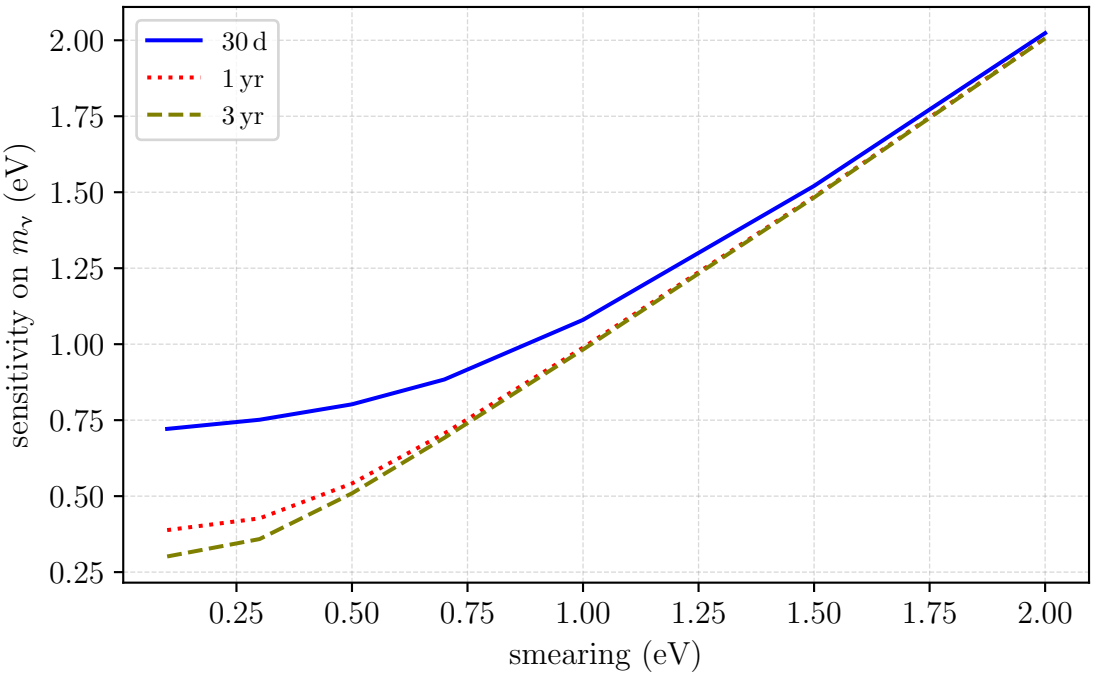

Figure 6.15.: **Sensitivity for energy smearing with analysts assumptions**. The 2 eV limit can be met with the same smearing for all three data sets. Smearing values represent the upper bound of the window that the smearing was chosen from. Larger smearing is required to get the same sensitivity as in fig. 6.14.

until the 1.645σ were reached. The resulting neutrino mass squared value was saved as the sensitivity. Thereby, sensitivity curves may also be constructed.

6.4.2.1. Final states distribution smearing

For simplicity, only the T_2 final states were smeared in the analysis presented in this section. There are also DT and HT molecules present in the gas mixture. However, the T_2 fraction for a tritium purity of $\epsilon_T = 95\%$ is 90% (also compare to secs. 2.2.2 and 2.2.2).

The blinded sensitivity curve for 30 days of KATRIN data is shown in fig. 6.16. Longer data taking periods will have better sensitivity for small smearing values, similar to the energy smearing shown in fig. 6.14. Since the final states distribution used in these studies does not contain higher angular momentum values, the resulting ground state is more skewed, i.e., less Gaussian (see fig. 6.8), and therefore the smearing effect causes shifts stronger than the expected $2\sigma^2$. The sign of the shift is different to that shown in sec. 6.3.1.3: the smearing of the final states causes a positive neutrino mass squared shift. It has to be noted that the χ^2_{red} starts to deviate from zero (expected without randomisation) for smearing values larger than 0.3 eV which is comparable to the energy smearing features. The endpoint is shifted to slightly more positive values starting at smearing values of 0.3 eV also, but not exceeding $\Delta E_{0,\text{max}} \approx 0.15\,\text{eV}$.

Though the fits with the smeared final states distribution do take a bit longer, no

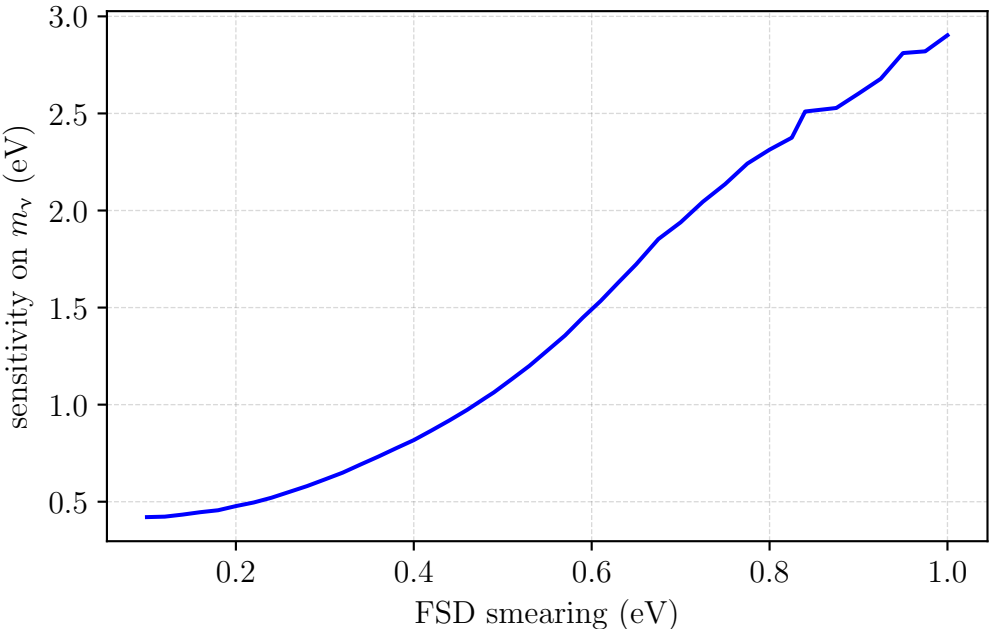

Figure 6.16.: **Sensitivity for FSD smearing**. The 2 eV limit can be met with a similar smearing value as for the energy smearing ($\mathcal{O}(1\,\text{eV})$, compare fig. 6.14). This result represents 30 days of simulated data. The longer data sets will only have better blinded sensitivity for small FSD smearing values, below 0.5 eV.

strong bias in any of the other estimated parameters could be observed. More importantly, the method can blind the neutrino mass by inducing a (positive) neutrino mass squared shift.

6.4.2.2. Imperfect energy loss function

As mentioned in sec. 6.3.2.2, the modification of the energy loss function offers the possibility to control the sign of the induced neutrino mass shift. Indeed, fig. 6.17 reveals that the neutrino mass sensitivity is decreased in both directions of the ratio change η. From eqs. (6.18), (6.19), and (6.20) it can be understood that a positive η causes a reduction of the relative excitation share (and increase of the ionisation share), and vice versa for negative values of η. Figure 6.17 covers both extremes, a large artificial increase of the ionisation share (positive η) as well as a large increase of the excitation share (negative η). Due to the construction via eqs. (6.19) and (6.20), there is a maximum value of 0.597 for η [Sib18]. Since the positive η cannot provide sufficient blinded sensitivities, the negative η need to be explored. However it has to be noted that the required $\eta \approx -0.7$ results in a very different energy loss function than the original one (compare fig. 6.10). Furthermore, it does not only hide the neutrino mass but also causes large biases to the other parameters [Sib18], which is the reason why this method is considered inferior to the other blinding methods discussed so far.

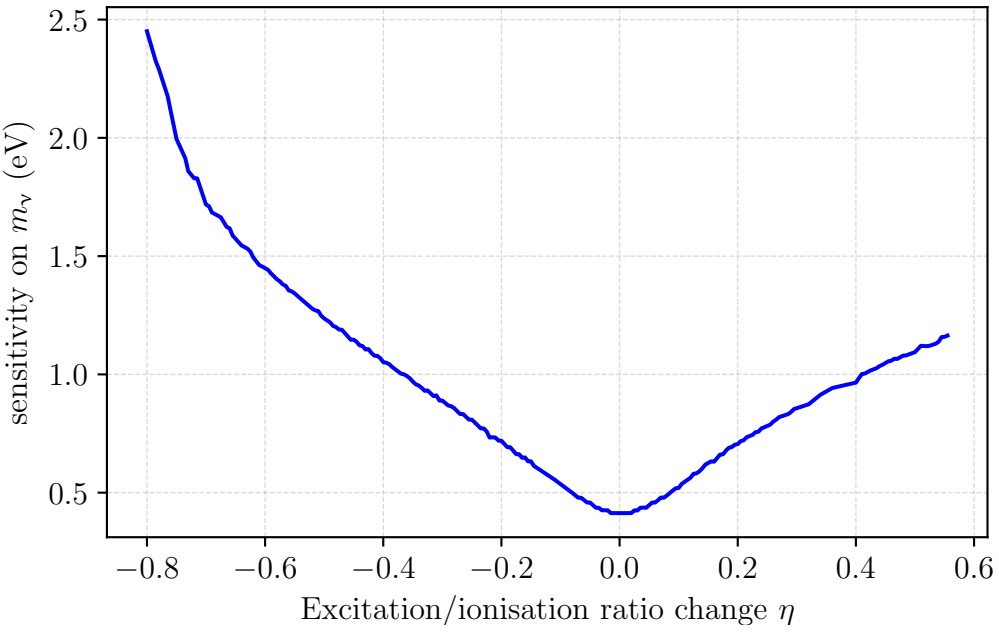

Figure 6.17.: **Sensitivity for imperfect energy loss.** The 2 eV limit can only be met with rather extreme changes of the excitation/ionisation ratio, $\eta < -0.7$. The result represents 30 days of simulated data. Credits V. Sibille.

6.4.3. Summary

We now have all the simulation results at hand and have introduced the different blinded sensitivities, therefore we can conduct a direct comparison of the different methods. Figure 6.18 gives an overview of the effects of all the five blinding methods discussed in this work. It can be seen that all blinding methods can achieve the decrease of the blinded neutrino mass sensitivity to the 2 eV target for the first 30 days of nominal neutrino mass data. On the left-hand side, the scales of the model blinding methods are shown and on the right-hand side the data blinding methods. It should be noted that both smearing methods – energy smearing and FSD smearing – result in comparable blinding levels, which shows the good agreement between the methods. Evaluation and discussion of the methods will be further presented in sec. 6.6 after results of testing some of the methods on krypton commissioning data are presented in sec. 6.5.

6.5. Application of the blinding methods to krypton data

After exploring the various blinding strategies with simulations, results of their application to krypton commissioning data will be presented in this section. Krypton data refers to the commissioning measurements performed with gaseous krypton ^{83m}Kr carried out in July 2017 [Are+18b]. The KATRIN settings for the krypton

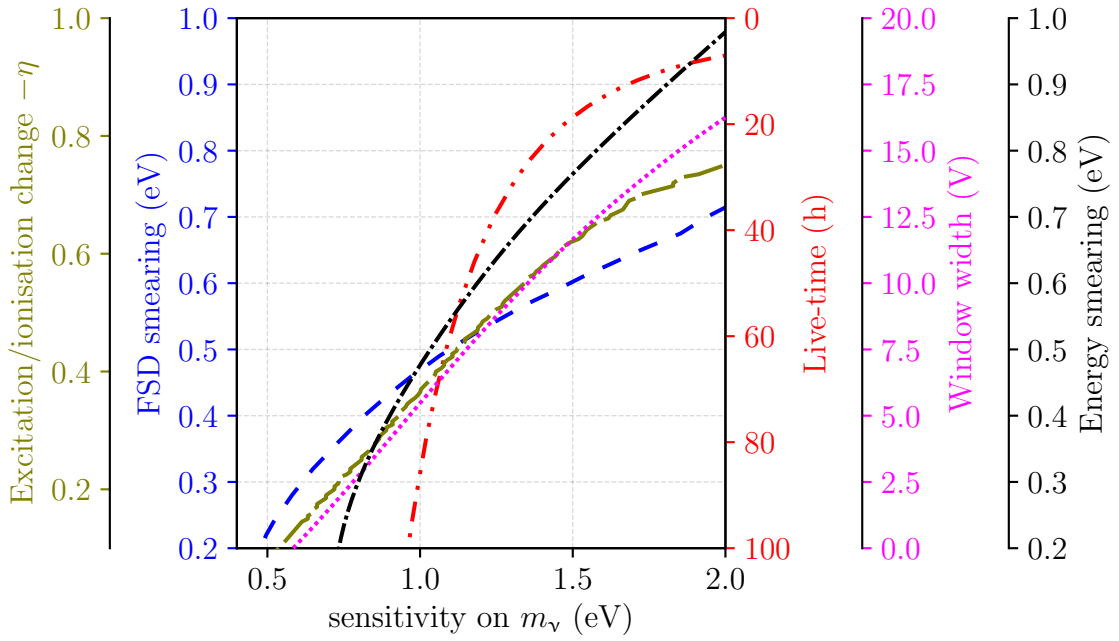

Figure 6.18.: **Sensitivity summary**. The 2 eV limit can be met with every blinding method. These results represent 30 days of simulated data.

commissioning measurements are described in detail in [Are+18b] and will briefly be recapitulated here. The gaseous ^{83m}Kr campaign served as a first test run of pure ^{83m}Kr spectroscopy without any carrier gas. Gaseous ^{83m}Kr was injected at the pump port PP2-F of the WGTS cryostat (compare sec. 3) via a dedicated krypton generator [Are+18b, SVS17, Sen+18] and pumped out at the CPS which was the only active pump running. A further difference in the krypton-mode set-up is the beam tube temperature of the WGTS: in ^{83m}Kr mode, the temperature is increased from 30 K (tritium mode) to 100 K to prevent ^{83m}Kr freeze-out.

In the course of this thesis, the ^{83m}Kr data is used to establish a first technical implementation of the necessary tools on a real data set and as a cross-check and validation of the data blinding methods. Therefore, the main interest is on relative changes of the parameters when fitting blinded instead of unblinded data. Despite marked difference between the mono-energetic krypton conversion electron lines compared to the continuous β-decay spectrum, this test implementation yields helpful insights because the krypton line spectrum is well known. Therefore, the impact on blinding techniques on the reconstruction of the spectrum can be studied. The krypton run used for the fits is run 33165, with run summary version 2c (also compare tab. 6.1).

^{83m}Kr produces a conversion-electron spectrum containing several lines. In the following, focus will be on investigating the data blinding effect on the K-32 conversion line from ^{83m}Kr. In the differential spectrum, the lines are defined as a Voigt profile with a Gaussian broadening [Are+18b]. The integrated spectrum of a line has the inverse transmission form, as can be seen from fig. 6.19 (for the cuts used see tab. 6.1). Similar to tritium fitting, krypton fitting requires four parameters:

1. background rate Bg,
2. line position,

3. line width (naturally about 2.7 eV for the K-32 line [Vén+18]),
4. line probability (translates into an amplitude).

The model for krypton analysis is simpler since it does not require final states (noble atomic gas) and due to the low amounts of krypton used in this campaign, energy loss processes are of no concern; this leaves only the data blinding methods which can be tested with krypton data. Since the reduced statistics method is trivial, focus is set on the window blinding and the energy smearing methods. The two methods are expected to result in different blinding outcomes: the window blinding should increase the uncertainty on all parameters while the energy smearing should broaden the estimated line width.

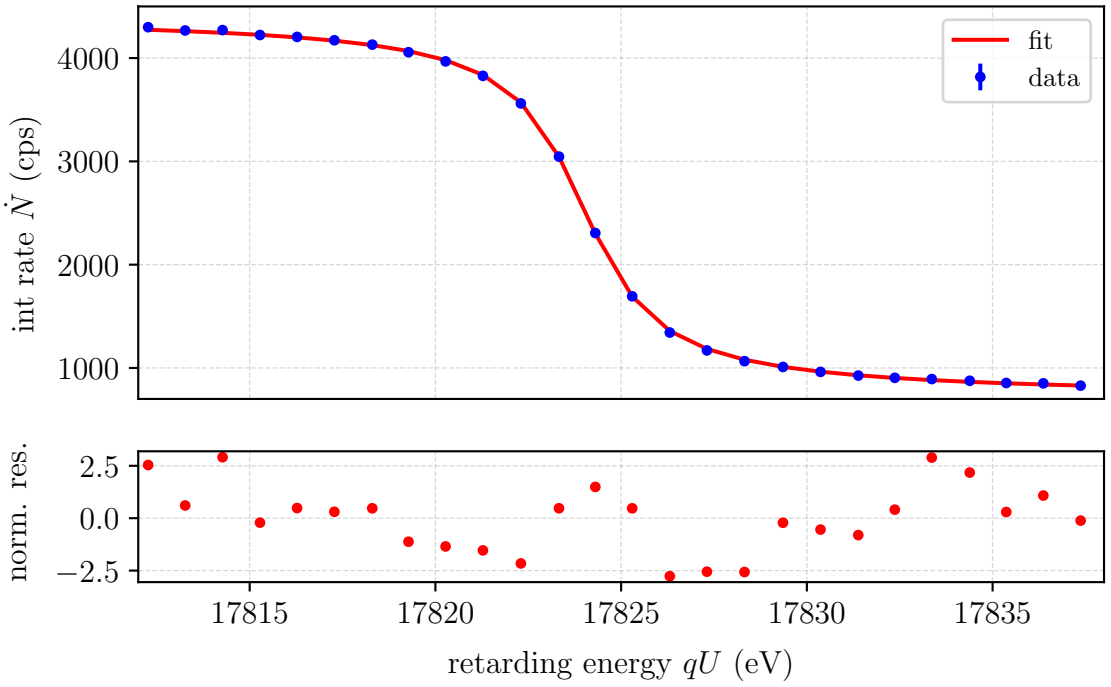

Figure 6.19.: **Unblinded integrated ^{83m}Kr spectrum (K-32 line region).** For the selection criteria used to obtain this spectrum, see tab. 6.1.

6.5.1. Window blinding

The implementation of the window blinding method on krypton data is slightly different than the one for the tritium data. Since the line extends to both sides around a central value, the window blinding is done symmetrically with respect to the expected line position. The effect on the spectrum is shown for a blinded window of $[17823 - 5, 17823 + 5]$ V in fig. 6.20. Though the complete line shape is cut out by this large window, the fitter manages to fit a line and get reasonable estimates of the line characteristics. Performing these fits for several windows for this example run 33165 enables investigation of the effect of an increasing window on the fit parameters. This effect is shown in fig. 6.21: the most prominent feature is the

[7] The two outermost rings with 12 pixels each see flux tube collisions with the beam tube [Are+18b].

Table 6.1.: **Selection criteria for the krypton data blinding tests.** Note that the FPD ROI cut is 10 keV above the electron energy due to the 10 keV post acceleration voltage.

parameter	value
run	33165
run summary	KryptonRunSummary2c-fpd0033165
hv cut	use $[17812, 18000]$ V
pixel cut	use pixels $[0, 124]$ (out of 149)[7]
detector model	uniform (sum of all counts)
FPD ROI cut	event energy $\in$ $[24932.3469, 30932.3469]$ eV

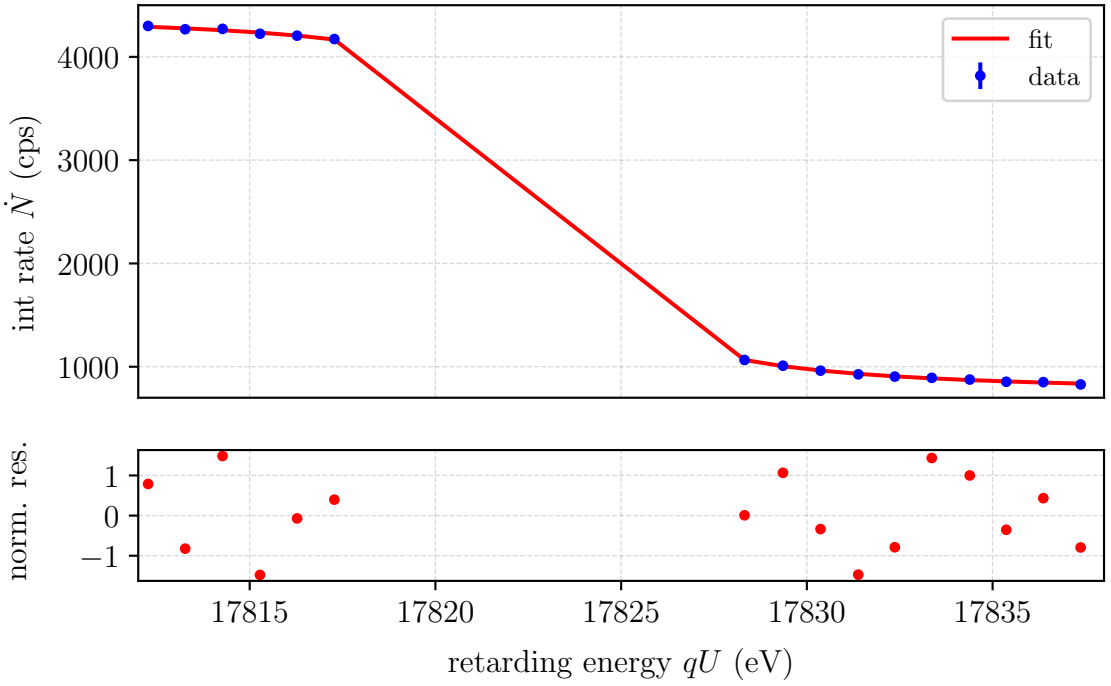

Figure 6.20.: **5 eV window blinded ^{83m}Kr spectrum**. For the selection criteria (apart from the blinding) used to obtain this spectrum, see tab. 6.1. Window blinded symmetrically with respect to 17 823 eV.

increase in the uncertainty of all fit parameters which was expected for this blinding method. The best fit values are not influenced significantly by the window blinding, which is also a confirmation of the findings from the simulations in sec. 6.3.1.2. Note that the windows larger than 5 eV completely hide the line signature, which explains the 1 eV shift in fig. 6.21 for those large windows.

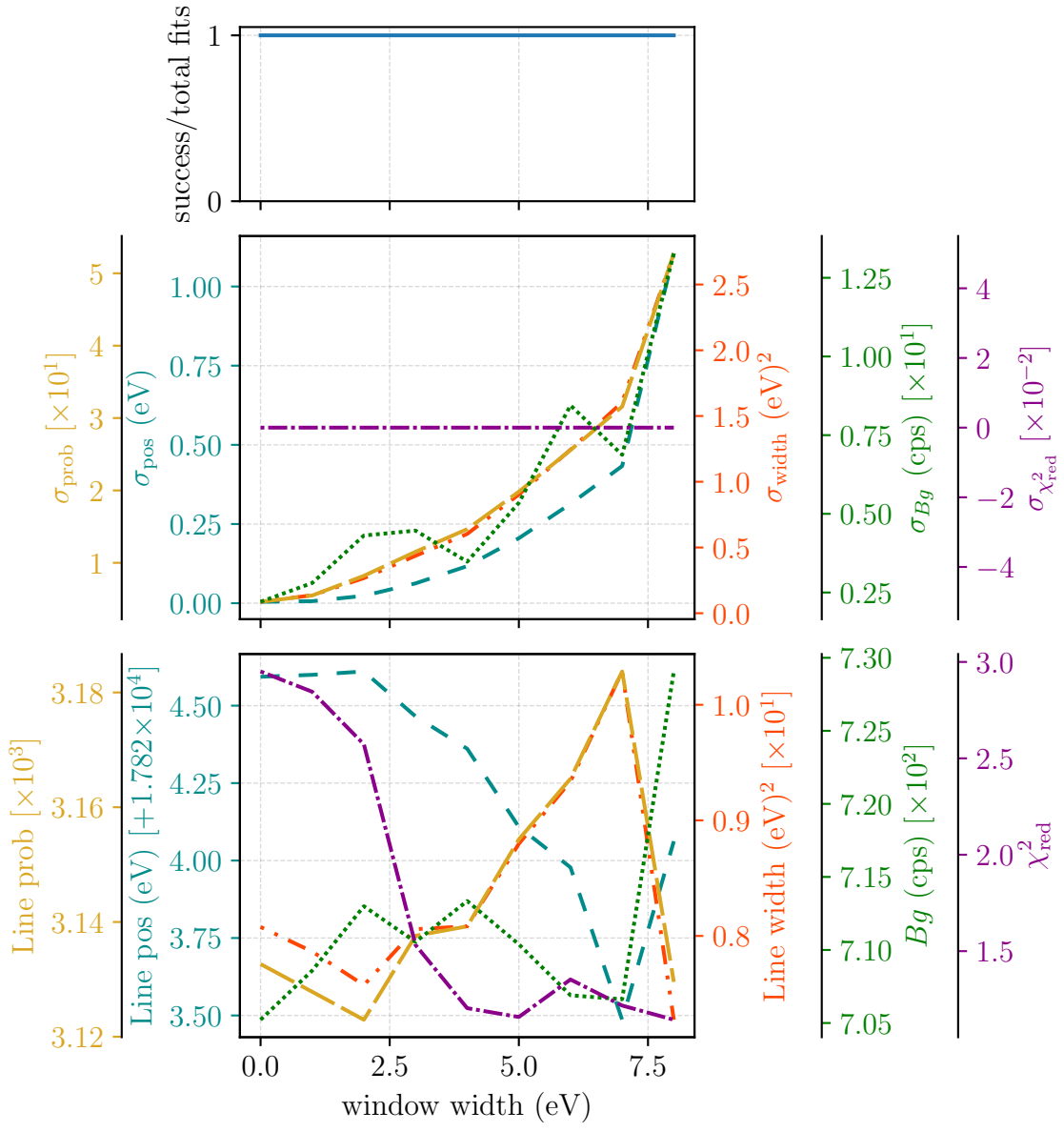

Figure 6.21.: **Window width dependence of ^{83m}Kr fit parameters**. Plots share the x-axis, results are for run 33165. There is a clear increase of all parameter uncertainties with increasing window width.

6.5.2. Energy smearing

To test the energy smearing method, the same algorithm was used as presented in sec. 6.3.1.3. However, due to the limited energy range scanned in the krypton measurements, it is expected that large smearings will result in very distorted spectra. The reason is that on both edges of the scanned energy range the smearing will cause artefacts due to non-conservation of counts. Nonetheless the most prominent

feature should be the broadening of the line width, regardless of what happens to the other parameters. Indeed, fig. 6.22 shows that, for an extreme smearing value of 5 eV, the line width is broadened significantly. Though the smearing in this example

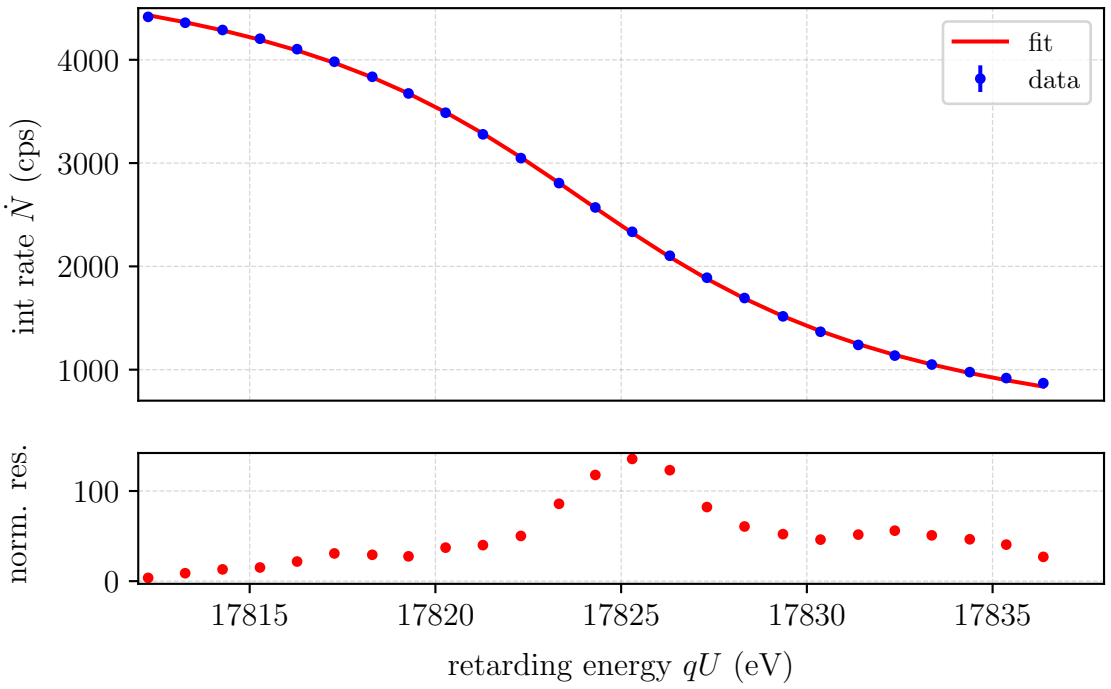

Figure 6.22.: **5 eV energy smeared ^{83m}Kr spectrum**. For the selection criteria used to obtain this spectrum, see tab. 6.1.

is rather extreme, the fitter manages to estimate reasonable values for the fit parameters except for the background: due to the large smearing and small number of measurement points above the line position, which could catch the smeared counts from lower voltages, the smeared counts at the upper energy edge are lost. That leads to a negative estimate of the background rate in this extreme case, which is attributed to the small scanned energy range. In nominal neutrino mass measurements, voltage steps at least $10 - 20$ V above the endpoint are foreseen which would catch smearing values up to 4 eV with $5\sigma_{\text{smear}}$. Investigating the effect of different smearings for the example run 33615 yields the systematic change of the smearing to the estimated parameters. Indeed, fig. 6.23 reveals that besides a large increase in χ^2_{red}, the line width is increased by the smearing. The strong dependence of the background rate can be explained by the end effects caused by the smearing; there are simply not enough measuring points above the line position to catch the smeared counts. Notably uninfluenced by the smearing is the line position, which changes – as expected – only marginally with the smearing.

6.5.3. Summary

The test of the two data blinding methods, energy smearing and window blinding, on krypton data may also be used to perform a blind analysis of future krypton spectra with KATRIN. Though the krypton spectrum (mono-energetic line) is not directly comparable to the tritium spectrum (continuous spectrum), this represents

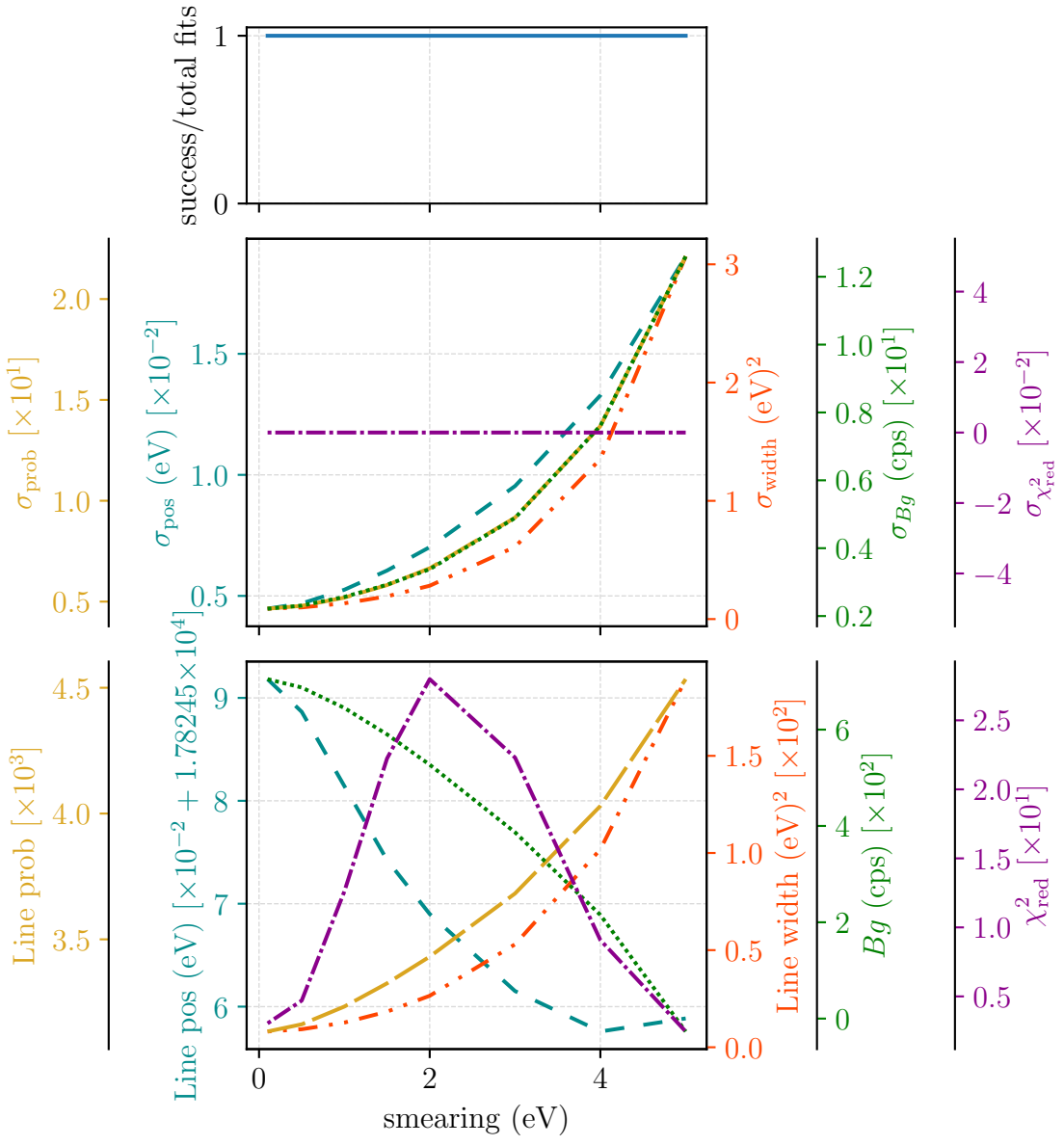

Figure 6.23.: **Energy smearing dependence of $^{83\mathrm{m}}$Kr fit parameters**. Plots share the x-axis, results are for run 33165. There is a clear increase of the line width and also large changes in χ^2_{red} and the estimated background rate observed.

an important cross-check. More importantly, this proof of principle is the first test of the implementation of the data blinding technique into the complete data-analysis chain of KATRIN from the Intermediate Data LayEr (IDLE) to the run summary stage and fitting software.

6.6. Discussion

Performing a blind analysis always comes at a price during the blind phase and requires careful planning beforehand. At KATRIN, the cost of an unbiased neutrino mass analysis is either the complication of estimation of nuisance parameters and systematics (data blinding) or the blinding is hard to control and enforce (model blinding). However, there are ways to reduce these costs of the targeted blinding strategy, which will be discussed in this section.

Data versus model blinding The most distinctive difference between data and model blinding is the implied level of control. If applying data blinding, all the users have to use the blinded data, for model blinding it is in the responsibility of the analysts to use the blinded model. A possible way to supervise the implementation of blinding is to use a hash in the model that checks whether, for instance, the smeared final states are used in the neutrino mass fit. When only fitting endpoint, amplitude and background the unsmeared final states could even be used. This check is mainly meant to prevent fitting the neutrino mass with unblinded model by accident rather than forcing users to use the blinded model.

First Tritium conclusions One major outcome of the First Tritium campaign is the fact that the model describes the data rather well [Are+19], also see sec. 5.3, and the fits work out of the box without applying a-posteriori modifications to the model. This opens new perspectives also for the blind analysis: run-wise fits to the unblinded data can be included in the automated run-processing right after the generation of the run summaries, as shown in fig. 2.8. These fits either hide the neutrino mass if fit or fix the neutrino mass, such that the fit results can be used as a stability control and thereby as a measure of data quality. A crucial point of these automated fits is that the cuts (ROI of the FPD, energy range of the tritium spectrum, etc.) are fixed before the data taking period starts and are left unchanged.

Implicit blinding A different option, which has not been discussed so far, is implicit blinding. This would give users full access to all data, with the possibility to systematically check the effect of adapting cuts in the analysis. The collaboration acceptance of any kind of analysis related to the neutrino mass would then imply point-by-point cross-checks and validation of all analysis steps. In order to maintain and safeguard unbiased neutrino mass data analysis, all cuts need to be justified without considering their effect on the neutrino mass. However, there is still the risk of unconsciously working towards an expected value without blinding.

6.6.1. Reduced statistics

The reduced statistics method provides access to the whole energy range analysed with KATRIN, without causing any changes to the shape of the spectrum. However, the β-spectrum measurement will be statistics dominated in the beginning. Therefore, the sensitivity will improve quickly and within $6 - 7\,\mathrm{h}$ of measuring time, the $2\,\mathrm{eV}$ limit will be exceeded. That drastically reduces the blinded time range for a

statistically blind neutrino mass analysis and relies on automated fits in the run processing to detect long-term drifts of fit parameters or systematic effects.

6.6.2. Window blinding

Hiding the events within a specific window around the signal region to perform an unbiased analysis is a technique well-known, for instance, from $0\nu\beta\beta$ decay searches (see e.g. [Ago+13]). As a data blinding method it provides strong control and can also be used to perform blind analysis of data taken after the first unblinding. Simulations in this work reveal that the removal of a window below the endpoint does not lead to a systematic bias of the parameter estimates[8], while the uncertainty on the neutrino mass can be increased by increasing the window width. As a downside, the window has to be quite large (about 16 V) for the first neutrino mass analysis and also studies of systematic effects in the endpoint region are complicated. In order to use all data available, these studies would need to be done by analysts not involved in neutrino mass analysis. On the other hand, the closer KATRIN gets to the end of neutrino mass data taking, the smaller the window can be in order to be "blind enough". Together with the long-term experience gained at that point, this makes the window blinding method a suitable candidate for the final neutrino mass analysis of KATRIN data.

6.6.3. Energy smearing

The idea of smearing out the neutrino mass signal in KATRIN data intrinsically involves a change of the spectral shape which might also smear out unexpected features in the spectrum. The shift of the estimated blinded neutrino mass has a fixed direction, for which an expectation of $\delta m_\nu^2 \approx -2\sigma_{\mathrm{smear}}^2$ can be applied. However, despite the strong control due to its data blinding nature, the energy smearing allows full access to the whole spectrum, providing full statistics to detect relative drifts. Also note that the smearing will happen in the automated run processing inside the intermediate data layer (IDLE), resulting in blinded run summaries (compare fig. 2.8). The raw data will always be available for full check of systematics. It is considered unlikely that analysts are willing to rebuild the complete analysis chain from raw data until preprocessed run summaries to get unblinded neutrino mass data. Also note the effect of analysts knowing the range the smearing was chosen from: this knowledge combined with the fixed direction of the shift requires larger smearing values (see sec. 6.4.1.3).

6.6.4. Final states distribution smearing

Similar to the energy smearing, the smearing of the final states distribution relies on hiding the neutrino mass signal in a change of the spectral shape. The main difference is that the FSD smearing applies model blinding and therefore is built on the responsibility of the users. The model blinding is targeted to prevent accidentally

[8] Since it does not cause a modification to the spectral shape.

revealing the unblinded neutrino mass by misconfiguration of the fitting program, for example. Therefore, it is foreseen to implement a check whether the smeared final states are used to fit the neutrino mass. This can be implemented via a hash and opens the possibility of having all data available unblinded. The most recent version of the final states calculation is not yet made available collaboration-wide, which would enable providing first the "blinded" final states. In an unblinding event, the unsmeared, more accurate final states distribution might then be provided to all analysts at the same time.

6.6.5. Imperfect energy loss function

As found in sec. 6.4.2.2, the change to the energy loss function to hide the neutrino mass has to be relatively extreme, as shown in this work, though it would provide full statistics of the complete measured spectrum. Despite being a model blinding technique and therefore relying on the responsibility of the users, blinding by using an imperfect energy loss function also faces other issues, as it causes stronger effects on the nuisance parameters than for instance the final states or the energy smearing technique. Furthermore, the final KATRIN energy loss function has not been measured yet, which intrinsically has some blinding effect. Measuring the energy loss function of 18.6 keV electrons in inactive deuterium gas is one of the critical points of the STS-IIIa commissioning measurements (conducted in autumn 2018). Though this is not the final T_2 energy loss function, discussions during the analysis of the D_2 energy loss function reveal enough information to construct an energy loss function that is deemed "good enough" to break the 2 eV sensitivity limit targeted for the first blind analysis. Furthermore, the effect of an artificially worse energy loss function has only been studied on the empirically derived energy loss function formula from the Troitsk experiment [Ase+00]. This empirically adapted parametrisation still shows discrepancies with theoretical calculations [Tro18]. The implications of these findings on the applicability of the method on KATRIN neutrino mass analysis are therefore not clear at this point.

6.6.6. Implicit blinding

When discussing about blinding techniques, it should not be forgotten that one option is to refrain from installing an explicit blinding scheme, but to rely on implicit blinding instead. Despite posing the risk of experimenter's bias, this would allow full access by everyone to the complete spectrum measured by KATRIN. Detection of relative drifts would be possible with full statistics as would be systematic studies in the endpoint region. The experimenter's bias might as well be caught in the well-established and accepted analysis review procedure which might reveal a poor basis or justification for choosing a specific cut (except for its effect on the neutrino mass). However, even if assuming 100% transparency of the analysis, the check of the analysis can only be done after the analysis is complete and might not reveal the bias.

Table 6.2.: **Overview of methods under study.** A (subjective) evaluation of the advantages and disadvantages of each method is given.

Method	Advantages	Disadvantages
Reduced statistics	• no modifications to the spectral shape • full access to the whole energy range • data blinding: strong control	• limited amount of data (measuring time) may enter in analysis • high uncertainty on systematics
Window blinding	• no modifications to the spectral shape • well-established blinding technique • data blinding: strong control	• large blinded energy window needed in the beginning • complicates systematic studies in endpoint region
Energy smearing	• full access to the whole energy range • detection of relative drifts possible • data blinding: strong control	• modifies the shape of the spectrum • uni-directional shift
FSD smearing	• full access to the whole energy range • detection of relative drifts possible	• model blinding: less control • uni-directional shift
Imperfect energy loss	• full access to the whole energy range • detection of relative drifts possible	• model blinding: less control • strong influence on nuisance parameter estimates
Implicit blinding	• full access to the whole energy range	• no control, rely on user's responsibility • risk of bias, community trust

6.6.7. Unblinding

If the KATRIN collaboration decides to perform a blind analysis, commitment is made to publish the result swiftly after unblinding. There is also the option to publish a blinded and an unblinded result, posing full transparency to the community and all information about the analysis. What is still to be defined is the road to unblinding: which criteria does the respective analysis need to fulfil, which checkpoints does it have to pass? Answers to those questions are directly related to the blinding technique used, therefore these criteria can only be fully defined after the decision for a certain blinding strategy has been made.

As a collaboration it is certainly a great moment to unblind an analysis. Independent of the method used, an "unblinding event" will bring together many members of the KATRIN collaboration in one place. The revealing of the blinding key is either granting access to the unblinded data or allowing analysts to use the unblinded model. Either way, the final analysis can be performed during this "unblinding event" and the result published shortly afterwards.

6.7. Conclusion and outlook

None of the KATRIN predecessor neutrino mass β-decay experiments (Los Alamos, Troitsk, and Mainz) performed a blind analysis of the measured tritium spectrum. This makes the presented blinded studies the first application of blinding techniques in neutrino mass β-decay spectroscopy. Intrinsically, this involved testing various methods with respect to their potential to blind the neutrino mass to a level comparable to the current experimental knowledge of bounds on the neutrino mass.

In the course of this chapter, two different roads for a blind neutrino mass analysis of KATRIN data have been presented: data and model blinding. The three data blinding methods (reduced statistics, window blinding, and energy smearing) and two model blinding methods (FSD smearing and imperfect energy loss function) were investigated not only with simulations and ensemble tests, but also have been successfully implemented for and tested on krypton data. An application of the blinding tests to tritium data from the First Tritium campaign has been started in the scope of this thesis, and is currently still under investigation – with very promising preliminary results. All methods presented so far enable performing a blind neutrino mass analysis of KATRIN data with an artificially decreased sensitivity below the current limit on the neutrino mass.

The discussion of the individual strengths and weaknesses of the five methods yielded several points in favour or against each specific method (compare tab. 6.2). Concerning the first neutrino mass analysis of KATRIN data, the author favours to blind the model. Though the commissioning measurements from the First Tritium campaign [Are+19] showed great agreement between model and data, the nominal high statistics data from a tritium purity larger by a factor of 200 might reveal features that are hidden in the low statistics of the First Tritium data. Therefore, it is proposed to use the first 30 d of nominal KATRIN data as a test run with automated unblinded fits[9] while applying FSD smearing model blinding on the analyst

[9] With fixed cuts in the run processing chain, either hiding or fixing the neutrino mass estimate.

side. The smeared final states will be provided to the analysts beforehand, with the smearing value hidden. As discussed in sec. 6.6.4, the analysts have to ensure that any neutrino mass analysis they perform before unblinding is using the smeared version of the final states via a hash-check in the fitter. Due to the importance of the first neutrino mass data, it could be considered to blind the data additionally to the model. For a combination of energy smearing and final states smearing with both smearings unknown, it is impossible to guess the neutrino mass shift as the two cause opposite effects. After the first "unblinding event", KATRIN could thus envision a neutrino mass sensitivity in the sub-eV range.

This intermediate sensitivity would subsequently serve as the blinded limit for the next data taking period. Since in this scenario the unblinded FSD would have been distributed in the course of the unblinding, either a new method has to be used for the next 1 yr of data taking, or a new version of the blinded FSD has to be distributed. During the first 30 d of nominal KATRIN operation, more cross-checks and data quality measures will be established aside to fit parameter stability to ensure adequate operation of the KATRIN experiment. This will enable using data blinding to ensure unbiased analysis of the next KATRIN neutrino mass data. Furthermore, the amount of data blinding necessary to meet the 0.7-0.8 eV sensitivity with the 1 yr data is reduced a lot compared to the initial 2 eV: for window blinding, the window can be as small as about 7 V while the energy smearing can be as small as 0.5 eV (without revealing its interval) or 0.75 eV (if revealing its interval). Also the experience gained during the Krypton and the First Tritium campaigns plus the first 30 d of nominal KATRIN data will help in determining whether KATRIN runs as expected. For the full 3 yrs of KATRIN data, the window blinding is the method favoured by the author: it requires only a window of about $2 - 3$ V to hold the $0.3 - 0.4$ eV sensitivity which could be targeted within about the first year of nominal KATRIN data. Compared to the measuring time interval that could be spread over more than 50 V, this is a price that might seem affordable to get a well-trusted and well-received final neutrino mass analysis. The energy smearing, by contrast, would intrinsically impose a change of the spectral shape which might hide features over a broader range than the $2 - 3$ V hidden by the window blinding.

CHAPTER 7

PHYSICS BEYOND THE NEUTRINO MASS

"All of physics is either impossible or trivial. It is impossible until you understand it, and then it becomes trivial."
– Sir Ernest Rutherford –

The evidence of non-zero neutrino masses [Fuk+98, Ahm+01] has opened the door towards an extension of the established Standard Model of particle physics (SM): in the SM, neutrinos are treated as massless (see sec. 1.1.2) and a consistent theory to explain the non-zero mass has not yet been established. In this sense, the determination of the neutrino mass itself already will shed a light on "new physics".

But besides determining the neutrino mass with sensitivity improved by one order of magnitude, the precision tritium β-spectrum to be measured with KATRIN also promises a chance at testing interesting new physics. One such opportunity, examined in [Mer+15], are sterile neutrinos at the keV scale, which form well-motivated candidates for warm dark matter, or at the eV scale [FB11, SH11, EO12, Kle14], motivated through various anomalies observed in short-baseline neutrino oscillations. In the thesis at hand, three more cases are investigated:

1. exotic light bosons which could be emitted during the β-decay, resulting in a 4-body decay,

2. hypothetical right-handed currents which might occur symmetrically to the standard left handed currents of the weak interaction,

3. the capture of relic neutrinos which trace back to the very beginning of our universe.

This chapter describes how the corresponding physics models are implemented in the KATRIN analysis and simulation frameworks SSC and KaFit. Thereby, the sensitivity of KATRIN to constrain parameters of these new physics models can be tested. At the end of this chapter, a conclusion summarises the findings and gives an overview of the results.

7.1. Light bosons

New physics often is expected to manifest at high energies. However, with recent more stringent bounds on heavy particles from collider experiments, the interest of particle-physics phenomenology is also drawn towards "light" new physics. With an energy range in the β-decay of tritium of up to 18.6 keV, the KATRIN experiment is well positioned to probe new physics on the eV to keV-scale. The following section will deal with the hypothetical emission of light bosons (*pseudoscalar* or *vector* bosons) from the neutrino and electron of tritium β-decay. This scenario was recently proposed by W. Rodejohann and coworkers and has been studied in [Arc+18]. In the course of the thesis at hand, the proposed scenarios were implemented into the KATRIN analysis framework to derive the statistical sensitivity of KATRIN in terms of constraining the additional emission of eV-scale light bosons, which is also described in ref. [Arc+18]. The keV-scale statistical sensitivity included in the same work was derived by M. Slezák and is described in this chapter to complete the picture of the two different mass regimes.

First, the experimental electron spectrum with this additional new interaction is introduced. Afterwards, the potential of KATRIN to constrain the additional emission of light bosons in β-decay is estimated for the current KATRIN set-up[1], that is, in a limited energy range close to the spectral endpoint, and also for a potential modification with a future TRISTAN-like detector [Mer+15, Mer+18] to access the full energy range in a differential spectrum measurement.

7.1.1. Behaviour of the spectral shape by introducing a light boson

The standard β-decay investigated by KATRIN is a three-body decay resulting in the transformation of tritium into helium and production of an electron anti-neutrino together with an electron (see eq. 2.1). The decay energy of 18.6 keV may also produce additional particles like a light boson with masses up to 18.6 keV, which would result in a four-body decay

$$\mathrm{T} \rightarrow {}^{3}\mathrm{He}^{+} + \mathrm{e}^{-} + \bar{\nu}_{\mathrm{e}} + \mathrm{X}\,, \tag{7.1}$$

with X being the new light boson, either of pseudoscalar or vector boson type.

The emission of this new light boson would result in a modified maximum energy of the emitted electron (with T representing ^{3}H):

$$E_e^{\max'} = \frac{m_{\mathrm{T}_2}^2 - \left(m_{\mathrm{T}^3\mathrm{He}^+} + m_\nu + m_{\mathrm{X}}\right)^2 + m_{\mathrm{e}}^2}{2m_{\mathrm{T}_2}}, \tag{7.2}$$

see eq. (10) of ref. [Arc+18]. In the aforementioned work, several well-motivated scenarios are derived for the emission of such a new boson.

Since the exact analytical representation is highly cumbersome, a suitable approximation can be used for the decay rate:

$$\frac{\mathrm{d}\Gamma}{\mathrm{d}E_{\mathrm{e}}} = K\sqrt{\frac{E_{\mathrm{e}}}{m_{\mathrm{e}}} - 1}\left(1 - \frac{E_{\mathrm{e}}}{E_{\mathrm{e}}^{\max'}}\right)^{n} F(Z, E_{\mathrm{e}})\,. \tag{7.3}$$

[1] The experimental settings assumed can be found in the appendix D.1.

Therein, $F(Z, E_\mathrm{e})$ is the Fermi function describing the interaction between the outgoing electron and the helium nucleus. K is a normalisation factor related to the coupling g_X. Both K and the index n are specific for the given type of boson. The different types of bosons are introduced in the following.

A. *Pseudoscalars emitted from neutrinos*: In majoron models [CMP81, SV82], pseudoscalars X may couple to neutrinos ν, represented by the Lagrangian

$$\mathcal{L}_\mathrm{A} = i\, g_{\nu\mathrm{X}}\, \bar{\nu}\, \gamma_5\, \nu\, \mathrm{X}\,. \tag{7.4}$$

For $m_\mathrm{X} < 100\,\mathrm{eV}$ which is about the range testable in the standard KATRIN set-up, Arcadi et al. [Arc+18] find $K \simeq 10^{-25} g_{\nu\mathrm{X}}^2$ and $n \simeq 2$.

B. *Pseudoscalars emitted from electrons*: In axion models or one-loop level majoron models [CMP81, SV82], pseudoscalars X may also couple to electrons e, represented by the Lagrangian

$$\mathcal{L}_\mathrm{B} = i\, g_{\mathrm{eX}}\, \bar{\mathrm{e}}\, \gamma_5\, \mathrm{e}\, \mathrm{X}\,. \tag{7.5}$$

Again, for $m_\mathrm{X} < 100\,\mathrm{eV}$, Arcadi et al. [Arc+18] find $K \simeq 10^{-27} g_{\mathrm{eX}}^2$ and $n \simeq 4$.

C. *Vector bosons emitted from neutrinos*: A Z-like coupling to left-handed[2] massless neutrinos is represented by the Lagrangian

$$\mathcal{L}_\mathrm{C} = g_{\nu\mathrm{L}}\, \bar{\nu}\, \gamma^\mu\, P_\mathrm{L}\, \nu\, \mathrm{X}_\mu + \mathrm{h.c.}\,, \tag{7.6}$$

with the left-handed projection operator $P_\mathrm{L} = \frac{1}{2}(1 - \gamma_5)$. For $m_\mathrm{X} < 100\,\mathrm{eV}$, Arcadi et al. [Arc+18] find $K \simeq 7 \times 10^{-22} g_{\nu L}^2 (\mathrm{keV}/m_\mathrm{X})^2$ and $n \simeq 4$. Note the characteristic $1/m_\mathrm{X}^2$ divergence due to the coupling to a non-conserved current [DLP17b, DLP17a].

D. *Vector bosons emitted from electrons*: A Z-like coupling to electrons[3] would result in the following Lagrangian

$$\mathcal{L}_\mathrm{D} = \bar{\mathrm{e}}\, \gamma^\mu\, (g_{\mathrm{eL}}\, P_\mathrm{L} + g_{\mathrm{eR}}\, P_\mathrm{R})\, \mathrm{e}\, \mathrm{X}_\mu + \mathrm{h.c.}\,. \tag{7.7}$$

As a simplification, the generally different couplings to the different chiralities will be taken to be equal, $g_{\mathrm{eL}} = g_{\mathrm{eR}} = g_{eV}$. For $m_\mathrm{X} < 100\,\mathrm{eV}$, Arcadi et al. [Arc+18] find $K \simeq 7 \times 10^{-22} g_{eV}^2 (\mathrm{keV}/m_\mathrm{X})^2$ and $n \simeq 4$. Note again the characteristic $1/m_\mathrm{X}^2$ divergence due to the coupling to a non-conserved current [DLP17b, DLP17a]. Since the $\mathrm{X} = \mathrm{Z}'$ coupling to electrons or neutrinos only shows differences for boson masses above 1 keV [Arc+18], they are treated as being equal on the eV scale.

E. *Vector bosons emitted from neutrinos and electrons*: In contrast to the cases C and D, this type of vector boson couples to the conserved electron-number current j_{L_e} through the Lagrangian

$$\mathcal{L}_\mathrm{E} = g_{L_e}\, j_{L_\mathrm{e}}^\alpha\, \mathrm{X}_\alpha = g_{L_e}\, (\bar{\nu}_\mathrm{e} \gamma^\alpha P_L \nu_\mathrm{e} + \bar{\mathrm{e}} \gamma^\alpha \mathrm{e})\, \mathrm{X}_\alpha\,. \tag{7.8}$$

This coupling has a qualitatively different behaviour than for C or D: the two divergences from C and D cancel each other such that K is approximately constant for $m_\mathrm{X} < 100\,\mathrm{eV}$. For $m_\mathrm{X} < 100\,\mathrm{eV}$, Arcadi et al. [Arc+18] find $K \simeq 4 \times 10^{-24} g_{L_\mathrm{e}}^2$ and $n \simeq 2$.

[2] Massless neutrinos can only be left-handed.

[3] massive electrons can be either left- or right-handed

For better readability and overview, tab. 7.1 summarises the different origins of the new light boson introduced in the aforementioned list, with g_X representing the different coupling of each boson type. For an overview of K and n over the whole energy range of 18.6 keV, the reader is referred to fig. D.6 in the appendix. The expected produced electron rates of the different types are shown in fig. 7.1.

Table 7.1.: **Overview of production mechanisms for new light bosons.** The table summarises the various production mechanisms with values K and n approximated for small $m_X < 100\,\text{eV}$ (compare fig. D.6).

Mechanism	K/g_X^2	n
A: Pseudoscalars emitted from neutrinos	10^{-25}	2
B: Pseudoscalars emitted from electrons	10^{-27}	4
C: Vector bosons emitted from neutrinos	$7 \times 10^{-16} \cdot (\text{eV}/m_X)^2$	4
D: Vector bosons emitted from electrons	$7 \times 10^{-16} \cdot (\text{eV}/m_X)^2$	4
E: Vector bosons emitted from ν and e	5×10^{-24}	2

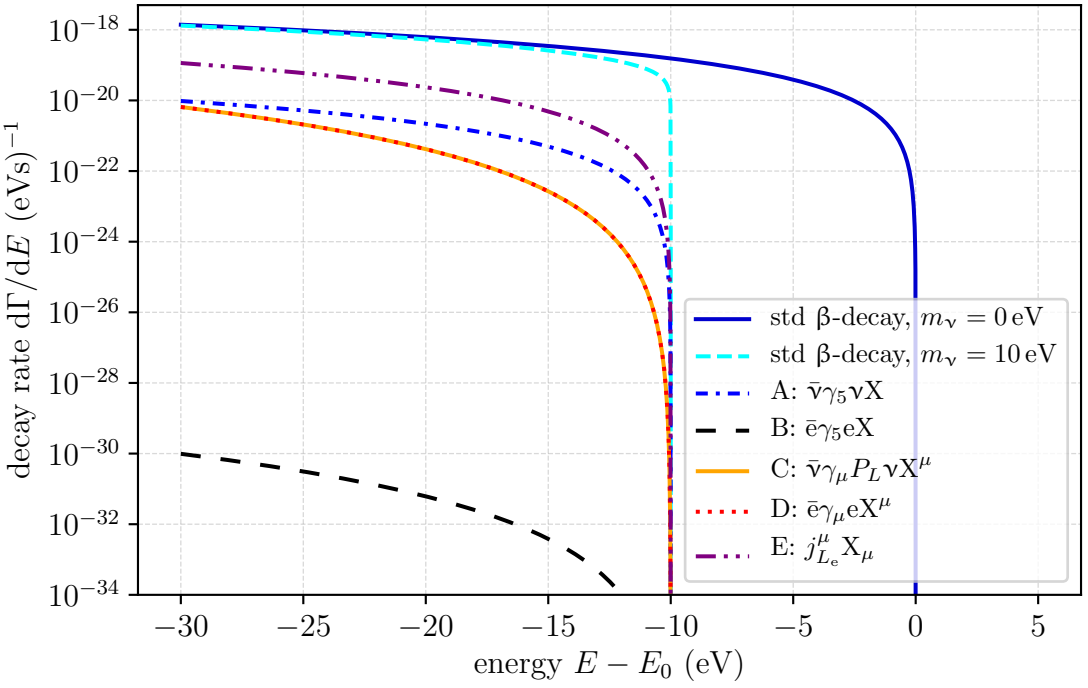

Figure 7.1.: **Decay rates for various scenarios as a function of $E - E_0$.** The standard β-decay w/o neutrino mass (a large neutrino mass of $m_\nu = 10\,\text{eV}$ is assumed for better visualisation), as well as the decay rates expected for the additional emission of a light boson X with $g_X = 1$, $m_X = 10\,\text{eV}$ are visualised. Figure from ref. [Arc+18].

In order to compare the theoretical prediction for the light bosons to data taken by the KATRIN experiment, several modifications to the theoretical form given in eq. (7.3) are applied. The extensions mostly account for characteristics of the gaseous, molecular tritium source of the experiment. In the end, the decay rate for

the emission of a new light boson takes the following form:

$$\left.\frac{\mathrm{d}\Gamma}{\mathrm{d}E}\right|_{\mathrm{X}} = \frac{K}{\hbar}\sqrt{\frac{E}{m_{\mathrm{e}}}} \cdot F(Z', E) \sum_{fs} P_{fs} \cdot f_{\mathrm{rad}}(E - E_{fs}) \cdot \left(\frac{E_{\mathrm{max},\, fs} - E}{E_{\mathrm{max},\, fs} + m_{\mathrm{e}}}\right)^{n}, \tag{7.9}$$

with E being the kinetic energy of the electron, $F(Z', E)$ the Fermi function, P_{fs} and E_{fs} the probability and energy of the corresponding final state, $f_{\mathrm{rad}}(E - E_{fs})$ the radiative correction and

$$E_{\mathrm{max}} = E_{\mathrm{e}}^{\mathrm{max}'} - m_{\mathrm{e}} - (m_{\nu} + m_{\mathrm{X}}) = E_0 - (m_{\nu} + m_{\mathrm{X}}) \tag{7.10}$$

the maximum kinetic energy of the electron (with endpoint energy E_0). The extension terms in eq. (7.9) are discussed in the following.

7.1.1.1. Modifications to the theoretical spectrum

The largest impact when going from the theoretical spectrum to the experimentally measured one is due to the excited final states the tritium decay daughter molecule may be left in (see sec. 2.2.2). The daughter molecule may be left in a rotational-vibrational or electronically excited state with energy E_{fs}, reducing the energy available for the electron accordingly:

$$E_{\mathrm{max},\, fs} = E_{\mathrm{max}} - E_{fs} = E_0 - E_{fs} - (m_{\nu} + m_{\mathrm{X}})\,. \tag{7.11}$$

As about 57 % of the decays result in the electronic ground state of the daughter molecule with only small ro-vibronic excitation energy, the final states reduce the electron rate in the endpoint region by about a factor of two. With the minor energy dependence of the molecular recoil energy in the endpoint region (see sec. 2.2.2), the 1.7 eV recoil energy is absorbed into the final states distribution [Kle+18]. Another notable effect is the Doppler broadening due to the non-zero temperature of the tritium gas inside the source (see sec. 2.2.1), which for 30 K results in a Gaussian broadening of the spectrum of about 100 meV [Kle+18]. Minor effects occur due to radiative corrections, which are implemented according to the recommendation by Repko and Wu [RW83].

7.1.1.2. Combination with standard β-decay

Since the coupling of the light boson is not constrained ab initio and shall be determined by experiment, the light boson electron spectrum is added without any pre-factor to the standard β-decay decay rate. This defines the form of the overall spectrum as

$$\frac{\mathrm{d}\Gamma}{\mathrm{d}E} = \left.\frac{\mathrm{d}\Gamma}{\mathrm{d}E}\right|_{\beta} + \left.\frac{\mathrm{d}\Gamma}{\mathrm{d}E}\right|_{\mathrm{X}}. \tag{7.12}$$

As introduced in sec. 2.3, KATRIN measures an integrated spectrum with the high voltage U at the main spectrometer acting as a high-pass filter [KAT05]. Using the concept of a response function $R(E, qU)$ [Kle+18], the measured spectrum can be written as

$$\dot{N} = C \int_{qU}^{\infty} R(E, qU) \left(\left.\frac{\mathrm{d}\Gamma}{\mathrm{d}E}\right|_{\beta} + \left.\frac{\mathrm{d}\Gamma}{\mathrm{d}E}\right|_{\mathrm{X}}\right) \mathrm{d}E + Bg, \tag{7.13}$$

with the constant C absorbing experimental characteristics like detection efficiency and number of tritium nuclei present in the source (compare sec. 2.3), and the background rate Bg. The effect on the integrated spectrum that KATRIN investigates is visualised in fig. 7.2 for $g_X = 5$, $m_X = 10\,\mathrm{eV}$. The effect of the light boson is mainly a normalisation effect on the amplitude, as the signature depends on the coupling strength g_X.

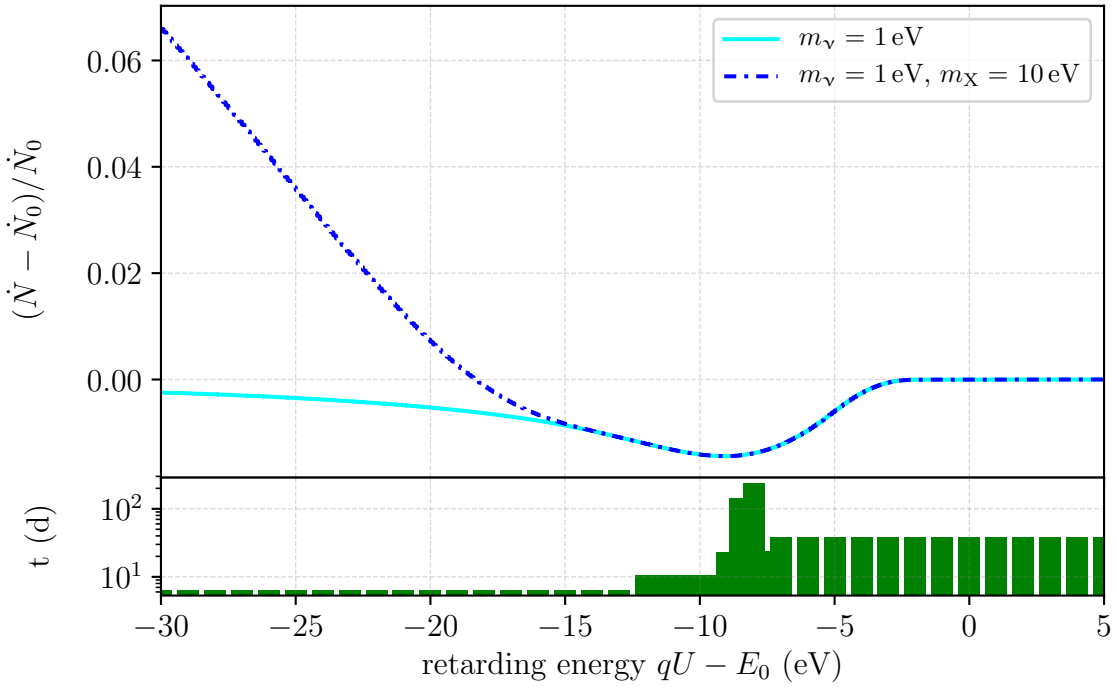

Figure 7.2.: **Effect of the additional light boson on the integrated rates spectrum.** The null-hypothesis is $\dot{N}_0$ with zero neutrino mass and no light boson. Solid cyan is the effect of a non-zero neutrino mass, while dash-dotted blue shows the imprint of a 10 eV light boson mass. For simplicity, only the $E_{fs} = 0$ component of the FSD is used in this figure. Lower plot shows an excerpt of the underlying MTD, note that it extends towards $E_0 - 50\,\mathrm{eV}$ (outside of the plotting range of the figure).

7.1.2. Statistical sensitivity for eV-scale light bosons

The potential of KATRIN to constrain the emission of a light boson additional to the standard β-decay can be investigated in form of confidence intervals in sensitivity curves. Estimation of confidence intervals in the presence of nuisance paramters π can easily lead to errors, for instance when neglecting correlations between the nuisance parameters and the parameters of interest Θ. Uncertainties on the parameters of interest may easily be underestimated thereby.

One method to minimise this risk is the profile likelihood [RLC05]. This method uses a likelihood ratio test statistic[4] to extract confidence limits from the likelihood

[4] converges to a χ^2 random variable

function, similar to the χ^2 method. The profile likelihood is defined as

$$L_p(\Theta) = L(\Theta, \hat{\pi}(\Theta)) \tag{7.14}$$

with $\hat{\pi}(\Theta)$ the function maximising the likelihood L with respect to its nuisance parameters π. With the best fit estimate $\hat{\Theta}$, the likelihood ratio test statistic can be defined as

$$\lambda(\Theta) = \frac{L_p(\Theta)}{L_p(\hat{\Theta})}. \tag{7.15}$$

Now the profile likelihood is scanned to obtain values for Θ where the evaluation of eq. (7.14) increases by a specific factor. One example is finding the 1σ intervals of a single parameter Θ. Likelihood values are searched for Θ where $-2\Delta \log L_p(\Theta) = -2 \log \lambda = 1$. To obtain exclusion or sensitivity curves, several values of Θ are used to compare the likelihood against the null-hypothesis while at each point minimising the likelihood with respect to the nuisance parameters.

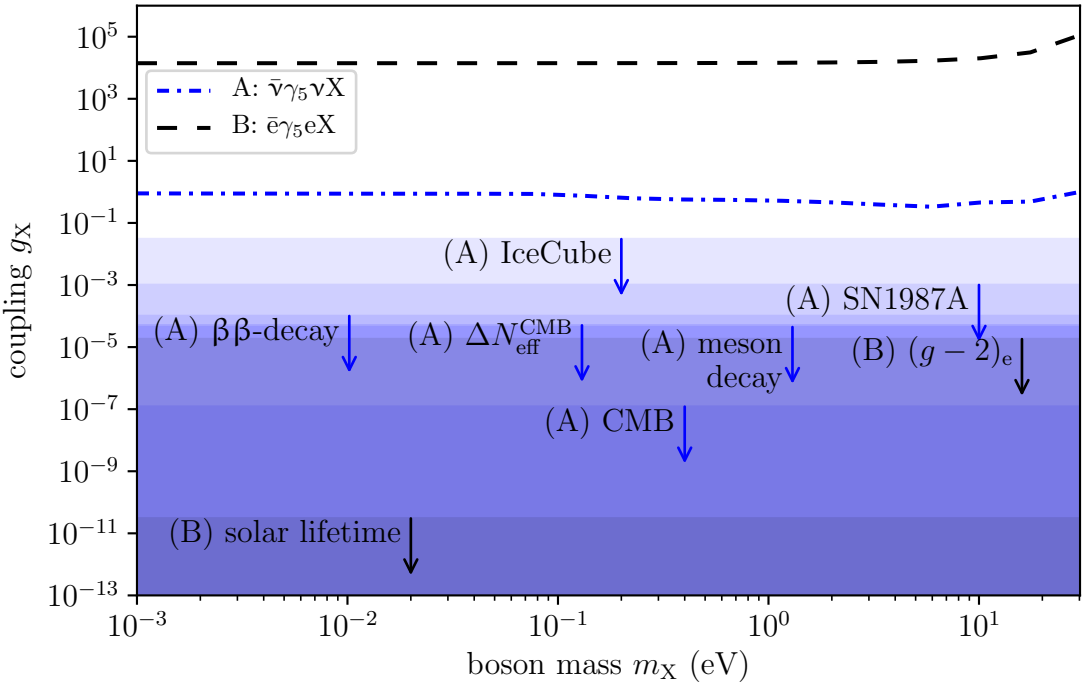

Figure 7.3.: **Statistical sensitivity for eV-scale pseudoscalars.** The lines represent the 90 % C.L. statistical sensitivity of KATRIN for types A, B (defined according to tab. 7.1). The parameter regions allowed from constraints discussed in sec. 7.1.4 are marked as shaded areas.

For the potential of KATRIN to constrain the additional emission of light bosons in β-decay, there are two parameters of interest: g_X and m_X. Therefore, the likelihood for non-vanishing (g_X, m_X) is compared to the null-hypothesis of no light boson $(0, 0)$. In details, this means minimisation of the likelihood over m_ν^2, E_0, *Amp* and *bg* (m_ν^2 is a nuisance parameter in this case) for every point in the 2-dim grid (g, m_X). Then it is possible to find likelihood ratios corresponding to 90 % C.L. Next, the five different scenarios introduced in sec. 7.1.1 will be inspected one by one.

A. *Pseudoscalars emitted from neutrinos*: the form of the spectrum suggests increasing sensitivity with increasing coupling g_X (see tab. 7.1). The sensitivity

curves in fig. 7.3 confirm this expectation. Furthermore it can be seen that the sensitivity decreases again for masses larger than 10 eV: the sensitivity on the mass m_X is affected by the range of retarding energies of the MTD. Since the MTD used to obtain the sensitivity curves only extends towards 50 eV below the endpoint (see sec. D.1 in the appendix), masses larger than 50 eV lie outside the measuring interval.

B. *Pseudoscalars emitted from electrons*: the branching ratio for this coupling is rather small compared to the other production mechanisms. Rather large couplings g_X are required in order for KATRIN to be sensitive towards this kind of light bosons. This expectation is confirmed from fig. 7.3: the coupling strength reachable is four to five orders of magnitude larger than the coupling which can be probed for bosons of type A (pseudoscalar coupled to neutrinos). As for type A, masses larger than 50 eV are outside the MTD used for these studies and are therefore not testable.

C. & D. *Vector bosons emitted from neutrinos or electrons*: Since the electron spectra of production mechanisms C and D are the same for eV-scale bosons (compare tab. 7.1), the sensitivity curve is the same for both. In contrast to types A and B, the spectrum for coupling to C and D exhibits a $1/m_X^2$ divergence in the normalisation factor K (compare eq. (7.3) and tab. 7.1). Therefore, small boson masses m_X are strongly favoured, which should lead to higher sensitivity of KATRIN for smaller boson masses. This expectation is confirmed from fig. 7.4: in contrast to cases A and B, KATRIN has increased statistical sensitivity to bosons of type C and D towards lower boson masses. Concerning larger boson masses, the limitations by the width of the MTD can be seen.

E. *Vector bosons emitted from neutrinos and electrons*: From the spectral form, a similar behaviour as for type A is expected (compare tab. 7.1). Figure 7.4 confirms this expectation, with best sensitivity for light bosons with mass of order eV.

7.1.3. Statistical sensitivity for keV-scale light bosons

An extension of the study, included in ref. [Arc+18], tests the statistical sensitivity of a differential measurement of the complete tritium β-spectrum towards probing of higher boson masses. These results are summarised here for the sake of completing the picture[5]. The study foresees to replace the FPD with a detector with an energy resolution of 300 eV [Mer+18] (one order of magnitude better) and thereby have the energy of the electrons determined by the detector, while the main spectrometer only guides the electrons to the detector. The measurement time foreseen for this new set-up is also three years, with a current estimate of the background of 2 mcps/keV (based on measurements with the current FPD detector [Har15]).

With the above mentioned profile likelihood method plus a Gaussian pull term on the neutrino mass of 2 eV[6], the sensitivity of a TRISTAN-like set-up towards the

[5] The keV-scale study was conducted by M. Slezák.

[6] The value representing the current neutrino mass limit from β-decay [Tan+18].

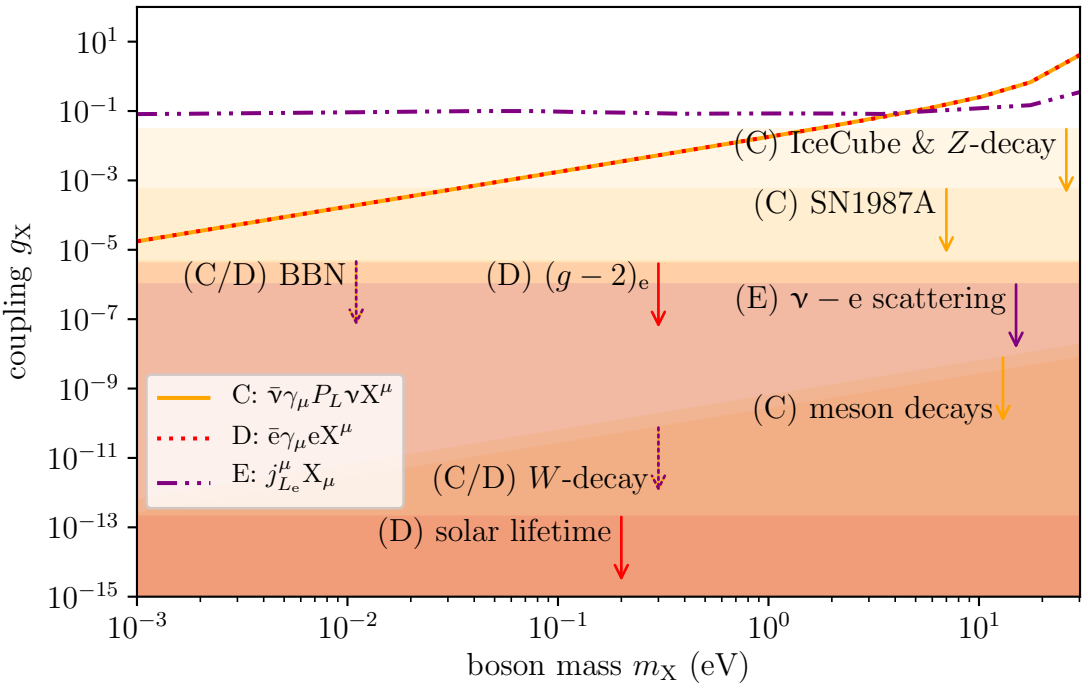

Figure 7.4.: **Statistical sensitivity for eV-scale vector bosons.** The lines represent the 90 % C.L. statistical sensitivity of KATRIN for types C, D, and E (defined according to tab. 7.1). The parameter regions allowed from constraints discussed in sec. 7.1.4 are marked as shaded areas.

emission of light bosons can be explored. The sensitivity drops for light boson masses approaching the maximum decay energy of 18.6 keV, as the corresponding phase space vanishes. Qualitatively, the sensitivity curves are similar to the eV-scale estimations with a relatively small branching ratio for type B, compared to the other mechanisms (see fig. 7.5). Also, the $1/m_X^2$ behaviour of the decay rate of types C & D is visible in the sensitivity curve of the vector bosons, fig. 7.6. For light boson masses larger than 5 keV, the sensitivity for type E and C are identical, in contrast to the case of eV-scale bosons. When comparing the estimated sensitivities for eV- and keV-scale light bosons, the different underlying experimental set-up should be taken into account (i.e., integral versus differential access to the β-spectrum).

7.1.4. Discussion and comparison to existing bounds

The scenario of tritium β-decay with additional emission of light bosons was proposed by W. Rodejohann and colleagues in ref. [Arc+18]. In the thesis at hand, the statistical sensitivity of KATRIN to test the emission of light bosons of eV-mass scale is elaborated. The settings of the KATRIN experiment used to obtain fig. 7.3 and fig. 7.4 slightly deviate from the ones used in ref. [Arc+18]. It was decided to use those hypothetical settings in order to test the effect of an elevated background rate compared to the design value, as found in several commissioning measurements [Har15, Are+18b, Blo18, Tro18]. With the hypothetical 20 eV widened scan range compared to ref. [Arc+18], the statistical sensitivity to the five eV-scale light boson scenarios is of the same order of magnitude, with at most a factor of

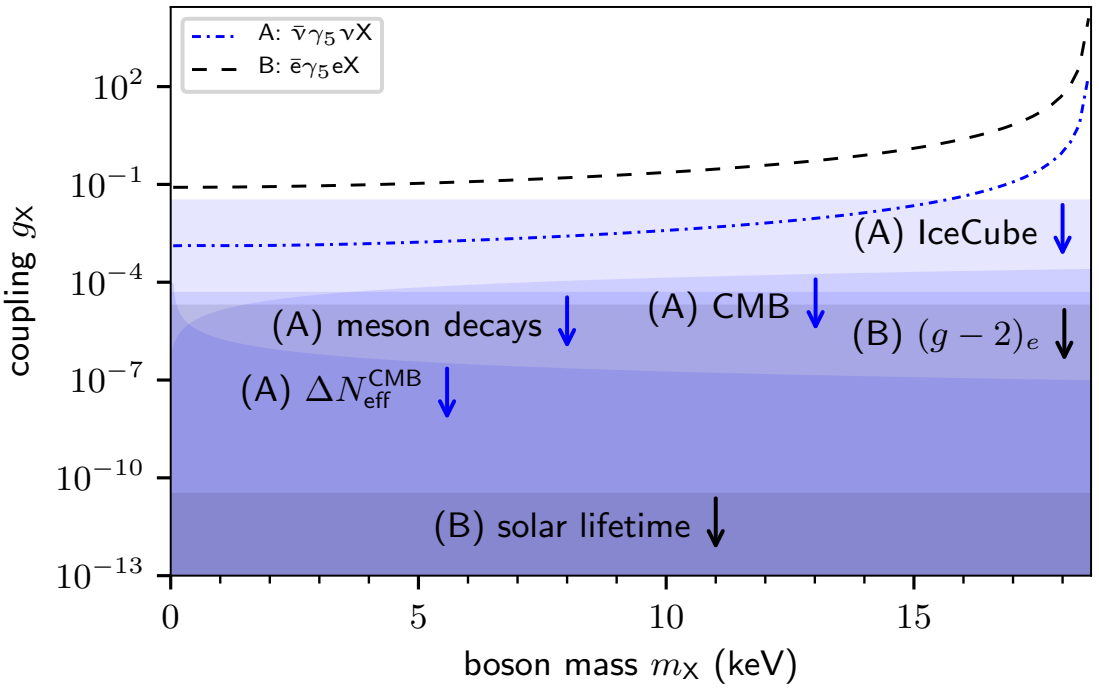

Figure 7.5.: **Statistical sensitivity for keV-scale pseudoscalars.** The lines represent the 90 % C.L. statistical sensitivity of a TRISTAN-like extension of KATRIN for light boson types A and B. The parameter regions allowed from constraints discussed in sec. 7.1.4 are marked as shaded areas. Figure taken from ref. [Arc+18], credits M. Slezák.

two difference. Therefore, the following discussion is qualitatively very similar to ref. [Arc+18].

In the work at hand, only the statistical sensitivity of KATRIN towards the additional emission of light bosons in β-decay is presented. For the final experimental sensitivity, also systematic effects as for the neutrino mass analysis [KAT05] (for the example of column density, see sec. 5.3.5) need to be included. Furthermore, it needs to be stressed that the eV- and keV-scale statistical sensitivity presented here only cover the case of one (physically most relevant) type of light boson. Some complications might arise when performing this study in light of additional sterile neutrinos. For eV-scale bosons, it was checked that moderate constraints on the coupling of the light boson (commensurate with present experimental bounds, e.g. $g_X < 1$ for boson type E) are enough to not impact the KATRIN neutrino mass sensitivity. This constraint is considered moderate, as existing bounds on the coupling of these light bosons are orders of magnitude more stringent than $g_X < 1$. A wide variety of these additional bounds is discussed in ref. [Arc+18], while in the following only a small excerpt is presented.

The most stringent bounds on the emission of light bosons discussed here come from observations of the sun. Since the light bosons are required to not alter the properties of the sun, constraints on the boson types coupled to electrons (B, D, E) can be derived. In case of a boson with pseudoscalar coupling to electrons (B), a limit of $g_X < 3 \times 10^{-11}$ has been obtained [GR09]. For vector bosons coupled to electrons, an even more stringent upper bound of $g_X < 2 \times 10^{-13}$ is obtained [GR09]. Since those bounds do not have a mass dependency, they apply to eV- and keV-scale

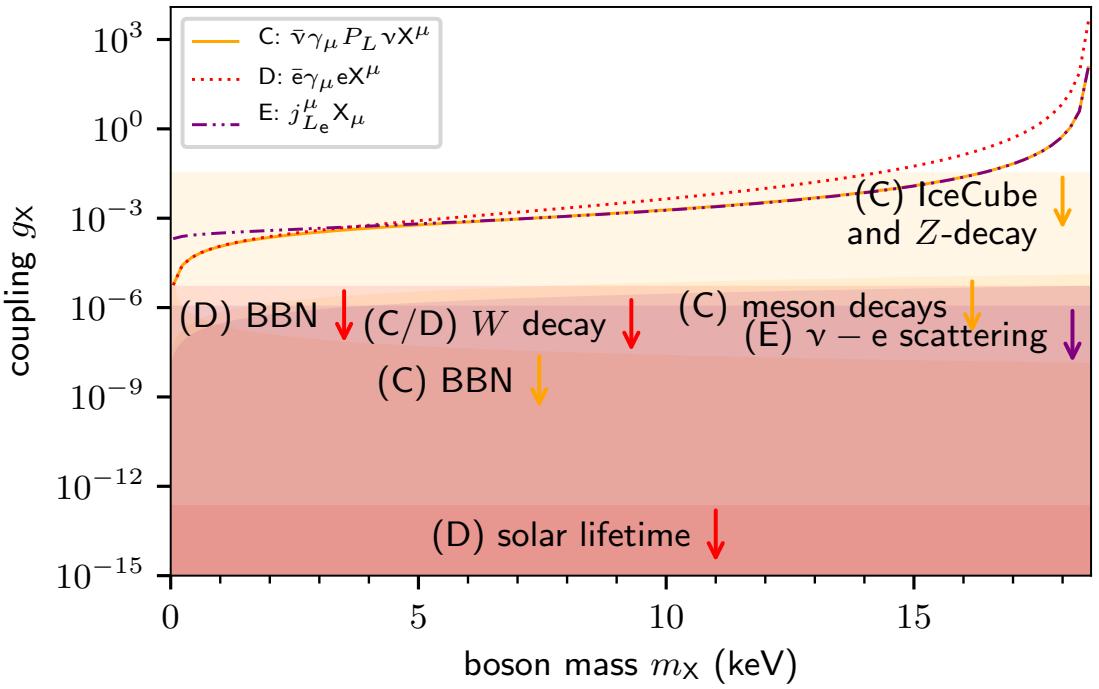

Figure 7.6.: **Statistical sensitivity contours for keV-scale vector bosons.** The lines represent the 90 % C.L. statistical sensitivity of a TRISTAN-like extension of KATRIN for light boson types C, D, and E. The parameter regions allowed from constraints discussed in sec. 7.1.4 are marked as shaded areas. Figure taken from ref. [Arc+18], credits M. Slezák.

bosons alike.

In contrast to bounds on bosons coupled to electrons, the bounds on neutrino coupled bosons are less stringent. For pseudoscalars coupled to neutrinos (A), with $m_X < 1\,\text{eV}$, neutrino annihilation becomes relevant. The corresponding coupling is constrained by Planck CMB data to $g_X < 1.2 \times 10^{-7}$ [AH14]. For vector bosons coupled to neutrinos (C), the most stringent bound is estimated from meson decays to $g_X < 2.2 \times 10^{-10} \frac{m_X}{\text{eV}}$ [BF17].

The bounds discussed so far are all below the parameter range accessible with KATRIN or the TRISTAN-modified KATRIN set-up[7]. However, it has to be noted that the laboratory experiment bounds from figs. 7.3, 7.4, 7.5, 7.6 are extrapolated from energies in the MeV range [Arc+18]. Furthermore, the IceCube [IM14] and Z-decay width [LDB14] constraints may be probed with both KATRIN set-ups for boson type C, and with TRISTAN for type A additionally (for an overview of all bounds, see tab. D.5). Therefore, an analysis of future KATRIN and TRISTAN data with respect to the emission of the light boson states discussed in this chapter represents a complementary approach to new physics at low energies on the eV and keV scale.

[7] For discussion of the intermediate bounds, the reader is referred to ref. [Arc+18].

7.2. Right-handed currents in presence of eV-scale sterile neutrinos

Numerous previous works have covered the sensitivity of KATRIN to sterile neutrinos on the eV [FB11, Kle14] as well as keV scale [Mer+15]. A model which could naturally lead to observable sterile neutrino masses and the seesaw mechanism is the Left-Right Symmetric Model (LRSM) [PS74, MP75, SM75]. As an extension to the Standard Model, it would restore parity on high energy scales by adding right-handed currents. W. Rodejohann and coworkers derived the general spectrum for tritium β-decay electrons with right-handed currents in presence of sterile neutrinos [BHR14]. Subsequently, N. Steinbrink et al. derived a model-independent parametrisation of this spectrum for eV-scale sterile neutrinos [Ste17, Ste+17]. The work at hand contributed substantially to the derivation of the statistical sensitivity of KATRIN to constrain the right-handed currents in presence of eV-scale sterile neutrinos in ref. [Ste+17] via an independent implementation of the spectra into a KATRIN simulation and analysis framework. In addition to ref. [Ste+17], the statistical sensitivity of KATRIN in the thesis at hand is evaluated for the scenario of an elevated background rate, based on a slightly different underlying measuring time distribution. The model-independent parametrisation of the LRSM used in ref. [Ste+17] is also the foundation of the results presented in this thesis.

First, a short introduction into the parametrisation is given, then exemplary MCMC results are shown before stating the statistical sensitivity of KATRIN to constrain right-handed currents in presence of eV-scale sterile neutrinos.

7.2.1. Spectral shape due to right-handed currents

In addition to the standard β-decay spectrum, we here deal with right-handed currents in presence of eV-scale sterile neutrinos. In ref. [Ste+17], a derivation of a model-independent parametrisation is given. Similar to the three active neutrinos being represented by one effective neutrino mass (see eq. (1.38)), the three additional sterile neutrinos from the LRSM are represented by one effective neutrino mass since it is possible to have at least one light sterile neutrino [Bor16]. The active neutrino mass in the following is defined as the light (electron-) neutrino mass m_l and the sterile neutrino mass as the heavy neutrino mass m_h. In line with the standard neutrino mixing, the active-sterile mixing is described by the mixing angle θ as $\sin\theta^2 = |U_{\mathrm{e}4}|^2$. Ignoring a potential CP-violating phase in the neutrino mixing matrix enables describing the mixing by a 2×2 rotation matrix. With some further re-parametrisation, it is possible to come up with a simpler form of the general spectrum derived in [BHR14].

7.2.1.1. Basic form of the spectrum

In refs. [Ste17, Ste+17], a model-independent parametrisation of the β-decay spectrum with right-handed currents in presence of eV-scale sterile neutrinos is derived:

$$\begin{aligned}\frac{\mathrm{d}\Gamma}{\mathrm{d}E} = &\left.\frac{\mathrm{d}\Gamma'}{\mathrm{d}E}\right|_{\mathrm{h}} \sin^2\theta_{\mathrm{eff}} + \left.\frac{\mathrm{d}\Gamma'}{\mathrm{d}E}\right|_{\mathrm{l}} \cos^2\theta_{\mathrm{eff}} \\ &+ c_{\mathrm{LR}} \cdot \left(\left.\frac{\mathrm{d}\Gamma'}{\mathrm{d}E}\right|_{\mathrm{h}} \frac{m_{\mathrm{h}}}{E_0 - E} - \left.\frac{\mathrm{d}\Gamma'}{\mathrm{d}E}\right|_{\mathrm{l}} \frac{m_{\mathrm{l}}}{E_0 - E} \right),\end{aligned} \tag{7.16}$$

with $(a_{\mathrm{LL}} + a_{\mathrm{RR}})$ being absorbed into the amplitude ($x = \mathrm{h}, \mathrm{l}$):

$$\left.\frac{\mathrm{d}\Gamma'}{\mathrm{d}E}\right|_{x} = (a_{\mathrm{LL}} + a_{\mathrm{RR}}) \cdot \left.\frac{\mathrm{d}\Gamma}{\mathrm{d}E}\right|_{x}. \tag{7.17}$$

Therein, $\left.\frac{\mathrm{d}\Gamma}{\mathrm{d}E}\right|_{x}$ is the β-spectrum with neutrino x as defined in eq. (1.37). The parametrisation of the interference term c_{LR} is given as [Ste+17]):

$$c_{\mathrm{LR}} = \frac{a_{\mathrm{LR}}}{a_{\mathrm{LL}} + a_{\mathrm{RR}}} \cdot \frac{m_{\mathrm{e}}}{m_{\mathrm{e}} + E_0} \cdot \cos\theta \sin\theta, \tag{7.18}$$

with the approximation $E \approx E_0$ in the endpoint region. The mixing angle in eq. (7.16) is an effective mixing angle, defined via

$$(a_{\mathrm{LL}} + a_{\mathrm{RR}}) \sin^2\theta_{\mathrm{eff}} = a_{\mathrm{LL}} \sin^2\theta + a_{\mathrm{RR}} \cos^2\theta, \tag{7.19}$$

$$(a_{\mathrm{LL}} + a_{\mathrm{RR}}) \cos^2\theta_{\mathrm{eff}} = a_{\mathrm{LL}} \cos^2\theta + a_{\mathrm{RR}} \sin^2\theta. \tag{7.20}$$

Since $a_{\mathrm{LL}} \approx 1$ and $a_{\mathrm{LR}}, a_{\mathrm{RR}} \approx 0$, the effective mixing angle θ_{eff} will essentially be equal to the physical mixing angle θ, causing the factor $(a_{\mathrm{LL}} + a_{\mathrm{RR}})$ to be 1 and therefore negligible in eq. (7.17). This model-independent parametrisation enables also to cover other conceivable mechanisms that need not to be based on left-right symmetry but cause the same effect on the β-spectrum.

The signature of β-decay electrons from right-handed currents in presence of light sterile neutrinos looks very similar to the one of sterile neutrinos without right-handed currents. At $E_0 - m_{\mathrm{h}}$, there is a kink in the spectrum, where the contribution of the heavy (sterile) neutrino mass m_{h} ends [Mer+15]. There is, however, one essential difference: the right-handed current may cause constructive and destructive interference. In the extreme case, this will manifest as a reduction of the rate, as can be seen from fig. 7.7. For the case of destructive interference (negative c_{LR}), the rate is reduced for $E < E_0 - m_{\mathrm{h}}$ (the heavy sterile part) and goes back to the standard case for $E_0 - m_{\mathrm{h}} < E < E_0$ (where only the light active neutrino contributes). For the case of constructive interference, the effect is the opposite. The boost and reduction are slightly more pronounced for the heavy (sterile) neutrino mass due to the m_ν / E_ν proportionality inside the interference term in eq. (7.16). Without the right-handed coupling interference term, the standard superposition of two spectra with different neutrino masses is observed, which manifests as a kink at $E_0 - m_{\mathrm{h}}$ as described in [Mer+15].

In order to show the mass dependency, the interference term is fixed to $c_{\mathrm{LR}} = 0.2$ with $\sin^2\theta_{\mathrm{eff}} = 0.2$ while the heavy (sterile) neutrino mass is varied. From fig. 7.8 it can be seen that the boost magnitude increases only slightly with m_{h}, but the region spans over a wider energy interval for larger m_{h}. As expected, the position of the kink is defined by m_{h}. These effects are less pronounced, when respecting the final states of the daughter molecule, as will be described in the next section.

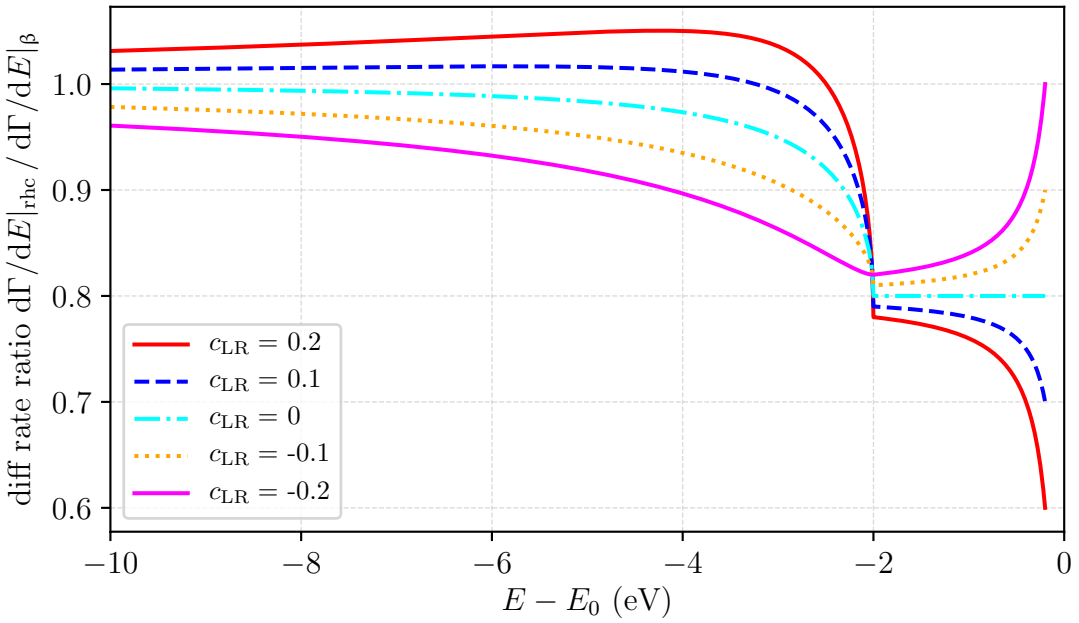

Figure 7.7.: **Effect of the right-handed coupling.** Shown is the ratio of a spectrum with left-right interference according to eq. (7.16) to a standard β-decay spectrum for different interference c_{LR}. Constant parameters are $\sin^2\theta_{\mathrm{eff}} = 0.2$, $m_{\mathrm{h}} = 2\,\mathrm{eV}$ and $m_{\mathrm{l}} = 0.2\,\mathrm{eV}$.

7.2.1.2. Model extensions

As introduced before (compare eq. (1.37) and eq. (2.2)), the basic form of the spectrum needs to be modified for several experimental effects. Since these modifications only affect the electron spectrum, they are treated in the same way (also see sec. 7.1.1). This section introduces the implementation of the final states into the right-handed currents spectrum. Since the final states can effectively be seen as a reduction of the maximum electron energy E_0, the implementation is straightforward. Equation (7.16) becomes

$$\begin{aligned}\frac{\mathrm{d}\Gamma}{\mathrm{d}E} = \sum_{fs} P_{fs} \Bigg[&\left.\frac{\mathrm{d}\Gamma'}{\mathrm{d}E}\right|_{\mathrm{h}} \sin^2\theta_{\mathrm{eff}} + \left.\frac{\mathrm{d}\Gamma'}{\mathrm{d}E}\right|_{\mathrm{l}} \cos^2\theta_{\mathrm{eff}} \\ &+ c_{\mathrm{LR}} \cdot \left(\left.\frac{\mathrm{d}\Gamma'}{\mathrm{d}E}\right|_{\mathrm{h}} \frac{m_{\mathrm{h}}}{E_0 - E_{fs} - E} - \left.\frac{\mathrm{d}\Gamma'}{\mathrm{d}E}\right|_{\mathrm{l}} \frac{m_{\mathrm{l}}}{E_0 - E_{fs} - E} \right) \Bigg].\end{aligned} \tag{7.21}$$

The effect of the final states on the spectrum is exactly the same as for the light bosons or the standard β-decay, the maximum kinetic energy of the electron is reduced and so is the electron rate close to the endpoint. Furthermore, the final states smear out distinct features of the spectrum, which can be seen from fig. 7.9 and fig. 7.10. Especially the position of the kink is not as clearly visible as before, which holds for all heavy neutrino masses (see fig. 7.10). Besides extending the model implementation by the final states, it needs to be respected that KATRIN measures an integrated spectrum

$$\dot{N} = C \cdot \int_{qU}^{\infty} R(E, qU) \frac{\mathrm{d}\Gamma}{\mathrm{d}E} \mathrm{d}E + Bg, \tag{7.22}$$

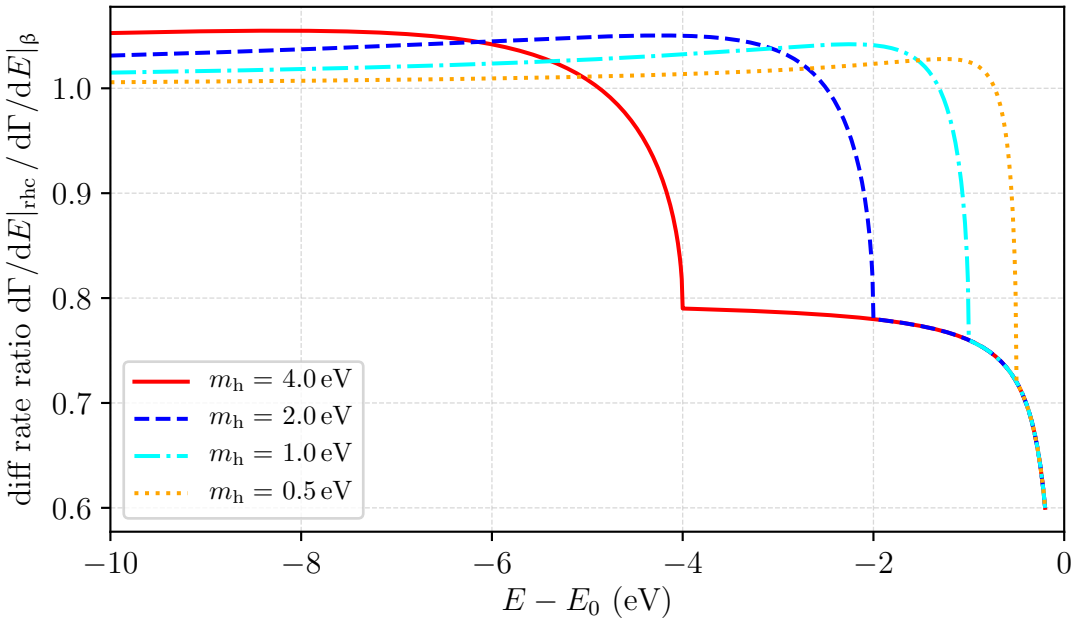

Figure 7.8.: **Effect of the heavy (sterile) neutrino mass.** Shown is the ratio of a spectrum with left-right interference according to eq. (7.16) to a standard β-decay spectrum for different heavy (sterile) neutrino masses m_{h}. Constant parameters are $\sin^2\theta_{\mathrm{eff}} = 0.2$, $c_{\mathrm{LR}} = 0.2$ and $m_{\mathrm{l}} = 0.2\,\mathrm{eV}$.

also compare sec. 2.3. In the following, the same KATRIN parameters as for the light boson estimates will be used (described in sec. D.1 and summarised in tab. D.4 in the appendix). With these settings, we can investigate the effect of the right-handed current coupling on the measured integrated spectrum.

In the integrated spectrum, the effect of the right-handed currents is weakened due to the integration. However, large interference values still have an effect on the shape of the integrated spectrum. The effect itself is similar to the effect on the differential spectrum, as can be seen from fig. 7.11 and fig. 7.12.

Compared to the differential spectrum, the relative c_{LR} signature is less pronounced by one order of magnitude for the same parameter combinations. In the differential spectrum, the parameters chosen cause a relative difference to the standard β-decay spectrum of up to 40 %, while in the integrated spectrum of only about 3 %. Still, the signal strength clearly increases with higher m_{h} (see fig. 7.12). Figure 7.12 also implies that heavy $m_{\mathrm{h}} \geq 1\,\mathrm{eV}$ stretch the signal beyond the KATRIN measuring interval assumed for the work in this thesis, while for smaller $m_{\mathrm{h}} \leq 1\,\mathrm{eV}$ the signal is essentially fully contained within the 50 eV measuring interval. This points towards limits for the sensitivity of KATRIN towards "heavier" sterile neutrinos. It is expected that there is a maximum sensitivity for the right-handed currents in presence of sterile neutrino masses below 50 eV, similar to the light bosons in sec. 7.1.

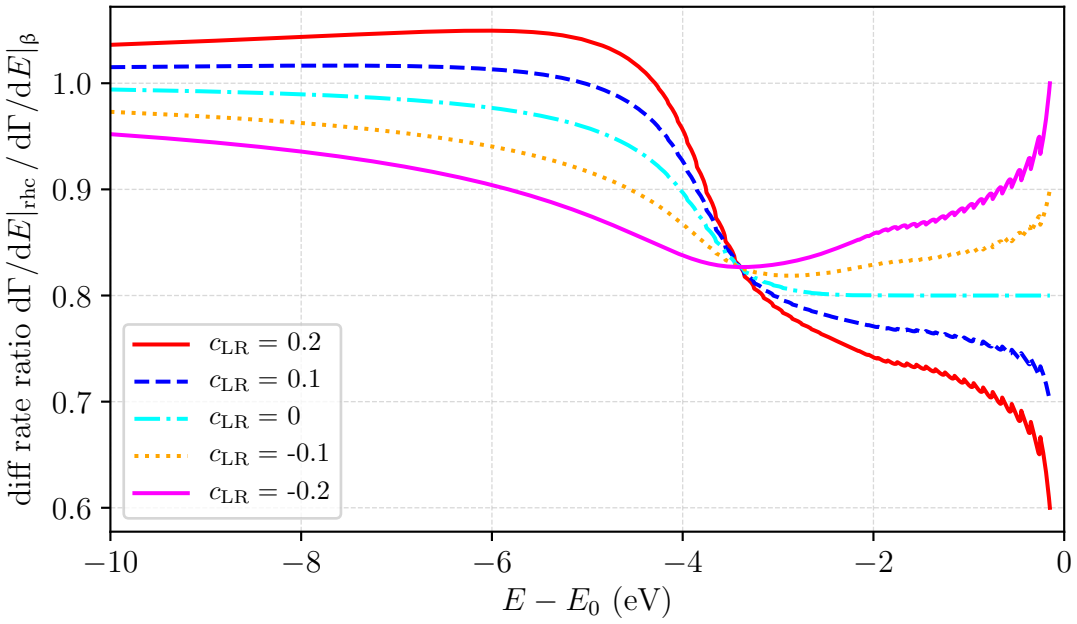

Figure 7.9.: **Effect of the right-handed coupling with final states.** Shown is the ratio of a spectrum with left-right interference according to eq. (7.21) to a standard β-decay spectrum for different interference c_{LR}. Constant parameters are $\sin^2\theta_{\mathrm{eff}} = 0.2$, $m_{\mathrm{h}} = 2\,\mathrm{eV}$ and $m_{\mathrm{l}} = 0.2\,\mathrm{eV}$. Compared to fig. 7.7, the kink is smeared out.

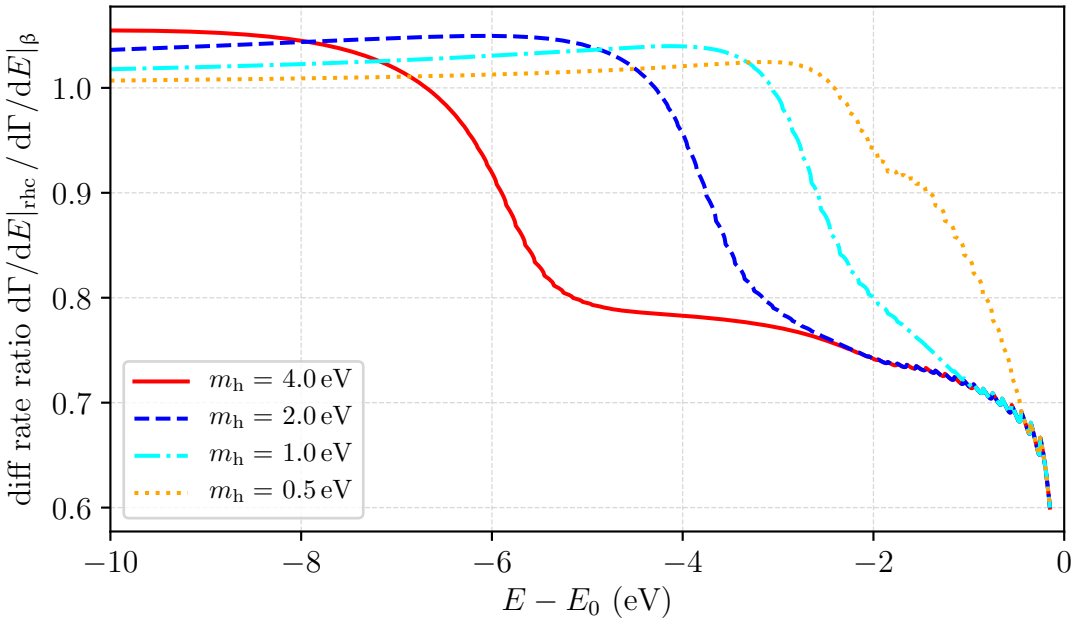

Figure 7.10.: **Effect of the heavy (sterile) neutrino mass with final states.** Shown is the ratio of a spectrum with left-right interference according to eq. (7.21) to a standard β-decay spectrum for different heavy (sterile) neutrino masses m_{h}. Constant parameters are $\sin^2\theta_{\mathrm{eff}} = 0.2$, $c_{\mathrm{LR}} = 0.2$ and $m_{\mathrm{l}} = 0.2\,\mathrm{eV}$. Again, the kink is smeared out by the final states.

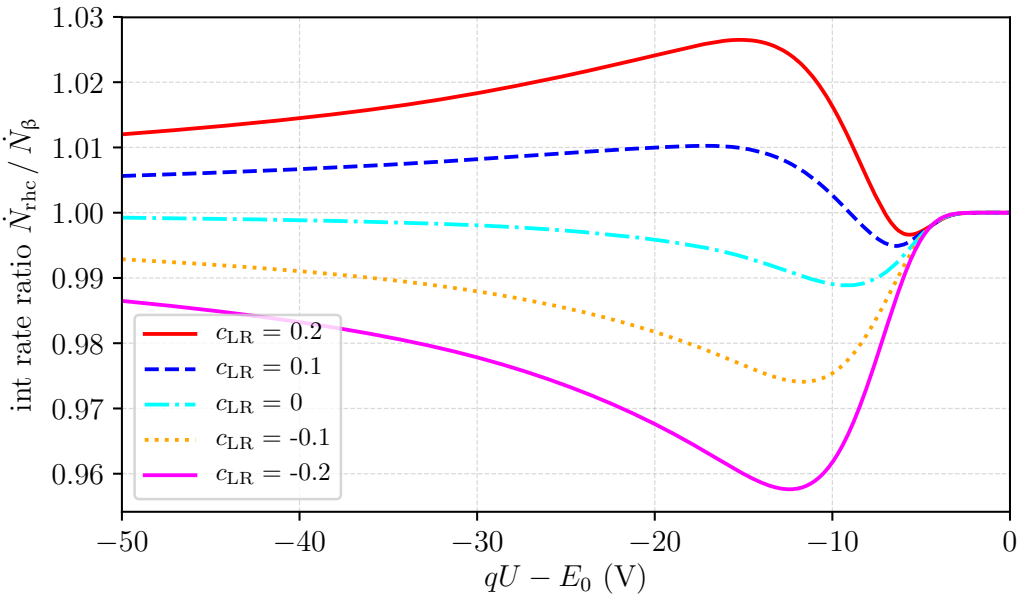

Figure 7.11.: **Effect of the right-handed coupling on the integrated spectrum.** Shown is the ratio of a spectrum with left-right interference according to eq. (7.22) to a standard β-decay spectrum for different interference c_{LR} ($\sin^2\theta_{\mathrm{eff}} = 0.2$, $m_{\mathrm{h}} = 2\,\mathrm{eV}$, and $m_{\mathrm{l}} = 0.2\,\mathrm{eV}$). Compared to fig. 7.9, the c_{LR} signal is weaker.

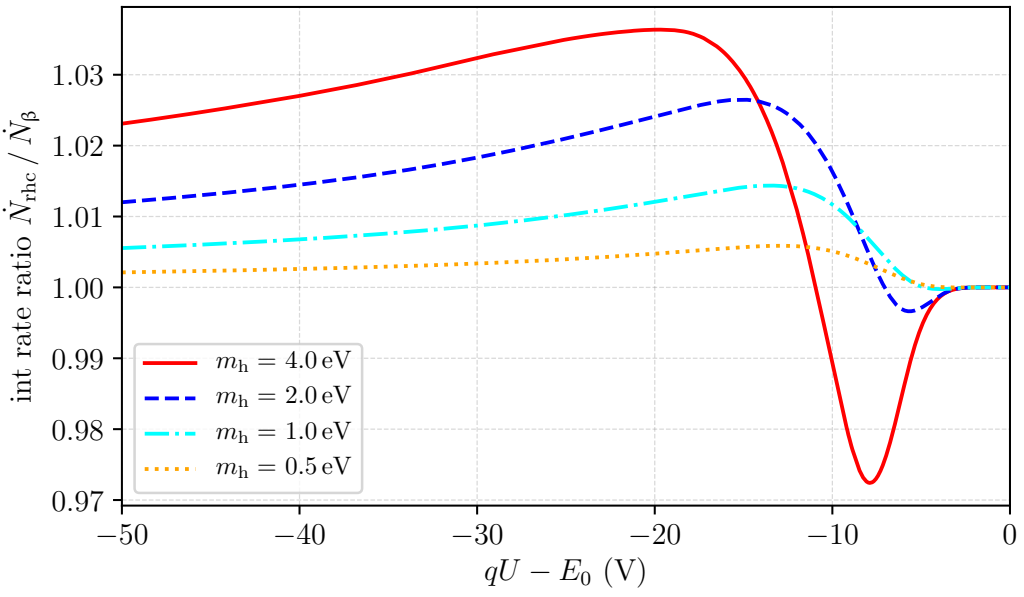

Figure 7.12.: **Effect of the heavy (sterile) neutrino mass on the integrated spectrum.** Shown is the ratio of a spectrum with left-right interference according to eq. (7.22) to a standard β-decay spectrum for different heavy (sterile) neutrino masses m_{h} ($\sin^2\theta_{\mathrm{eff}} = 0.2$, $c_{\mathrm{LR}} = 0.2$, and $m_{\mathrm{l}} = 0.2\,\mathrm{eV}$). Compared to fig. 7.10, the c_{LR} signal is weaker.

7.2.2. Parameter inference with right-handed currents

Fitting an additional three parameters for the right-handed currents in presence of eV-scale sterile neutrinos is challenging. The free parameter c_{LR} will easily lead to plain wrong estimation of the other parameters due to its interference nature. Therefore it was decided to use a Metropolis-Hastings MCMC [Met+53] to marginalise the likelihood function for parameter inference. It has proven to be a very robust and reliable algorithm which can be tuned to estimate solutions for tricky problems.

Concerning the settings of the MCMC, a burn-in phase of up to 2×10^5 steps was chosen and a total chain length of at least 10^6 steps with a proposal acceptance rate of 0.234. In each step, the simulated measurement and the spectrum obtained with the inferred parameters are compared and the parameters are adapted accordingly via acceptance of the proposal. During the burn-in phase, the MCMC varies the parameters in a wide range to find the parameter regions where the MCMC might converge. These regions are then explored in detail in the remaining steps to result in the shown posterior distributions of the fit parameters. In order to circumvent low effective sample sizes due to the long burn-in phase, multiple chains were run in parallel to ensure effective sample sizes of order 1000 for each setting. Flat priors were used for all parameters, representing physical constraints in terms of lower and upper limits as shown in tab. 7.2.

Table 7.2.: **Priors on the parameters.** The heavy neutrino mass is kept fixed.

param	lower bound	upper bound
m_{l}^2 (eV^2)	0	100
E_0 (eV)	18475	18675
Amp	0.5	1.5
Bg (cps)	0	1
$\sin^2\theta_{\mathrm{eff}}$	0	1
c_{LR}	-1	1

The marginalised posterior distribution for an example MCMC run with fixed $m_{\mathrm{h}}^2 = 16\,\mathrm{eV}^2$, and true $m_{\mathrm{l}}^2 = 0\,\mathrm{eV}^2$, $E_0 = 18\,575\,\mathrm{eV}$, $Amp = 1$, $Bg = 0.4\,\mathrm{cps}$, $\sin^2\theta_{\mathrm{eff}} = 0.1$, $c_{\mathrm{LR}} = 0$ is visualised in fig. 7.13. A slight bias of the estimated endpoint E_0 and the right-handed coupling c_{LR} is visible, with strong anti-correlation of the two parameters. Furthermore, larger light neutrino masses are favoured by negative right-handed couplings, as evident from eq. (7.21). Similar results were obtained in ref. [Ste+17] with a Differential Evolution Markov Chain Monte Carlo [Bra06] algorithm and the KATRIN nominal operational settings.

In order to minimise the bias of c_{LR} and E_0, a constraint on E_0 is considered. Penning trap measurements have the potential to constrain the ^{3}He-^{3}H mass difference down to 30 meV [Str+14], which could be translated into a corresponding constraint on the Q-value of the tritium β-decay spectrum. In order to use this constraint on the Q-value as a constraint on E_0 for the analysis of KATRIN data, also the absolute

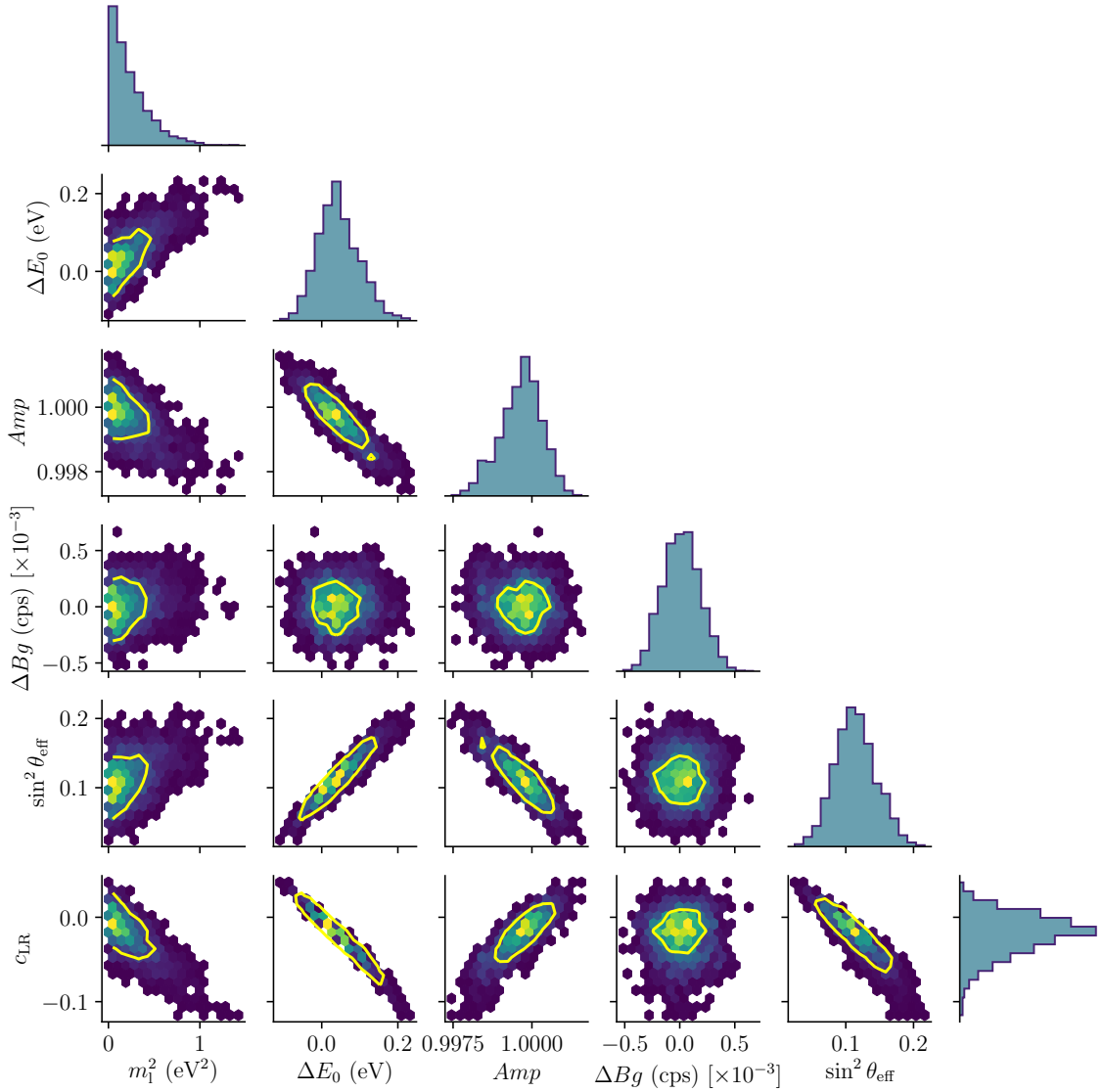

Figure 7.13.: **Posterior parameter distributions.** True values are $m_1^2 = 0\,\mathrm{eV}^2$, $E_0 = 18\,575\,\mathrm{eV}$, $Amp = 1$, $Bg = 0.4\,\mathrm{cps}$, $\sin^2\theta_{\mathrm{eff}} = 0.1$, $c_{\mathrm{LR}} = 0$ and fixed $m_4^2 = 16\,\mathrm{eV}^2$. The yellow lines mark the 90 % credible region.

energy scale of KATRIN needs to be determined. In particular, this comprises the work function difference between the source and the main-spectrometer, as well as potential plasma effects inside the source [Kuc16], and the final states of the tritium daughter molecule [BPR15]. All these effects need to be known to the meV level as well, which is why a conservative constraint on the endpoint of 50 meV is used to minimise the bias. In the next section, sensitivity estimates for c_{LR} are given for free and constrained endpoint, for different heavy neutrino masses.

7.2.3. Statistical sensitivity to constrain the right-handed coupling

Up to now, the heavy (sterile) neutrino mass was kept fixed during the MCMC run. In ref. [Ste+17], we show that the posterior distributions for $\sin^2\theta_{\mathrm{eff}}$, m_4^2 and

c_{LR}^2 estimate the input parameters with free m_{h} only for $m_{\mathrm{h}}^2 \geq 16\,\mathrm{eV}^2$. The reason is the degeneracy of m_{l} and m_{h} in case the two are not distinguishable with the KATRIN energy resolution. Only for large enough heavy neutrino masses, sensible credible intervals can be derived for the parameters of interest. In the following, it is assumed that the heavy sterile neutrino mass is obtained from other measurements and used as an input parameter for the estimation of the right-handed coupling c_{LR}. Current constraints on c_{LR} are obtained from LHC bounds on the mass of the right-

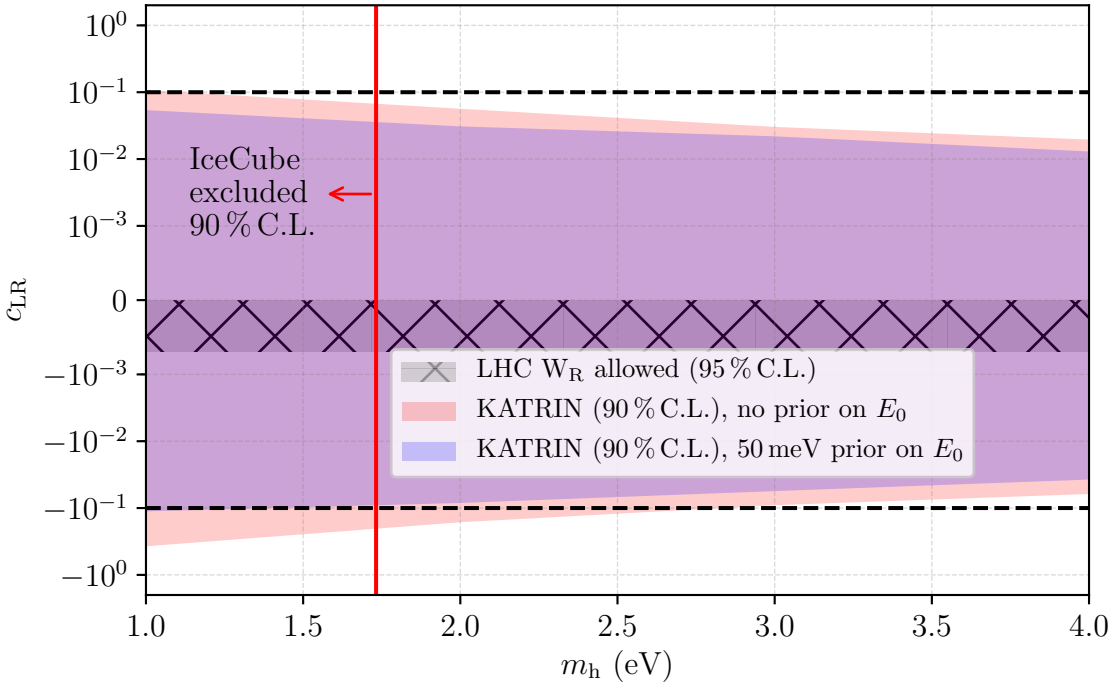

Figure 7.14.: **Statistical sensitivity on right-handed currents.** The red line shows the upper end of the IceCube excluded m_{h} range [Aar+16], the cross-hatched region marks the LHC allowed range for c_{LR} [Sir+18]. The results are compared to the KATRIN sensitivity for $\sin^2\theta \approx \sin^2\theta_{\mathrm{eff}} = 0.1$, with and without endpoint constraint. The dotted black horizontal lines mark the LRSM prior on c_{LR} for $\sin^2\theta_{\mathrm{eff}} = 0.1$.

handed current mediator, $m_{\mathrm{W_R}} \gtrsim 3.4\,\mathrm{TeV}$ (95 % C.L.) [Sir+18]. This limit can be translated into a lower limit on the LR mixing angle, $|\xi| \lesssim m_{\mathrm{W_L}}^2/m_{\mathrm{W_R}}^2 \approx 10^{-3}$ [BR13, Kha+14]. Maximum LR coupling is then given for $\xi = -10^{-3}$, since [Ste+17]

$$c_{\mathrm{LR}} \approx a_{\mathrm{LR}} = -2 \cdot (m_{\mathrm{W_L}}^2/m_{\mathrm{W_R}}^2 + C \cdot \tan\xi \cdot \cos\alpha), \tag{7.23}$$

with the CP-violating phase α (set to 0 in the course of this thesis). The corresponding lower limit to $\xi = -10^{-3}$ is $c_{\mathrm{LR}} \geq -7 \times 10^{-4}$ (95 % C.L.). A conservative limit on c_{LR} is obtained by having $m_{\mathrm{W_R}} \to \infty$, resulting in $c_{\mathrm{LR}} \to 0$.

For a mixing of sterile neutrinos with the 2$^{\mathrm{nd}}$ mass eigenstate, $\sin^2\theta_{\mathrm{eff}} \approx \sin^2\theta_{24}$, IceCube excludes sterile neutrino masses in the range $0.2\,\mathrm{eV} < m_{\mathrm{h}} < 1.7\,\mathrm{eV}$ (90 % C.L.) [Aar+16]. Though KATRIN is sensitive to θ_{14}, we can use the IceCube sterile neutrino mass exclusion, assuming both mixing angles are essentially equal [BRZ11].

The statistical sensitivity of KATRIN towards right-handed currents in the presence of eV-scale sterile neutrinos is visualised in fig. 7.14. Without endpoint constraint,

the statistical sensitivity of KATRIN is not high enough to test whether the LR-symmetry prior of $|c_{\mathrm{LR}}| \leq \sin^2\theta_{\mathrm{eff}}$ holds. When applying the 50 meV constraint on E_0, KATRIN can test the LR symmetry prior for large masses ($m_{\mathrm{h}} \gtrsim 3\,\mathrm{eV}$) of the sterile neutrino for the hypothetical settings used in this work. Compared to the KATRIN nominal operational settings derived in ref. [Ste+17], the elevated background assumed in this work slightly decreases the statistical sensitivity towards the right-handed currents, as the larger background decreases the signal-to-noise ratio in the endpoint region. Approximately, the 90 % credible interval obtained in this work matches the 95 % credible interval obtained in ref. [Ste+17].

However, while it has to be noted that KATRIN may not improve existing limits on c_{LR}, KATRIN provides a complementary way to access the left-right coupling through the kinematics of β-decay. Furthermore, the LHC limits on the right-handed current coupling obtained from $\mathrm{W_R}$ mass are only valid for LRSM. If the interference term in eq. (7.16) is caused by a different mechanism, KATRIN may have a chance to test this model.

7.3. Relic neutrinos

"About every neutrino physicist goes through a phase in his or her career and asks 'There's got to be a way to measure the relic neutrino background"'. This quote attributed to Peter Fisher describes one of the biggest challenges remaining in experimental physics: the direct detection of the cosmic relic neutrino background (CνB). Similar to the cosmic microwave background (CMB), the measurement of the cosmic neutrino background would yield information about the early universe. However, instead of a time scale of 3.7×10^5 yr as for the CMB, its detection would allow testing cosmological models one second after the Big Bang.

In ref. [Hei15], the statistical sensitivity of KATRIN to constrain the CνB is estimated for various scenarios, based on a calculation for the relic neutrino capture rate on tritium by Fässler et al. [Fäs+13]. As an extension to ref. [Hei15], the work at hand estimates the statistical sensitivity of KATRIN to constrain the CνB for a conceivable scenario accommodating an elevated background rate (see appendix, D.1). In addition, the implementation of the final states distribution (see sec. 7.3.2.2) is improved compared to ref. [Hei15].

This section starts with a quick recapitulation of the underlying theory of the cosmic neutrino background in sec. 7.3.1, before introducing its potential signal identification at a tritium β-decay experiment such as KATRIN in sec. 7.3.2. One step towards estimating the sensitivity of KATRIN to constrain the relic neutrino background is testing if KATRIN may resolve the CνB capture signal, which is shown in sec. 7.3.3. Before concluding this chapter, sec. 7.3.4 states the statistical sensitivity of KATRIN to constrain the relic neutrino background.

7.3.1. Theory of the relic neutrino background and detection techniques

The detection of the cosmic microwave background (CMB) by Penzias and Wilson in the 1960s [PW65] provided solid experimental support for the hypothesis of the thermal development of the universe, starting with the Big Bang. In the following, the CMB is used as a point in favour of the existence of the CνB, justified by Big Bang theory [Per09]. The description of the CMB and the CνB follows the textbook by Perkins [Per09].

7.3.1.1. Cosmic microwave background

In the radiation-dominated era, thermal equilibrium between fermions and bosons manifested in the formation and ionisation of hydrogen, which is the origin of CMB radiation:

$$\mathrm{e}^- + \mathrm{p} \leftrightarrow {}^1\mathrm{H} + \gamma. \tag{7.24}$$

Iteratively solving the Saha equation shows that the CMB photons decouple from this equilibrium shortly after the universe expanded and cooled down to the ionisation energy of hydrogen, $k_\mathrm{B}T < 13.6\,\mathrm{eV}$. Due to the tail of the Planck black body distribution of the photons, the CMB decouples at $k_\mathrm{B}T \approx 0.3\,\mathrm{eV}$, which translates to a decoupling time of

$$t_\gamma = 3.7 \times 10^5\,\mathrm{yr}. \tag{7.25}$$

Today, the CMB is measured to be a black body radiation example par excellence with a temperature of $T_\gamma = 2.73\,\mathrm{K}$ [Tan+18]. Using the Bose-Einstein distribution for the spectrum of the CMB, the photon number density can be calculated to be

$$n_\gamma = \frac{1}{\pi^2}\left(\frac{k_\mathrm{B}T_\gamma}{\hbar c}\right)^3 2.404 \approx 411\,\mathrm{cm}^{-3}. \tag{7.26}$$

This shows that the CMB photons are the most abundant particles in the universe by far. The only species not being totally outnumbered are the relic neutrinos, the origin of which will now be discussed.

7.3.1.2. Cosmic neutrino background

Similar to the CMB, the production mechanism of the cosmic neutrino background (CνB) can be described by an equilibrium reaction. The CνB originates from the thermal equilibrium of photons, electrons and neutrinos, mediated through electroweak interactions:

$$\gamma\gamma \leftrightarrow \mathrm{e}^+\mathrm{e}^- \leftrightarrow \nu_\alpha\bar{\nu}_\alpha \qquad (\alpha = \mathrm{e}, \mu, \tau). \tag{7.27}$$

The decoupling of the CνB follows the exactly same rules as the decoupling of the CMB. When the expansion rate of the universe - described by the Hubble parameter H - exceeds the reaction rate, the neutrinos form their own fireball, developing independently from the rest of the universe. Respecting the additional radiation

contributions from fermions (compare eq. (7.27) to eq. (7.24)), the decoupling energy can be estimated to $k_\mathrm{B}T \approx 3\,\mathrm{MeV}$. This energy translates to a decoupling time of

$$t_\nu = 1\,\mathrm{s}. \tag{7.28}$$

Using the Fermi-Dirac distribution for the spectrum of the CνB allows estimating today's temperature of the CνB from the measured CMB temperature:

$$T_\nu = \left(\frac{4}{11}\right)^{1/3} T_\gamma = 1.95\,\mathrm{K}. \tag{7.29}$$

Similarly, today's number density of the CνB can be estimated from today's CMB number density:

$$n_\nu = \frac{g_\nu}{2}\frac{1}{\pi^2}\left(\frac{k_\mathrm{B}T_\nu}{\hbar c}\right)^3 \frac{3}{4} \cdot 2.404 \cdot n_\gamma = 336\,\mathrm{cm}^{-3}. \tag{7.30}$$

This shows that the number densities of CMB (7.26) and of CνB (7.30) are indeed comparable. The remarkable difference, however, is that neutrinos are proven to have a non-zero rest mass [Fuk+98, Ahm+01] – a discovery so influential to fundamental physics that it got rewarded with a Nobel prize in 2015 [The15]. From a cosmological perspective, the finite mass of neutrinos leads to the hypothesis that the – today non-relativistic – relic neutrinos of the CνB may cluster on accumulations of cold dark matter (CDM) or baryonic matter.

7.3.1.3. Cosmic neutrino background clustering

In ref. [RW04], Ringwald and Wong describe potential forms of a localised cosmic neutrino background overdensity with focus on clustering on CDM. Ringwald and Wong estimate the neutrino clustering based on a NFW[8] profile as lower bound and the clustering based on the present Milky Way mass profile as upper bound. Ringwald and Wong conclude that the true relic neutrino overdensity $\eta = n_\nu/\bar{n}_\nu$ might lie somewhere in between. At the position of our solar system (8 kpc distance to center of Milky Way), Ringwald and Wong estimate overdensity factors between 1.4 and 20. The larger the neutrino mass is, the larger is the local relic neutrino overdensity: larger mass reduces the velocity of thermal relics. Another possibility for a locally increased density of the relic neutrinos is neutrino clustering similar to the baryon overdensity in galaxy clusters as found by Lazauskas et al [LVV08]. This would enable overdensities of 10^3 to 10^4 for a cluster size of 50 Mpc. Combining now these two results, Fässler et al. [Fäs+13] scale down the cluster-scale findings of Lazauskas to the scale of the Milky Way. This would enable overdensities of $\eta \approx 10^6$ inside the Milky Way. Even higher overdensities are estimated by Hwang and Ma [HM05], who use high neutrino clustering factors (10^2 to 10^{14}) as explanation for the GZK cut-off[9] [Gre66, ZK66]. This small excerpt of conceivable origins of a local relic neutrino overdensity inside the Milky Way motivates efforts in finally detecting the cosmic neutrino background.

[8] Navarro, Frenk and White [NFW96] derive a universal dark matter profile with two parameters: density and radius.

[9] The GZK cut-off proposes an explanation for the cut-off of the ultra-high energetic cosmic rays, as those protons may interact with the CMB [Gre66, ZK66].

7.3.1.4. Cosmic neutrino background detection

An experimenter trying to detect the CνB has to face two fundamental challenges: the solely weak interaction of neutrinos in general and the particularly low energy of the CνB. Several possibilities for the CνB detection are proposed in the literature: from resonant absorption of ultra-high-energy cosmic ray neutrinos on the low-energy CνB leading to a boosted "Z burst" [FKR02] over "detecting the mechanical force on macroscopic targets due to the 'neutrino wind'" [Hag99] to induced β-decay [Fäs+11, Bar+18]. The following investigation will focus on the possible signal identification of the CνB at KATRIN.

Already proposed by Weinberg in 1962 [Wei62], the induced β-decay is a neutrino capture process transforming the β-decay into a two body problem:

$$ {}^{A}_{Z}N + \nu_e \rightarrow {}^{A}_{Z+1}N' + e^- \qquad \text{and} \qquad {}^{A}_{Z}N + \bar{\nu}_e \rightarrow {}^{A}_{Z-1}N' + e^+. \tag{7.31} $$

The induced β-decay has the advantage of lacking any energy threshold. Fässler et al. derive the reaction rate for this process as the capture rate [Fäs+11] (one incoming neutrino per volume V):

$$ d\Gamma_\nu = \sum \frac{1}{V} \left|\langle f \,|\, T \,|\, i \rangle\right|^2 2\pi\delta(E_e + E_f - E_i - E_\nu) \frac{d\mathbf{p}_e}{(2\pi)^3}, \tag{7.32} $$

with i and f initial and final state, E_i and E_f initial and final energy and T the transition matrix element. Since the neutrinos are found to be massive particles [Fuk+98, Ahm+01] (also compare sec. 1.1.3) with yet unknown mass, this process received new interest: the signal of the relic neutrino capture is a sharp line, located one neutrino mass above the endpoint of the β-decay electron spectrum (cf. fig. 7.15). Calculating the transition matrix element in eq. (7.32) and integrating over the electron momenta yields [Fäs+11]:

$$ \Gamma_\nu({}^3\mathrm{H}) = \frac{1}{\pi}(G_\mathrm{F} \cos\vartheta_\mathrm{C})^2 F_0(Z+1, E_e) \left[B_\mathrm{F}({}^3\mathrm{H}) + B_\mathrm{GT}({}^3\mathrm{H})\right] p_e E_e \frac{1}{V} \tag{7.33} $$

$$ = 4.2 \cdot 10^{-25} \eta_{\nu_e}\, \mathrm{yr}^{-1} =: \Gamma'_\nu({}^3\mathrm{H})\eta, \tag{7.34} $$

with $1/V = \eta_{\nu_e} \langle n_{\nu_e} \rangle$ and $\langle n_{\nu_e} \rangle = 56\,\mathrm{cm}^{-3}$. The reaction rate derived in eq. (7.34) will serve as fundamental input for the identification of the potential signal of the CνB in KATRIN, discussed in the next section.

7.3.2. Induced β-decay spectrum

In sec. 7.3.1.4, the electron production rate stemming from the capture of relic neutrinos was derived. Taking one more step towards estimating the sensitivity of KATRIN for measuring the relic neutrino background, one needs to include some characteristics of the KATRIN experiment.

7.3.2.1. Basic form

From eq. (7.34), the CνB capture signal would be an infinitesimally sharp line, located one neutrino mass above the endpoint at $E_0 + m_\nu$. Since KATRIN measures an

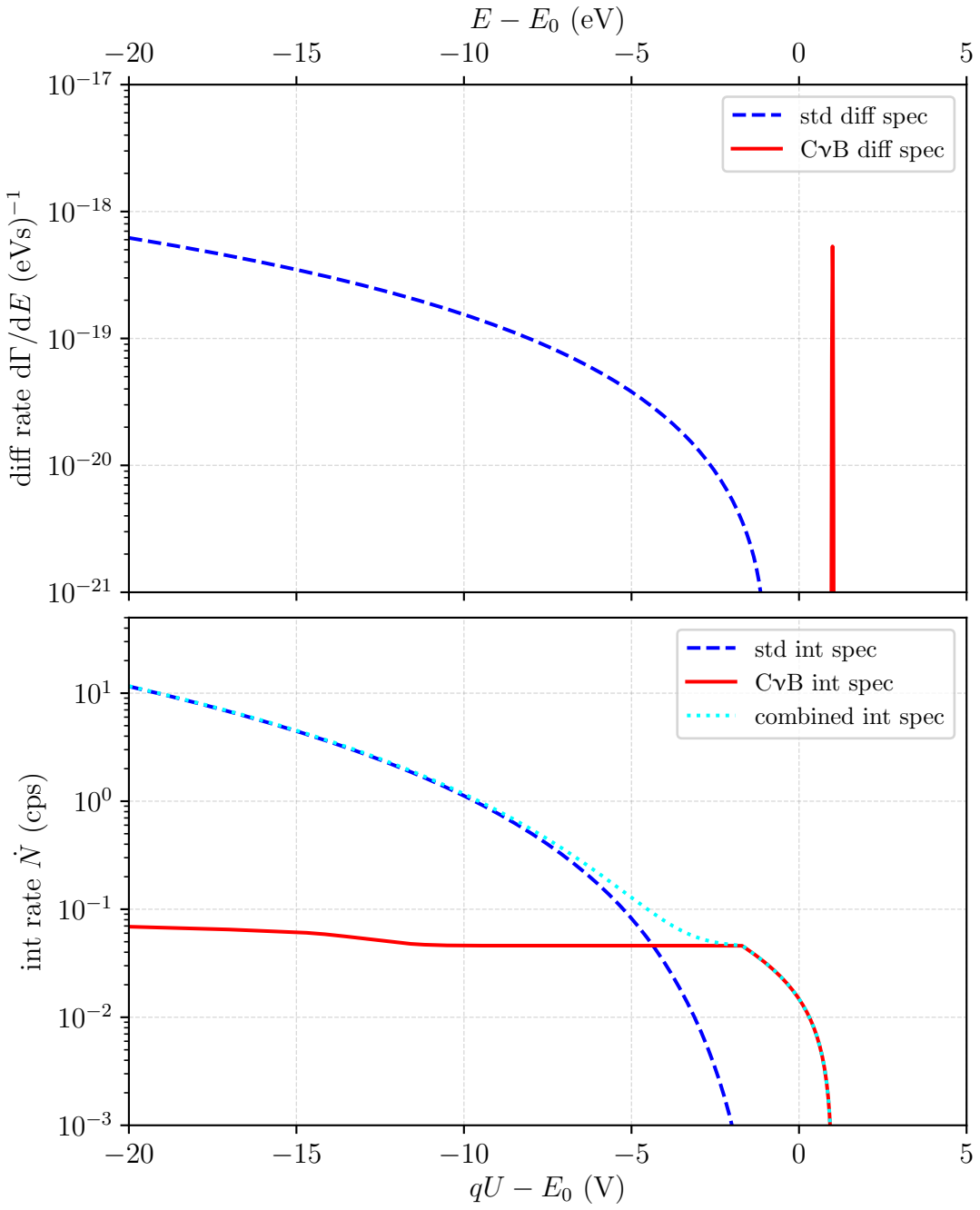

Figure 7.15.: **Basic spectrum** - Upper panel: the relic neutrino capture signal (red) is modelled as a Gaussian peak at $E_0 + m_\nu$ (see eq. (7.35)). Lower panel: the peak manifests as a shoulder in the spectrum as measured by KATRIN. Spectra for $m_\nu = 1\,\mathrm{eV}$ and $\eta = 10^{12}$, no background rate included.

integrated spectrum, the line needs to be integrated: this leads to the conclusion that the sharp line can be approximated by a Gaussian with a width of 10 meV. Though this might seem an arbitrary choice: it is not. As long as it is smaller than e.g. the Doppler broadening, the width of the CνB-Gaussian only influences the differential spectrum and its integrability. Due to the signal being a normalised Gaussian,

the integration will yield the same result for the count rate even if $\sigma_{\mathrm{C\nu B}}$ differs. Therefore, $\sigma_{\mathrm{C\nu B}} = 10\,\mathrm{meV}$ was chosen because it increases the numerical stability of the integration. The capture (and therefore decay) rate for the CνB induced β-decay thereby takes the following form:

$$\frac{\mathrm{d}\Gamma}{\mathrm{d}E} \coloneqq \Gamma'_{\nu}(^3\mathrm{H}) \cdot \eta \cdot \frac{\mathrm{e}^{-(E-(E_0+m_\nu))^2/2\sigma^2_{\mathrm{C\nu B}}}}{\sqrt{2\pi\sigma^2_{\mathrm{C\nu B}}}}. \tag{7.35}$$

In the modelled spectrum of fig. 7.15, the CνB signal is at 18 576 eV as expected for an example neutrino mass of $m_\nu = 1\,\mathrm{eV}$. The distance between the maximum energy of the standard β-decay spectrum (shown in dotted blue) and the CνB signal (solid red) is exactly $2m_\nu = 2\,\mathrm{eV}$.

7.3.2.2. Model extensions

As for the standard β-decay spectrum, light bosons and the potential right handed currents: the basic spectrum expected for the relic neutrinos described in sec. 7.3.2.1 needs to be extended and refined to include effects of the KATRIN set-up into the fit model. Here only the final states as one of the dominating influences will be discussed.

The effect of the final states manifests in a shift and a broadening of the CνB signal: at a probability P_{fs}, the daughter molecule may be left in an electronically or rotational-vibrational excited final state fs with an excitation energy E_{fs}. The final state energy reduces the maximum kinetic energy E_0 of the electron, therefore the decay rate becomes

$$\left.\frac{\mathrm{d}\Gamma}{\mathrm{d}E}\right|_{\mathrm{C\nu B}} = \sum_{fs} \Gamma'_{\nu}(^3\mathrm{H}) \cdot \eta \cdot P_{fs} \cdot \frac{\mathrm{e}^{-(E-(E_0-E_{fs}+m_\nu))^2/2\sigma^2_{\mathrm{C\nu B}}}}{\sqrt{2\pi\sigma^2_{\mathrm{C\nu B}}}}. \tag{7.36}$$

As for the light bosons in sec. 7.1.1.1, also a 100 meV rebinned version of the final states is used due to the Doppler effect being of the same size. The effect of the final states on the CνB spectrum is visualised in fig. 7.16: the electronically excited states show up deep in the standard β-decay spectrum (beneath $E_0 - 20\,\mathrm{eV}$). Anyway, the large count rate of the standard β-decay spectrum will hide the visibility of the CνB electrons in this region.

7.3.2.3. Combination with standard β-decay

The Superposition of the CνB decay rate and the standard β-decay rate gives the combined decay rate as a sum:

$$\frac{\mathrm{d}\Gamma}{\mathrm{d}E} = \left.\frac{\mathrm{d}\Gamma}{\mathrm{d}E}\right|_{\beta} + \left.\frac{\mathrm{d}\Gamma}{\mathrm{d}E}\right|_{\mathrm{C\nu B}}. \tag{7.37}$$

With the concept of a response function $R(E, qU)$ [Kle+18], the measured integrated spectrum can be written as

$$\dot{N} \propto \int_{qU}^{\infty} R(E, qU) \left(\left.\frac{\mathrm{d}\Gamma}{\mathrm{d}E}\right|_{\beta} + \left.\frac{\mathrm{d}\Gamma}{\mathrm{d}E}\right|_{\mathbf{C\nu B}} \right) \mathrm{d}E\,. \tag{7.38}$$

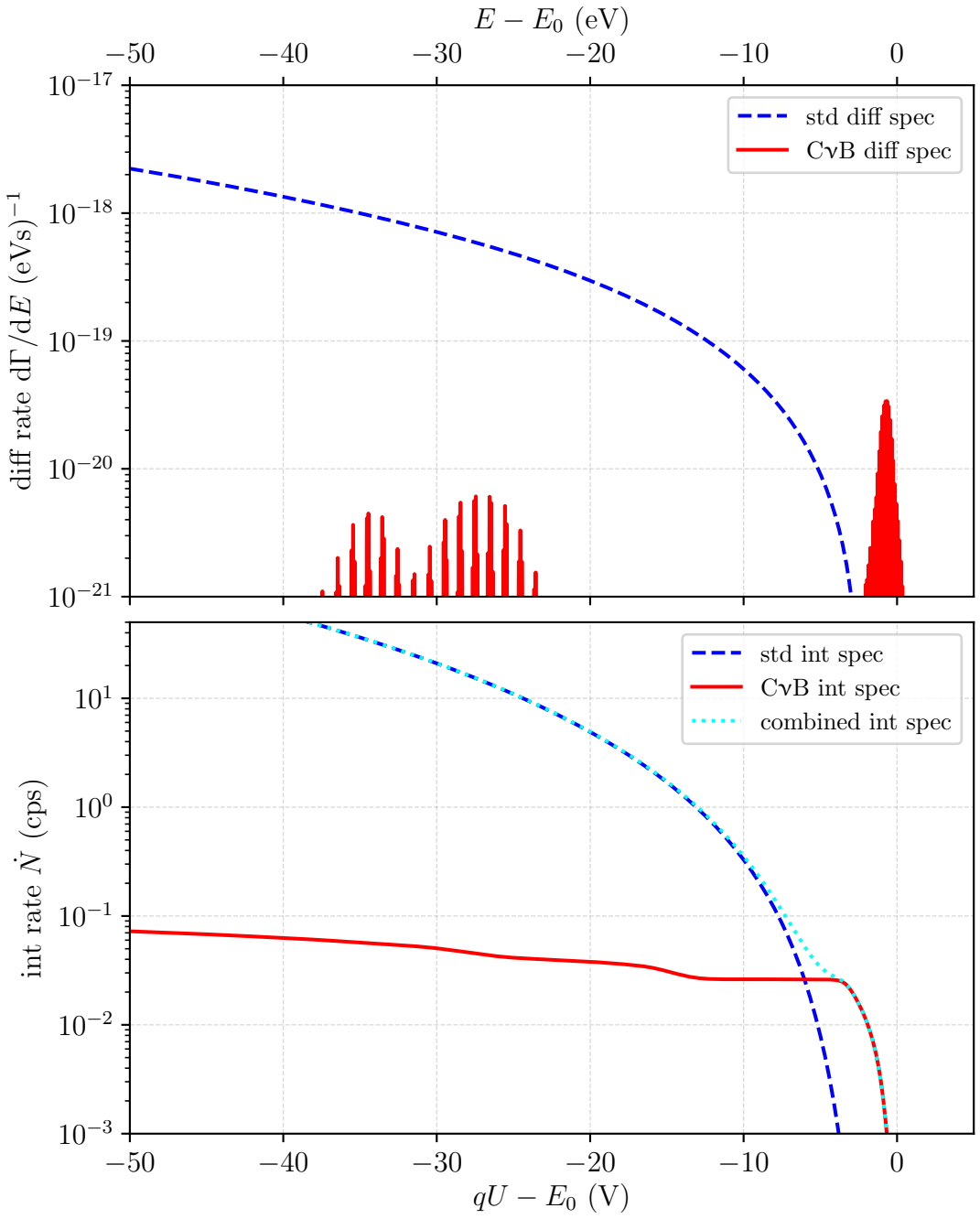

Figure 7.16.: **Spectrum** - Upper panel: the relic neutrino capture signal (red) is shifted to lower energies due to the final states. Lower panel: the strength of the CνB signal shoulder is reduced compared to fig. 7.15. Spectra for $m_\nu = 1\,\mathrm{eV}$ and $\eta = 10^{12}$, no background rate included.

From eq. (7.38), we expect to see the shape of the response function in the CνB part of the integrated spectrum. This is nicely confirmed by fig. 7.15 and 7.16: the modulation of the CνB signal towards lower retardation voltage values is due to the shape of the response function. With lower retardation voltage, also the inelastically scattered electrons from CνB capture reach the detector, causing an increase of the CνB signal. However, this increase is not visible in the combined spectrum due to

the large signal rate from the standard β-decay farther away from the endpoint.

7.3.3. Parameter inference with relic neutrinos

First estimates of the potential of KATRIN to constrain the relic neutrino background can be gathered from fits. Even more, important insights into the correlations of the additional fit parameter η with the standard four parameters can be gained. To investigate this, 1000 fits were performed. In each fit, a simulated measurement (including Poisson randomisation of the counts) was compared to a model and the five fit parameters m_ν^2, E_0, *Amp*, *bg* and η were minimised via Minuit2 of the ROOT framework [BR97]. The KATRIN settings used were the same as for the other simulations in this chapter and can be found in sec. D.1 and tab. D.4 in the appendix. The first thing to be mentioned here is the effect of the sharp line of the CνB signal:

Table 7.3.: **Exemplary best fit estimates of the parameters.** 1000 fits with $\eta = 10^{12}$ and neutrino mass $m_\nu = 1\,\text{eV}$ were performed.

param	true	μ	σ
m_ν^2 (eV^2)	1.0	1.000	0.003
E_0 (eV)	18575	18575.000	0.002
Amp	1.0	1.000	0.0001
bg (cps)	0.4	0.400	0.0001
η	1×10^{12}	9.995×10^{11}	8.1×10^9

it requires a lot of integration steps in the regions where the FSD-smeared signal is expected. Otherwise, the numerical instability of the integration prevents correct reproduction of the true values. Results from the 1000 simulated KATRIN measurements and following fits are shown in fig. 7.17. Since the CνB signal position directly depends on the neutrino mass, see eq. 7.36, there is a correlation between m_ν and η. In terms of potential signal identification, a positive point is that there seems not to be a distinct bias of one of the estimated parameters.

All parameters reproduce their respective true value, which is also demonstrated in the overview presented in tab. 7.3. Furthermore, the additional fit parameter η shows correlations with all the four standard parameters, which reveals the challenge of including the CνB signal into the fits. Also, a first hint as to the potential of KATRIN to constrain the relic neutrino background occurs: the 1σ uncertainty on η is 8.1×10^9, so KATRIN is expected to be able to set constraints on η at the level of approximately 10^{10}.

7.3.4. Statistical sensitivity to constrain the relic neutrino background

The potential of KATRIN to constrain the relic neutrino background can be seen in fig. 7.18. In the course of this thesis, the statistical sensitivity to the local relic

neutrino overdensity η is estimated to be of order 10^{10}. This value is one order of magnitude larger than the one estimated by Kaboth et al. [KFM10], which can be explained by the different experimental settings. Mostly it is the background that limits the potential of KATRIN, as outlined in ref. [Hei15]. Furthermore, as also discussed in ref. [Hei15], Kaboth et al. use a simplified model for the KATRIN experiment (no detection efficiency, simpler scattering model, larger amount of effective column density), which is why it is refrained from giving a quantitative comparison here.

Current limits on η from β-decay experiments trace back to the Los Alamos [Rob+91] and Troitsk [Lob+99b] experiment, which were motivated by the negative neutrino mass squared estimates. KATRIN will be capable of improving this limit by at least one order of magnitude in the current set-up. In fig. 7.18, also the estimates introduced in sec. 7.3.1.3 are shown. The baseline of the overdensity is given by $\eta = 1$, which corresponds to no local clustering of the relic neutrinos. Estimates of the relic neutrino overdensity based on the clustering of dark matter, baryons, as well as combinations of both, range from 1 to 10^6 [RW04, LVV08, Fäs+13].

In the scope of this thesis, also CνB-adapted MTDs are tested for their effect on the sensitivity on η. However, the increase in sensitivity is found to be only minor. No order of magnitude increase can be achieved, even with a "CνB-focused" MTD. The reason is the dominant effect of the background rate, which generally limits the KATRIN sensitivity for the CνB. For larger neutrino masses, the statistical sensitivity is found to improve marginally by about a factor 1.4.

While KATRIN most likely will not be able to detect the CνB, it can rule out speculative models about the origin of the GZK cut-off [HM05] and improve existing β-decay limits on η by at least one order of magnitude.

Note that only the statistical sensitivity is investigated in this thesis. In order to derive an upper limit from the neutrino mass data, also systematic effects need to be studied very carefully.

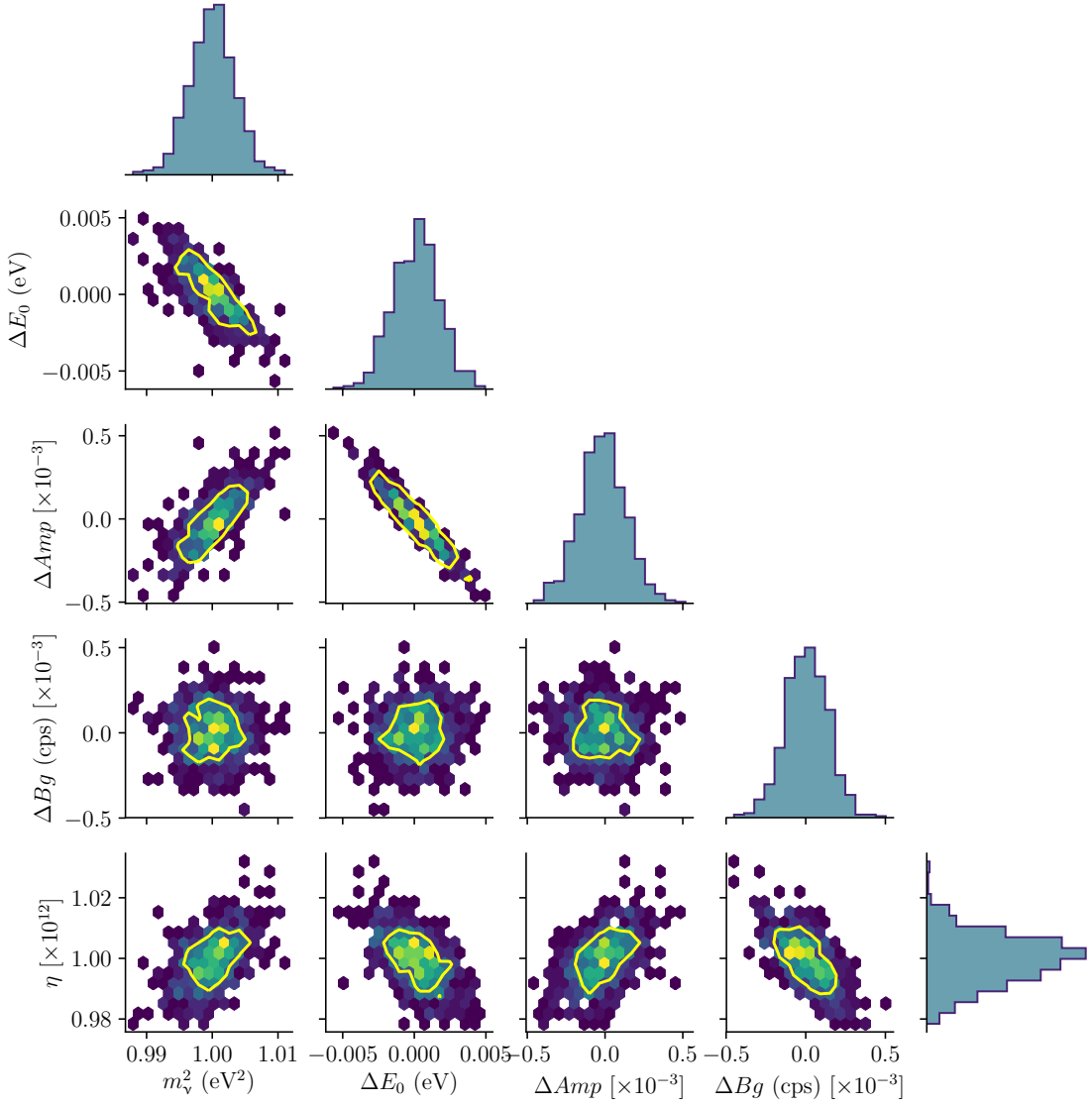

Figure 7.17.: **Distribution of fitted parameters for the relic neutrino model.** Shown is the distribution of the fitted parameters after performing 1000 fits with minimization via Minuit. True values are $m_\nu = 1\,\text{eV}$, $E_0 = 18\,575\,\text{eV}$, $Amp = 1$, $bg = 0.4\,\text{cps}$, $\eta = 1 \times 10^{12}$. The yellow line represents the 90 % C.L. contour.

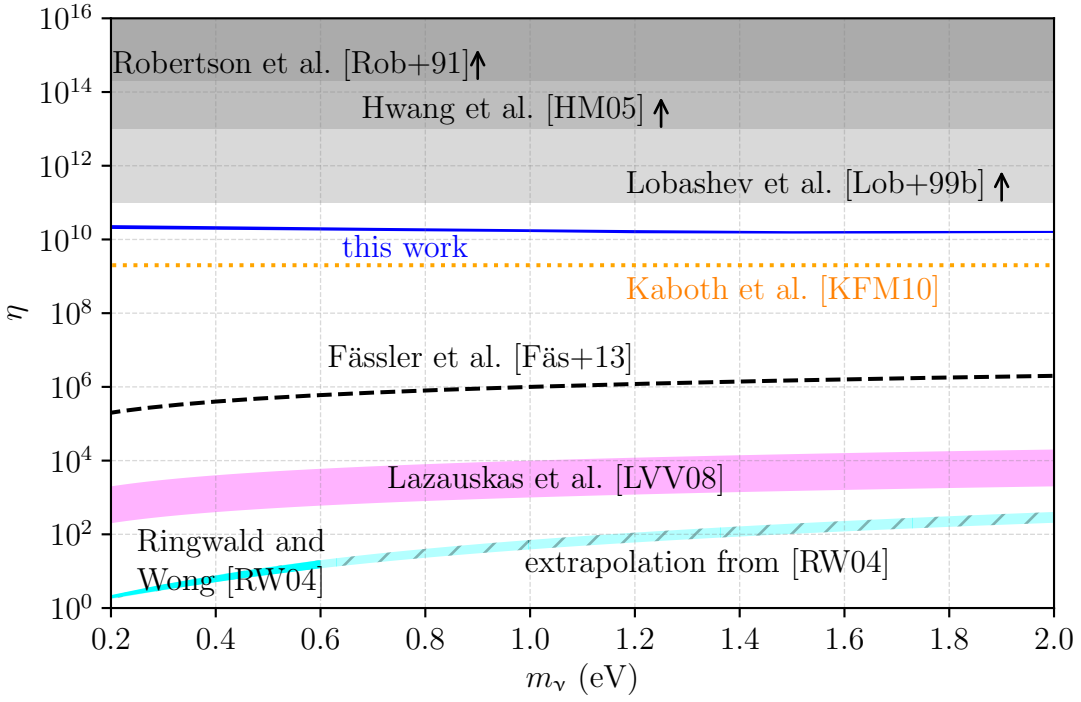

Figure 7.18.: **Statistical sensitivity for relic neutrinos.** Shown is the statistical sensitivity of KATRIN for the detection of the CνB (solid blue). The values obtained by Robertson et al. [Rob+91] and Lobashev et al. [Lob+99b] present upper limits obtained from β-decay spectroscopy (Los Alamos and Troitsk neutrino mass experiments). The other values for the CνB overdensity are predictions from various models.

7.4. Conclusion

In this chapter, three different examples for expanding the physics reach of KATRIN beyond the neutrino mass search have been studied: light bosons, right-handed currents and relic neutrinos. For each of these study cases, the possible signature in the β-decay spectrum measured by KATRIN was derived, from including the interaction into the differential spectrum of the physics model and finally the integrated spectrum including all the experimental characteristics of the KATRIN apparatus. The ability of KATRIN to resolve the specific new kind of interaction was tested through performing either ensemble tests or MCMC runs. Finally, the statistical sensitivity of KATRIN for the respective scenario was estimated.

Light bosons were considered to couple to either the neutrino, the electron or both in the β-decay, leading to the emission of either pseudoscalar or axial vector bosons in a modified four-body decay. The resulting spectrum derived by Arcadi et al. [Arc+18] has the observables mass m_X and coupling g_X of the boson with a shape very similar to the standard β-decay spectrum. The coupling of the light boson g_X was found to be strongly correlated with its mass m_X and the standard fit parameters endpoint E_0 and amplitude Amp. Due to the parametrisation of the spectrum (divergence in m_X by virtue of a non-conserved current), the best sensitivity for the coupling can be derived for eV-scale vector bosons coupling to either neutrino or electron. It can potentially allow to test the constraints by IceCube of order 10^{-2} [IM14]. For pseudoscalars coupling to electrons, KATRIN will most likely not be able to set a competitive limit: it would need couplings g_X of $\mathcal{O}(10^4)$ in order for KATRIN to exclude the null-hypothesis at 1.645σ. Pseudoscalars coupling to neutrinos have a stronger imprint on the spectrum: here the best sensitivity is of order $\mathcal{O}(10^{-1})$. Finally, the sensitivity of KATRIN for vector bosons coupling to electron and neutrino and thereby conserving the weak current is estimated to be of order $\mathcal{O}(10^{-1})$, as well. For keV-scale light bosons however, the large statistics of a differential TRISTAN detector upgrade to KATRIN enables testing existing limits for all types except pseudoscalars coupling to electrons, though most likely no lower limits than the existing ones can be placed from either standard KATRIN or a TRISTAN-like extension data.

Right-handed currents in presence of eV-scale sterile neutrinos were considered to arise exemplarily by left-right symmetry of the weak interaction. The interaction was parametrised by Steinbrink et al. [Ste+17] in a model-independent, yet model-motivated way that also covers interactions not necessarily based on left-right symmetry but also encompassing any other mechanism causing the same signature in the spectrum. In addition to the sterile mixing angle θ_eff and the mass of the heavy sterile neutrino m_h, this parametrisation introduces an interference term c_LR. The interference might be positive or negative, thus causing interesting effects on the spectrum. In this work as well as in ref. [Ste+17], strong correlations of these three additional fit parameters with the standard four parameters were found. In hand with these strong correlations, a bias is observed in the posterior distribution of the endpoint obtained by an MCMC run, in agreement with [Ste+17]. The sensitivity regarding $\sin^2\theta_\mathrm{eff}$ and c_LR is estimated for different fixed values of the sterile neutrino mass. Without constrained endpoint, KATRIN will most likely not be able to test the LR-symmetry of the potential sterile neutrinos. However, future external measurements of the endpoint by Penning trap experiments combined with the pre-

cision determination of the absolute energy scale of the KATRIN experiment might reach an accuracy of about 50 meV. These constraints should enable KATRIN to test the LR-symmetry of potential sterile neutrinos and provide a complementary way to access the right-handed coupling additional to LHC bounds [Sir+18].

Already in [KFM10, Hei15], the potential of KATRIN to constrain the **relic neutrino background** was investigated. This work was substantially refined in the scope of this thesis by a consistent implementation of the signal in the KATRIN analysis framework and the use of realistic experimental settings. Since the position of the potential signal depends only on the neutrino mass, the additional parameter introduced was the local overdensity of the CνB, η, as it defines the amplitude of the signal. The (local) CνB overdensity η also shows correlations with the standard four fit parameters for the neutrino mass search. The potential of KATRIN to constrain the relic neutrino background was found to be of $\eta \approx \mathcal{O}(10^{10})$ (90 % C.L.), with negligible dependence on the neutrino mass. Though the sensitivity of KATRIN towards the relic neutrino background is orders of magnitude away from testing most of the predictions, it will improve existing direct limits from β-decay experiments by at least one order of magnitude.

Besides its main scientific goal, the determination of the neutrino mass, KATRIN offers the possibility to search for a wide variety of interesting new physics. As a high-precision experiment, KATRIN will be able to perform independent, kinematics-based tests of physics beyond the neutrino mass. The three categories investigated in this work exemplarily give a hint and outlook of the kind of physics search possible with KATRIN.

CHAPTER 8

SUMMARY AND CONCLUSIONS

The project of the thesis at hand evolves around the commissioning, simulation, and characterisation of the Windowless Gaseous Tritium Source, as well as analysing the first tritium spectra for the KATRIN experiment located at the Karlsruhe Institute of Technology (KIT). This includes testing individual temperature sensors for short circuits in the cryostat to spectral fitting and statistical analysis of tritium data. Key findings of this journey will be summarised in the following, before concluding this chapter with an outlook on the near future.

Source modelling An essential cornerstone for the work presented in this thesis is the extension and uniform integration of the source model. The input from various sensor readings (temperature, gas flow) is implemented to allow near-online calculation of the source density distribution and to initiate the spectrum model computation. In the course of the First Tritium campaign, the sensor information was used to provide a run-wise estimation of the column density in the WGTS to the individual fitting teams of the KATRIN analysis group, enabling the high-level tritium spectrum fitting. Temperature readings and gas flow readings are now integrated into the gas dynamics part of the source and spectrum calculation (SSC) framework. Thereby, two new methods were implemented to calculate the sensor based (deuterium) column density using the estimated gas injection rate. The increased flexibility of the two generalised gas models allows their usage for deuterium (commissioning) and tritium mode of the source, particularly when the e-gun is not available to provide column density calibration measurements. For most of the First Tritium runs, the D_2 column density is estimated to be $4.5 \times 10^{21}\,\mathrm{m}^{-2}$, with a relative uncertainty of about 5 %. A cross-check via the pressure of the Krypton capillary showed good agreement within about 3-4 %. Moreover, a dedicated WGTS magnetic stray field measurement system was designed, developed and commissioned. After proper position determination, its measurements can be used to validate and anchor the magnetic field simulations of the WGTS.

Analysis of First Tritium data With the sensor based source model, it was possible to analyse the tritium spectra taken during the Very First Tritium and the First Tritium commissioning campaigns. The agreement between spectral model

and the data was found to be very good, therefore several analysis methods for the tritium spectrum could be tested. Different methods to include systematic effects were investigated using the column density simulated by the source model as an illustrative example. The resulting estimates of the effective endpoint were compared against each other, as well as to the expected value obtained from T-^{3}He atomic mass difference measurements [Mye+15]. All estimates were found to agree within the assumed range of 1 eV (a sizeable uncertainty stemming from the current accuracy of the absolute energy scale of the KATRIN experiment [WVH]). From the appended run estimation with the column density as free fit parameter, a column density of $(4.61 \pm 0.12) \times 10^{21}\,\mathrm{m}^{-2}$ was found, which is within the uncertainty of the simulation result. Additional estimations of the column density were possible due to the active commissioning. The FBM and PULCINELLA estimates also agree with the column density simulation. Adapting the model input parameters for the slightly higher column density estimate of the aforementioned independent detectors and fit results yields excellent agreement ($\mathcal{N} = 4.6 \times 10^{21}\,\mathrm{m}^{-2}$) for Boltzmann and Knudsen based flow for an accommodation coefficient $\alpha = 1$ (instead of 0.97) and an outlet to inlet pressure ratio of $p_{\mathrm{out}}/p_{\mathrm{in}} = 0.05$ (instead of 0.02).

Blind analysis and methods Looking ahead, the neutrino mass data taking of KATRIN is about to begin in early 2019. As a key outcome of this thesis, several possible schemes for performing a blind analysis were developed. Three data blinding techniques (reduced statistics, window blinding, and energy smearing) and two model blinding techniques (imperfect energy loss function and FSD smearing) were investigated and their effect on the neutrino mass estimation quantified. After evaluation of the latter, four blinding techniques are considered viable for KATRIN neutrino mass analysis. For the first neutrino mass data, two blinding techniques are favoured, namely FSD and energy smearing. Application of either one will introduce a unidirectional artificial shift of the reconstructed neutrino mass. As the two techniques yield opposite signs for this shift, a combination of both methods is considered as the strongest blinding scheme plausible for the first neutrino mass data. Note that the model blinding techniques rely on the analyst's responsibility and are meant to prevent accidental bias by analysing unblinded data. Since the raw data will always be available unblinded to check for systematic effects, the only data blinded will be neutrino mass data. That is, the data blinding will be applied in the intermediate data layer such that the high-level neutrino mass analysis will work on blinded run summaries. The generation of blinded run summaries was tested successfully, along with the FSD smearing model blinding technique. All methods tested on krypton (and tritium) data worked as expected. Based on the findings of this thesis, a proposal of viable techniques and a recommended strategy will be put forward for the KATRIN collaboration to deliberate and decide on.

Physics beyond the neutrino mass Besides serving its main scientific goal, the model-independent determination of the effective electron neutrino mass, the KATRIN data can be used to probe various interesting models of physics beyond the Standard Model. In the course of this thesis, three such opportunities were subject to a detailed investigation: the statistical sensitivity of KATRIN to constrain the additional emission of light bosons in β-decay, the existence of right-handed currents in presence of eV-scale sterile neutrinos, and the relic neutrino background

was investigated. Though the sensitivity of KATRIN towards the additional emission of light vector bosons or pseudoscalars is found not to surpass existing limits for the present KATRIN set-up, KATRIN may provide a complementary limit. In a TRISTAN-like future extension for a differential measurement of the tritium spectrum, the large statistics available from the full tritium spectrum enables testing existing limits e.g. from IceCube [IM14]. The statistical sensitivity of KATRIN towards right handed currents in β-decay was found to be not competitive to existing constraints from LHC data; however, KATRIN can provide a model-independent cross-check. The latter is especially important as the LHC bounds are based on LR-symmetry, while KATRIN can probe different effects that may result in this model independent parametrisation. The findings of the right handed currents match the ones obtained in ref. [Ste+17], though this thesis assumes slightly different KATRIN settings. The latter mainly accommodate for a scenario with an elevated background rate, a decreased energy resolution due to higher analysing plane magnetic field, and an extended energy range of the measurement interval. These alternative settings were also used to re-evaluate KATRIN's statistical sensitivity to constrain the relic neutrino background. KATRIN will be able to improve the existing direct limit on the local relic neutrino overdensity by at least one order of magnitude and thereby also exclude some of the more progressive astrophysical models. However, most predictions of the relic neutrino overdensity are clearly below the sensitivity of the KATRIN experiment.

Conclusions The focus of this thesis was on the opportunities offered by the unique tritium source of the KATRIN experiment. The automated estimation of the column density based on a gas model using sensor data enabled first comparisons between the modelled and the measured tritium spectra. It was shown that the KATRIN experiment is performing as expected and ready for the start of neutrino mass data taking, including a possible blind analysis. Furthermore, the unique tritium source paired with the high-resolution electrostatic spectrometer enables testing aspects of hypothetical new physics beyond the Standard Model, thus allowing to broaden the scientific reach of the experiment beyond the hunt for the neutrino mass.

Outlook In the course of the past two years, the KATRIN collaboration has successfully accomplished several important milestones en route to the start of neutrino mass data taking: from completing the beam line in 2016, to recording first high-resolution spectra of ^{83m}Kr-conversion electron lines in 2017, up to the measuring of first tritium β-spectra in 2018. During the time of writing this thesis, another important milestone is reached, which is the extensive commissioning phase with the e-gun at the rear section. Together with the measurements of the column density developed in the course of this thesis, the e-gun will enable accurate and precise determination of the column density in the nominal tritium set-up. In early 2019, KATRIN will start its eagerly awaited nominal tritium running, which will allow the start of the physics harvest to be continued over the next years.

APPENDIX

A. Source modelling

A.1. Temperature

Fig. A.1 shows a CAD model of the connection of the central WGTS beam tube to the pump port PP1-R. It can be seen that the beam tube cooling does not start right at the pump port and that the temperature sensors only are placed in region with active beam tube cooling.

A.2. First Tritium set-up

Table A.1.: **Times used for the injection rate calibration.** Only times with ensured stable circulation were chosen, year is 2018.

start	end
06-11, 0:00 h	06-12, 5:00 h
06-12, 7:00 h	06-12, 15:00 h
06-12, 17:00 h	06-13, 7:00 h
06-13, 15:00 h	06-14, 8:00 h
06-14, 19:00 h	06-15, 6:00 h
06-15, 8:00 h	06-15, 21:00 h

A.3. Magnetic field measurements

As described in sec. 4.5.2, the longitudinal position of the hall probe needs to be determined with a sub-mm uncertainty. WayCon states a 0.02 % linearity deviation of the rope sensor, however the calibration certificate in fig. A.2 provided by WayCon lists a maximum linearity deviation of 0.002 %.

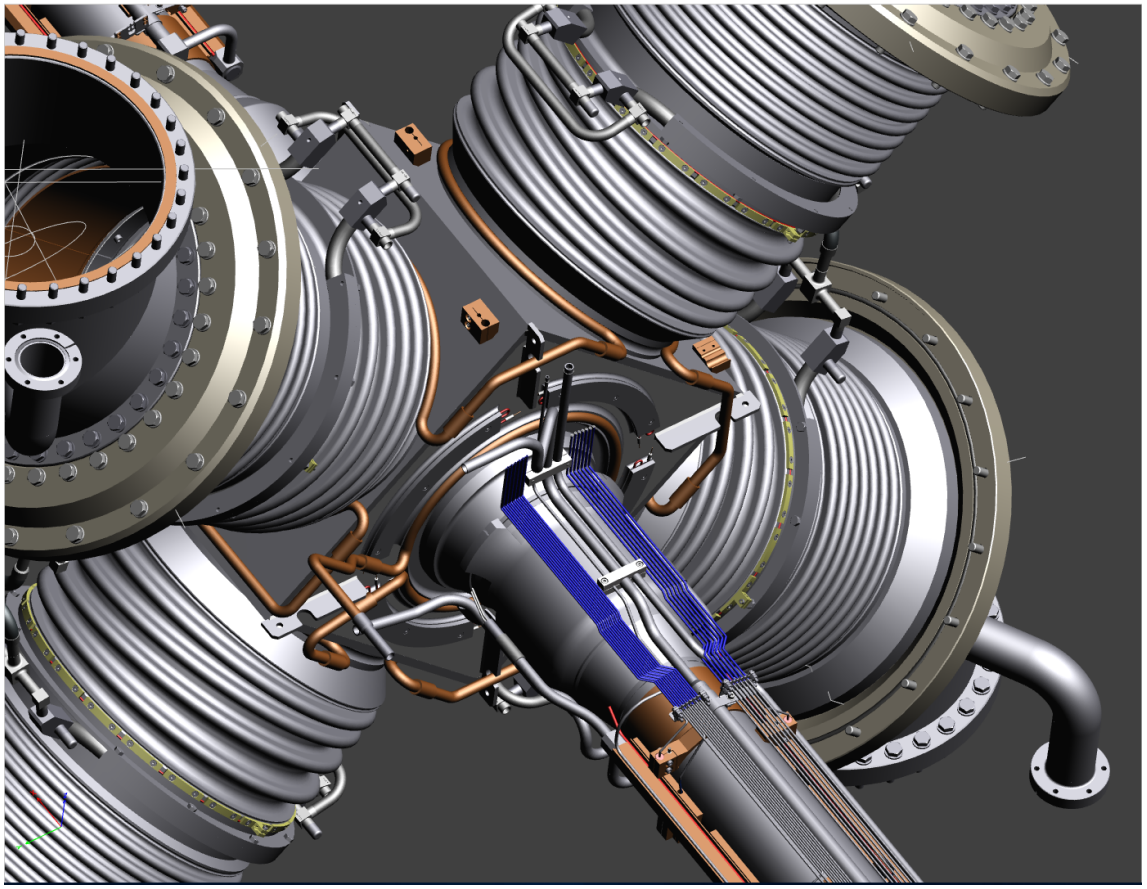

Figure A.1.: **Connection between beam tube and pump port.** The position of the Pt500 temperature sensors as well as the 2-phase neon cooling and the pump port cooling are shown in copper.

B. Analysis of First Tritium data

B.1. Estimation of the column density

During the readout of the FBM spectrum, it was discovered that the cut is better to be done on the ADC spectrum, not on the calibrated one: when cutting at 5 keV on the calibrated spectrum, the result is shown in fig. B.4. Therefore, the rate was estimated by cutting on the ADC equivalent of 5 keV, which is also shown on fig. B.4.

C. Blind analysis & methods

C.1. Sensitivity estimates

It has to be noted that not all methods have been tested with the exact same settings of the background rate Bg and energy resolution. However, the high level of blinding required for the first KATRIN neutrino mass data requires effects in systematic or statistic uncertainty one order of magnitude larger than the effect of an elevated background rate: if the MTD is adapted for an elevated background

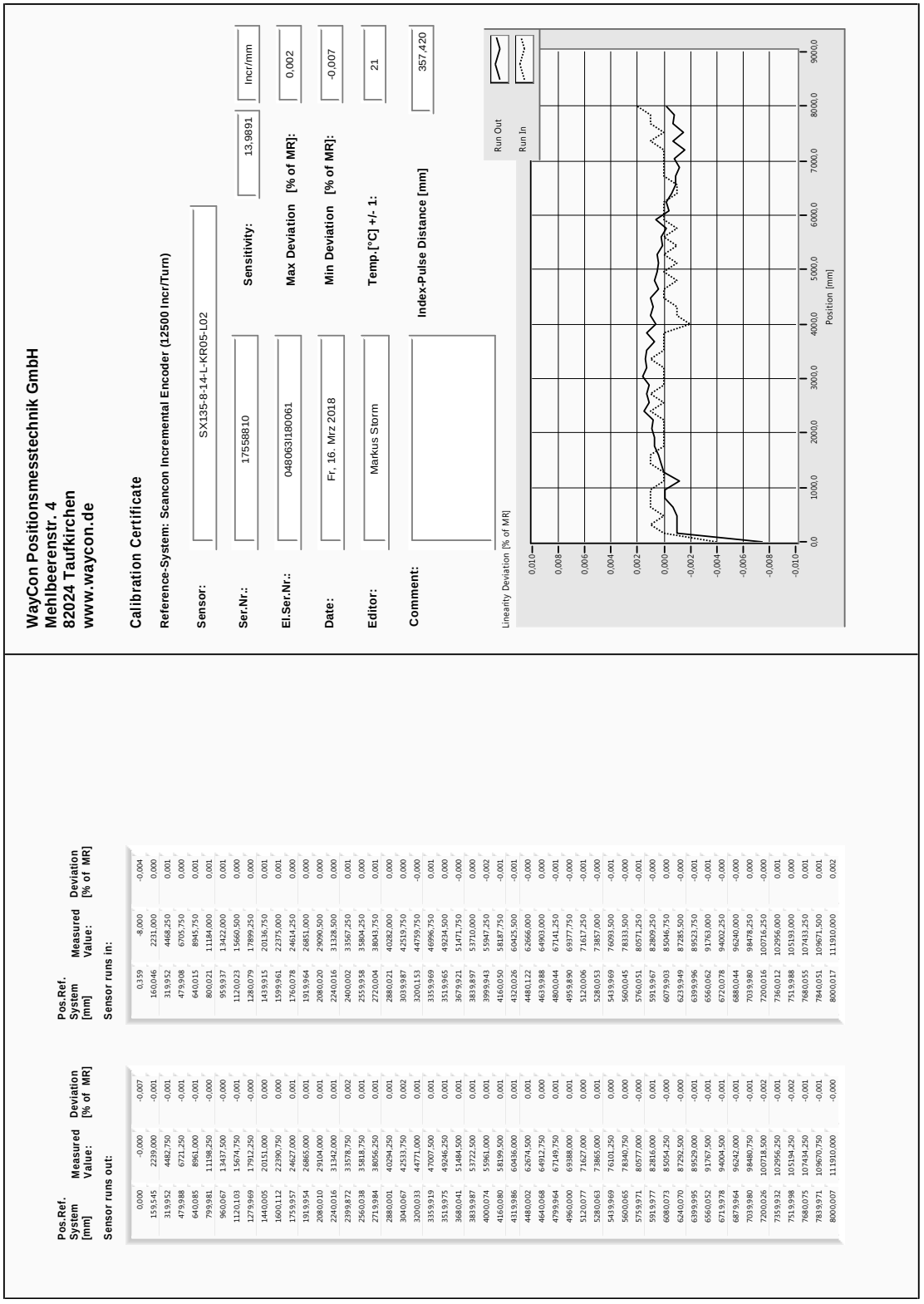

Figure A.2.: **Rope sensor calibration table.** This table for one of the used *SX135* rope sensor underlines that the accuracy of the distance measurement is within the sub-mm requirement.

rate of 0.225 cps[1] instead of designed 0.01 cps [KAT05], the estimated neutrino mass

[1]F. Harms found an increased spectrometer background rate of 691 ± 1 mcps in commissioning measurements with different settings than the ones used in this thesis [Har15].

$$\begin{array}{c} \\ E_{0,\mathrm{eff}} \\ Amp \\ Bg \end{array} \begin{bmatrix} 1 & -0.833116 & -0.283638 \\ -0.833116 & 1 & 0.207279 \\ -0.283638 & 0.207279 & 1 \end{bmatrix} \tag{8.1}$$

Figure B.3.: **Correlation matrix of the fit parameters.** The values were obtained from the example run 40667.

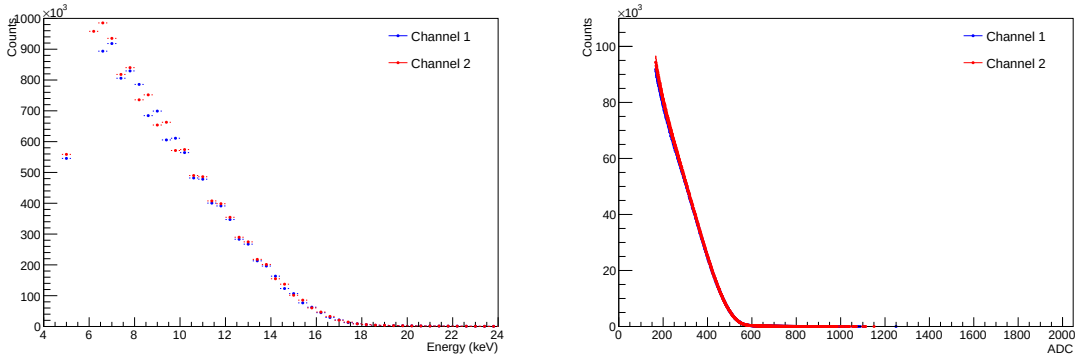

Figure B.4.: **FBM spectra.** Left: energy-calibrated spectrum, right: ADC raw spectrum. FBM runs analysed: 145-147 (June 6, 2018).

sensitivity decreases to 0.24 eV instead of 0.20 eV. In contrast, a sensitivity as high as 2 eV is to be reached with blind analysis of the first neutrino mass data.

Table C.2.: **Settings for data blinding.** Some of them differ from the Design Report [KAT05] and were adapted to account for higher background.

setting	Design Report	data blinding
Bg (cps)	0.01	0.225
B_{S} (T)	3.6	3.6
B_{Ana} (G)	3	9
B_{PCH} (T)	6.0	6.0
$\mathcal{N}$ (m^2)	5×10^{21}	5×10^{21}
ϵ_{T}	0.95	0.95

C.2. Window blinding

In tab. C.3, exemplary neutrino mass sensitivity estimates are shown to underline the principal understanding of the effect of this method described in sec. 6.3.1.2. Only after removing all data up to the estimated endpoint (row 5 in tab. C.3), a significant worsening of the neutrino mass can be observed. Also note that though

nearly 70% of the measuring time needs to be blinded, this translates to hiding about 20% of all events measured in that time.

Table C.3.: **Sensitivities for different partial blinding schemes for the neutrino mass region**. Also compare fig. 6.3. Standard settings from Design Report used [KAT05]. This will look different for more realistic values of background and MTD and is shown here to underline the principal understanding of this blinding method.

blinded window (eV)	% blinded of MTD	% blinded of events	$\sigma_{m_\nu^2}$ (eV^2)	90 % CL sens on m_ν (eV)
–	0.0	0.0	0.017	0.198
$[E_0 - 4.5, E_0 - 4]$	34.6	0.4	0.029	0.235
$[E_0 - 9, E_0 - 4]$	43.5	0.9	0.040	0.268
$[E_0 - 14, E_0 - 4]$	49.0	3.9	0.041	0.269
$[E_0 - 14, E_0]$	61.6	4.0	0.612	1.004
$[E_0 - 19, E_0]$	67.1	14.0	1.570	1.607
$[E_0 - 21, E_0]$	69.3	21.4	2.652	2.089

C.3. Imperfect energy loss function

In fig. C.5, the different ϵ_c are shown for several changes of the excitation/ionisation ratio η. Note that due to the form of eq. (6.21), the root yields a positive and a negative solution. Since the negative solution refers to the left side of the Gaussian function, the critical energy that is needed for this analysis is defined by the positive solution of the root. Exemplary, no change of the ratios ($\eta = 0$) yields $\epsilon_c = 14.09\,\mathrm{eV}$.

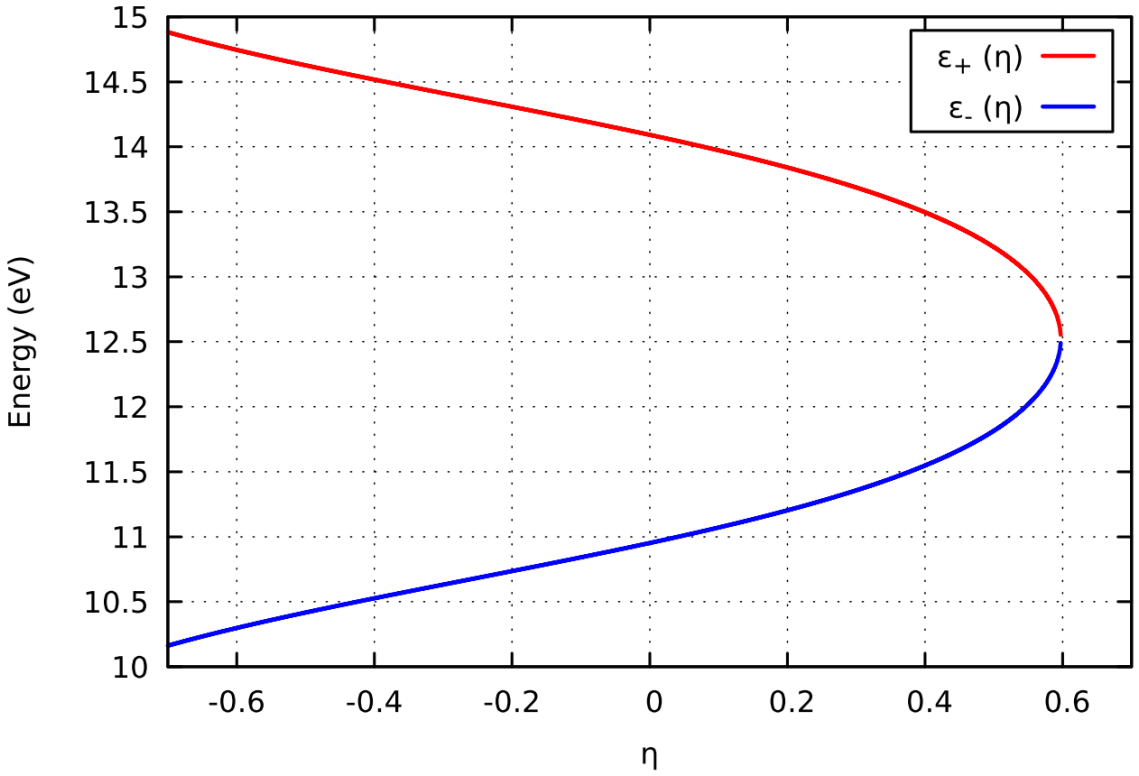

Figure C.5.: **Energy loss critical energy**. X axis is the change of the excitation/ionisation ratio, y axis shows the resulting solutions of eq. (6.21). Figure taken from ref. [Sib18], credits V. Sibille.

D. Physics beyond the neutrino mass

D.1. Experiment configuration for the new physics studies

Recent commissioning measurements [Har15, Are+18b, Blo18, Tro18] (also see sec. 5.1) with the current KATRIN set-up yield an elevated background rate compared to the design settings [KAT05]. Due to its volume effect, the background rate can be decreased by applying a larger magnetic field in the analysing plane. A magnetic field in the analysing plane of $B_{\mathrm{ana}} = 6\,\mathrm{G}$ combined with all other magnetic fields of the beam line scaled to 70 % of their design value results in a background rate of about 0.4 cps. This increased background rate will cause modifications to the measuring time distribution (MTD), as the neutrino mass signature manifests farther away from the spectral endpoint. The effect is shown in fig. 6.1, exemplarily for a neutrino mass of 1 eV. Further changes to the MTD used in the following simulations, as a conceivable scenario, occur from scanning a wider energy range $[E_0-50\,\mathrm{eV}, E_0+5\,\mathrm{eV}]$ compared to the $[E_0 - 30\,\mathrm{eV}, E_0 + 5\,\mathrm{eV}]$ of the design report. Apart from that, the total amount of measuring time is the 3 yr net worth of data taking, which translates into approximately 5 yr KATRIN operation time. Commissioning measurements with the final KATRIN setup [Are+18b, Are+18c] revealed the optimum setting of the magnetic fields to be at 70% of the fields proposed in the design report, so for instance the WGTS has a field of 2.52 T in the following [Hac17]. For the simulations, the nominal tritium purity of $\epsilon_{\mathrm{T}} = 0.95$ and the nominal amount of gas column density in the WGTS of $\mathcal{N} = 5 \times 10^{21}\,\mathrm{cm}^{-2}$ is used.

Table D.4.: **Operational parameters used for the simulations.** Most notable differences are the wider measuring window and the different magnetic fields compared to the Design Report (DR) settings [KAT05].

param	value	value in DR
E_0 (eV)	18575	18575
Bg (cps)	0.4	0.01
B_{ana} (G)	6	3
B_{S} (T)	2.52	3.6
B beam line	70 %	100 %
MTD range (eV)	$[E_0 - 50, E_0 + 5]$	$[E_0 - 30, E_0 + 5]$
total time (yr)	3	3
$\mathcal{N}$ (m^{-2})	5×10^{21}	5×10^{21}
ϵ_{T}	0.95	0.95
ϵ_{det}	0.9	0.9

D.2. Light bosons

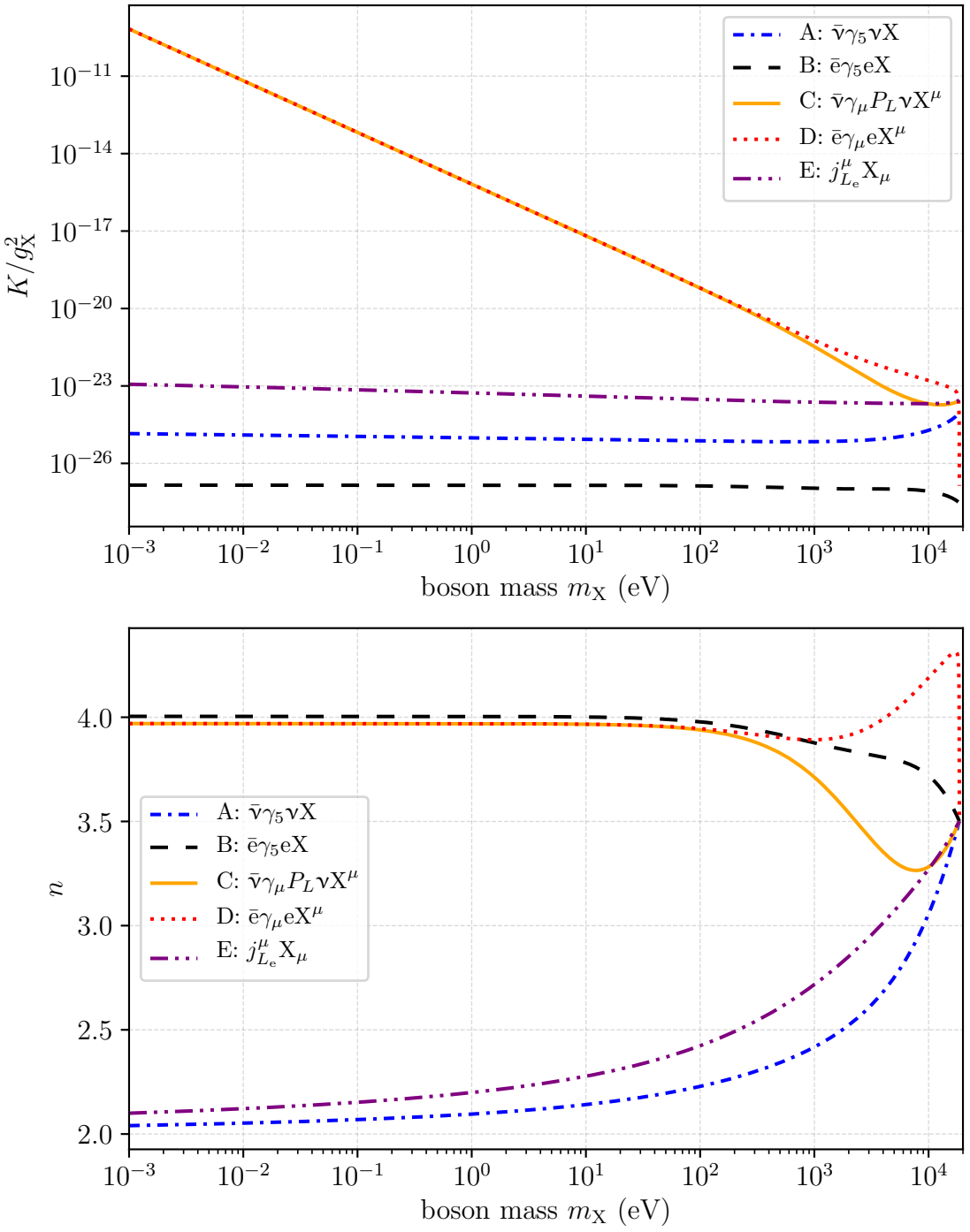

Figure D.6.: **Parameters for the spectrum approximation of the light bosons.** Note the increasing K for small m_X for mechanisms C and D. Figure adapted from ref. [Arc+18].

Table D.5.: Summary table including all the laboratory, astroparticle, and cosmological constraints which apply to the models discussed in ref. [Arc+18] and this thesis. LNV stands for lepton number violating coupling. Table taken from ref. [Arc+18].

Model A	$\bar{\nu}\gamma_5 \nu \mathrm{X}$
Double β decay (only LNV)	$g_{\nu J} \lesssim 10^{-(4 \div 5)}$ [BNS18, BP18]
Meson decays	$g_{\nu J} \lesssim 4.4 \times 10^{-5}$ [PP16]
CMB	$g_{\nu J} \lesssim 1.2 \times 10^{-2} \left(\frac{m_J}{1\,\mathrm{MeV}}\right)$ $(m_J \gg 1\,\mathrm{eV})$
	$g_{\nu J} \lesssim 1.2 \times 10^{-7}$ $(m_J \ll 1\,\mathrm{eV})$ [AH14]
Supernova 1987A	$g_{\nu J} \lesssim 10^{-3}$ $(m_J \leq \mathcal{O}(1\,\mathrm{eV}))$ [KT87]
IceCube	$g_{\nu J} \lesssim 0.03$ [IM14]
$\Delta N_{\mathrm{eff}}^{\mathrm{CMB}}$	$g_{\nu J} \lesssim 1.6 \times 10^{-6} \left(\frac{1\,\mathrm{keV}}{m_J}\right)$ $(m_J \simeq \mathcal{O}(\mathrm{keV})$
	$g_{\nu J} \lesssim 5 \times 10^{-5}$ $(m_J \simeq \mathcal{O}(\mathrm{eV}))$ [HOZ18, Agh+18]
Model B	$\bar{\mathrm{e}}\gamma_5 \mathrm{eX}$
Solar lifetime	$g_{eJ} \lesssim 3 \times 10^{-11}$ [GR09]
$(g-2)_e$	$g_{eJ} \lesssim 1.8 \times 10^{-5}$ [Par+18, LWW18]
Model C	$\bar{\nu}\gamma_\mu P_L \nu \mathrm{X}^\mu$
Z decay	$g_{\nu L} \lesssim 3 \times 10^{-2}$ [LDB14]
Meson decays	$g_{\nu L} \lesssim 2.5 \times 10^{-7} \left(\frac{m_{Z'}}{1\,\mathrm{keV}}\right)$ [LDB14]
BBN	$g_{\nu L} \lesssim 2.2 \times 10^{-7} \left(\frac{1\,\mathrm{keV}}{m_{Z'}}\right)$ $(m_{Z'} \simeq \mathcal{O}(\mathrm{keV}))$
	$g_{\nu L} \lesssim 4.6 \times 10^{-6}$ $(m_{Z'} \simeq \mathcal{O}(\mathrm{eV}))$ [HOZ18]
CMB	$g_{\nu L} \lesssim 1.2 \times 10^{-2} \left(\frac{m_{Z'}}{1\,\mathrm{MeV}}\right)$ $(m_{Z'} \gg 1\,\mathrm{eV})$ [AH14]
Supernova 1987A	$g_{\nu L} \lesssim 12 \left(\frac{m_{Z'}}{1\,\mathrm{MeV}}\right)$ $(m_{Z'} \geq 60\,\mathrm{eV})$
	$g_{\nu L} \lesssim 5.6 \times 10^{-4}$ $(m_{Z'} < 60\,\mathrm{eV})$ [KT87]
IceCube	$g_{\nu L} \lesssim 0.03$ [IM14]
Model D	$\bar{\mathrm{e}}\gamma_\mu \mathrm{eX}^\mu$
W decays	$g_{eV} \lesssim 2.5 \times 10^{-7} \left(\frac{m_{Z'}}{1\,\mathrm{keV}}\right)$ [LDB14]
Solar lifetime	$g_{eV} \lesssim 2 \times 10^{-13}$ [GR09]
BBN	$g_{eV} \lesssim 4.6 \times 10^{-6}$
$(g-2)_{\mathrm{e}}$	$g_{eV} \lesssim 4.0 \times 10^{-6}$ [Par+18, LWW18]
Model E	$j^\mu_{L_{\mathrm{e}}} \mathrm{X}_\mu$
Z decay	$g_{L_{\mathrm{e}}} \lesssim 3 \times 10^{-2}$ [LDB14]
ν–e scattering	$g_{L_{\mathrm{e}}} \lesssim 10^{-6}$ [LDB14, Lin+18]

LIST OF FIGURES

LIST OF TABLES

LIST OF ACRONYMS

BEANS	Building Elements for ANalysis Sequence
BIXS	Beta Induced X-ray Spectroscopy
CAD	Computer-Aided Design
CC	Charged Current
CDM	Cold Dark Matter
CKM	Cabibbo-Kobayashi-Maskawa quark mixing matrix
CMB	Cosmic Microwave Background
CνB	Cosmic Neutrino Background
CPS	Cryogenic Pumping Section
DAQ	Data Acquisition system
DPS	Differential Pumping Section
DSMC	Direct Simulation Monte Carlo
FBM	Forward Beam Monitor
FPD	Focal Plane Detector
FPGA	Field Programmable Gate Array
FSD	Final States Distribution
GHe	Gaseous Helium
IDLE	Intermediate Data Layer
KaFit	Fit environment for KATRIN-spectra
KASPER	KATRIN C++ software package
KATRIN	KArlsruhe TRItium Neutrino (experiment)
KESS	KATRIN Electron Scattering in Silicon Simulation package, MC simulation code for low-energy electron interactions in silicon detectors

KaLi	KAtrin LIbrary
LARA	LAser RAman spectroscopy system
LHC	Large Hadron Collider
LHe	Liquid Helium
LN	Liquid Nitrogen
LRSM	Left-Right Symmetric Model
MAC-E	Magnetic Adiabatic Collimation with Electrostatic filtering
MCMC	Markov Chain Monte Carlo
MSW	Mikheyev, Smirnov, Wolfenstein effect
MTD	Measuring Time Distribution
NC	Neutral Current
NMR	Nuclear Magnetic Resonance
ORCA	Object-oriented Real-time Control and Acquisition software
PCH	Pinch magnet (maximum magnetic field in KATRIN)
PCS7	SIMATIC Process Control System 7
PMNS	Pontecorvo-Maki-Nakagawa-Sakata neutrino mixing matrix
PMT	Photo Multiplier Tube
PS	Pre-Spectrometer
PULCINELLA	Precision Ultra-Low Current Integrating Normalization Electrometer for Low-Level Analysis
ROI	Region Of Interest cut applied to FPD data
RS	Rear Section
SDS	Spectrometers and Detector Section
SSC	Source and Spectrum Calculation package of the KASPER suite
SSM	Standard Solar Model
SM	Standard Model of particle physics
SNO	Sudbury Neutrino Observatory
SSM	standard solar model
STS	source and transport section
SuperK	SuperKamiokande
TLK	Tritium Laboratory Karlsruhe
TMP	turbo-molecular pump
TRISTAN	Tritium Beta Decay to Search for Sterile Neutrinos
WGTS	Windowless Gaseous Tritium Source

INDEX

BIBLIOGRAPHY

[Aal+18] C. E. Aalseth et al. "Search for Neutrinoless Double-β Decay in ^{76}Ge with the MAJORANA DEMONSTRATOR". In: *Physical Review Letters* 120.13 (2018), p. 132502. DOI: 10.1103/PhysRevLett.120.132502. arXiv: 1710.11608 [nucl-ex].

[Aar+15] M. G. Aartsen et al. "Determining neutrino oscillation parameters from atmospheric muon neutrino disappearance with three years of IceCube DeepCore data". In: *Physical Review D* 91.7 (2015), p. 072004. DOI: 10.1103/PhysRevD.91.072004. arXiv: 1410.7227 [hep-ex].

[Aar+16] M. G. Aartsen et al. "Searches for Sterile Neutrinos with the IceCube Detector". In: *Physical Review Letters* 117.7 (2016), p. 071801. DOI: 10.1103/PhysRevLett.117.071801. arXiv: 1605.01990 [hep-ex].

[Abe+11] S. Abe et al. "Measurement of the 8B Solar Neutrino Flux with the KamLAND Liquid Scintillator Detector". In: *Physical Review C* 84 (2011), p. 035804. DOI: 10.1103/PhysRevC.84.035804. arXiv: 1106.0861 [hep-ex].

[Abe+12a] Y. Abe et al. "Indication of Reactor $\bar{\nu}_e$ Disappearance in the Double Chooz Experiment". In: *Physical Review Letters* 108 (2012), p. 131801. DOI: 10.1103/PhysRevLett.108.131801. arXiv: 1112.6353 [hep-ex].

[Abe+12b] Y. Abe et al. "Reactor $\overline{\nu}_e$ disappearance in the Double Chooz experiment". In: *Physical Review D* 86 (5 2012), p. 052008. DOI: 10.1103/PhysRevD.86.052008.

[Abe+16] K. Abe et al. "Solar Neutrino Measurements in Super-Kamiokande-IV". In: *Physical Review D* 94.5 (2016), p. 052010. DOI: 10.1103/PhysRevD.94.052010. arXiv: 1606.07538 [hep-ex].

[Abe+17] K. Abe et al. "Measurement of neutrino and antineutrino oscillations by the T2K experiment including a new additional sample of ν_e interactions at the far detector". In: *Physical Review D* 96.9 (2017), p. 092006. DOI: 10.1103/PhysRevD.96.092006. arXiv: 1707.01048 [hep-ex]. Erratum in: *Physical Review D* 98.1 (2018), p. 019902. DOI: 10.1103/PhysRevD.98.019902.

[Ada+13] C. Adams et al. "The Long-Baseline Neutrino Experiment: Exploring Fundamental Symmetries of the Universe". In: (2013). arXiv: 1307.7335 [hep-ex].

[Ada+14] P. Adamson et al. "Combined Analysis of ν_μ Disappearance and $\nu_\mu \to \nu_e$ Appearance in MINOS Using Accelerator and Atmospheric neutrinos". In: *Physical Review Letters* 112 (2014), p. 191801. DOI: 10.1103/PhysRevLett.112.191801. arXiv: 1403.0867 [hep-ex].

[Ada+17] P. Adamson et al. "Measurement of the Neutrino Mixing Angle θ_{23} in NOvA". In: *Physical Review Letters* 118.15 (2017), p. 151802. DOI: 10.1103/PhysRevLett.118.151802. arXiv: 1701.05891 [hep-ex].

[Agh+18] N. Aghanim et al. "Planck 2018 results. VI. Cosmological parameters". In: (2018). arXiv: 1807.06209 [astro-ph.CO].

[Ago+13] M. Agostini et al. "Results on Neutrinoless Double-β Decay of ^{76}Ge from Phase I of the GERDA Experiment". In: *Physical Review Letters* 111.12 (2013), p. 122503. DOI: 10.1103/PhysRevLett.111.122503. arXiv: 1307.4720 [nucl-ex].

[Ago+17a] M. Agostini et al. "First Simultaneous Precision Spectroscopy of *pp*, ^{7}Be, and *pep* Solar Neutrinos with Borexino Phase-II". In: (2017). arXiv: 1707.09279 [hep-ex].

[Ago+17b] M. Agostini et al. "Improved measurement of 8B solar neutrinos with 1.5 kt y of Borexino exposure". In: (2017). arXiv: 1709.00756 [hep-ex].

[Ago+18] M. Agostini et al. "Improved Limit on Neutrinoless Double-β Decay of ^{76}Ge from GERDA Phase II". In: *Physical Review Letters* 120.13 (2018), p. 132503. DOI: 10.1103/PhysRevLett.120.132503. arXiv: 1803.11100 [nucl-ex].

[AH14] M. Archidiacono and S. Hannestad. "Updated constraints on non-standard neutrino interactions from Planck". In: *Journal of Cosmology and Astroparticle Physics* 1407 (2014), p. 046. DOI: 10.1088/1475-7516/2014/07/046. arXiv: 1311.3873 [astro-ph.CO].

[Ahm+01] Q. R. Ahmad et al. "Measurement of the rate of $\nu_e + d \to p + p + e^-$ interactions produced by ^{8}B solar neutrinos at the Sudbury Neutrino Observatory". In: *Physical Review Letters* 87 (2001), p. 071301. DOI: 10.1103/PhysRevLett.87.071301. arXiv: nucl-ex/0106015 [nucl-ex].

[Ahn+12] J. K. Ahn et al. "Observation of Reactor Electron Antineutrinos Disappearance in the RENO Experiment". In: *Physical Review Letters* 108 (19 2012), p. 191802. DOI: 10.1103/PhysRevLett.108.191802.

[Ala+17] S. Alam et al. "The clustering of galaxies in the completed SDSS-III Baryon Oscillation Spectroscopic Survey: cosmological analysis of the DR12 galaxy sample". In: *Monthly Notices of the Royal Astronomical Society* 470.3 (2017), pp. 2617–2652. DOI: 10.1093/mnras/stx721. arXiv: 1607.03155 [astro-ph.CO].

[Alb+18] J. B. Albert et al. "Search for Neutrinoless Double-Beta Decay with the Upgraded EXO-200 Detector". In: *Physical Review Letters* 120.7 (2018), p. 072701. DOI: 10.1103/PhysRevLett.120.072701. arXiv: 1707.08707 [hep-ex].

[Ald+18] C. Alduino et al. "First Results from CUORE: A Search for Lepton Number Violation via $0\nu\beta\beta$ Decay of ^{130}Te". In: *Physical Review Letters* 120.13 (2018), p. 132501. DOI: 10.1103/PhysRevLett.120.132501. arXiv: 1710.07988 [nucl-ex].

[Ams+12] J. F. Amsbaugh et al. *Prototype focal-plane detector system for the KATRIN experiment*. Technical report. KATRIN detector section working group, Jan. 2012. URL: https://fuzzy.fzk.de/bscw/bscw.cgi/d722700/FPD_System_Prototype_Jan2012.pdf.

[Ams+15] J. Amsbaugh et al. "Focal-plane detector system for the KATRIN experiment". In: *Nuclear Instruments and Methods in Physics Research Section A: Accelerators, Spectrometers, Detectors and Associated Equipment* 778 (2015), pp. 40–60. DOI: 10.1016/j.nima.2014.12.116.

[AMW86] M. J. Assael, S. Mixafendi, and W. A. Wakeham. "The Viscosity and Thermal Conductivity of Normal Hydrogen in the Limit of Zero Density". In: *Journal of Physical and Chemical Reference Data* 15.4 (1986), pp. 1315–1322. DOI: 10.1063/1.555764.

[AMW87] M. J. Assael, S. Mixafendi, and W. A. Wakeham. "The Viscosity of Normal Deuterium in the Limit of Zero Density". In: *Journal of Physical and Chemical Reference Data* 16.2 (1987), pp. 189–192. DOI: 10.1063/1.555778.

[An+12] F. P. An et al. "Observation of Electron-Antineutrino Disappearance at Daya Bay". In: *Physical Review Letters* 108 (17 2012), p. 171803. DOI: 10.1103/PhysRevLett.108.171803.

[An+13] F. P. An et al. "Improved Measurement of Electron Antineutrino Disappearance at Daya Bay". In: *Chinese Physics C* 37 (2013), p. 011001. DOI: 10.1088/1674-1137/37/1/011001. arXiv: 1210.6327 [hep-ex].

[An+16] F. P. An et al. "Neutrino Physics with JUNO". In: *Journal of Physics G* 43.3 (2016), p. 030401. DOI: 10.1088/0954-3899/43/3/030401. arXiv: 1507.05613 [physics.ins-det].

[An+17] F. P. An et al. "Measurement of electron antineutrino oscillation based on 1230 days of operation of the Daya Bay experiment". In: *Physical Review D* 95.7 (2017), p. 072006. DOI: 10.1103/PhysRevD.95.072006. arXiv: 1610.04802 [hep-ex].

[Ara+05] T. Araki et al. "Measurement of neutrino oscillation with KamLAND: Evidence of spectral distortion". In: *Physical Review Letters* 94 (2005), p. 081801. DOI: 10.1103/PhysRevLett.94.081801. arXiv: hep-ex/0406035 [hep-ex].

[Arc+18] G. Arcadi et al. "Tritium beta decay with additional emission of new light bosons". In: (2018). arXiv: 1811.03530 [hep-ph].

[Are+16] M. Arenz et al. "Commissioning of the vacuum system of the KATRIN Main Spectrometer". In: *Journal of Instrumentation* 11 (2016), P04011. DOI: 10.1088/1748-0221/11/04/P04011. arXiv: 1603.01014 [physics.ins-det].

[Are+18a] M. Arenz et al. "Calibration of high voltages at the ppm level by the difference of ^{83m}Kr conversion electron lines at the KATRIN experiment". In: *The European Physical Journal C* 78.5 (2018), p. 368. DOI: 10.1140/epjc/s10052-018-5832-y.

[Are+18b] M. Arenz et al. "First transmission of electrons and ions through the KATRIN beamline". In: *Journal of Instrumentation* 13.04 (2018), P04020. DOI: 10.1088/1748-0221/13/04/P04020.

[Are+18c] M. Arenz et al. "The KATRIN Superconducting Magnets: Overview and First Performance Results". In: *Journal of Instrumentation* 13.08 (2018), T08005. DOI: 10.1088/1748-0221/13/08/T08005.

[Are+19] M. Arenz et al. *Results from first tritium β-spectroscopy of the KATRIN experiment*. Forthcoming work. 2019.

[Ase+00] V. N. Aseev et al. "Energy loss of 18 keV electrons in gaseous T_2 and quench condensed D_2 films". In: *The European Physical Journal D* 10 (1 2000), pp. 39–52. DOI: 10.1007/s100530050525.

[Ase+11] V. N. Aseev et al. "Upper limit on the electron antineutrino mass from the Troitsk experiment". In: *Physical Review D* 84 (11 2011), p. 112003. DOI: 10.1103/PhysRevD.84.112003.

[Asn+15] D. M. Asner et al. "Single electron detection and spectroscopy via relativistic cyclotron radiation". In: *Physical Review Letters* 114.16 (2015), p. 162501. DOI: 10.1103/PhysRevLett.114.162501. arXiv: 1408.5362 [physics.ins-det].

[ATL12] ATLAS Collaboration. "Observation of a new particle in the search for the Standard Model Higgs boson with the ATLAS detector at the LHC". In: *Physics Letters* 716 (2012), pp. 1–29. DOI: 10.1016/j.physletb.2012.08.020. arXiv: 1207.7214 [hep-ex].

[Ayr+04] D. S. Ayres et al. "NOvA: Proposal to Build a 30 Kiloton Off-Axis Detector to Study $\nu_\mu \rightarrow \nu_e$ Oscillations in the NuMI Beamline". In: (2004). arXiv: hep-ex/0503053 [hep-ex].

[Bab+12] M. Babutzka et al. "Monitoring of the operating parameters of the KATRIN Windowless Gaseous Tritium Source". In: *New Journal of Physics* 14.10 (2012), p. 103046. DOI: 10.1088/1367-2630/14/10/103046.

[Bab14] M. Babutzka. "Design and development for the Rearsection of the KATRIN experiment". PhD thesis. Karlsruher Institut für Technologie (KIT), 2014. DOI: 10.5445/IR/1000045598.

[Bah64a] J. N. Bahcall. "Solar Neutrino Cross Sections and Nuclear Beta Decay". In: *Physical Review* 135 (1B July 1964), B137–B146. DOI: 10.1103/PhysRev.135.B137.

[Bah64b] J. N. Bahcall. "Solar Neutrinos. I. Theoretical". In: *Physical Review Letters* 12 (11 Mar. 1964), pp. 300–302. DOI: 10.1103/PhysRevLett.12.300.

[Bar+18] E. Baracchini et al. "PTOLEMY: A Proposal for Thermal Relic Detection of Massive Neutrinos and Directional Detection of MeV Dark Matter". In: (2018). arXiv: 1808.01892 [physics.ins-det].

[BC84] S. Baker and R. D. Cousins. "Clarification of the use of CHI-square and likelihood functions in fits to histograms". In: *Nuclear Instruments and Methods in Physics Research* 221 (1984), pp. 437–442. DOI: 10.1016/0167-5087(84)90016-4.

[Beu+11] F. Beutler et al. "The 6dF Galaxy Survey: Baryon Acoustic Oscillations and the Local Hubble Constant". In: *Monthly Notices of the Royal Astronomical Society* 416 (2011), pp. 3017–3032. DOI: 10.1111/j.1365-2966.2011.19250.x. arXiv: 1106.3366 [astro-ph.CO].

[BF17] P. Bakhti and Y. Farzan. "Constraining secret gauge interactions of neutrinos by meson decays". In: *Physical Review D* 95.9 (2017), p. 095008. DOI: 10.1103/PhysRevD.95.095008. arXiv: 1702.04187 [hep-ph].

[BHR14] J. Barry, J. Heeck, and W. Rodejohann. "Sterile neutrinos and right-handed currents in KATRIN". In: *Journal of High Energy Physics* 07 (2014), p. 081. DOI: 10.1007/JHEP07(2014)081. arXiv: 1404.5955 [hep-ph].

[Bir94] G. A. Bird. *Molecular Gas Dynamics and the Direct Simulation of Gas Flows*. Oxford University Press, 1994. ISBN: 9780198561958.

[Blo18] F. Block. "Characterisation of the Background in the KATRIN Experiment". Master thesis. Karlsruher Institut für Technologie (KIT), 2018. URL: https://www.katrin.kit.edu/publikationen/mth_fblock.pdf.

[BNS18] K. Blum, Y. Nir, and M. Shavit. "Neutrinoless double-beta decay with massive scalar emission". In: *Physics Letters B* 785 (2018), pp. 354–361. DOI: 10.1016/j.physletb.2018.08.022. arXiv: 1802.08019 [hep-ph].

[Bor16] D. Borah. "Light sterile neutrino and dark matter in left-right symmetric models without a Higgs bidoublet". In: *Physical Review* 94.7 (2016), p. 075024. DOI: 10.1103/PhysRevD.94.075024. arXiv: 1607.00244 [hep-ph].

[Bos18] Bosch Rexroth. *EcoSlide 45x45x160*. 2018. URL: https://www.boschrexroth.com/ics/cat/?cat=Assembly-Technology-Catalog&m=XC&u=si&o=Desktop&p=p896855&pi=0EE028A5-EFB5-8D9D-2FBBED63042B817C_ICS_82 (visited on 09/22/2018).

[BP18] T. Brune and H. Päs. "Majoron Dark Matter and Constraints on the Majoron-Neutrino Coupling". In: (2018). arXiv: 1808.08158 [hep-ph].

[BP34] H. Bethe and R. Peierls. "The "neutrino"". In: *Nature* 133 (1934), p. 532.

[BPB01] J. N. Bahcall, M. H. Pinsonneault, and S. Basu. "Solar Models: Current Epoch and Time Dependences, Neutrinos, and Helioseismological Properties". In: *The Astrophysical Journal* 555.2 (2001), p. 990. URL: http://stacks.iop.org/0004-637X/555/i=2/a=990.

[BPR15] L. I. Bodine, D. S. Parno, and R. G. H. Robertson. "Assessment of molecular effects on neutrino mass measurements from tritium β decay". In: *Physical Review C* 91.3 (2015), p. 035505. DOI: 10.1103/PhysRevC.91.035505. arXiv: 1502.03497 [nucl-ex].

[BPT80] G. Beamson, H. Q. Porter, and D. W. Turner. "The collimating and magnifying properties of a superconducting field photoelectron spectrometer". In: *Journal of Physics E: Scientific Instruments* 13.1 (1980), p. 64. DOI: 10.1088/0022-3735/13/1/018.

[BR13] J. Barry and W. Rodejohann. "Lepton number and flavour violation in TeV-scale left-right symmetric theories with large left-right mixing". In: *Journal of High Energy Physics* 09 (2013), p. 153. DOI: 10.1007/JHEP09(2013)153. arXiv: 1303.6324 [hep-ph].

[BR97] R. Brun and F. Rademakers. "ROOT: An object oriented data analysis framework". In: *Nuclear Instruments and Methods in Physics A* 389 (1997), pp. 81–86. DOI: 10.1016/S0168-9002(97)00048-X.

[Bra06] C. J. F. T. Braak. "A Markov Chain Monte Carlo version of the genetic algorithm Differential Evolution: easy Bayesian computing for real parameter spaces". In: *Statistics and Computing* 16.3 (Sept. 2006), pp. 239–249. ISSN: 1573-1375. DOI: 10.1007/s11222-006-8769-1.

[BRZ11] J. Barry, W. Rodejohann, and H. Zhang. "Light Sterile Neutrinos: Models and Phenomenology". In: *Journal of High Energy Physics* 07 (2011), p. 091. DOI: 10.1007/JHEP07(2011)091. arXiv: 1105.3911 [hep-ph].

[Bur+08] A. Burck et al. "Microstructured Magnetic Calorimeter with a Meander-Shaped Pickup Coil". In: *Journal of Low Temperature Physics* 151.1 (Apr. 2008), pp. 337–344. ISSN: 1573-7357. DOI: 10.1007/s10909-007-9659-4.

[Cen18] Center for Experimental Nuclear Physics and Astrophysics. *Annual Report 2018*. Technical report. Universtiy of Washington, 2018. URL: https://www.npl.washington.edu/sites/default/files/annual-reports/2018-CENPA-Annual-Report.pdf (visited on 10/28/2018).

[Cha14] J. Chadwick. "Intensitätsverteilung im magnetischen Spectrum der β-Strahlen von Radium B + C". In: *Verhandlungen der Deutschen Physikalischen Gesellschaft* 16 (1914), p. 383.

[Cho+16] J. H. Choi et al. "Observation of Energy and Baseline Dependent Reactor Antineutrino Disappearance in the RENO Experiment". In: *Physical Review Letters* 116.21 (2016), p. 211801. DOI: 10.1103/PhysRevLett.116.211801. arXiv: 1511.05849 [hep-ex].

[Chr90] C. Christiansen. "Die atmolytische Strömung der Gase". In: *Annalen der Physik* 277.11 (Jan. 1890), pp. 565–587. ISSN: 1521-3889. DOI: 10.1002/andp.18902771115.

[CL71] C. Cercignani and M. Lampis. "Kinetic models for gas-surface interactions". In: *Transport Theory and Statistical Physics* 1.2 (1971), pp. 101–114. DOI: 10.1080/00411457108231440. eprint: https://doi.org/10.1080/00411457108231440.

[CMP81] Y. Chikashige, R. N. Mohapatra, and R. D. Peccei. "Are there real goldstone bosons associated with broken lepton number?" In: *Physics Letters B* 98 (1981), pp. 265–268. DOI: 10.1016/0370-2693(81)90011-3.

[CMS12] CMS Collaboration. "Observation of a new boson at a mass of 125 GeV with the CMS experiment at the LHC". In: *Physics Letters B* 716 (2012), pp. 30–61. DOI: 10.1016/j.physletb.2012.08.021. arXiv: 1207.7235 [hep-ex].

[COM14] COMSOL Multiphysics. *Introduction to COMSOL Multiphysics*. 2014. URL: http://cdn.comsol.com/documentation/5.0.1.276/IntroductionToCOMSOLMultiphysics.pdf (visited on 10/25/2018).

[Cow+56] C. L. Cowan et al. "Detection of the Free Neutrino: a Confirmation". In: *Science* 124.3212 (1956), pp. 103–104. ISSN: 0036-8075. DOI: 10.1126/science.124.3212.103.

[Dan+62] G. Danby et al. "Observation of High-Energy Neutrino Reactions and the Existence of Two Kinds of Neutrinos". In: *Physical Review Letters* 9 (1 July 1962), pp. 36–44. DOI: 10.1103/PhysRevLett.9.36.

[Dec+89] D. Decamp et al. "Determination of the number of light neutrino species". In: *Physics Letters B* 231 (1989), p. 519. DOI: 10.1016/0370-2693(89)90704-1.

[DHH68] R. Davis, D. S. Harmer, and K. C. Hoffman. "Search for Neutrinos from the Sun". In: *Physical Review Letters* 20 (21 May 1968), pp. 1205–1209. DOI: 10.1103/PhysRevLett.20.1205.

[DKT85] M. Doi, T. Kotani, and E. Takasugi. "Double Beta Decay and Majorana Neutrino". In: *Progress of Theoretical Physics Supplement* 83 (1985), p. 1. DOI: 10.1143/PTPS.83.1.

[DLP17a] J. A. Dror, R. Lasenby, and M. Pospelov. "Dark forces coupled to nonconserved currents". In: *Physical Review D* 96.7 (2017), p. 075036. DOI: 10.1103/PhysRevD.96.075036. arXiv: 1707.01503 [hep-ph].

[DLP17b] J. A. Dror, R. Lasenby, and M. Pospelov. "New constraints on light vectors coupled to anomalous currents". In: *Physical Review Letters* 119.14 (2017), p. 141803. DOI: 10.1103/PhysRevLett.119.141803. arXiv: 1705.06726 [hep-ph].

[Dos+06] N. Doss et al. "Molecular effects in investigations of tritium molecule β decay endpoint experiments". In: *Physical Review C* 73 (2006), p. 025502. DOI: 10.1103/PhysRevC.73.025502.

[Dos07] N. Doss. "Calculated final state probability distributions for T_2 β-decay measurements". PhD thesis. University College London, 2007. URL: https://www.npl.washington.edu/TRIMS/sites/sand.npl.washington.edu.TRIMS/files/manuals-documentation/Doss_thesis_2007.pdf.

[Dre+13] G. Drexlin et al. “Current Direct Neutrino Mass Experiments”. In: *Advances in High Energy Physics* 2013 (2013). DOI: 10.1155/2013/293986.

[DT08] N. Doss and J. Tennyson. “Excitations to the electronic continuum of $^3HeT^+$ in investigations of T_2 β-decay experiments”. In: *Journal of Physics B* 41.12 (2008), pp. 125701+. ISSN: 0953-4075. DOI: 10.1088/0953-4075/41/12/125701.

[Dun33] F. G. Dunnington. “A Determination of e/m for an Electron by a New Deflection Method”. In: *Physical Review* 43 (6 Mar. 1933), pp. 404–416. DOI: 10.1103/PhysRev.43.404.

[Egu+03] K. Eguchi et al. “First results from KamLAND: Evidence for reactor anti-neutrino disappearance”. In: *Physical Review Letters* 90 (2003), p. 021802. DOI: 10.1103/PhysRevLett.90.021802. arXiv: hep-ex/0212021 [hep-ex].

[Ell18] E. Ellinger. “Development and investigation of the Forward Beam Monitor for the KATRIN experiment”. Forthcoming work. PhD thesis. Bergische Universität Wuppertal, 2018.

[EM17] J. Engel and J. Menéndez. “Status and future of nuclear matrix elements for neutrinoless double-beta decay: a review”. In: *Reports on Progress in Physics* 80.4 (2017), p. 046301. DOI: 10.1088/1361-6633/aa5bc5. arXiv: 1610.06548 [nucl-th].

[EO12] A. Esmaili and P. L. G. Orlando. “KATRIN sensitivity to sterile neutrino mass in the shadow of lightest neutrino mass”. In: *Physical Review D* 85 (11 2012), p. 117301. DOI: 10.1103/PhysRevD.85.117301.

[Esf+17] A. A. Esfahani et al. “Determining the neutrino mass with cyclotron radiation emission spectroscopy - Project 8”. In: *Journal of Physics G* 44.5 (2017), p. 054004. DOI: 10.1088/1361-6471/aa5b4f. arXiv: 1703.02037 [physics.ins-det].

[FAR18] FARO Technologies Inc. *FaroArm®*. 2018. URL: https://www.faro.com/de-de/produkte/industrielle-messtechnik/faroarm/ (visited on 09/24/2018).

[Fäs+11] A. Fässler et al. “Tritium and rhenium as a probe of cosmic neutrino background”. In: *Journal of Physics G* 38 (2011), p. 075202. DOI: 10.1088/0954-3899/38/7/075202.

[Fäs+13] A. Fässler et al. “Search for the Cosmic Neutrino Background and KATRIN”. In: *Romanian Journal of Physics* 58.9-10 (2013), pp. 1221–1231. arXiv: 1304.5632 [nucl-th].

[FB11] J. Formaggio and J. Barrett. “Resolving the reactor neutrino anomaly with the KATRIN neutrino experiment”. In: *Physics Letters B* 706.1 (2011), pp. 68–71. DOI: 10.1016/j.physletb.2011.10.069.

[Fer34] E. Fermi. “Versuch einer Theorie der β-Strahlen.” In: *Zeitschrift für Physik* 88.3–4 (1934), pp. 161–177. DOI: 10.1007/BF01351864.

[FG18] E. Förstner and F. Glück. “Electron backscattering at the FBM Faraday cup and the Pulcinella disk”. Internal report. 2018.

[Fis+11] S. Fischer et al. "Monitoring of tritium purity during long-term circulation in the KATRIN test experiment LOOPINO using laser Raman spectroscopy". In: *Fusion Science and Technology* 60.3 (2011), pp. 925–930. URL: http://www.ans.org/pubs/journals/fst/a_12567.

[Fis14] S. Fischer. "Commissioning of the KATRIN Raman system and durability studies of optical coatings in glove box and tritium atmospheres". PhD thesis. Karlsruher Institut für Technologie (KIT), 2014. DOI: 10.5445/IR/1000043697.

[FKR02] Z. Fodor, S. D. Katz, and A. Ringwald. "Determination of Absolute Neutrino Masses from Bursts of Z Bosons in Cosmic Rays". In: *Physical Review Letters* 88 (17 Apr. 2002), p. 171101. DOI: 10.1103/PhysRevLett.88.171101.

[Fri+18] F. Friedel et al. "Time-dependent simulation of the flow reduction of D_2 and T_2 in the KATRIN experiment". In: (2018). arXiv: 1807.10126 [physics.ins-det]. URL: https://arxiv.org/abs/1807.10126.

[Fuk+96] Y. Fukuda et al. "Solar Neutrino Data Covering Solar Cycle 22". In: *Physical Review Letters* 77 (9 Aug. 1996), pp. 1683–1686. DOI: 10.1103/PhysRevLett.77.1683.

[Fuk+98] Y. Fukuda et al. "Evidence for oscillation of atmospheric neutrinos". In: *Physical Review Letters* 81 (1998), pp. 1562–1567. DOI: 10.1103/PhysRevLett.81.1562. arXiv: hep-ex/9807003 [hep-ex].

[Fur+15] D. Furse et al. *Kassiopeia: Simulation of electric and magnetic fields and particle tracking*. 2015. URL: https://github.com/KATRIN-Experiment/Kassiopeia.

[Fur+17] D. Furse et al. "Kassiopeia: a modern, extensible C++ particle tracking package". In: *New Journal of Physics* 19.5 (2017), p. 053012. DOI: 10.1088/1367-2630/aa6950.

[FY86] M. Fukugita and T. Yanagida. "Baryogenesis without grand unification". In: *Physics Letters B* 174 (1986), pp. 45–47. DOI: 10.1016/0370-2693(86)91126-3.

[Gal+02] M. Galassi et al. "GNU scientific library". In: *Network Theory Ltd* 3 (2002). URL: http://www.gnu.org/software/gsl/.

[Gan+13] A. Gando et al. "Reactor on-off antineutrino measurement with KamLAND". In: *Physical Review* 88.3 (2013), p. 033001. DOI: 10.1103/PhysRevD.88.033001. arXiv: 1303.4667 [hep-ex].

[Gan+15] A. Gando et al. "^{7}Be solar neutrino measurement with KamLAND". In: *Physical Review C* 92.5 (2015), p. 055808. DOI: 10.1103/PhysRevC.92.055808. arXiv: 1405.6190 [hep-ex].

[Gan+16] A. Gando et al. "Search for Majorana Neutrinos near the Inverted Mass Hierarchy Region with KamLAND-Zen". In: *Physical Review Letters* 117.8 (2016), p. 082503. DOI: 10.1103/PhysRevLett.117.082503. arXiv: 1605.02889 [hep-ex]. Addendum in: *Physical Review Letters* 117.10 (2016), p. 109903. DOI: 10.1103/PhysRevLett.117.109903.

[Gas+17] L. Gastaldo et al. "The electron capture in ^{163}Ho experiment – ECHo". In: *The European Physical Journal Special Topics* 226.8 (2017), pp. 1623–1694. DOI: 10.1140/epjst/e2017-70071-y.

[Gei64] J. Geiger. "Streuung von 25 keV-Elektronen an Gasen". In: *Zeitschrift für Physik* 181.4 (Aug. 1964), pp. 413–425. ISSN: 0044-3328. DOI: 10.1007/BF01380873.

[GGS58] M. Goldhaber, L. Grodzins, and A. W. Sunyar. "Helicity of Neutrinos". In: *Physical Review* 109 (3 Feb. 1958), pp. 1015–1017. DOI: 10.1103/PhysRev.109.1015.

[Giu04] C. Giunti. "Theory of neutrino oscillations". In: *Proceedings, 16th Conference on High Energy Physics (IFAE 2004): Turin, Italy, April 14-16, 2004*. 2004, pp. 427–438. DOI: 10.1142/9789812702074_0005. arXiv: hep-ph/0409230 [hep-ph].

[Glü03] Glück, F. "Gas flow in the WGTS tube". Internal report. 2003. URL: https://fuzzy.fzk.de/bscw/bscw.cgi/d736618/120410_FGlueck_gasflow-in-the-WGTS-tube.pdf.

[GLW57] R. L. Garwin, L. M. Lederman, and M. Weinrich. "Observations of the Failure of Conservation of Parity and Charge Conjugation in Meson Decays: The Magnetic Moment of the Free Muon". In: *Physical Review* 105 (1957), pp. 1415–1417. DOI: 10.1103/PhysRev.105.1415.

[GR09] P. Gondolo and G. Raffelt. "Solar neutrino limit on axions and keV-mass bosons". In: *Physical Review* 79 (2009), p. 107301. DOI: 10.1103/PhysRevD.79.107301. arXiv: 0807.2926 [astro-ph].

[Gre66] K. Greisen. "End to the cosmic ray spectrum?" In: *Physical Review Letters* 16 (1966), pp. 748–750. DOI: 10.1103/PhysRevLett.16.748.

[Gro+08] S. Grohmann et al. "Cryogenic design of the KATRIN source cryostat". In: *AIP Conference Proceedings* 985 (2008), pp. 1277–1284. DOI: 10.1063/1.2908483.

[Gro+11] S. Grohmann et al. "Precise temperature measurement at 30 K in the KATRIN source cryostat". In: *Cryogenics* 51.8 (2011), pp. 438–445. DOI: 10.1016/j.cryogenics.2011.05.001.

[Gro+13] S. Grohmann et al. "The thermal behaviour of the tritium source in KATRIN". In: *Cryogenics* 55-56.0 (2013), pp. 5–11. DOI: 10.1016/j.cryogenics.2013.01.001.

[Gro09] S. Grohmann. "Stability analyses of the beam tube cooling system in the KATRIN source cryostat". In: *Cryogenics* 49.8 (2009), pp. 413–420. DOI: 10.1016/j.cryogenics.2009.06.001.

[Gro15] S. Groh. "Modeling of the response function and measurement of transmission properties of the KATRIN experiment". PhD thesis. Karlsruher Institut für Technologie (KIT), 2015. DOI: 10.5445/IR/1000046546.

[GRS79] M. Gell-Mann, P. Ramond, and R. Slansky. "Complex Spinors and Unified Theories". In: *Conference Proceedings* C790927 (1979), pp. 315–321. arXiv: 1306.4669 [hep-th].

[Hac17] M. T. Hackenjos. "KATRIN "First Light" - Commissioning and Modelling of the Beamline". PhD thesis. Karlsruher Institut für Technologie (KIT), 2017. DOI: 10.5445/IR/1000078933.

[Had+12] M. Hadj-Nacer et al. "Experimental study of the gas flows through channels with circular cross sections". In: *Journal of Physics: Conference Series* 362.1 (2012), p. 012025. URL: http://stacks.iop.org/1742-6596/362/i=1/a=012025.

[Hag99] C. Hagmann. "A Relic neutrino detector". In: *AIP Conference Proceedings* 478.1 (1999), pp. 460–463. DOI: 10.1063/1.59428. arXiv: astro-ph/9902102 [astro-ph].

[Ham+99] W. Hampel et al. "GALLEX solar neutrino observations: results for GALLEX IV". In: *Physics Letters B* 447.1 (1999), pp. 127–133. ISSN: 0370-2693. DOI: 10.1016/S0370-2693(98)01579-2.

[HAM18] HAMAMATSU. *Si PIN photodiodes*. 2018. URL: https://www.hamamatsu.com/resources/pdf/ssd/s5971_etc_kpin1025e.pdf (visited on 10/20/2018).

[Han+17] V. Hannen et al. "Deconvolution of the energy loss function of the KATRIN experiment". In: *Astroparticle Physics* 89 (2017), pp. 30–38. DOI: 10.1016/j.astropartphys.2017.01.010.

[Har15] F. Harms. "Characterization and Minimization of Background Processes in the KATRIN Main Spectrometer". PhD thesis. Karlsruher Institut für Technologie (KIT), 2015. DOI: 10.5445/IR/1000050027.

[Hau18] N. Haussmann. "Simulation and measurement of the Forward Beam Monitor detector signal in KATRIN". Forthcoming work. PhD thesis. Bergische Universität Wuppertal, 2018.

[Hei+18] F. Heizmann et al. "Status of the unbiased neutrino mass analysis of KATRIN data ('Blinding')". Internal report. 2018. URL: https://neutrino.ikp.kit.edu/katrin/images/1/10/Blinding-report-2018-02-13.pdf.

[Hei15] F. Heizmann. "Optimization of a KATRIN source analysis tool and investigations of the potential to constrain the relic neutrino background". Master thesis. Karlsruher Institut für Technologie (KIT), 2015. URL: http://www.katrin.kit.edu/publikationen/mth_heizmann.pdf.

[Hey04] E. T. Heyn. "BERLIN'S WONDERFUL HORSE – He Can Do Almost Everything But Talk - How He Was Taught". In: *The New York Times* (Sept. 1904). URL: https://timesmachine.nytimes.com/timesmachine/1904/09/04/101396572.pdf.

[HM05] W.-Y. P. Hwang and B.-Q. Ma. "Detection of cosmic neutrino clustering by cosmic ray spectra". In: *New Journal of Physics* 7 (2005), p. 41. DOI: 10.1088/1367-2630/7/1/041. arXiv: astro-ph/0502377 [astro-ph].

[Höt12] M. Hötzel. "Simulation and analysis of source-related effects for KATRIN". PhD thesis. Karlsruher Institut für Technologie (KIT), 2012. DOI: 10.5445/IR/1000031259.

[HOZ18] G.-y. Huang, T. Ohlsson, and S. Zhou. "Observational Constraints on Secret Neutrino Interactions from Big Bang Nucleosynthesis". In: *Physical Review D* 97 (2018), p. 075009. DOI: 10.1103/PhysRevD.97.075009. arXiv: 1712.04792 [hep-ph].

[HS17] F. Heizmann and H. Seitz-Moskaliuk. "The Windowless Gaseous Tritium Source (WGTS) of the KATRIN experiment". In: *Journal of Physics: Conference Series* 888.1 (2017), p. 012071. DOI: 10.1088/1742-6596/888/1/012071.

[ide10] idealvac. *TURBOVAC and MAG, Excerpt from the Oerlikon Leybold Vacuum Full Line Catalog*. 2010. URL: https://www.idealvac.com/files/brochures/Oerlikon_Leybold_TurboVac_SpecSheet.pdf (visited on 09/30/2018).

[IM14] K. Ioka and K. Murase. "IceCube PeV-EeV neutrinos and secret interactions of neutrinos". In: *Progress of Theoretical and Experimental Physics* 2014.6 (2014), 061E01. DOI: 10.1093/ptep/ptu090. arXiv: 1404.2279 [astro-ph.HE].

[Jac99] J. D. Jackson. *Classical electrodynamics*. Vol. 3. John Wiley & Sons, Inc., 1999. ISBN: 047130932X.

[Jan17] A. Jansen. *Vakuumeinbruch Beamtube*. Elog entry. July 2017. URL: https://ikp-neu-katrin.ikp.kit.edu/elog/WGTS-Main/143.

[JSF99] S. Jonsell, A. Saenz, and P. Froelich. "Neutrino-mass determination from tritium β decay: Corrections to and prospects of experimental verification of the final-state spectrum". In: *Physical Review C* 60 (3 1999), p. 034601. DOI: 10.1103/PhysRevC.60.034601.

[Käf12] W. Käfer. "Sensitivity studies of the KATRIN experiment". PhD thesis. Karlsruher Institut für Technologie (KIT), 2012. DOI: 10.5445/IR/1000026021.

[KAT05] KATRIN collaboration. *KATRIN Design Report*. FZKA scientific report 7090. 2005. URL: http://bibliothek.fzk.de/zb/berichte/FZKA7090.pdf.

[KFM10] A. Kaboth, J. A. Formaggio, and B. Monreal. "Sensitivity of neutrino mass experiments to the cosmic neutrino background". In: *Physical Review D* 82 (6 Sept. 2010), p. 062001. DOI: 10.1103/PhysRevD.82.062001.

[Kha+14] V. Khachatryan et al. "Search for heavy neutrinos and W bosons with right-handed couplings in proton-proton collisions at $\sqrt{s} = 8\,\text{TeV}$". In: *The European Physical Journal C* 74.11 (2014), p. 3149. DOI: 10.1140/epjc/s10052-014-3149-z. arXiv: 1407.3683 [hep-ex].

[Kle+18] M. Kleesiek et al. "β-Decay Spectrum, Response Function and Statistical Model for Neutrino Mass Measurements with the KATRIN Experiment". In: *Submitted to Eur. Phys. J. C.* (2018). In review. arXiv: 1806.00369 [physics.data-an].

[Kle14] M. Kleesiek. "A Data-Analysis and Sensitivity-Optimization Framework for the KATRIN Experiment". PhD thesis. Karlsruher Institut für Technologie (KIT), 2014. DOI: 10.5445/IR/1000043301.

[Kle18] M. Klein. "Tritium ions in KATRIN: detection, blocking and removal". To be published. PhD thesis. Karlsruher Institut für Technologie (KIT), 2018.

[Knu09] M. Knudsen. "Die Gesetze der Molekularströmung und der inneren Reibungsströmung der Gase durch Röhren". In: *Annalen der Physik* 333.1 (Jan. 1909), pp. 75–130. ISSN: 1521-3889. DOI: 10.1002/andp.19093330106.

[Kod+01] K. Kodama et al. "Observation of tau neutrino interactions". In: *Physics Letters B* 504.3 (2001), pp. 218–224. ISSN: 0370-2693. DOI: 10.1016/S0370-2693(01)00307-0.

[KR05] J. R. Klein and A. Roodman. "Blind analysis in nuclear and particle physics". In: *Annual Review of Nuclear and Particle Science* 55.1 (2005), pp. 141–163. DOI: 10.1146/annurev.nucl.55.090704.151521.

[KR83] P. Kruit and F. H. Read. "Magnetic field paralleliser for 2π electron-spectrometer and electron-image magnifier". In: *Journal of Physics E: Scientific Instruments* 16.4 (1983), p. 313. URL: http://stacks.iop.org/0022-3735/16/i=4/a=016.

[Kra+05] C. Kraus et al. "Final results from phase II of the Mainz neutrino mass search in tritium β decay". In: *The European Physical Journal C* 40.4 (2005), pp. 447–468. DOI: 10.1140/epjc/s2005-02139-7.

[KRS85] V. A. Kuzmin, V. A. Rubakov, and M. E. Shaposhnikov. "On anomalous electroweak baryon-number non-conservation in the early universe". In: *Physics Letters B* 155 (1985), p. 36. DOI: 10.1016/0370-2693(85)91028-7.

[KT87] E. W. Kolb and M. S. Turner. "Supernova SN 1987a and the Secret Interactions of Neutrinos". In: *Physical Review D* 36 (1987), p. 2895. DOI: 10.1103/PhysRevD.36.2895.

[Kuc+18] L. Kuckert et al. "Modelling of gas dynamical properties of the KATRIN tritium source and implications for the neutrino mass measurement". In: *Vacuum* 158 (2018), pp. 195–205. DOI: 10.1016/j.vacuum.2018.09.036.

[Kuc16] L. Kuckert. "The Windowless Gaseous Tritium Source of the KATRIN Experiment – Characterisation of Gas Dynamical and Plasma Properties". PhD thesis. Karlsruher Institut für Technologie (KIT), 2016. DOI: 10.5445/IR/1000065077.

[KW75] A. Kundt and E. Warburg. "Ueber Reibung und Wärmeleitung verdünnter Gase". In: *Annalen der Physik* 231.5 (Jan. 1875), pp. 337–365. ISSN: 1521-3889. DOI: ark:/12148/bpt6k15239z.

[KZ18] B. Krasch and G. Zeller. *Laser Raman spectroscopy @KATRIN*. July 17, 2018. URL: https://neutrino.ikp.kit.edu/katrin/images/b/b0/20180709_analysis_workshop_LARA.pptx (visited on 11/09/2018).

[LDB14] R. Laha, B. Dasgupta, and J. F. Beacom. "Constraints on New Neutrino Interactions via Light Abelian Vector Bosons". In: *Physical Review D* 89.9 (2014), p. 093025. DOI: 10.1103/PhysRevD.89.093025. arXiv: 1304.3460 [hep-ph].

[LEM18] LEM. *ITN 600-S ULTRASTAB*. 2018. URL: https://www.lem.com/en/itn-600s-ultrastab (visited on 09/19/2018).

[LH90] S. K. Loyalka and S. A. Hamoodi. "Poiseuille flow of a rarefied gas in a cylindrical tube: Solution of linearized Boltzmann equation". In: *Physics of Fluids A: Fluid Dynamics* 2.11 (1990), pp. 2061–2065. DOI: 10.1063/1.857681. eprint: https://doi.org/10.1063/1.857681.

[Li14] Y.-F. Li. "Overview of the Jiangmen Underground Neutrino Observatory (JUNO)". In: *International Journal of Modern Physics: Conference Series* 31 (2014), p. 1460300. DOI: 10.1142/S2010194514603007. arXiv: 1402.6143 [physics.ins-det].

[Lin+18] M. Lindner et al. "Neutrino-electron scattering: general constraints on Z' and dark photon models". In: *Journal of High Energy Physics* 05 (2018), p. 098. DOI: 10.1007/JHEP05(2018)098. arXiv: 1803.00060 [hep-ph].

[Liu87] J. W. Liu. "Total cross sections for high-energy electron scattering by H_2 ($^1\Sigma_g^+$), N_2 ($^1\Sigma_g^+$), and O_2 ($^3\Sigma_g^-$)". In: *Physical Review A* 35 (2 Jan. 1987), pp. 591–597. DOI: 10.1103/PhysRevA.35.591.

[LL02] T. J. Loredo and D. Q. Lamb. "Bayesian analysis of neutrinos observed from supernova SN-1987A". In: *Physical Review D* 65 (2002), p. 063002. DOI: 10.1103/PhysRevD.65.063002. arXiv: astro-ph/0107260 [astro-ph].

[Lob+99a] V. M. Lobashev et al. "Direct search for mass of neutrino and anomaly in the tritium beta spectrum". In: *Physics Letters B* B460 (1999), pp. 227–235. DOI: 10.1016/S0370-2693(99)00781-9.

[Lob+99b] V. M. Lobashev et al. "Neutrino mass and anomaly in the tritium beta-spectrum. Results of the 'Troitsk nu mass' experiment". In: *Nuclear Physics B - Proceedings Supplements* 77 (1999), pp. 327–332. DOI: 10.1016/S0920-5632(99)00438-7.

[LS85] V. M. Lobashev and P. E. Spivak. "A method for measuring the electron antineutrino rest mass". In: *Nuclear Instruments and Methods in Physics Research Section A: Accelerators, Spectrometers, Detectors and Associated Equipment* 240.2 (1985), pp. 305–310. DOI: 10.1016/0168-9002(85)90640-0.

[LT93] L. M. Lederman and D. Teresi. *The God Particle*. Dell Publishing, 1993. ISBN: 0385312113.

[Luk+12] S. Lukić et al. "Measurement of the gas-flow reduction factor of the KATRIN DPS2-F differential pumping section". In: *Vacuum* 86.8 (2012), pp. 1126–1133. DOI: 10.1016/j.vacuum.2011.10.017.

[LV11] M. Lusignoli and M. Vignati. "Relic Antineutrino Capture on 163-Ho decaying Nuclei". In: *Physics Letters B* B697 (2011), pp. 11–14. DOI: 10.1016/j.physletb.2011.01.047. arXiv: 1012.0760 [hep-ph]. Erratum in: *Physics Letters B* 701 (2011), p. 673. DOI: 10.1016/j.physletb.2011.06.008.

[LVV08] R. Lazauskas, P. Vogel, and C. Volpe. "Charged current cross section for massive cosmological neutrinos impinging on radioactive nuclei". In: *Journal of Physics G* 35 (2008), p. 025001. DOI: 10.1088/0954-3899/35/2/025001. arXiv: 0710.5312 [astro-ph].

[LWW18] J. Liu, C. E. M. Wagner, and X.-P. Wang. "A light complex scalar for the electron and muon anomalous magnetic moments". In: (2018). arXiv: 1810.11028 [hep-ph].

[Mal07] O. B. Malyshev. "Characterisation of a turbo-molecular pumps by a minimum of parameters". In: *Vacuum* 81.6 (2007). Proceedings of the European Vacuum Conference (EVC-9), pp. 752–758. ISSN: 0042-207X. DOI: https://doi.org/10.1016/j.vacuum.2005.11.055.

[Mar17] A. Marsteller. "Measurement of Temperature Stability and Homogeneity of the KATRIN WGTS Cryostat". Master thesis. Karlsruher Institut für Technologie (KIT), 2017. URL: https://www.katrin.kit.edu/publikationen/mth_marsteller.pdf.

[Mar18] A. Marsteller. Private communication. 2018.

[Mer+15] S. Mertens et al. "Sensitivity of Next-Generation Tritium Beta-Decay Experiments for keV-Scale Sterile Neutrinos". In: *Journal of Cosmology and Astroparticle Physics* 1502 (2015), p. 020. DOI: 10.1088/1475-7516/2015/02/020. arXiv: 1409.0920 [physics.ins-det].

[Mer+18] S. Mertens et al. "A novel detector system for KATRIN to search for keV-scale sterile neutrinos". In: (2018). arXiv: 1810.06711 [physics.ins-det].

[Met+53] N. Metropolis et al. "Equation of state calculations by fast computing machines". In: *Journal of Chemical Physics* 21 (1953), pp. 1087–1092. DOI: 10.1063/1.1699114.

[MF09] B. Monreal and J. A. Formaggio. "Relativistic Cyclotron Radiation Detection of Tritium Decay Electrons as a New Technique for Measuring the Neutrino Mass". In: *Physical Review D* 80 (2009), p. 051301. DOI: 10.1103/PhysRevD.80.051301. arXiv: 0904.2860 [nucl-ex].

[Min77] P. Minkowski. "$\mu \to e\gamma$ at a rate of one out of 10^9 muon decays?" In: *Physics Letters B* 67 (1977), pp. 421–428. DOI: 10.1016/0370-2693(77)90435-X.

[MNS62] Z. Maki, M. Nakagawa, and S. Sakata. "Remarks on the unified model of elementary particles". In: *Progress of Theoretical Physics* 28 (1962), pp. 870–880. DOI: 10.1143/PTP.28.870.

[MP75] R. N. Mohapatra and J. C. Pati. "A Natural Left-Right Symmetry". In: *Physical Review D* D11 (1975), p. 2558. DOI: 10.1103/PhysRevD.11.2558.

[MS80] R. N. Mohapatra and G. Senjanovic. "Neutrino Mass and Spontaneous Parity Violation". In: *Physical Review Letters* 44 (1980). [,231(1979)], p. 912. DOI: 10.1103/PhysRevLett.44.912.

[MS86] S. P. Mikheyev and A. Y. Smirnov. "Resonant amplification of ν oscillations in matter and solar-neutrino spectroscopy". In: *Il Nuovo Cimento C* 9.1 (Jan. 1986), pp. 17–26. ISSN: 0390-5551. DOI: 10.1007/BF02508049.

[Mye+15] E. G. Myers et al. "Atomic Masses of Tritium and Helium-3". In: *Physical Review Letters* 114 (1 2015), p. 013003. DOI: 10.1103/PhysRevLett.114.013003.

[NFW96] J. F. Navarro, C. S. Frenk, and S. D. M. White. "The Structure of cold dark matter halos". In: *The Astrophysical Journal* 462 (1996), pp. 563–575. DOI: 10.1086/177173. arXiv: astro-ph/9508025 [astro-ph].

[NI16] NI. *National Instruments - LabVIEW*. 2016. URL: http://www.ni.com/en-us/shop/labview.html (visited on 09/20/2018).

[Nuc+18] A. Nucciotti et al. "Status of the HOLMES Experiment to Directly Measure the Neutrino Mass". In: *Journal of Low Temperature Physics* (2018). DOI: 10.1007/s10909-018-2025-x. arXiv: 1807.09269 [physics.ins-det].

[OW08] E. W. Otten and C. Weinheimer. "Neutrino mass limit from tritium β decay". In: *Reports on Progress in Physics* 71.8 (2008), p. 086201. DOI: 10.1088/0034-4885/71/8/086201.

[Par+18] R. H. Parker et al. "Measurement of the fine-structure constant as a test of the Standard Model". In: *Science* 360.6385 (2018), pp. 191–195. ISSN: 0036-8075. DOI: 10.1126/science.aap7706.

[PB13] F. Priester and B. Bornschein. "TriToP - A compatibility experiment with turbomolecular pumps under tritium atmosphere". In: *Vacuum* 98.0 (2013), pp. 22–28. DOI: 10.1016/j.vacuum.2012.09.006.

[Per+75] M. L. Perl et al. "Evidence for Anomalous Lepton Production in $e^+ - e^-$ Annihilation". In: *Physical Review Letters* 35 (22 Dec. 1975), pp. 1489–1492. DOI: 10.1103/PhysRevLett.35.1489.

[Per09] D. H. Perkins. *Particle astrophysics*. 10. Oxford University Press, 2009.

[Pfu07] O. Pfungst. *Das Pferd des Herrn von Osten (Der kluge Hans). Ein Beitrag zur experimentellen Tier- und Menschen-Psychologie*. Leipzig: Barth, 1907. URL: https://archive.org/details/daspferddesherr00stumgoog.

[Phy18] Physics and Astronomy Department. *Object-oriented Real-time Control and Acquisition*. 2018. URL: http://orca.physics.unc.edu/~markhowe/Orca_Help/Home.html.

[Pic+92] A. Picard et al. "A solenoid retarding spectrometer with high resolution and transmission for keV electrons". In: *Nuclear Instruments and Methods in Physics Research Section B: Beam Interactions with Materials and Atoms* 63.3 (1992), pp. 345–358. DOI: 10.1016/0168-583X(92)95119-C.

[PKW64] W. E. F. Pauli, R. Kronig, and V. F. Weisskopf. *Collected scientific papers*. Offener Brief an die Gruppe der Radioaktiven bei der Gauvereinstagung zu Tübingen (datiert 4. Dez. 1930). New York, NY: Interscience, 1964.

[Pon57] B. Pontecorvo. "Mesonium and anti-mesonium". In: *Journal of Experimental and Theoretical Physics* 6 (1957), p. 429.

[Pon58] B. Pontecorvo. "Inverse beta processes and nonconservation of lepton charge". In: *Journal of Experimental and Theoretical Physics* 7 (1958), pp. 172–173.

[Pon68] B. Pontecorvo. "Neutrino Experiments and the Problem of Conservation of Leptonic Charge". In: *Journal of Experimental and Theoretical Physics* 26 (1968), pp. 984–988.

[PP16] P. S. Pasquini and O. L. G. Peres. "Bounds on Neutrino-Scalar Yukawa Coupling". In: *Physical Review D* 93 (2016), p. 053007. DOI: 10.1103/PhysRevD.93.053007. arXiv: 1511.01811 [hep-ph]. Erratum in: *Physical Review D* 93 (2016), p. 079902. DOI: 10.1103/PhysRevD.93.079902.

[Pra+12] M. Prall et al. "The KATRIN pre-spectrometer at reduced filter energy". In: *New Journal of Physics* 14.7 (2012), p. 073054. DOI: 10.1088/1367-2630/14/7/073054.

[Pra11] M. Prall. "Background Reduction of the KATRIN Spectrometers: Transmission Function of the Pre-Spectrometer and Systematic Test of the Main-Spectrometer Wire Electrode". PhD thesis. Westfälische Wilhelms-Universität Münster, 2011. URL: http://www.researchgate.net/publication/238418212_Transmission_Function_of_the_Pre-Spectrometer_and_Systematic_Tests_of_the_Main-Spectrometer_Wire_Electrode_%28PHD_thesis%29.

[Pri13] F. Priester. "Tritiumtechnologie für die fensterlose Quelle WGTS von KATRIN". German. PhD thesis. Karlsruher Institut für Technologie (KIT), 2013. DOI: 10.5445/IR/1000035699.

[PS74] J. C. Pati and A. Salam. "Lepton Number as the Fourth Color". In: *Physical Review D* 10 (1974), pp. 275–289. DOI: 10.1103/PhysRevD.10.275. Erratum in: *Physical Review D* 11 (1975), p. 703. DOI: 10.1103/PhysRevD.11.703.2.

[PS95] M. E. Peskin and D. V. Schroeder. *An Introduction to Quantum Field Theory*. Ed. by D. Pines. Westview Press, 1995. ISBN: 9780813345437.

[PSB15] F. Priester, M. Sturm, and B. Bornschein. "Commissioning and detailed results of KATRIN inner loop tritium processing system at Tritium Laboratory Karlsruhe". In: *Vacuum* 116 (2015), pp. 42–47. DOI: 10.1016/j.vacuum.2015.02.030.

[PVS14] S. Pantazis, D. Valougeorgis, and F. Sharipov. "End corrections for rarefied gas flows through circular tubes of finite length". In: *Vacuum* 101 (2014), pp. 306–312. ISSN: 0042-207X. DOI: 10.1016/j.vacuum.2013.09.015.

[PW65] A. A. Penzias and R. W. Wilson. "A Measurement of Excess Antenna Temperature at 4080 Mc/s." In: *The Astrophysical Journal* 142 (1965), pp. 419–421.

[Ren11] P. Renschler. "KESS - A new Monte Carlo simulation code for low-energy electron interactions in silicon detectors". PhD thesis. Karlsruher Institut für Technologie (KIT), 2011. DOI: 10.5445/IR/1000024959.

[RH09] J. E. Ricker and J. H. Hendricks. *Unit Conversions*. NIST. 2009. URL: https://www.nist.gov/pml/div685/grp01/unit_conversions.

[RK88] R. G. H. Robertson and D. A. Knapp. "Direct Measurements of Neutrino Mass". In: *Annual Review of Nuclear and Particle Science* 38.1 (1988), pp. 185–215. DOI: 10.1146/annurev.ns.38.120188.001153.

[RLC05] W. A. Rolke, A. M. Lopez, and J. Conrad. "Limits and confidence intervals in the presence of nuisance parameters". In: *Nuclear Instruments and Methods in Physics* A551 (2005), pp. 493–503. DOI: 10.1016/j.nima.2005.05.068. arXiv: physics/0403059 [physics].

[Rob+91] R. G. H. Robertson et al. "Limit on anti-electron-neutrino mass from observation of the beta decay of molecular tritium". In: *Physical Review Letters* 67 (1991), pp. 957–960. DOI: 10.1103/PhysRevLett.67.957.

[Röl15] M. Röllig. "Tritium analytics by beta induced X-ray spectrometry". PhD thesis. Karlsruher Institut für Technologie (KIT), 2015. DOI: 10.5445/IR/1000054050.

[Ros+15] A. J. Ross et al. "The clustering of the SDSS DR7 main Galaxy sample - I. A 4 per cent distance measure at $z = 0.15$". In: *Monthly Notices of the Royal Astronomical Society* 449.1 (2015), pp. 835–847. DOI: 10.1093/mnras/stv154. arXiv: 1409.3242 [astro-ph.CO].

[RW04] A. Ringwald and Y. Y. Y. Wong. "Gravitational clustering of relic neutrinos and implications for their detection". In: *Journal of Cosmology and Astroparticle Physics* 0412 (2004), p. 005. DOI: 10.1088/1475-7516/2004/12/005. arXiv: hep-ph/0408241 [hep-ph].

[RW83] W. Repko and C.-E. Wu. "Radiative corrections to the end point of the tritium β decay spectrum". In: *Physical Review C* 28 (6 1983), pp. 2433–2436. ISSN: 0556-2813. DOI: 10.1103/physrevc.28.2433.

[Sch13] M. Schlösser. "Accurate calibration of the Raman system for the Karlsruhe Neutrino Experiment". PhD thesis. Karlsruher Institut für Technologie (KIT), 2013. DOI: 10.1007/978-3-319-06221-1.

[Sch14] J. S. Schwarz. "The Detector System of the KATRIN Experiment - Implementation and First Measurements with the Spectrometer". PhD thesis. Karlsruher Institut für Technologie (KIT), 2014. DOI: 10.5445/IR/1000042772.

[Sch15] C. Schönfeld. "Commissioning of the KATRIN Pinch Magnet". Bachelor thesis. Karlsruher Institut für Technologie (KIT), 2015. URL: https://fuzzy.fzk.de/bscw/bscw.cgi/d1236629/BA2015-Sch%C3%B6nfeld.pdf.

[Sei19] H. Seitz-Moskaliuk. "Characterisation of the KATRIN tritium source and minimisation of systematic effects". Forthcoming work. PhD thesis. Karlsruher Institut für Technologie (KIT), 2019.

[Sen+18] J. Sentkerestiová et al. "Gaseous ^{83m}Kr generator for KATRIN". In: *Journal of Instrumentation* 13.04 (2018), P04018. DOI: 10.1088/1748-0221/13/04/P04018.

[SEN18] SENIS. *3-Axis Digital Teslameter 3MH3A-0.1%-200mT*. 2018. URL: http://c1940652.r52.cf0.rackcdn.com/5a7090adb8d39a6f2d00212a/Magnetic-Teslameter-3MH3A-Datasheet-r3.pdf (visited on 09/22/2018).

[SF97a] A. Saenz and P. Froelich. "Effect of final-state interactions in allowed β decays. I. General formalism". In: *Physical Review C* 56 (1997), pp. 2132–2161. DOI: 10.1103/PhysRevC.56.2132.

[SF97b] A. Saenz and P. Froelich. "Effect of final-state interactions in allowed β decays. II. Reliability of the β-decay spectrum for T_2". In: *Physical Review C* 56 (1997), pp. 2162–2184. DOI: 10.1103/PhysRevC.56.2162.

[SH11] A. Sejersen Riis and S. Hannestad. "Detecting sterile neutrinos with KATRIN like experiments". In: *Journal of Cosmology and Astroparticle Physics* 2011.02 (2011), p. 011. DOI: 10.1088/1475-7516/2011/02/011.

[Sha04a] F. Sharipov. "Calculations of tritium flow between the buffer vessel up to the first vacuum system". Internal report. 2004. URL: https://fuzzy.fzk.de/bscw/bscw.cgi/d100305/10-ME-2102-0.pdf.

[Sha04b] F. Sharipov. "Data on the velocity slip and temperature jump coefficients [gas mass, heat and momentum transfer]". In: *5th International Conference on Thermal and Mechanical Simulation and Experiments in Microelectronics and Microsystems, 2004. EuroSimE 2004. Proceedings of the*. May 2004, pp. 243–249. DOI: 10.1109/ESIME.2004.1304046.

[Sha08] F. Sharipov. "Analytical and Numerical Calculations of Rarefied Gas Flows". In: *Handbook of Vacuum Technology*. Wiley-VCH, 2008. Chap. 5, pp. 163–220. ISBN: 9783527407231.

[Sha09] F. Sharipov. "Gas Circulation Due an Azimuthal Temperature Distribution Over a Micro-Tube Wall". In: *Proceedings, ASME 2009 7th International Conference on Nanochannels, Microchannels, and Minichannels: Pohang, South Korea, June 22-24, 2009*. 43499. 2009, pp. 373–381. DOI: 10.1115/ICNMM2009-82028.

[Sha10] F. Sharipov. "Tritium flow through a non-symmetrical source. Simulation of gas flow through an injection hole." Internal report. 2010. URL: https://fuzzy.fzk.de/bscw/bscw.cgi/d100305/10-ME-2109-0.pdf.

[Sha16] F. Sharipov. *Rarefied Gas Dynamics. Fundamentals for Research and Practice*. Wiley - VCH, 2016. ISBN: 9783527413263.

[Sha96] F. Sharipov. "Rarefied gas flow through a long tube at any temperature ratio". In: *Journal of Vacuum Science & Technology A* 14.4 (1996), pp. 2627–2635. DOI: 10.1116/1.579991. eprint: https://doi.org/10.1116/1.579991.

[Sha97] F. Sharipov. "Rarefied gas flow through a long tube at arbitrary pressure and temperature drops". In: *Journal of Vacuum Science & Technology A* 15.4 (1997), pp. 2434–2436. DOI: 10.1116/1.580904. eprint: https://doi.org/10.1116/1.580904.

[Sib18] V. Sibille. "Energy loss blinding". Internal report. 2018. URL: https://neutrino.ikp.kit.edu/katrin/images/5/53/Energy_loss_modifications.pdf.

[Sie18] Siemens. *SIMATIC PCS 7*. 2018. URL: https://w3.siemens.com/mcms/process-control-systems/en/distributed-control-system-simatic-pcs-7/Pages/distributed-control-system-simatic-pcs-7.aspx (visited on 09/22/2018).

[Sir+18] A. M. Sirunyan et al. "Search for heavy resonances decaying to a top quark and a bottom quark in the lepton+jets final state in proton-proton collisions at 13 TeV". In: *Physics Letters B* 777 (2018), pp. 39–63. DOI: 10.1016/j.physletb.2017.12.006. arXiv: 1708.08539 [hep-ex].

[SJF00] A. Saenz, S. Jonsell, and P. Froelich. "Improved Molecular Final-State Distribution of HeT^+ for the β-Decay Process of T_2". In: *Physical Review Letters* 84 (2000), pp. 242–245. DOI: 10.1103/PhysRevLett.84.242.

[SK05] F. Sharipov and D. Kalempa. "Separation phenomena in the tritium source and numerical simulations of turbo-molecular pumps". Internal report. 2005. URL: https://fuzzy.fzk.de/bscw/bscw.cgi/d968578/10-ME-2112-0.pdf.

[SK10] F. Sharipov and D. Kalempa. "Separation phenomenon in the Windowless Gaseous Tritium Source of KATRIN experiment. Ternary mixtures". Internal report. 2010. URL: https://fuzzy.fzk.de/bscw/bscw.cgi/d932757/10-ME-2108-0.pdf.

[Sle17] M. Slezák. "Analysis of the gaseous ^{83m}Kr source measurements". talk presented at 33rd KATRIN collaboration meeting. Oct. 2017. URL: https://fuzzy.fzk.de/bscw/bscw.cgi/d1186394/95-TRP-6316-P4-MSlezak.pdf.

[SM75] G. Senjanovic and R. N. Mohapatra. "Exact Left-Right Symmetry and Spontaneous Violation of Parity". In: *Physical Review D* 12 (1975), p. 1502. DOI: 10.1103/PhysRevD.12.1502.

[Sou86] P. C. Souers. *Hydrogen Properties for Fusion Energy*. University of California Press, 1986. ISBN: 0-520-05500-4.

[SS98] F. Sharipov and V. Seleznev. "Data on Internal Rarefied Gas Flows". In: *Journal of Physical and Chemical Reference Data* 27.3 (1998), pp. 657–706. DOI: 10.1063/1.556019.

[Ste+17] N. M. N. Steinbrink et al. "Statistical sensitivity on right-handed currents in presence of eV scale sterile neutrinos with KATRIN". In: *Journal of Cosmology and Astroparticle Physics* 1706.06 (2017), p. 015. DOI: 10.1088/1475-7516/2017/06/015. arXiv: 1703.07667 [hep-ph].

[Ste17] N. M. N. Steinbrink. "Beyond-Standard Model Neutrino Physics Sensitivity with KATRIN". PhD thesis. Westfälische Wilhelms-Universität Münster, 2017.

[Str+14] S. Streubel et al. "Toward a more accurate Q value measurement of tritium: status of THe-Trap". In: *Applied Physics B* 114.1 (Jan. 2014), pp. 137–145. ISSN: 1432-0649. DOI: 10.1007/s00340-013-5669-x.

[Stu10] M. Sturm. "Aufbau und Test des Inner-Loop-Systems der Tritiumquelle von KATRIN". German. PhD thesis. Karlsruher Institut für Technologie (KIT), 2010. DOI: 10.5445/IR/1000019355.

[Stu18] M. Sturm. Private communication. 2018.

[Sut16] C. Sutton. "Ghosts in the machine". In: *CERN courier* (2016). URL: https://cerncourier.com/ghosts-in-the-machine/.

[SV80] J. Schechter and J. W. F. Valle. "Neutrino Masses in SU(2) x U(1) Theories". In: *Physical Review D* 22 (1980), p. 2227. DOI: 10.1103/PhysRevD.22.2227.

[SV82] J. Schechter and J. W. F. Valle. "Neutrino Decay and Spontaneous Violation of Lepton Number". In: *Physical Review* 25 (1982), p. 774. DOI: 10.1103/PhysRevD.25.774.

[SVS17] J. Sentkerestiová, D. Vénos, and M. Slezák. "Gaseous ^{83m}Kr generator of monoenergetic electrons based on ^{83}Rb deposited in zeolite". In: *Journal of Physics: Conference Series* 888.1 (2017), p. 012072. DOI: 10.1088/1742-6596/888/1/012072.

[Tan+18] M. Tanabashi et al. "Review of Particle Physics". In: *Physical Review D* 98 (3 Aug. 2018), p. 030001. DOI: 10.1103/PhysRevD.98.030001.

[The04] The London Standard. ""CLEVER HANS" AGAIN – Expert Commission Decides That the Horse Actually Reasons". In: *The New York Times* (Oct. 1904). URL: https://timesmachine.nytimes.com/timesmachine/1904/10/02/120289067.pdf.

[The15] The Royal Swedish Academy of Sciences. *Metamorphosis in the particle world*. Press release. 2015. URL: https://www.nobelprize.org/prizes/physics/2015/press-release/ (visited on 10/19/2018).

[Tro18] N. Trost. "Modeling and measurement of Rydberg-State mediated Background at the KATRIN Main Spectrometer". To be published. PhD thesis. Karlsruher Institut für Technologie (KIT), 2018.

[Vén+18] D. Vénos et al. "Properties of ^{83m}Kr conversion electrons and their use in the KATRIN experiment". In: *Journal of Instrumentation* 13.02 (2018), T02012. DOI: 10.1088/1748-0221/13/02/T02012.

[Way18a] WayCon. *Seilzugsensor Serie SX135*. 2018. URL: https://www.waycon.de/fileadmin/seilzugsensoren/Seilzug-Sensor-SX135.pdf (visited on 09/22/2018).

[Way18b] WayCon. *Seilzugsensor Serie SX80*. 2018. URL: https://www.waycon.de/fileadmin/seilzugsensoren/Seilzug-Sensor-SX80.pdf (visited on 09/22/2018).

[Wei62] S. Weinberg. "Universal Neutrino Degeneracy". In: *Physical Review* 128 (3 Nov. 1962), pp. 1457–1473. DOI: 10.1103/PhysRev.128.1457.

[Wol78] L. Wolfenstein. "Neutrino oscillations in matter". In: *Physical Review D* 17 (9 May 1978), pp. 2369–2374. DOI: 10.1103/PhysRevD.17.2369.

[Wu+57] C. S. Wu et al. "Experimental Test of Parity Conservation in Beta Decay". In: *Physical Review* 105 (1957), pp. 1413–1414. DOI: 10.1103/PhysRev.105.1413.

[WVH] C. Weinheimer, K. Valerius, and F. Heizmann. *Erwartete Unsicherheit auf den effektiven KATRIN Endpunkt*. Private communication.

[Yan80] T. Yanagida. "Horizontal Symmetry and Masses of Neutrinos". In: *Progress of Theoretical Physics* 64 (1980), p. 1103. DOI: 10.1143/PTP.64.1103.

[Zel17] G. Zeller. "Development of a calibration procedure and calculation of the uncertainty budget for the KATRIN laser Raman system". Master thesis. Karlsruher Institut für Technologie (KIT), 2017. URL: https://www.katrin.kit.edu/publikationen/mth-Zeller.pdf.

[Zel18] G. Zeller. *Remarks on updates in RunSummary2f*. July 4, 2018. URL: https://neutrino.ikp.kit.edu/katrin/images/0/09/RemarksOnRunSummary2f-LARA.pdf (visited on 11/08/2018).

[ZK66] G. T. Zatsepin and V. A. Kuzmin. "Upper limit of the spectrum of cosmic rays". In: *Journal of Experimental and Theoretical Physics Letters* 4 (1966), pp. 78–80.

ACKNOWLEDGEMENTS

Finally, I want to express my gratitude that I was given the chance of being part of the lively KATRIN collaboration during this work. I would like to thank all the persons who supported me friendly and professionally to complete this thesis. In particular, I want to give thanks to

- Prof. Guido Drexlin for the possibility to perform this interesting and challenging work in the framework of the KATRIN collaboration,
- Prof. Ulrich Husemann for the evaluation of this thesis as second reviewer,
- Dr. Kathrin Valerius for her inspiring and caring supervision, her infectious enthusiasm for physics, and her support for my stay in the U.S.,
- Prof. Diana Parno (CMU) and Prof. Joe Formaggio (MIT) for inviting me to CMU and MIT,
- the Karlsruhe School of Elementary Particle and Astroparticle Physics: Science and Technology (KSETA), especially Dr. Irmgard Langbein, for supporting my doctoral project, enabling several business trips, and facilitating my participation in the MBA fundamentals programme of the HECTOR business school,
- the Karlsruhe House of Young Scientists (KHYS), especially Gaby Weick, for enabling and supporting my stay in the U.S. at CMU and MIT,
- Dr. Ferenc Glück for the support with the gas dynamics calculations, magnetic fields and general numerical problems,
- Prof. Felix Sharipov for the support with the gas dynamics calculations,
- Dr. Valérian Sibille and Dr. Joachim Wolf for the huge support and fruitful discussions concerning blind analysis of KATRIN data,
- Hendrik Seitz-Moskaliuk for legendary double rooms at various conferences, with the highlight of the shared Neutrino2016 poster prize,
- Dr. Alexander Jansen for skilful and professional management of the WGTS task,
- Maximilian Kristen, Klaus Mehret, and Steffen Lichter for the fast support with the WGTS magnetic field measuring system,

- Heike Boltz and the WGTS team for the inspiring atmosphere and technical insights during the (electrical) WGTS commissioning,
- Alexander Marsteller for answering my endless questions about the loop system,
- Karol Debowski and Manuel Klein for the nice office atmosphere,
- Manuel Klein for sharing the pressure of the same defense date and the film career,
- Dr. Martin Babutzka and Dr. Laura Kuckert as former office mates,
- all members of Kathrin's YIG, for the nice and productive working atmosphere,
- the secretaries and assistants Marion Behechti, Diana Fellner, Katharina Fischer, Anna Friedrich, Brigitte Gering, Barabara Lepold, and Eva Porter for friendly and fast support in administrative procedures,
- Thomas Csabo for providing fast support with (laboratory) laptops,
- Dr. Marco Kleesiek and Prof. Sanshiro Enomoto for exhaustive C++ and other programming support,
- all readers and correctors of this thesis,
- Dr. Moritz Hackenjos, Anton Huber, and Carsten Röttele for being colleagues and friends at the same time,
- C. Schürle, J. Faiß, and S. Koch for the "writing holidays", and A. Fiedler for the (short) distractions during writing this thesis,
- all who have been forgotten on this list...

Special thanks goes to my family and all my friends.

The biggest thank you is for my girlfriend Carola Schürle for her tireless support and distraction, especially in the final phase of this thesis. Thank you for being my light!